

**VIBRATION, BUCKLING AND DYNAMIC INSTABILITY  
STUDIES ON FGM PLATES UNDER CONSERVATIVE  
AND NON-CONSERVATIVE SYSTEM OF FORCES**

Thesis

Submitted in partial fulfilment of the requirements for the degree of

**DOCTOR OF PHILOSOPHY**

by

**SACHIN H.  
(177123CV011)**



**DEPARTMENT OF CIVIL ENGINEERING  
NATIONAL INSTITUTE OF TECHNOLOGY KARNATAKA  
SURATHKAL, MANGALURU – 575 025**

**FEBRUARY, 2024**



**VIBRATION, BUCKLING AND DYNAMIC INSTABILITY  
STUDIES ON FGM PLATES UNDER CONSERVATIVE  
AND NON-CONSERVATIVE SYSTEM OF FORCES**

Thesis

Submitted in partial fulfilment of the requirements for the degree of

**DOCTOR OF PHILOSOPHY**

by

**SACHIN H.  
(177123CV011)**

Under the Guidance of

**Dr. Pavan G. S.  
Assistant Professor**

**Dr. K. Swaminathan  
Professor**



**DEPARTMENT OF CIVIL ENGINEERING  
NATIONAL INSTITUTE OF TECHNOLOGY KARNATAKA  
SURATHKAL, MANGALURU – 575 025  
FEBRUARY, 2024**



## DECLARATION

I hereby declare that the Research Thesis entitled "**Vibration, Buckling and Dynamic Instability Studies on FGM Plates under Conservative and Non-Conservative System of Forces**" which is being submitted to the National Institute of Technology Karnataka, Surathkal in partial fulfilment of the requirements for the award of the degree of Doctor of Philosophy in Department of Civil Engineering, is a bonafide report of the research work carried out by me. The material contained in this Research Thesis has not been submitted to any university or institution for the award of any degree.

*Sachin H.*

177123CV011, SACHIN H.  
Department of Civil Engineering

Place: NITK - Surathkal

Date: 23/02/2024

## CERTIFICATE

This is to certify that the Research Thesis entitled “**Vibration, Buckling and Dynamic Instability Studies on FGM Plates under Conservative and Non-Conservative System of Forces**” submitted by **Mr. SACHIN H. (Register Number: 177123CV011)**, as the record of the research work carried out by him, is accepted as the Research Thesis submission in partial fulfilment of the requirements for the award of the **Degree of Doctor of Philosophy** in the **Department of Civil Engineering**.

Research Guides



Dr. PAVAN G. S.  
Assistant Professor



Dr. K. SWAMINATHAN  
Professor (Retired)



Chairperson-DRPC

**Chairman (DRPC)**  
**Department of Civil Engineering**  
**National Institute of Technology Karnataka**  
**Surathkal, Mangalore - 575 025, Karnataka, INDIA**  
Department of Civil Engineering

Date: 23/02/2024



## ACKNOWLEDGEMENT

I would like to express my heartfelt gratitude and indebtedness to my research supervisors, Dr. K. Swaminathan, Professor, and Dr. Pavan G. S., Assistant Professor, Department of Civil Engineering, National Institute of Technology Karnataka, Surathkal, for their inspiring guidance, constant encouragement, and diligent assistance in allowing me to conduct the studies presented in this thesis. The timely guidance and the scientific support received from my supervisors is sincerely acknowledged.

I would like to offer my sincere thanks to Professor and Head of the Department (HOD) Prof. Subhash C. Yaragal, former HOD Prof. B. R. Jayalekshmi and all faculty members of the Department of Civil Engineering, NITK, Surathkal, for their precious teaching, suggestions, constant encouragement, incubating the learning environment, and family atmosphere and for providing necessary facilities during the period of my research work. I also like to extend my gratitude to Prof. Sitaram Nayak, Dr. Prasanth M. H., Assistant Professor and all the teaching and nonteaching staff of Civil Engineering Department for their help provided during the research work.

I am thankful to the members of the Research Progress Assessment Committee (RPAC), Dr. Rajasekaran C., Assistant Professor, Department of Civil Engineering and Dr. Debabrata Karmakar, Assistant Professor, Department of Water Resource and Ocean Engineering, for their patient hearing to my seminars and for their suggestions, evaluation and constant encouragement.

I would like to place it on record my thanks and appreciation to the, Chairman (H.O.D) and members of the Doctoral Research Program Committee (DRPC), Civil Engineering Department for extending all facilities to carry out my research work in time.

Similar, profound gratitude goes to Dr. Rajanna T., Assistant Professor who has helped me in the coding and providing technical inputs for the research from Bhusanayana Mukundadas Sreenivasaiah College of Engineering (B.M.S.C.E), Bangalore.

I would like to offer my sincere appreciation to all the research scholars in and outside the Department of Civil engineering for their relentless motivation and support. Special mention goes to Dr. Kesav B Rao, Dr. Ashik Bellary, Dr. Naveen Kumar D. T., Dr. Sreya, Dr. Sangeetha D. M., Dr. Sarathchandra, Dr. Pavankumar R Sondar, Dr. Yathish Muddappa P. P., Dr. Subash Chandra K. S., Dr. Vinayak Kallannavar, Dr. Rakesh Patil, Dr. Dylan Carvalho, Dr. Ravi Kiran Hiremath, Dr. Mohammad Sohail Bhakshi, Mr. Purnachandra Tanti, Mr. Hemanth Kumar, Mr. Nagesh, Mr. Chethan H. C., Mr. Vinod Krishna, Mr Akshay Kumar, Mr. Arichandran, Mrs. Prakruthi Vasanth, Mr. Akshay Prakash Kalgutkar, Mr. Pruthvik B. M, Mr. Dhanush S Ganig and Mr. Aiyappa for their constant encouragement throughout my research work.

Mr. Afsal K. P., Mr. Anil K Sagar, Mr. Jithin Raj, Mrs. Ashwaty Shaji, and Mr. Pratyush Kumar Gautam from my research team deserve special recognition for their consistent backing throughout my research

Most significantly, I would like to express thanks my family members especially my parents, Mr. N. Hirannaiah and Mrs. Nagarathna K., brother Mr. Suhas H., who always supported and encouraged me in this endeavour and their support kept me going through hard times and gave me confidence, courage and inspiration.

NITK, Surathkal

(Sachin H.)

Date: 23/02/2024

## ABSTRACT

The present study investigates the vibration and buckling behaviour of porous Functionally Graded Sandwich Plates (FGSP) with and without cutouts subjected to Non-uniform Inplane Edge Loads (NIELs) and localised in-plane edge loads in non-thermal (mechanical) and thermal environment (thermo-mechanical) using Finite Element (FE) method. Additionally, the study explores dynamic instability characteristics of the FGSP under a non-thermal environment. The study is carried out by selecting different kinds of sandwich configurations such that there is no material mismatch along the thickness directions. Due to the material asymmetry occurring in the sandwich configurations, a physical neutral surface is incorporated in the formulation. The porosity imperfections that occur during the manufacturing process of FGSPs are accounted for in this study by considering different types of porosity distribution models and are modelled as the criteria of stiffness reduction. The plate members made up of FGSPs commonly features cutouts due to practical requirements and experience flutter due to a non-conservative system of forces. As a result, structural responses such as vibration, buckling and dynamic instability of porous FGSP are affected. Therefore, this work aims to examine the vibration, buckling and dynamic instability characteristics of porous FGSP with and without geometric discontinuity subjected to NIELs and localised edge loads under non-thermal and thermal environments. The material properties of porous FGSPs are evaluated using modified power law and sigmoid function and are assumed to be temperature-dependent for plates studied in a thermal environment. The application of different cases of NIELs on the plate with cutouts in thermal and non-thermal environments results in non-uniform stress distribution. Hence a novel dynamic approach has been proposed to evaluate buckling loads by implementing two sets of boundary conditions. The first set of the boundary conditions calculates pre-buckling stress, while the second set calculates critical buckling loads.

The study includes a convergence analysis of the proposed FE formulations and further validation through comparisons with numerical results available in the published literature. After verifying the theoretical formulations and solution methodologies, parametric studies are conducted by varying aspect ratios, layer

schemes, support conditions, side-to-thickness ratios, sandwich configurations, cutout ratios, and more. The numerical solutions based on the current First-order Shear Deformation Theory (FSDT) can serve as a benchmark for future reference when dealing with porous FGSPs containing cutouts. It is expected that the findings from this study will offer valuable insights for the analysis and design of Functionally Graded Material (FGM) plates in practical engineering applications.

**Keywords:** FGM sandwich plates; Vibration; Buckling; Dynamic Instability; Non-uniform loads; Thermo-mechanical loads; Cutout; Porosity.

# CONTENTS

	<b>Page No.</b>
<b>LIST OF FIGURES</b>	<b>vii</b>
<b>LIST OF TABLES</b>	<b>xvii</b>
<b>NOMENCLATURE</b>	<b>xxi</b>
<b>1. INTRODUCTION</b>	<b>1</b>
1.1 PRELIMINARY REMARKS	1
1.2 AIM AND SCOPE	7
1.3 LAYOUT OF THESIS	9
<b>2. LITERATURE REVIEW</b>	<b>13</b>
2.1 PRELIMINARY REMARKS	13
2.2 VIBRATION ANALYSIS OF FGM	14
2.2.1 Vibration without Temperature	14
2.2.2 Vibration with Temperature	17
2.3 BUCKLING ANALYSIS OF FGM	18
2.3.1 Buckling without Temperature	19
2.3.2 Buckling with Temperature	21
2.4 DYNAMIC INSTABILITY ANALYSIS OF FGM	23
2.5 RESEARCH GAP	25
<b>3. THEORETICAL FORMULATION AND SOLUTION</b>	<b>27</b>
3.1 GENERAL	27
3.1.1 Assumptions	27
3.2 EFFECTIVE MATERIAL PROPERTIES OF FGSP	28
3.2.1 Power Law Functionally Graded Sandwich Plate (PFGSP)	30
3.2.2 Sigmoidal Based Functionally Graded Sandwich Plate (SFGSP)	31
3.3 POROSITY DISTRIBUTION MODELS	33
3.4 GEOMETRY OF SANDWICH PLATE	35
3.5 DISPLACEMENT MODEL	36
3.6 STRAIN–DISPLACEMENTS RELATION	36
3.7 CONSTITUTIVE RELATIONSHIP	37

3.8	LINEAR STRAIN-NODAL DISPLACEMENT MATRIX	39
3.9	FINITE ELEMENT FORMULATION	40
3.9.1	Iso-Parametric Element	40
3.9.2	Elemental Stiffness Matrix	42
3.9.3	Geometric Stiffness Matrix	43
3.10	ELEMENTAL MASS MATRIX	47
3.10.1	Work Done by Follower Force	48
3.11	GOVERNING EQUATION	50
3.12	CLASSIFICATION OF PROBLEMS	51
3.13	SUPPORT CONDITIONS	52
3.14	COMPUTER IMPLEMENTATION	53
3.15	CLOSURE	53
<b>4.</b>	<b>VIBRATION AND BUCKLING ANALYSIS OF POROUS FG SANDWICH PLATE WITH/WITHOUT CUTOUT SUBJECTED TO LOCALISED IN- PLANE EDGE LOADS</b>	<b>55</b>
4.1	PRELIMINARY REMARKS	55
4.2	PROBLEM DESCRIPTION	56
4.3	RESULTS AND DISCUSSION	56
4.3.1	Convergence and Validation Studies	57
4.3.2	Parametric Studies	62
4.3.2.1	Vibration behaviour of single layer FGM and FGSP with and without Porosity under localised edge loads	63
4.3.2.2	Buckling characteristics of single layer FGM plate without porosity under load Type-I and Type-II	67
4.3.2.3	Buckling characteristics of different cases of FGM plates with porosity under load Type-I and Type-II	70
4.3.2.4	Buckling characteristics of single layer FGM plates without Porosity under load Type-III and Type-IV	74
4.3.2.5	Buckling behaviour of different cases of FGM plate with porosity under load Type-III & Type-IV	77
4.3.2.6	Effect of side-to-thickness and support conditions on different cases of FGM sandwich plate with porosity	81

4.3.2.7	Buckling characteristics of FGSP with porosity and cutout under load Type-I and Type-II	83
4.3.2.8	Buckling characteristics of FGSP with porosity and cutout under load Type-III and Type-IV	85
4.4	CLOSURE	86
<b>5.</b>	<b>VIBRATION AND BUCKLING ANALYSIS OF POROUS FG SANDWICH PLATES WITH AND WITHOUT CUTOUT UNDER NONUNIFORM IN-PLANE EDGE LOADS</b>	<b>89</b>
5.1	PRELIMINARY REMARKS	89
5.2	PROBLEM DESCRIPTION	89
5.3	RESULTS AND DISCUSSION	90
5.3.1	Convergence and Validation Studies	92
5.3.2	Parametric Studies	94
5.3.2.1	Vibration characteristics of porous FGSPs with cutouts subjected to NIELs	97
5.3.2.2	Effect of different cases of NIELs and cutout ratios on buckling characteristics of porous FGSPs	101
5.3.2.3	Effect of material idealisation technique on buckling characteristics of porous FGSPs with cutouts	104
5.3.2.4	Effect of porosity distribution on buckling characteristics of porous FGSPs with cutouts	106
5.3.2.5	Effect of different sandwich layer schemes on buckling characteristics of porous FGSPs with cutouts	108
5.3.2.6	Effect of support conditions and side-to-thickness ratio on buckling characteristics of porous FGSPs with cutouts	109
5.3.2.7	Effect of varying aspect ratio and cutout ratio on buckling characteristics of porous FGSPs	112
5.3.2.8	Effect of varying position of the cutouts and cutout ratio on buckling characteristics of porous FGSPs	113
5.4	CLOSURE	116

<b>6. VIBRATION AND BUCKLING ANALYSIS OF POROUS FG SANDWICH PLATES WITH AND WITHOUT CUTOUT UNDER THERMO-MECHANICAL LOADS</b>	<b>117</b>
6.1 PRELIMINARY REMARKS	117
6.2 PROBLEM DESCRIPTION	118
6.3 RESULTS AND DISCUSSION	119
6.3.1 Convergence and Validation Studies	120
6.3.2 Parametric Studies	125
6.3.2.1 Vibration characteristics of porous FGSPs with cutouts subjected to thermomechanical loads	125
6.3.2.2 Effect of cutout size, temperature and nonuniform loads on buckling response of porous FGSPs under thermomechanical loads	129
6.3.2.3 Effect of cutout size and porosity on buckling response of porous FGSPs under thermomechanical loads	130
6.3.2.4 Effect of porosity index and volume fraction exponent on buckling response of porous FGSPs under thermomechanical loads	130
6.3.2.5 Effect of porosity distributions and sandwich configurations on buckling response of porous FGSPs under thermomechanical loads	132
6.3.2.6 Effect of support condition on buckling response of porous FGSPs under thermomechanical loads	135
6.3.2.7 Effect of material thermal expansion coefficient on buckling response of porous FGSPs under thermomechanical loads	138
6.3.2.8 Stability region	140
6.4 CLOSURE	140

<b>7. DYNAMIC INSTABILITY ANALYSIS OF POROUS FG SANDWICH PLATE WITH/WITHOUT CUTOUT</b>	<b>143</b>
7.1 PRELIMINARY REMARKS	143
7.2 PROBLEM DESCRIPTION	143
7.3 RESULTS AND DISCUSSION	144
7.3.1 Validation Studies	145
7.3.2 Parametric Studies	146
7.3.2.1 Effect of volume fraction exponent	146
7.3.2.2 Effect of porosity distribution	147
7.3.2.3 Effect of porosity index	149
7.3.2.4 Effect of sandwich layer scheme	149
7.3.2.5 Effect of load control parameter under uniform follower load	150
7.3.2.6 Effect of different non-uniform follower loads.	151
7.3.2.7 Effect of aspect ratio	152
7.3.2.8 Effect of cutout ratio	152
7.3.2.9 Effect sandwich configuration and material idealization technique	153
7.3.2.10 Effect of localised edge loads and cutout ratio	155
7.4 CLOSURE	156
<b>8. CONCLUSION</b>	<b>158</b>
8.1 GENRAL	158
8.2 SUGGESTIONS FOR FUTURE WORK	164
REFERENCE	167



## LIST OF FIGURES

<b>Figure No.</b>	<b>Description</b>	<b>Page No.</b>
Figure 1.1(a)	FGM (a) Continuous distribution	02
Figure 1.1(b)	FGM (b) Specimen of Al <sub>2</sub> O <sub>3</sub> -Ni FGM having layers with different compositions	02
Figure 1.2(a)	FGM in nature (a) Human teeth	02
Figure 1.2(b)	FGM in nature (b) Organic bone	02
Figure 1.2(c)	FGM in nature (c) Plant fibre	02
Figure 1.3(a)	Schematic side-view of a plate under a follower force acting at an angle $\phi\theta$ ; $0 \leq \phi \leq 1$ .	05
Figure 1.3(b)	Type of instabilities that can be captured using this formulation - $\text{Im}(\gamma) < 0$ and $\text{Re}(\gamma) = 0$ : Divergence type of instability	05
Figure 1.3(c)	Divergence type of instability (c) $\text{Im}(\gamma) < 0$ and $\text{Re}(\gamma) \neq 0$ : Flutter type of instability	05
Figure 2.1	A breakdown of significant moments in the history of the study and the development of FGMs	14
Figure 2.2	Flowchart showing the organization of literature presented in this study	15
Figure 3.1(a)	Schematics of configurations of FG plates Single layer	28
Figure 3.1(b)	Schematics of configurations of FG plates FCF Sandwich	28
Figure 3.1(c)	Schematics of configurations of FG plates MFC Sandwich	28
Figure 3.1(d)	Schematics of configurations of FG plates MFM Sandwich	28
Figure 3.2	Variation of volume fraction of ceramic material along the dimensionless thickness of single layer FGM plates for different volumes fraction exponent	30
Figure 3.3(a)	Effective Young's modulus versus dimensionless thickness of FCF –PFGSP for several volume fraction exponent ( $n$ )	31
Figure 3.3(b)	Effective Young's modulus versus dimensionless thickness of FCF–SFGSP for several volume fraction exponent ( $n$ )	31
Figure 3.4	The position of middle surface and neutral surface for FGSP	32

Figure 3.5	Schematic cross-section of 1-1-1 FCF FGSP with porosity distribution	34
Figure 3.6	Schematic cross-section of 1-1-1 MFC FGSP with porosity distribution	35
Figure 3.7	Schematic of FGSP with circular cutout	36
Figure 3.8	Rectangular Element with natural coordinates and local node number	41
Figure 3.9	Plate with tangential follower load	49
Figure 3.10	Support conditions considered in the current study	52
Figure 4.1(a)	Representation of loading cases Type-I	57
Figure 4.1(b)	Representation of loading cases Type-II	57
Figure 4.1(c)	Representation of loading cases Type-III	57
Figure 4.1(d)	Representation of loading cases Type-IV	57
Figure 4.2(a)	Variation of non-dimensional natural frequency of single layer FGM plate for different load width ratios	64
Figure 4.2(b)	Variation of non-dimensional natural frequency of single layer FGM plate for different volume fraction exponents	64
Figure 4.3(a)	Variation of non-dimensional natural frequency for plates subjected to load Type-III and different porosity distributions (Single layer FGM)	65
Figure 4.3 (b)	Variation of non-dimensional natural frequency for plates subjected to load Type-III and different layer schemes (FCF sandwich)	65
Figure 4.4(a)	Variation of non-dimensional natural frequency with porosity indices for FCF 1-2-1 sandwich plates having U-D type of porosity under load Type-II with $c/b = 0.6$	66
Figure 4.4(b)	Variation of the non-dimensional natural frequency with porosity indices for MFM 1-2-1 sandwich plates having U-D type of porosity under load Type-II with $c/b = 0.6$	66
Figure 4.5(a)	Variation of non-dimensional natural frequency for FCF 1-2-1	

	FGSP having V-D porosity distribution subjected to different types of localised edges load with $c/b = 0.2$ .	67
Figure 4.5(b)	Variation of non-dimensional natural frequency for MFM 1-2-1 FGSP having V-D porosity distribution subjected to different types of localised edges load with $c/b = 0.2$ .	67
Figure 4.6(a)	Variation of non-dimensional critical buckling load with load width ratios for single layer FGM plates without porosity subjected to Types-I loading -Influence of various volumes fraction exponents influence of various volumes fraction exponents	68
Figure 4.6(b)	Variation of non-dimensional critical buckling load with load width ratios for single layer FGM plates without porosity subjected to Type-I loading -Influence of different aspect ratio of the plates	68
Figure 4.7	Modes shapes for various aspect ratios of single layer FGM plates without porosity and $n = 1$ under load Type-I	69
Figure 4.8(a)	Variation of non-dimensional critical buckling load with load width ratios for single layer FGM plates without porosity subjected to Type-II loadings-Influence of various volume fraction exponent	70
Figure 4.8(b)	Variation of non-dimensional critical buckling load with load width ratios for single layer FGM plates without porosity subjected to Type-II loadings-Influence of various aspects the ratio of the plate	70
Figure 4.9	Variation of effective Young's modulus through the thickness of single layer FGM plates with V-D type porosity distribution	72
Figure 4.10	Variation in the non-dimensional critical buckling load ( $\bar{P}_{cr}$ ) of simply supported single layer FGM plates under localised edge load with porosity index and porosity distribution (Type-I and Type-II, $n = 2.0$ , $c/b = 0.2$ , $b/h = 100$ )	75

Figure 4.11(a)	Variation of non-dimensional critical buckling load with load width ratios of single layer FGM plates without porosity subjected to Type-III loading effect of volume fraction exponent	76
Figure 4.11 (b)	Variation of non-dimensional critical buckling load with load width ratios of single layer FGM plates without porosity subjected to Type-III loading effect of aspect ratio of the plates	76
Figure 4.12(a)	Variation of non-dimensional critical buckling load with load width ratio for single layer FGM plates without porosity subjected to Type-IV loadings -Effect of volumes fraction exponents	77
Figure 4.12(b)	Variation of non-dimensional critical buckling with load width ratio for single layer FGM plates without porosity subjected to Type-IV loadings -Effect of aspect ratio of the plate	77
Figure 4.13	Variation of non-dimensional critical buckling load ( $\bar{P}_{cr}$ ) for simply supported single layer FGM plates subjected to localised edge load with different porosity indices and porosity distribution (Type-III and Type-IV, $n = 2.0$ , $c/b = 0.2$ )	81
Figure 4.14(a)	Variation of non-dimensional critical buckling load with load width ratios for FCF FGM plates with porosity and varying cutout ratio subjected to Type-I	85
Figure 4.14(b)	Variation of non-dimensional critical buckling load with load width ratios for FCF FGM plates with porosity and varying cutout ratio subjected to Type-II	85
Figure 4.15(a)	Variation of non-dimensional critical buckling load with load width ratios for FCF FGM plates with porosity and varying cutout ratio subjected to Type-III	86
Figure 4.15(b)	Variation of non-dimensional critical buckling load with load width ratios for FCF FGM plates with porosity and varying cutout ratio subjected to Type-IV	86
Figure 5.1	Various cases of linearly varying in-plane edge loads	90
Figure 5.2	Various cases of nonlinearly varying in-plane edge loads	90

Figure 5.3	Detailed Mesh pattern over full plate featuring a circular shaped cutout acted by NIELs	92
Figure 5.4	Variation of $\bar{\omega}$ for square porous FCF PFGSP with cutout subjected to nonlinearly varying loads	97
Figure 5.5	Variation of $\bar{\omega}$ for square porous FCF PFGSP with cutout subjected to NL-1 for different sandwich layer schemes	98
Figure 5.6	Variation of $\bar{\omega}$ for square porous FCF PFGSP with cutout for different cutout ratios	99
Figure 5.7	Variation of $\bar{\omega}$ for square porous FCF PFGSP and SFGSP with cutout for different porosity distributions	100
Figure 5.8	Variation of $\bar{\omega}$ for square porous FCF SFGSP with cutout for different porosity distributions and porosity indices	100
Figure 5.9	Variation of $\bar{\omega}$ for square porous FCF SFGSP with cutout for different cutout ratios and volume fraction exponent	101
Figure 5.10(a)	Effect of different cases of NIELs and cutout ratio on $\bar{P}_{cr}$ of FCF PFGSP subjected to linearly varying loads	102
Figure 5.10(b)	Effect of different cases of NIELs and cutout ratio on $\bar{P}_{cr}$ of FCF PFGSP subjected to nonlinearly varying loads	102
Figure 5.11	In-plane stress contours for FCF PFGSP subjected to uniaxial linearly and nonlinearly varying in-plane edge loads	103
Figure 5.12(a)	Effect of porosity on $\bar{P}_{cr}$ of FCF PFGSP subjected to linearly varying loads	104
Figure 5.12(b)	Effect of porosity on $\bar{P}_{cr}$ of FCF PFGSP subjected to nonlinearly varying loads	104
Figure 5.13(a)	Effect of type of material idealization technique on $\bar{P}_{cr}$ of PFGSP and SFGSP, FCF with cutouts subjected to load NL-6	105
Figure 5.13(b)	Effect of type of material idealization technique on $\bar{P}_{cr}$	

	of PFGSP and SFGSP MFC with cutouts subjected to load NL-6	105
Figure 5.14	Effective Young's modulus versus dimensionless thickness of FCF SFGSP with different porosity distribution model.	108
Figure 5.15(a)	Effect of sandwich layer scheme on $\bar{P}_{cr}$ for FCF with cutout subjected to load NL-5	109
Figure 5.15 (b)	Effect of sandwich layer scheme on $\bar{P}_{cr}$ for MFC PFGSP with cutout subjected to load NL-5.	109
Figure 5.16(a)	Effect of $a/b$ and $d/b$ on $\bar{P}_{cr}$ of FCF PFGSP (1-1-1) subjected to NL-7	114
Figure 5.16(b)	Effect of $a/b$ and $d/b$ on $\bar{P}_{cr}$ of FCF PFGSP (1-1-1) subjected to LL-6.	114
Figure 5.17	In-plane stress distribution and buckling mode shapes for FCF PFGSP with various cutout ratios with (a) $a/b = 1.0$ and (b) $a/b = 2.0$ subjected to load NL-6	114
Figure 5.18(a)	Effect of position of cutout and cutout ratio on $\bar{P}_{cr}$ of FCF PFGSP with $a/b = 1.0$	115
Figure 5.18(b)	Effect of position of cutout and cutout ratio on $\bar{P}_{cr}$ of FCF PFGSP with $a/b = 2.0$	115
Figure 5.19	Buckling mode shapes for FCF PFGSP of $a/b = 2.0$ and subjected to load NL- 5	116
Figure 6.1	Various cases of in-plane compressive edge load	118
Figure 6.2(a)	Variation of temperature dependent properties -Young's modulus with temperature	121
Figure 6.2(b)	Variation of temperature dependent properties -thermal coefficient of expansion with temperature	121
Figure 6.3	Detailed Mesh pattern over full plate featuring a circular shaped cutout acted by NIELs	122

Figure 6.4(a)	Comparison of frequency of CFR laminated composite plate with cutout	123
Figure 6.4(b)	Comparison of frequency of GFR laminated composite plate with cutout	123
Figure 6.5	Effect of cutout ratio on $\bar{\omega}$ of square porous FCF SFGSPs ( $a/b = 1.0$ ) subjected to in-plane load and $\Delta T = 100$ .	127
Figure 6.6	Effect of different NIEL on $\bar{\omega}$ for porous FCF SFGSPs ( $a/b = 1.0$ ) with cutout under $\Delta T = 100$	127
Figure 6.7	Effect of porosity distribution on $\bar{\omega}$ for porous FCF SFGSPs ( $a/b = 1.0$ ) with cutout under inplane load and $\Delta T = 100$	128
Figure 6.8	Effect of $p_i$ and temperature rise on $\bar{\omega}$ of porous FCF PFGSPs ( $a/b = 1.0$ ) under inplane load	128
Figure 6.9	Effect of $p_i$ and temperature rise on $\bar{\omega}$ of porous MFC PFGSPs ( $a/b = 1.0$ ) under inplane load	129
Figure 6.10	Effect of different boundary condition on $\bar{\omega}$ of porous FCF PFGSPs ( $a/b = 1.0$ ) under inplane load and $\Delta T = 100$	129
Figure 6.11(a)	Effect of various cutout ratio, temperature and nonuniform loading on $\bar{P}_{cr}$ of square simply supported porous FCF SFGSPs under thermomechanical loading -Graphical line plot	131
Figure 6.11(b)	Effect of various cutout ratio, temperature and nonuniform loading on $\bar{P}_{cr}$ of square simply supported porous FCF SFGSP under thermomechanical loading -Histogram	131
Figure 6.12(a)	Coupled influence of porosity, cutout size and temperature on $\bar{P}_{cr}$ of square simply supported FCF SFGSP porous plates under thermomechanical loading -Graphical line plot	131
Figure 6.12 (b)	Coupled influence of porosity, cutout size and temperature on $\bar{P}_{cr}$ of square simply supported FCF SFGSP porous plates under thermomechanical loading -Histogram	131
Figure 6.13(a)	Effect of $p_i$ and $n$ on $\bar{P}_{cr}$ of porous FCF PFGSP under	

	uniform temperature environment	132
Figure 6.13(b)	Effect of $p_i$ and $n$ on $\bar{P}_{cr}$ of porous FCF SFGSP under uniform temperature environment	132
Figure 6.14(a)	Effect of $p_i$ and $n$ on $\bar{P}_{cr}$ of MFC–PFGSP under uniform temperature environment	133
Figure 6.14(b)	Effect of $p_i$ and $n$ on $\bar{P}_{cr}$ of MFC–SFGSP under uniform temperature environment	133
Figure 6.15(a)	Effect of porosity distribution on the $\bar{P}_{cr}$ of FCF–SFGSP under a thermomechanical environment ( $n=2.0, b/h=10, d/b = 0.5$ )	135
Figure 6.15 (b)	Effect of porosity distribution on the $\bar{P}_{cr}$ of MFC SFGSP under a thermomechanical environment ( $n=2, b/h=10, d/b = 0.5$ )	135
Figure 6.16(a)	Effect of sandwich layer scheme and porosity distribution on the $\bar{P}_{cr}$ of FCF and MFC SFGSP ( $\text{Si}_3\text{N}_4/\text{SUS304}$ ) $\Delta T = 50$ under thermomechanical environment ( $b/h = 10$ )	138
Figure 6.16 (b)	Effect of sandwich layer scheme and porosity distribution on the $\bar{P}_{cr}$ of FCF and MFC SFGSP ( $\text{Si}_3\text{N}_4/\text{SUS304}$ ) $\Delta T = 300$ under thermomechanical environment ( $b/h = 10$ )	138
Figure 6.17(a)	Impact of material, $n$ and porosity on the $\bar{P}_{cr}$ of MFC SFGSP $\text{Si}_3\text{N}_4/\text{SUS304}$ under thermomechanical loads ( $b/h = 10$ )	139
Figure 6.17 (b)	Impact of material, $n$ and porosity on the $\bar{P}_{cr}$ of MFC SFGSP $\text{ZrO}_2/\text{SUS304}$ under thermomechanical loads ( $b/h = 10$ )	139
Figure 6.18(a)	Influence of loading pattern on the stability region of FCF SFGSP under thermomechanical environment	140
Figure 6.18(b)	Influence of $d/b$ on the stability region of FCF SFGSP under thermomechanical environment	140
Figure 7.1	Representation of loading cases (a) Type-I, (b) Type-III	144
Figure 7.2	Various cases of in-plane edge loads	144

Figure 7.3(a)	Influence of volume fraction exponent on variation of non-dimensional natural frequency-real part with non-dimensional follower force for CFSS FGSP	147
Figure 7.3(b)	Influence of volume fraction exponent on variation of non-dimensional natural frequency-imaginary part with non-dimensional follower force for CFSS FGSP	147
Figure 7.4(a)	Influence of porosity distribution on variation of non-dimensional natural frequency-real part with non-dimensional follower force for CFSS FGSP	149
Figure 7.4(b)	Influence of porosity distribution on variation of non-dimensional natural frequency-imaginary part with non-dimensional follower force for CFSS FGSP	149
Figure 7.5(a)	Influence of porosity index on variation of non-dimensional natural frequency-real part with non-dimensional follower force for CFSS FGSP	150
Figure 7.5(b)	Influence of porosity indices on variation of non-dimensional natural frequency-imaginary part with non-dimensional follower force for CFSS FGSP	150
Figure 7.6(a)	Influence of sandwich layer configuration on variation of non-dimensional natural frequency-real part with non-dimensional follower force for CFSS FGSP	150
Figure 7.6(b)	Influence of sandwich layer configuration on variation of non-dimensional natural frequency-imaginary part with non-dimensional follower force for CFSS FGSP	150
Figure 7.7(a)	Influence of load control parameter on variation of non-dimensional natural frequency-real part with non-dimensional follower force for CFSS FGSP	151
Figure 7.7(b)	Influence of load control parameter on variation of non-dimensional natural frequency-imaginary part with non-dimensional follower force for CFSS FGSP	151

Figure 7.8(a)	Influence of non-uniform loads on variation of non-dimensional natural frequency-real part with non-dimensional follower force for CFSS FGSP	152
Figure 7.8(b)	Influence of non-uniform loads on variation of non-dimensional natural frequency-imaginary part with non-dimensional follower force for CFSS FGSP	152
Figure 7.9(a)	Influence of aspect ratio on variation of non-dimensional natural frequency-real part with non-dimensional follower force for CFSSFGSP	153
Figure 7.9(b)	Influence of aspect ratio on variation of non-dimensional natural frequency-imaginary part with non-dimensional follower force for CFSSFGSP	153
Figure 7.10(a)	Influence of cutout ratio on variation of non-dimensional natural frequency-real part with non-dimensional follower force for CFSS FGSP	153
Figure 7.10(b)	Influence of cutout ratio on variation of non-dimensional natural frequency-imaginary part with non-dimensional follower force for CFSS FGSP	153
Figure 7.11(a)	Influence of cutout ratio and load width ratio on variation of non-dimensional natural frequency-real part with non-dimensional follower force for CFSS FGSP	156
Figure 7.11(b)	Influence of cutout ratio and load width ratio on variation of non-dimensional natural frequency-imaginary part with non-dimensional follower force for CFSS FGSP	156

## LIST OF TABLES

Table No.	Description	Page No.
Table 3.1	Various layer schemes of FCF and MFC FGSPs	30
Table 3.2	Porosity models and corresponding distribution functions for single layer FGM plate	33
Table 3.3	Porosity models and corresponding distribution functions for FCF	34
Table 3.4	Porosity models and corresponding distribution functions for MFC	35
Table 4.1	Materials Properties used in FGM plate	58
Table 4.2	Convergences of non-dimensional critical buckling loads ( $\bar{P}_{cr}$ ) and non-dimensional natural frequencies ( $\bar{\omega}$ ) of thin square single layer FGM plate subjected to load Type-III with $c/b = 0.2$ .	59
Table 4.3	Variation of $\bar{P}_{cr}/\bar{P}_{cr}^*$ for an isotropic thin square plate ( $a/h = 100$ ) subjected to Types-III load	59
Table 4.4	Comparison of non-dimensional critical buckling load ( $\bar{P}_{cr} = P_{cr}b/D_{ce}$ ; $D_{ce} = E_{ce}h^3/12(1 - \nu^2)$ ) of SSSS and CSCS single-layer FGM (Al/ZrO <sub>2</sub> ) plates subjected to Type-IV load	60
Table 4.5	Comparison of non-dimensional critical buckling loads ( $\bar{P}_{cr} = P_{cr} a^2/100E_0h^3$ , $E_0 = 1 \text{ GPa}$ ) of simply supported FCF FGM (Al/Al <sub>2</sub> O <sub>3</sub> ) sandwich plate subjected to uniformly distributed uniaxial compressive load	60
Table 4.6	Comparison of non-dimensional natural frequency ( $\bar{\omega} = \omega \left(\frac{a^2}{h}\right)\sqrt{\rho_0/E_0}$ , $E_0 = 1 \text{ GPa}$ , $\rho_0 = 1 \text{ kg/m}^3$ ) of simply supported FCF FGM (Al/Al <sub>2</sub> O <sub>3</sub> ) sandwich plate	62
Table 4.7	Comparison of non-dimensional natural frequency ( $\bar{\omega} = \frac{\omega a^2}{h}\sqrt{\rho_0/E_0}$ , $E_0 = 1 \text{ GPa}$ , $\rho_0 = 1 \text{ kg/m}^3$ ) of simply supported square FCF FGM (Al/Al <sub>2</sub> O <sub>3</sub> ) sandwich plates	

	with porosity	63
Table 4.8	Comparison of non-dimensional critical buckling load ( $\bar{P}_{cr} = P_{cr}a^2/100E_0h^3$ , $E_0 = 1 \text{ GPa}$ ) of simply supported square FCF (Al/Al <sub>2</sub> O <sub>3</sub> ) sandwich plate with porosity and subjected to uniform compressive in-plane edge loads.	63
Table 4.9	Effect of volume fraction exponent and porosity index on the non-dimensional critical buckling load ( $\bar{P}_{cr}$ ) of single layer FGM plates subjected to Type-I and Type-II localised edge loads ( $c/b = 0.2$ )	71
Table 4.10	Effects of porosity index on the non-dimensional critical buckling load ( $\bar{P}_{cr}$ ) of square simply supported FCF and MFM FGM sandwich plate with porosity subjected to Type-I and Type-II localised edge loads (U-D, $n = 5.0$ $b/h = 100$ )	73
Table 4.11	Effects of volume fraction exponents and porosity index on non-dimensional critical buckling loads of single layer FGM plates subjected to Type-III and Type-IV localised edge loads ( $c/b = 0.2$ )	78
Table 4.12	Effect of porosity index on the non-dimensional critical buckling load ( $\bar{P}_{cr}$ ) of square simply supported FCF and MFM FGM sandwich plate with porosity subjected to Type-III and Type-IV localised edge loads (U-D, $n = 5$ , $b/h = 100$ )	80
Table 4.13	Non-dimensional critical buckling loads ( $\bar{P}_{cr}$ ) of SSSS and CCCC supported single layer FG plates with varying side-to thickness ratio ( $c/b = 0.2$ , $n = 2.0$ , $p_i = 0.1$ ).	82
Table 4.14	Non-dimensional critical buckling loads ( $\bar{P}_{cr}$ ) of SSSS and CCCC support condition FCF and MFM FGM sandwich plate with varying side-to-thickness ratio subjected to load Type-I ( $c/b = 0.2$ , $n = 2.0$ , $p_i = 0.2$ ).	84
Table 5.1	Loading Equations	91
Table 5.2	Convergence of $\bar{P}_{cr}$ for a simply supported single layer FG	

	plate with a central circular cutout under the action of LL-1	93
Table 5.3	Comparison of $\bar{P}_{cr}$ for FCF PFGSP (Al/Al <sub>2</sub> O <sub>3</sub> ) with U-D porosity distributions and subjected to LL-6.	93
Table 5.4	Comparison of $\bar{\omega}$ for FCF PFGSP and SFGSP (Al/Al <sub>2</sub> O <sub>3</sub> ) simply supported porous sandwich plate of various types of porosity distributions and porosity indices.	95
Table 5.5	Comparison of $\bar{P}_{cr}$ for FCF PFGSP and SFGSP (Al/Al <sub>2</sub> O <sub>3</sub> ) simply supported porous sandwich plate of various types of porosity distributions and porosity indices.	96
Table 5.6	Comparison of $\bar{P}_{cr}$ for isotropic square simply supported plate with various cutout ratios and support conditions.	97
Table 5.7	Effect of porosity distribution on $\bar{P}_{cr}$ for FCF SFGSP with cutouts subjected to nonlinearly varying in-plane edge load for various volume fraction exponent and sandwich layer schemes.	107
Table 5.8	Effect of support conditions and $b/h$ on $\bar{P}_{cr}$ of porous FCF and MFC SFGSP with cutouts.	110
Table 6.1	Metal and ceramic material temperature-dependent physical properties	119
Table 6.2	Temperature independent material properties of metal and ceramics	120
Table 6.3	Convergence of $\bar{P}_{cr}$ for a square simply supported porous FCF PFGSP with a centrally situated circular cutouts under the actions of LC-1 and uniform temperature rise $\Delta T = 100$ ( $b/h = 10$ , 1-1-1, U-D, $pi = 0.3$ )	121
Table 6.4	Natural frequency parameters ( $\bar{\omega}$ ) for CCCC rectangular Si <sub>3</sub> N <sub>4</sub> /SUS304 FGM plates exposed to uniform temperature rise $\Delta T = 300$ K	122
Table 6.5	Comparison of for MFC PFGSP (Ti-Al <sub>6</sub> -4V/ZrO <sub>2</sub> ) square simply supported FGSP of different sandwich layer	

	schemes and thickness ratio	124
Table 6.6	Comparison of $\bar{P}_{cr(T=0)}$ , $\bar{T}_{cr}$ and $\bar{P}_{cr(T/2)}$ of simply supported FCF PFGSP ( $a/b = 1.0$ , $b/h = 10.0$ ) (Ti-Al <sub>6</sub> -4V/ZrO <sub>2</sub> ) of various sandwich layer schemes and $n$ .	125
Table 6.7	Comparison of $\bar{T}_{cr}$ for porous FCF PFGSP and SFGSP simply supported square plate ( $b/h = 10.0$ , $n = 2.0$ ) subjected to uniform temperature rise across the thickness	126
Table 6.8	Comparison of $\bar{T}_{cr}$ simply supported square FGM plate consisting cutout ( $d/b = 0.2$ ) exposed to temperature load	126
Table 6.9	Effects of porosity distribution and sandwich layer scheme on the $\bar{P}_{cr}$ of square simply supported FCF SFGSP under thermal environment ( $n = 2$ , $b/h = 10$ )	136
Table 6.10	Consequence of porosity distribution and sandwich layer scheme on the $\bar{P}_{cr}$ of MFC SFGSP exposed to thermal environment ( $n = 2.0$ , $b/h = 10$ )	137
Table 6.11	Effect of support condition and temperature on $\bar{P}_{cr}$ of FCF SFGSP under thermomechanical load ( $b/h = 10$ , $n = 2$ )	139
Table 7.1	Comparison of flutter load and flutter frequencies for a SSSS edged isotropic laminated plate ( $b/h = 100$ , $\nu = 0.3$ ) subjected to uniform follower loading	145
Table 7.2	Comparison of non-dimensional flutter load and flutter frequency of CFSS plate subjected to load from center edge ( $E_{11} = E_{22} = 40$ ; $G_{12} = G_{13} = 0.6E_{22}$ ; $G_{23} = 0.5E_{22}$ ; $\nu = 0.25$ )	148
Table 7.3	Comparison of non-dimensional flutter load and flutter frequency of CFSS plate subjected to load from one edge ( $E_{11} = E_{22} = 40$ ; $G_{12} = G_{13} = 0.6E_{22}$ ; $G_{23} = 0.5E_{22}$ ; $\nu = 0.25$ )	148
Table 7.4	Influence of sandwich configuration and material idealization technique on non-dimensional flutter load for a CFSS edged FGSP lam ( $b/h = 100$ ) subjected to NL-6	154

## NOMENCLATURE

$x, y, z$	Cartesian co-ordinate axes of FGM plate
$u, v, w$	Displacement components along $x, y$ and $z$ directions at any point $(x, y, z)$ in an FGM plate space
$u_0, v_0, w_0$	Displacement components along $x, y$ and $z$ directions at any point $(x, y, 0)$ in an FGM plate space
$\theta_x, \theta_y$	The rotations of transverse normal at the plate mid-surface with respect to $y$ and $x$ direction
$\dot{u}, \dot{v}, \dot{w}$	Translational velocities along $x, y$ and $z$ directions at any point in an FGM plate space
$\dot{\theta}_x, \dot{\theta}_y$	Rotational velocities along $x, y$ and $z$ directions at any point in an FGM plate space
$h$	Total thickness of plate
$\sigma_x, \sigma_y, \sigma_z$	Normal stresses at any point in the plate with reference to the FGM plate axes
$\varepsilon_x, \varepsilon_y$	Linear in-plane normal strains at point in plate with reference to plate axes
$\gamma_{xy}, \gamma_{yz}, \gamma_{xz}$	Transverse shear strains at any point in the plate with reference to the FGM plate axes
$\varepsilon_{xnl}, \varepsilon_{ynl}, \gamma_{xynl}$	Nonlinear inplane normal and shear strains at point in plate with reference to plate axes
$N_x, N_y, N_{xy}$	Membrane stress-resultants at any point in the plate mid-surface with reference to the FGM plate axes
$N_x^T, N_y^T, N_{xy}^T$	Membrane stress-resultants at any point in the plate mid-surface due to thermal effect with reference to the FGM plate axes
$M_x, M_y, M_{xy}$	Flexure stress-resultants at any point in the plate mid-surface with reference to the FGM plate axes
$M_x^T, M_y^T, M_{xy}^T$	Flexure stress-resultants at any point in the plate mid-surface due to thermal effect with reference to the FGM plate axes
$\bar{A}_{ij}$	Extension-extension matrix
$\bar{B}_{ij}$	Extension-bending matrix
$\bar{D}_{ij}$	Bending-bending matrix
$k$	Shear correction factor
$d$	Shift in neutral surface

$E_c, E_m$	Young's modulus of the ceramic and metal
$\rho_c, \rho_m$	Mass density of the ceramic and metal
$n$	Volume fraction exponent
$\nu$	Poisson's ratio
$V_c$	Volume fraction of the ceramic material
$V_f^b(z), V_f^{co}(z), V_f^t(z)$	Volume fraction of bottom, core and top sheets along the thickness direction of FGM sandwich plate
$P_d^t, P_d^b$	Porosity distribution function of top and bottom sheet in FGM sandwich plate
$p_i$	Porosity index
$\eta, \xi$	Natural coordinate axes of elements
$\tilde{P}_0, \tilde{P}_{-1}, \tilde{P}_1, \tilde{P}_2, \tilde{P}_3$	Temperature coefficients
$\alpha$	Thermal expansion coefficient
$\Delta T$	Temperature rise
$U_l, U_{nl}$	Strain energy due to linear and nonlinear strains
$T$	Kinetic energy
$\bar{P}_{cr}$	Non-dimensional critical buckling load
$\lambda_{cr}$	Non-dimensional flutter load
$\gamma_{cr}$	Non-dimensional flutter frequency
$[I]$	Inertia Matrix
$[J]$	Jacobian Matrix
$[K_e]$	Global linear stiffness matrix
$[K_G]$	Global Geometric stiffness matrix
$[M]$	Global Mass matrix
$[K_G^T]$	Global geometrics stiffness matrix due to temperature
$[K_F]$	Global Follower force matrix
$\delta W_f$	Variational work done by non-conservative force
$\varphi$	Load control parameter





# CHAPTER 1

## INTRODUCTION

### 1.1 PRELIMINARY REMARKS

Fibre-reinforced laminated composites have gained widespread utilisation in aerospace, defence, automotive, shipbuilding, and various other industries, owing to their ability to be designed with the desired strength and stiffness. However, conventional laminated composites exhibit variations in their mechanical properties at the interface due to the bonding of two distinct materials. Consequently, stress concentration often arises, leading to potential damages such as delamination resulting from matrix cracking and adhesive bond separation. Furthermore, laminated composites also experience thermal distortion. Functionally Graded Materials (FGM) were introduced to address these drawbacks of conventional laminated composites. FGMs are designed with a gradual variation in material properties through the thickness, effectively mitigating the issues associated with stress concentration, delamination, and thermal distortion.

In 1984, a pioneering material scientist introduced the idea of FGM while working on a space project to create heat-shielding structural material. The main objective was to design a material capable of withstanding extreme temperatures, precisely 2100K, while accommodating a temperature gradient of 1600K across a 10 mm thick section. The innovation that drove the project forward involved the gradual transition from heat-resistant ceramic on the high-temperature side to tough metals with high thermal conductivity on the low-temperature side within the composition of the material. FGMs are advanced materials in a group of composites formed by continuous gradation of two or more constituent phases over a specified volume. This gradation of properties can be appropriately tailored to achieve optimized characteristics of each component. The typical continuous gradation of materials in FGM is shown in Figs. 1.1(a) and (b) represents a cross-section of manufactured FGM specimen. The material property variation can be either unidirectional or multidirectional, and it can be continuously or step-wise graded from one surface to another. After that, various kinds of research were carried out by integrating various dissimilar materials and properties

to create new FGMs for various potential applications. Besides the manmade FGM structures, some natural FGMs, such as bone, human skin, bamboo trees, etc., already exist in nature, as shown in Fig. 1.2.

Sandwich structures find unique potential in many engineering fields, including planetary exploration landers, return capsules, submarines, etc. Most of the sandwich structures were recently developed using fibre-reinforced laminated composites. These laminated composites in the form of sandwich structures also showed delamination due to stress concentration at the face sheet core interface due to abrupt changes in material properties.

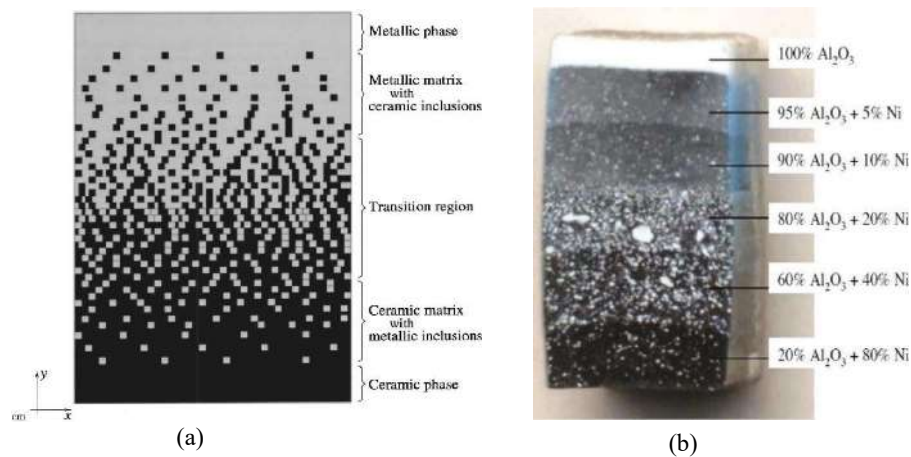


Fig. 1.1 FGM (a) Continuous distribution and (b) Specimen of  $\text{Al}_2\text{O}_3$ -Ni FGM having layers with different compositions

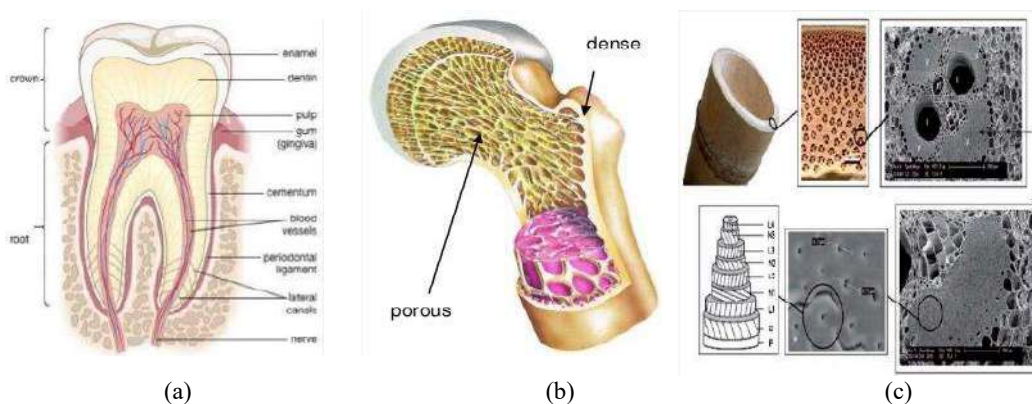


Fig. 1.2 FGM in nature (a) Human teeth (b) Organic bone and (c) Plant fibre (Saleh et al. 2020)

This problem is evaded by using Functionally Graded Sandwich Plates (FGSP). FGSPs, unlike laminated composites, show smooth variations in stress distribution due to

gradual changes in the material properties across the core-face sheet interface, thus avoiding the problem of delamination. In recent research focusing on FGSPs, investigations have been conducted to consider the diverse material properties resulting from various homogenisation techniques like sigmoidal function and exponential law. The aim is to enhance the overall characteristics of the materials. These unique features of FGSP have thus elicited the application of Functionally Graded (FG) plate in various engineering fields such as aerospace, marine, civil, defence energy, etc. The main application of the FGSP has been in high-temperature environments such as rocket exhaust chambers, heat exchange plates, nuclear reactors, solar power components and energy conversion devices such as capacitors, sensors and electrodes (Saleh et al. 2020). Micro-defects such as porosity are known to arise in FGSPs as a result of the manufacturing processes. These defects arise due to significant disparities in the solidification temperatures of the constituent materials used in FGSPs. In some cases, the temperature difference between the die and the material being poured results in a higher percentage of porosity at the surface, while in other situations, longer solidification times cause the porosity to be more concentrated near the core of the samples (Vynnycky 2020). This variability in porosity distribution contributes to the mechanical strength variation of FGM, resulting in the decrease of overall stiffness and mass of the structures. Consequently, it becomes crucial to investigate the impact of different porosity distributions and percentages on vibration, buckling, and flutter stability characteristics during the analysis phase. To address this concern, various porosity distributions are mathematically modelled across the thickness.

It is well known that these FGSPs are a small portion of a complex composite structure. The load transfer between these plates takes place in the form of in-plane edge loads through the plate edges. These in-plane loads are rarely uniform due to the relative stiffness of adjacent members, support restraints, damage to plate edges and the nature of the external loading conditions. These non-uniform loads lead to high-stress concentration in the plate. Owing to the geometric discontinuity in the form of cutouts, which are typically created to allow passage for fuel lines, electrical conduits, providing access to other parts of the structure, structural connections, venting, altering the resonant frequency and occasionally to lower the weight, the stiffness of such member is further reduced. These cutouts also alter the plate's stress distribution and modify the

plate's buckling and vibration characteristics. The presence of cutouts adds to the complexity of the analysis and design of such structures. The non-uniformity in the stress due to in-plane load will further increase due to the formation of porosity and cutouts, significantly affecting the vibration, buckling and dynamic instability characteristics of FGSPs. In extension, FGSPs, with or without cutouts, find numerous applications in high thermal environments in the form of the thermal barrier. In such applications, it is necessary to investigate the influence of mechanical and thermal loads on the vibration and buckling behaviour. The FGSP are to be studied and designed to perform under the combined action of mechanical and thermal loads. Such loads acting separately or in a combined form lead to the failure of the member due to vibration and buckling.

It has been established that the nature of forces acting on the structure governs the type of possible instability of structural components. The forces that act on a structure can be divided into two categories: conservative forces and nonconservative forces. Conservative force is a type of force in which the work done by the force depends on the initial and final position of the point of application only. Static instability is commonly generated when the type of in-plane loading is conservative. On the other hand, if the work done depends on the path through which force traverses from the initial to the final state, i.e., the work done is a path function, then such a force is non-conservative. Nonconservative force 'follow' the direction of deflection, thereby changing its orientation as the structure deforms. Nonconservative forces are, therefore, called follower forces. Because of the flexible nature of structural components, the follower forces change the directions (known as the tangency parameter), and the structures undergo static instability (divergence) or dynamic instability (flutter). As the magnitude of the in-plane follower forces acting over a thin plate increases, the component may lose its stability at some stage. In dynamic analysis, loss of stability can be identified by the way natural frequencies alter with an increase in load. Fig. 1.3 (a) shows a schematic diagram (side-view) of a plate under a follower force. If any of the eigenvalues reduces to zero with an increase in load ( $P$ ), then instability is by divergence (i.e., static instability), as shown in Fig. 1.3 (b). Many times, it so happens that two natural frequencies coalesce with each other with an increase in load, leading to the flutter-type instability, giving rise to unbounded deformation or growth of

vibration without bound, as in Fig. 1.3 (c). Thus, the nature of the eigenvalues obtained dictates the type of instability. Here in Fig. 1.3,  $\text{Re}(\gamma)$  and  $\text{Im}(\gamma)$  represent the real part and imaginary of the frequency ( $\gamma$ ). The term  $\phi$  denotes the load control parameter.

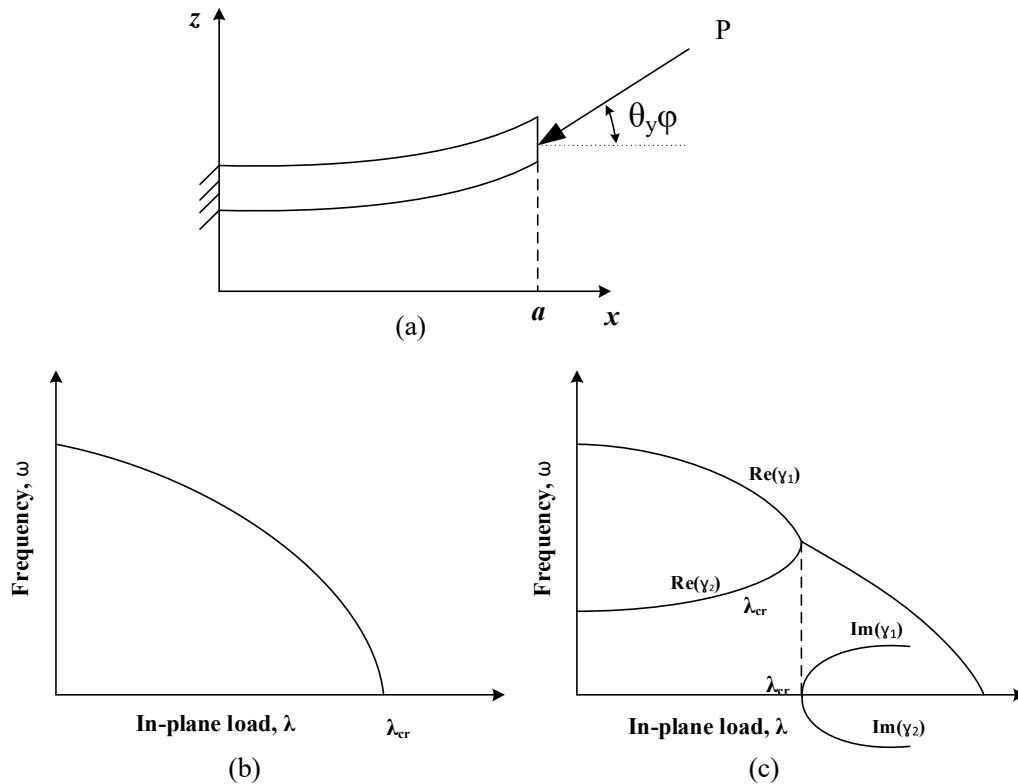


Fig. 1.3 (a) Schematic side-view of a plate under a follower force acting at an angle  $\phi\theta_y$ ;  $0 \leq \phi \leq 1$ .  
 Type of instabilities that can be captured using this formulation (b)  $\text{Im}(\gamma) < 0$  and  $\text{Re}(\gamma) = 0$ :  
 Divergence type of instability (c)  $\text{Im}(\gamma) < 0$  and  $\text{Re}(\gamma) \neq 0$ : Flutter type of instability

The wing of an aircraft carrying jet engines is subjected to concentrated follower forces (engine thrust), rockets and missiles are subjected to follower end thrust, and large plate-like space structures are subjected to concentrated or localised distributed edge follower force, etc. Friction piles carry the load completely or partially by the action of the frictional resistance developed between the pile surface and the surrounding soil. The pre-tensioned beams in which the pre-stress is transferred to the concrete by the tendons through bond are some of the examples where time-independent nonconservative forces are encountered in civil engineering practice. According to previous research, the loss of stability in these elements can occur due to follower forces, resulting in either divergence (static instability) or flutter (dynamic instability).

Failure by dynamic instability is when the loss of stability is caused by a unidirectional unbounded motion.

The analytical solution for problems involving cutouts and nonuniform loads requires a lot of time and high computation effort. However, considering the complexity involved, numerical methods offer a feasible approach. The Finite Element (FE) method emerges as the prominent numerical technique for solving intricate engineering, mathematical, and physics problems (Logan (2016)). As a result, the current study adopts the versatile and advantageous FE solution methodology, which efficiently manages geometry discontinuities through the use of isoparametric elements for domain discretisation. After considering the preceding discussion, it becomes evident that there is a compelling need for a robust mathematical model capable of accurately predicting the structural response (including vibration, buckling, and dynamic instability) of FGSP. This model must effectively handle non-uniform stress resulting from various factors such as nonuniform loads, geometric discontinuity (cutout), porosity, thermomechanical loads, and follower forces. To address these challenges, numerous researchers have conducted theoretical analyses using analytical or numerical methods. Among these methods, the FE method has proven valuable for handling complex practical scenarios. Consequently, a novel mathematical model is proposed here, based on First-order Shear Deformation Theory (FSDT), Green-Lagrange's nonlinear strain relationship, and temperature-dependent properties of FGM. The insights gained from this study have the potential to significantly improve the reliability of analyses and designs for FGSPs.

Based on the previous discussion, it is realised that there is a strong requirement for a mathematical model to predict precisely the structural response (vibration, buckling and dynamic instability) of FGSP. The developed model should be proficient in dealing with nonuniform stress due to nonuniform loads, geometric discontinuity (cutout), porosity, thermomechanical loads and follower forces. To address such problems, many investigators have performed theoretical analyses using analytical or numerical methods. To take care of complex problems, a numerical method, such as the FE method, is incorporated to deal with practical scenarios. In this regard, a general mathematical model is proposed based on FSDT, Green-Lagrange's nonlinear strain

relationship and temperature-dependent properties of FGM. The outcomes from the current study would benefit reliable analysis and design of FGSPs.

## **1.2 AIM AND SCOPE**

FGSP offer a promising solution to address delamination and inter-laminar stress commonly found in layered structures. The gradual change in material composition, typically including ceramic and metal, provides these plates with high-temperature resistance from ceramics and fracture resistance due to the metal's toughness properties. As a result, FGM has garnered significant attention from researchers and has found diverse applications in aerospace, civil, marine, and defence industries. Moreover, modern engineering applications have shown extensive interest in sandwich FG structures due to their low weight-to-strength ratio, bending rigidity, and excellent fatigue properties. Throughout their service life, FGSPs are subjected to in-plane mechanical loads. While many researchers assume these loads to be uniformly distributed, practical cases demonstrate that localised and nonuniform loads are more common. These non-uniform loads create stress concentration, impacting the plates' vibration, buckling, and dynamic instability behaviour. Thus, a comprehensive investigation is necessary to understand how FGSPs respond to various non-uniform in-plane edge loads. Additionally, considering the cutout effect is essential, as these cutouts are required in structural members for venting, fuel pipes, inspection, passage of electrical lines, and weight reduction. Cutouts introduce free edges in the plate, leading to decreased stiffness and changes in stress distribution, significantly altering vibration and buckling characteristics. The combination of nonuniform loads and cutouts adds complexity to the analysis and has been less explored in existing literature. Porosity defects that occur during the fabrication process of FGSP, with varying intensities and distributions, can also decrease the stiffness of structural elements. While initially designed as thermal barriers for aerospace applications and fusion reactors, FGSPs are now utilised in other high-temperature environments, subjecting them to mechanical and thermal loads during their lifespan. The cumulative impacts of these loads can substantially influence their functional behaviour, hence providing the motivation for the present study. Additionally, it is worth noting that research in this particular field is currently scarce.

The FGSP finds widespread applications but often faces flutter instability caused by follower forces during its service life, leading to member failure due to unbounded motion. Moreover, existing flutter stability studies have mainly focused on isotropic and laminated composites. Therefore, a thorough flutter stability analysis of porous FGSP, considering localised and nonuniform follower forces, is essential to design such systems efficiently. Additionally, the fabrication of FGSP is costly and complex, primarily due to the challenging task of achieving proper material grading, posing a constant challenge for producers. Consequently, conducting experimental analysis on FGM plates becomes expensive and difficult, especially in complex environmental conditions. In such scenarios, a numerical approach is preferred to investigate structural responses, mainly when dealing with complex material properties, geometries, and loading conditions.

It is apparent from the comprehensive literature review that most of the earlier studies focused on the vibration, buckling and dynamic instability behaviour of porous single-layer FG plates with/without cutout under uniform in-plane edge load. Further, very few works considered the effect of thermomechanical loads but are restricted to single-layer FGM plates without porosity. So, the present work has been carried out to address the lacuna in the literature related to vibration, buckling and dynamic instability analysis of porous FGSP with cutout. Therefore, numerical studies relating to vibration, buckling, and dynamic instability of porous FGSP with cutout subjected to localised and Nonuniform In-plane Edge Loads (NIELs) in non-thermal and thermal environments hitherto not reported in the literature are presented.

Keeping this in view, the aims and objectives set for the present work are as follows:

- i. To develop generalized theoretical formulations and FE solutions using the FSDT for the vibration and buckling analyses of porous FGSP under a conservative system of forces and for the dynamic instability analysis of FGSP under a nonconservative system of forces. Plates with or without cutouts and subjected to non-uniform mechanical and thermomechanical loads are considered. For all the plate problems,  $C^0$  continuity isoparametric 8-noded plate element will be adopted.
- ii. To study the vibration behaviour of porous FGSP with or without geometric discontinuity subjected to various non-uniform and localised in-plane edge

- loads, either compression or tension (conservative system of forces), under non-thermal and thermal environments.
- iii. To study the bucking behaviour of porous FGSP with or without geometric discontinuity subjected to various non-uniform and localised in-plane edge loads, either compression or tension (conservative system of forces), under non-thermal and thermal environments.
  - iv. To study the dynamic instability characteristics of porous FGSP with or without geometric discontinuity subjected to localised and nonuniform in-plane follower edge forces (nonconservative system of forces).
  - v. To undertake the parametric studies of porous FGSP with varying parameters viz., load direction control, load width ratio, volume fraction exponent, sandwich configurations, geometrical properties (sandwich layer scheme, aspect ratio, thickness ratio, cutout ratio) and support conditions.

### 1.3 LAYOUT OF THESIS

The following chapters systematically present the significant work done during the investigation to accomplish the aforementioned aims and objectives.

The **Chapter 2** comprises a comprehensive and systematic review of existing research on porous single-layer FG plate and FGSP with or without a cutout, focusing on natural frequency, critical buckling load, flutter frequency, and flutter load evaluations using numerical analysis. This has been presented under three broad headings viz., 1) vibration analysis of FGM, 2) buckling analysis of FGM, and 3) dynamic instability analysis of FGM. Available literature under both analytical and numerical methods is reviewed to give a clear picture of research work carried out on the free vibration, buckling, and dynamic instability (flutter) analyses of FGM plates.

**Chapter 3** introduces the proposed general mathematical formulations for FGSP, developed for vibration, buckling, and dynamic instability behaviours under localised, non-uniform mechanical and thermomechanical loadings. The model incorporates a Green-Lagrange type of geometrical nonlinearity within the FSDT kinematics framework, considering temperature-dependent material properties of the FGM constituents. The chapter includes detailed explanations of the kinematic field, constitutive relations, governing equations, FE formulations, and solution techniques.

In **Chapter 4**, a detailed investigation of vibration and buckling responses of porous FGSP with and without cutout under localised in-plane edge load is presented numerically. Initially, four types of localised in-plane edge loads considered for the current study are mentioned. Also, different kinds of FGSP configurations and porosity distributions considered are explained and followed by a convergence study and thorough validation study to show the correctness of the current FE formulation. Further detailed numerical results are presented to show the effect of the different parameters (geometrical and material) on the vibration and buckling responses that are computed using the developed mathematical model and discussed in detail.

**Chapter 5** addresses the influence of porosity and nonuniform loads on vibration and buckling responses of porous FGSP, both with and without cutout. The chapter encompasses various types of NIELs, two kinds of FGSP configurations (FGM-Ceramic-FGM and Metal-FGM-Ceramic), and several porosity distributions. Similar to Chapter 4, this chapter includes convergence and validation studies, followed by detailed numerical results and discussions on the impact of different parameters on the vibration and buckling characteristics of porous FGSP.

The vibration and buckling behaviour of porous FGSP with/without cutout under thermomechanical loads are presented through numerical discussion in **chapter 6**. The chapter starts with a detailed description of different types of NIELs, mechanical in nature, and uniform temperature fields considered in the current study. This is followed by convergence and a thorough validation study to present the current FE formulation's correctness. Further, various kinds of sandwich configurations and porosity distributions considered are reported. The detailed numerical results with discussion are presented considering different parameters (geometrical and material) to arrive at suitable conclusions.

**Chapter 7** focuses on the numerical results and discussions of flutter instability characteristics of porous FGSP, with and without cutouts, subjected to localised and nonuniform follower in-plane edge loads. The chapter begins with a description of the different types of loads considered for the study, followed by mentions of several porosity distributions and sandwich configurations. Convergence and validation studies are presented, and detailed parametric studies on geometrical and material parameters are conducted and discussed to understand the dynamic instability behaviour of FGSP.

**Chapter 8** presents the general conclusions drawn from the present investigation based on the objectives framed and offers suggestions for future work. This chapter summarises the research findings and provides insights for future research directions. To achieve the objectives and scope of the current work, a review of earlier research related to the current field is essential. Therefore, the next chapter offers a detailed review of earlier work in this research area.



## CHAPTER 2

### LITERATURE REVIEW

#### 2.1 PRELIMINARY REMARKS

The idea of FGM structures and their applications in modern engineering domains has been covered in the preceding chapter. The suitability and performance of FG structures for thermal protection systems, in particular, have piqued the interest of many researchers over the past several decades. Researchers and scientists have often tried to develop new mathematical models and solution methods to get beyond the limitations of prior studies. The historical overview of development of FGM is represented in Fig. 2.1. The FGSPs are gaining demand due to low weight-to-strength ratio, bending rigidity, and fatigue characteristics. These FGSPs contains porosity imperfection that occurs during manufacturing process and require cutout due to practical requirement. The FGSPs are subjected to thermal and nonuniform in-plane loads in their service life. These members are susceptible to buckling and vibration in their design life. Further, the nonconservative nature of forces acting on the FGSP member can lead to flutter instability, where it experiences an unbounded increase in the amplitude of vibration. So, the studies have also been modified regularly in the past to make predictions that are more accurate and to get closer to what happens in real life.

In this context, many researchers (Swaminathan and Sangeetha (2017); Jha et al. (2013a); Garg et al. (2021); Saleh et al. (2020); Swaminathan et al. (2015); Udupa et al. (2014); Zhang et al. (2019); Thai and Kim (2015); Datta and Biswas (2011)) have published several review articles describing vibration, buckling and dynamic instability characteristics of FGM. Further, to keep the discussion concise, we will only discuss some of the already published literature in the following sections. To summarise, the available literature has been divided into the following sub-sections:

- i. Vibration analysis of FGM
- ii. Buckling analysis of FGM
- iii. Dynamic instability studies of FGM

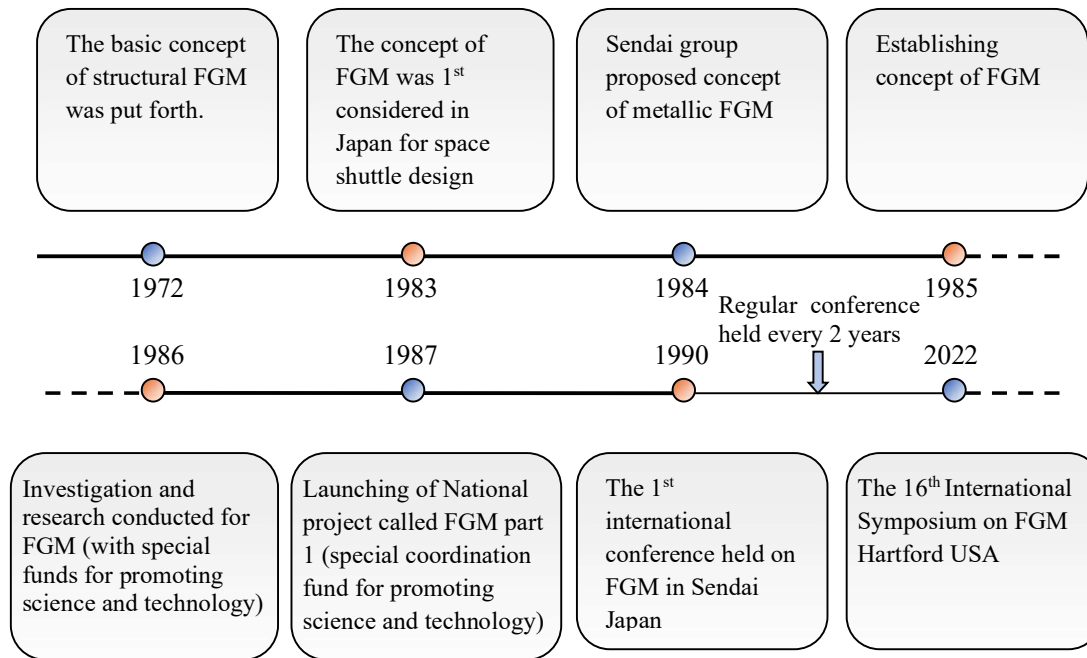


Fig. 2.1 A breakdown of significant moments in history of the study and the development of FGMs

For clarity the organization of literature review of the current study is presented in the form of flowchart in Fig 2.2

## 2.2 VIBRATION ANALYSIS OF FGM

This segment discusses the free vibration characteristics of the FGM plate exposed to ambient and thermal environments with and without temperature-dependent material properties of the individual material constituent. Here, works related to the vibration of the FGM plates with geometric discontinuity and porosity are also discussed. The review has been divided into two major categories—vibration without and with temperature effect—in order to retain brevity.

### 2.2.1 Vibration Without Temperature

Multiple research studies on the free vibration responses of FGM plates under ambient circumstances have been documented. In the following lines, a few lately made contributions to free vibration analysis are brought to light and addressed below:

Zenkour (2005) arrived at sinusoidal shear deformation theory for vibration and buckling analysis of power law based simply supported FGM-Ceramic-FGM (FCF)

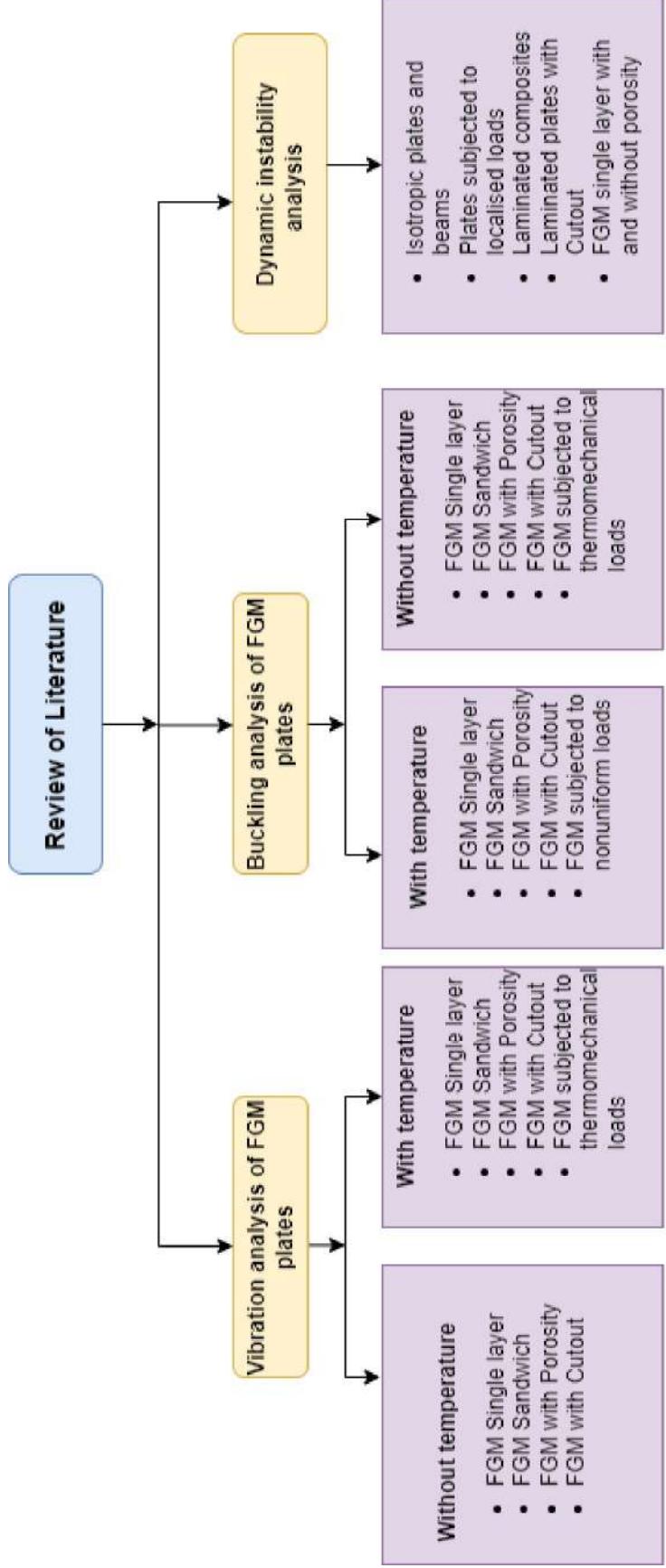


Fig 2.2 Flowchart showing the organization of literature review presented in this study

FGSP. Zhao et al. (2009a) studied the vibration characteristics of FGM plates with arbitrary boundary conditions incorporating the element free-kp Ritz method and FSDT kinematics. Hosseini-Hashemi et al. (2010) presented an analytical solution to study the free vibration response of FGM plates with different support conditions and in turn resting on an elastic foundation based on FSDT kinematics. Jha et al. (2013b) have investigated vibration behaviour of simply supported FGM plates based on higher-order shear deformation theories analytically. Reddy et al. (2014) developed an analytical solution to study the free vibration characteristics of FGM plates using HSDT. Talha and Singh (2010) studied the vibration and static response of FGM plates using the FE technique and HSDT. The authors modified the transverse direction term of the displacement field to improve accuracy. Zhao et al. (2018) developed 3-D elasticity solutions to obtain natural frequencies of rectangular power law-based FGM plates with even, uneven, and logarithmic porosity distributions with different boundary conditions. Thai and Choi (2013) presented a closed-form solution for bending and free vibration analysis of power law based simply supported FGM plate using FSDT. Chakraverty and Pradhan (2014) have used the Rayleigh-Ritz method to investigate the free vibration characteristics of plates with material variation according to exponential law. The authors considered different sets of boundary conditions and Kirchhoff's plate kinematics. Here the authors used Chebyshev polynomials to expand three displacements and the Ritz method to obtain natural frequency. Jin et al. (2014) arrived a three-dimensional exact solution for the free vibration analysis of thick FG plates supported on arbitrary boundary conditions.

Defects in the form of porosity or micro-voids may also occur in the FGSPs during the sintering procedure owing to the considerable variation in the solidification temperatures of constituent materials. These defects affect the vibration characteristics of FGM plates; hence, several studies have been carried out recently considering plates with porosity. In this context, the FE technique and FSDT were used for nonlinear free vibration studies of FGM plates considering the influence of several porosity distributions by Kumar et al. (2021). Kiran et al. (2018) studied the consequence of porosity defect on static and free vibration characteristics of Functionally Graded Skew Magneto-Electro-Elastic (FGSMEE) plates using the FE method and FSDT kinematics. Further, Addou et al. (2019) analyzed the influence of porosity and an elastic foundation

(Winkler/Pasternak/Kerr) on the dynamic response of FGM plates by employing simple quasi-3D hyperbolic shear deformation plate theory.

Closed-form solutions are obtained by Kaddari et al. (2020) to study bending and free vibration characteristics of simply supported FGM plates with graded porosity resting on Winkler, Pasternak, or Kerr foundation. Kumar et al. (2021) investigated the vibration response of variable thickness of porous FGM plate resting on Winkler and Pasternak elastic foundation using Galerkin Vlasov's method. The authors adopted power, exponential, and sigmoidal material idealization techniques and FSDT kinematics. The free vibration and static behaviour of the FGM plate due to different porosity models was investigated analytically using FSDT kinematics and Navier's solution by Akbaş (2017). Merdaci et al. (2021) analyzed the vibration behaviour of rectangular and square FGM plates with various porosity distributions using HSDT. Here authors adopted the Navier solution technique. Rezaei et al. (2017) investigated the vibration response of the FGM plate with porosities analytically for the Levy-type boundary condition plate. The authors considered uniform and central distributed porosity distributions in their studies.

### **2.2.2 Vibration with Temperature**

This part offers a comprehensive analysis of the free vibration behaviours exhibited by plates made of FGMs in a thermal environment. It explores several studies that investigate the effects of temperature-dependent material properties of the FGM constituents on these vibration responses.

In this context, the vibration and dynamic behaviour of an FGM plate in a thermal environment is inspected by Huang and Shen (2004), HSDT and von-Karman type geometric nonlinear strain equations. Natarajan and Manickam (2012) studied the bending and free vibration behaviour of FGSP using different displacement models. The temperature profile was assumed linear through the thickness, and properties were supposed to be independent of temperature. Pandey and Pradyumna (2015) adopted a layer-wise FE technique to study the vibration behaviour of FGSP in the thermal environment using FSDT. The authors considered Mori-Tanaka and the rule of mixture material homogenization techniques on two sandwich configurations, i.e., FGM-Ceramic-FGM (FCF) and Metal-FGM-Ceramic (MFC). Burlayenko and Sadowski

(2019) presented a computationally efficient approach to obtain accurate free vibration results of FGSPs in a thermal environment incorporating 3-D elements in the ABAQUS FE package. The study conducted by Gupta and Talha (2018a) employed nonpolynomial higher-order shear and normal deformation theory to examine the impact of porosity on the flexure and free vibration properties of FGM plates subjected to heat conditions.

The geometric discontinuity in the form of cutouts is provided in the plate to pass fuel lines, electrical conduits, and structural connections, and sometimes to alleviate the weight. These cutouts change the plate's stiffness and affect the vibration response of the FGM plate. In this context, Do and Lee (2019) presented a vibration analysis of FGM plates with complex cutouts using HSDT. Bansal et al. (2020a) analyzed the consequence of porosity on the vibration behaviour of FGM plates with circular cutouts and resting on partial supports. The researchers adopted closed-form and FE solution techniques to analyze the vibration response of the plates. Bansal et al. (2020b) explored the free vibration behaviour of porous FGM plates with cutouts resting on an elastic foundation in a thermal environment. The authors have considered unconventional boundary conditions such as partial support incorporating the FE technique in their study. Singh et al. (2022) investigated the influence of cutout and porosity on the vibration response of power law-based MFC FGSP resting on an elastic foundation using a non-polynomial-based HSDT resting in a hygro-thermal environment. It was observed that natural frequency variation with increased cutout size is not monotonic. Now in the subsequent subsections, various studies related to the stability of plates are discussed.

### **2.3 BUCKLING ANALYSIS OF FGM**

The phenomenon of plate buckling is widely recognised as a consequence of the effects of in-plane loading situations. These loads can be mechanical, thermal, or thermomechanical in nature. The FGM plates may contain porosity due to the manufacturing process, thereby degrading the stiffness and in turn affecting the buckling behaviour of the FGM plate. Further, FGM plates containing cutouts are susceptible to buckling when subjected to thermal or mechanical loads individually or under thermomechanical loads in their service life. Many research works on the

buckling performance of FGM plates with and without a cutout, with and without porosity under axial compression and thermal load, have been published in the past. In this regard, various approaches are implemented to accomplish the desired analysis, and the details are discussed in the following subsections. In order to ensure conciseness, the review has been divided into two broad categories: buckling with temperature and buckling without temperature effect.

### **2.3.1 Buckling without Temperature**

This section discusses the literature on the buckling characteristics of FGM plates subjected to mechanical in-plane edge loads. Many research articles are available in the open literature on the buckling behaviour of plates exposed to uniform in-plane edge loads. Reddy et al. (2013) developed closed-form solutions using Navier's solution to examine buckling characteristics of simply supported FGM plates subjected to uniform in-plane edge loads. Swaminathan and Naveenkumar (2014) developed an analytical solution for simply supported FGSP subjected to uniform in-plane loads considering HSDT. Bakoura et al. (2021) discussed the stability characteristics of FGM plate acted upon by uniform in-plane mechanical loading incorporating HSDT with the stress function method. To arrive at important conclusions, the authors conducted several parametric studies with varying geometric and material properties.

In practical scenarios, uniform loads are very rare, and hence researchers started investigating the buckling behaviour of plates considering localised and non-uniform loads. In this regard, Chen and Liew (2004) studied the buckling response of FGM plates subjected to localised, concentrated, and parabolic in-plane edge loads using a mesh-free-based numerical method. In this study, non-uniform prebuckling stresses due to applied loads are found in the initial step, followed by the evaluation of buckling loads. Based on classical plate theory, Bodaghi and Saidi (2011) developed analytical solutions for buckling analysis of FGM plates subjected to NIELs. They were using Classical Plate Theory (CPT) and the differential quadrature method. Lal and Saini (2013) examined the buckling and vibration response of exponentially graded FGM plates subjected to linearly varying in-plane edge loads. Uymaz (2021) analyzed the buckling behaviour of FGM plates under uniaxial and biaxial linearly varying in-plane

edge loads incorporating the Ritz method. Chaabani et al. (2022) recently presented buckling characteristics of porous FGSP subjected to NIELs using the FE approach. The defects in the form of porosity or micro-voids may also occur in the FGSPs during the sintering procedure owing to the considerable variation in the solidification temperatures of constituent materials. In this context, Gupta and Talha (2018b) studied the influence of porosity and imperfection in geometry on the buckling behaviour of FGM plates considering nonpolynomial higher order and normal deformation theory. The authors employed eight noded isoparametric elements to analyze using minimum computational effort. Chen et al. (2019) proposed a novel form of FG porous plates and compared its bending and buckling performance of sandwich plates with uniform porous core. The authors employed the Ritz method with Chebyshev polynomial and FSDT kinematics. Daikh and Zenkour (2019) reported analytical solutions for vibration and buckling analysis of power law and sigmoidal function-based porous FCF FGSP under uniform axial and biaxial in-plane edge loads. The authors reported that natural frequency and critical buckling load decreases with an increase in the porosity indices. Singh and Harsha (2020b) studied the influence of vibration and buckling characteristics of FGSP having different boundary conditions employing Galerkin Vlasov's method. They have considered sigmoidal function and introduced an uneven unsymmetric type of porosity. Van Vinh and Huy (2021) examined the consequence of porosity on bending, free vibration, and buckling responses of FGSPs by means of the FE technique. Bekkaye et al. (2020) studied the effects of porosity on the bending and buckling response of simply supported FGM plates with power law and exponential function material variation analytically using Navier's solution technique. Recently, the effect of micro-structural defects such as porosity on the stability behaviour of power law and sigmoidal function-based FGM plates and spherical caps under uniaxial, biaxial compression, biaxial compression, and tension in-plane edge loads were carried out by Zghal and Dammak (2021) with the aid of FE technique. The influence of porosity distribution on natural frequency and critical buckling load of FG sandwich plates have been investigated analytically by Sah and Ghosh (2022a) using the Navier solution technique.

Further, geometric discontinuity in the form of cutout also exists in the FGMs due to many practical requirements. Natarajan et al. (2014) addressed the consequence of

cracks and cutouts on the buckling response of non-porous single-layer FGM plates exposed to mechanical and temperature loads in the framework of the extended FE method using shear flexible four-noded quadrilateral element.

### **2.3.2 Buckling with Temperature**

Numerous investigations have been reported on the buckling responses of the FGM plates in thermal environments, as FGM plates find multiple applications in thermal environments. A few recent contributions based on the buckling analysis under thermal loads are discussed in the following lines. Here works with and without temperature-dependent properties are included.

Lanhe (2004) adopted the FSDT displacement model to study the buckling behaviour of moderately thick FGM plates under thermal loads by obtaining analytical solutions. Materials properties were varied according to power law, and it is reported that critical buckling temperature increase with the increase in aspect and thickness ratio. Shariat and Eslami (2006) investigated the thermal buckling behaviour of FGM plates using closed-form solutions. The influence of geometrical imperfections is considered, and CPT is used. The critical buckling temperature was found to be greater than the perfect plates. In a subsequent study, Prakash et al. (2009) expanded upon their previous research to investigate the impact of the neutral surface's position on the stability characteristics of FGM plates. Matsunaga (2009) examined the thermal buckling behaviour of simply supported FGM plates. The author used the method of power series expansion of displacement components and the principle of virtual work to arrive at the equations of the higher-order theory. A pseudo-spectral method that involves a FE method and collocation method was used by Jalali et al. (2010) to study the thermal stability of laminated FGM circular plates based on the FSDT and subjected to uniform temperature rise. A thermal buckling analysis was presented by Zenkour and Sobhy (2010) for simply supported FGSP considering sinusoidal shear deformation theory. The governing equations are solved analytically, and the authors noticed that critical buckling temperature decreases with an increase in the core thickness. The element-free Galerkin method approximation was used by Jaberzadeh et al. (2013) to study the thermal buckling of FGM skew and trapezoidal plates based on CPT. Ghiasian et al. (2014) developed a solution procedure to determine the critical buckling temperature

of an annular plate considering temperature-dependent properties and FSDT kinematics.

Lee et al. (2016) investigated the thermal buckling behaviour of FGM plates based on FSDT kinematics and incorporated a neutral surface as a reference plane due to asymmetry in the material property variation across the thickness direction. Daikh and Megueni (2018) presented analytical solutions to obtain critical buckling temperature of power law-based FGSP using HSDT. The authors discussed the effect of two configurations of FGM (Homogenous face layers with FGM core and FGM face layers with homogenous core). It was found that thick plates offered higher critical temperatures in comparison with thin plates. Also, the significant effect of the volume fraction exponent is noticed. The critical buckling temperature difference decreases as the side-to-thickness ratio increases, while it increases as the plate aspect ratio increases. Atmane et al. (2016) arrived at equilibrium and stability equations to determine critical buckling temperature for simply supported sigmoidal function-based  $\text{Al}_2\text{O}_3$ -Al FGM plate using FSDT. Singh and Harsha (2020a) examined the consequence of porosity and thermal loads on the stability behaviour of sigmoidal-based FGSP resting on an elastic foundation. Sah and Ghosh (2022b) reviewed analytically the result of the several porosity distributions on thermal buckling behaviour of power law and sigmoidal-based FGSP based on sinusoidal shear deformation theory.

Prakash et al. (2008) used an eight-nodded  $C^0$  shear flexible quadrilateral plate element to study the nonlinear bending and pseudo-post-buckling behaviour of FGM plates based on the Mindlin formulation under thermo-mechanical load. They concluded that temperature-dependent material properties overestimate the thermal buckling resistance. Zhao et al. (2009b) carried out buckling analysis of FGM plates with and without cutouts subjected to mechanical and thermal loads incorporating element-free-kp-Ritz and FSDT kinematics. Talha and Singh (2011) investigated the buckling characteristics of FGM plates subjected to thermomechanical loading using the FE technique. An improved higher-order shear deformation plate theory is employed to account for the transverse shear strains by maintaining the stress-free top and bottom faces of the plate with the  $C^0$  plate element. The effective material properties of FGM plates are assumed to be temperature-dependent and vary in the thickness direction by

employing power-law distribution of the volume fractions of the constituents. Numerical results have been presented for different volume fraction exponent, thickness ratios, temperature rise, and varying combinations of the boundary conditions. It is concluded that the gradation in the material properties and the temperature field have a considerable influence on the buckling load parameter of the FGM plates. Yaghoobi and Yaghoobi (2013) studied the buckling behaviour of power law-based FCF FGSP subjected to thermomechanical loads by arriving at a closed-form solution and incorporating FSDT kinematics.

Abolghasemi et al. (2014) presented the stability analysis of an FGM plate with a cutout subjected to thermomechanical loads using the FE technique. The study used four noded isoparametric elements and considered uniaxial, biaxial, biaxial compression, and tension-type of in-plane edge mechanical loadings. Sharma and Kumar (2017) presented buckling, post-buckling, and failure analysis of perforated FGM plates exposed to thermomechanical loads. The study considered temperature-dependent material properties, nonlinear FE formulation, and FSDT plate kinematics. Rezaei et al. (2015) investigated the stability characteristics of rectangular FGM plates with eccentrically placed cutouts exposed to temperature loads in the framework of the FE technique. Hussein and Mulani (2018) investigated the buckling behaviour of silicon carbide and aluminium-based square and rectangular FGM plates with cutouts under uniaxial uniform in-plane edge loads. The authors considered volume fraction variations in terms of the polynomial expansion approach. Now in the subsequent subsections, various studies related to the dynamic stability of plate structures are discussed.

## **2.4 DYNAMIC INSTABILITY ANALYSIS OF FGM**

Forces in engineering structures can be classified into several types based on how they affect the structure's functionality. As the structure is subjected to a nonconservative system of forces (follower force) whose direction changes with deformation, it may exhibit dynamic instability (flutter) depending on system parameters, causing unbounded deformation or vibration. Therefore, it is essential to study the dynamic instability characteristics of plates. In this regard, various researchers have studied the dynamic instability of isotropic, laminated, FGM plates with or without cutouts

subjected to intricate loading conditions. In this section, the literature concerning the effects of the nonconservative system of forces on the structural stability behaviour of plates is discussed briefly.

Adali (1982) studied a rectangular plate's flutter and divergence instabilities with two independent loading parameters. Galerkin's theory was used to analyze the plate with distributed follower forces acting on the surface of the plate by Leipholz and Pfenndt (1983). The plate is subjected to the combined action of a tangential follower force and a unidirectional axial force along one edge. Two opposite sides of the plate are simply supported, one side being clamped and the other being a free edge where the in-plane forces act. The influence of Poisson's ratio and the elastic foundation on the flutter load and frequency is investigated. Datta and Deolasi (1996) studied the flutter characteristics of a plate subjected to localised follower forces positioned at the center and applied on the free edge in the framework of the FE technique. Kim and Kim (2000) studied the dynamic stability of isotropic, orthotropic, and nonsymmetric laminated composite plate under follower force considering Mindlin assumption. They investigated the effect of shear deformation and rotary inertia under follower force. Park and Kim (2000) extensively studied the dynamic stability characteristics of completely free circular cylindrical and stiff edged cylindrical shells subjected to follower force using the FE method.

Kumar et al. (2003) presented the dynamic instability characteristics of laminated composite plates subjected to partial follower type of edge load with damping. Cross-ply and angle ply laminated plate is subjected to nonuniform follower load, analyzed using the FE method, and discretized using 8 noded isoparametric quadratic element. The effect of the direction control parameter, load width ratio, and structural damping are studied. Flutter is observed to be more common than divergence due to follower load. Load bandwidth and type of load condition have significant effects on flutter. Using the FE approach, Biswas et al. (2012) studied vibration, buckling, and dynamic instability characteristics in damaged cross-ply and angle-ply curved panels. The panels are subjected to non-uniform, centrally, and edge-distributed localised follower forces. The dynamic instability of isotropic and variable stiffness rectangular composite under nonconservative compressive or shearing follower forces is studied using the FE method by Rasool and Singha (2019). The authors also employed eigenvalue or method

of multiple scale to understand dynamic instabilities regions under pulsating follower forces.

Ruan et al. (2012) analyzed the instability behaviour of power law-based FGM skew plates subjected to uniformly distributed tangential follower forces on its surface incorporating the differential quadrature method and Kirchhoff thin plate theory. The impact of volume fraction exponent, skew angle, and aspect ratio on the instability behaviour of the FGM plate is studied. Toriki et al. (2015) explored the consequence of axial deformation on flutter characteristics of FG structure subjected to axial follower force.

## **2.5 RESEARCH GAP**

A literature review of various studies about vibration, buckling, and dynamic instability analyses of FGM sandwich plates and FGM plates has been presented in the preceding section. The gaps in the current literature are identified and listed as follows:

- i. Most of the approaches employed for the analysis of FGM plates are the extensions of similar methods used either for laminated composite plates or for isotropic plates
- ii. The vibration and buckling problems of FGM plates were investigated under in-plane edge loads that are uniform in nature; however, in most cases, the in-plane loads are non-uniform due to practical circumstances. The studies considering the effect of non-uniform in-plane loads on vibration, buckling and dynamic instability characteristics of FGM plates are scanty.
- iii. In most of the literature, closed-form solutions are incorporated to predict the exact response of the structure, but they can only be used for simple problems. For problems with geometric discontinuities, the solution method involves mathematical complexities, making them computationally tedious and time-consuming. Hence numerical approach such as FE method needs to be adopted, which is flexible to handle.
- iv. The porous sandwich plates with cutouts significantly affect the FGSP members' vibration and buckling response when acted upon by NIELs,

resulting in premature failure at the lower stress levels. The investigation of such a problem is not found in the literature and requires more research.

- v. Several investigations are reported on evaluating material properties using the power law homogenization technique. It was observed that power law leads to stress concentration. In contrast, the sigmoidal function reasonably reduces the stress concentration due to the smooth distribution of constituent materials across the thickness direction of the plate.
- vi. It is observed from previously reported literature that the mid surface is considered as the reference plane in the formulation for the analysis of FGM. In such cases, stretching–bending coupling effect is observed due to the asymmetry of material properties in the thickness direction. However, the coupling effect vanishes using a neutral surface as a reference plane in the formulation.
- vii. A more general mathematical formulation is required to predict the vibration and buckling response of FGSP with a cutout capable of dealing with the combined effect of several porosity distributions and thermomechanical loads considering temperature-dependent properties. Such studies were not dealt with in the literature already reported.
- viii. The flutter behaviour study is important as it leads to failure of members due to unbounded motion. Most of the investigations found in literature where restricted to flutter behaviour of isotropic and laminated composite plate. The studies on flutter behaviour of FGSP are minimal.

## CHAPTER 3

### THEORETICAL FORMULATION AND SOLUTION

#### 3.1 GENERAL

There are two primary approaches utilised for ascertaining structural reactions, namely laboratory testing and numerical simulation. The present investigation centres on the numerical analysis of the FGM plate, which exhibits inherent microscopic-scale heterogeneity. The prototype testing of structural components poses significant challenges due to the grading disparities between two distinct materials, namely metal and ceramic. It is indeed accurate to state that closed-form solutions are straightforward to obtain for simple geometries, material models, and support conditions. However, the complexity of the problem increases substantially when considering coupled situations. The utilisation of the numerical method known as FE, characterised by reduced mathematical intricacy, facilitates the straightforward resolution of these intricate issues.

##### 3.1.1 Assumptions

The currently used mathematical formulation has been created based on a set of fundamental assumptions as below:

- i. The fundamental geometric arrangement under consideration in this context is a plate that exhibits a square or rectangular shape.
- ii. The plate is modelled employing a 2D equivalent single-layer theory.
- iii. It is presumed that the transverse normal is unable to achieve extension.
- iv. The impact of transverse normal stress on the overall behaviour of the plate is insignificant, resulting in a plane stress condition.
- v. The FGM exhibits isotropy and inhomogeneity.
- vi. For the current analysis, it is assumed that the system is undamped.
- vii. It is postulated that the metal-rich and ceramic-rich phases are located at the lower and upper surfaces of the FGM plate, respectively.

- viii. The unidirectional gradation of FGM constituents is assumed, i.e., along the thickness direction only.

### 3.2 EFFECTIVE MATERIAL PROPERTIES OF FGSP

In the current investigation, a single layer and three distinct configurations of FGSPs are investigated. The details are as follows.

- i. *Single layer FG*: A single layer plate in which metal properties are gradually varying from the ceramic phase at the top surface to the metal phase at the bottom surface, as shown in Fig. 3.1(a).
- ii. *Homogenous ceramic core and FG face sheets (FCF)*: An FCF sandwich is a plate with FG face sheets on the top and bottom surfaces with ceramic material in the core, as shown in Fig. 3.1(b).
- iii. *FG core and homogenous faces sheets (MFC)*: MFC sandwich refers to a sandwich plate with a homogeneous metal bottom face sheet and a ceramic top face sheet with FG material as the core, as shown in Fig. 3.1(c).

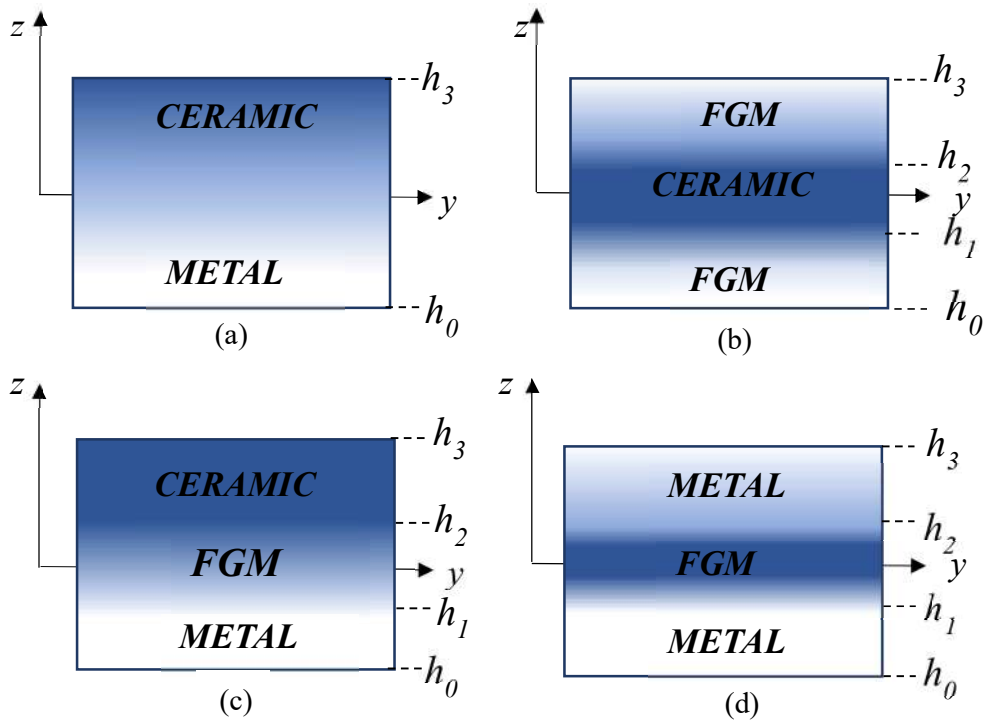


Fig. 3.1 Schematics of configurations of FG plates (a) Single layer (b) FCF Sandwich (c) MFC Sandwich (d) MFM Sandwich

- iv. *FG core and metal homogenous faces sheets (MFM)*: MFM sandwich refers to a sandwich plate with a homogeneous metal top and bottom face sheet with FG material as the core, as shown in Fig. 3.1 (d).

member, correspondingly, whereas  $h_1$  signifies the interface point amid the core sheet and bottom face sheets. Likewise,  $h_2$  represents the z-direction interface location amongst the core and top face sheets. The plate is shown in a rectangular coordinate system, with a z-axis pointing in the thickness direction and a y-axis pointing in the width direction (Fig. 3.1). Additionally, various sandwich layer schemes are obtained by changing the thickness of the core and face sheets. The various sandwich layer schemes considered in the current study are charted in Table 3.1

To effectively predict the vibration and buckling responses of the FGSP used in a high-temperature environment, the temperature dependence of the constituent materials should be considered. Therefore, material properties such as Young's modulus  $E(z)$ , density, and thermal expansion coefficient of FGM constituents are expressed as general term  $\tilde{P}(T)$  and can be expressed as a function of temperature (Singh and Harsha (2020c)) as Eq. (3.1):

$$\tilde{P}(T) = \tilde{P}_0(\tilde{P}_{-1}T^{-1} + 1 + \tilde{P}_1T + \tilde{P}_2T^2 + \tilde{P}_3T^3) \quad (3.1)$$

where  $\tilde{P}_0$ ,  $\tilde{P}_1$ ,  $\tilde{P}_{-1}$  and  $\tilde{P}_2$  are the coefficients of temperature  $T$  (K) and are exclusive to the constituent materials. It is assumed that the temperature field exhibits uniformity in the direction of thickness. The initial temperature of the surroundings is represented by  $T_0 = 300$  K, and the distribution of temperature is indicated by the equation (3.2).

$$T(z) = T_0 + \Delta T \quad (3.2)$$

Where  $\Delta T$  denotes temperature rise. Utilising rule of mixture and  $z$  indicating the location in the thickness path, the FGM effective material properties may be stated as in Eq. (3.3)

$$\tilde{P}(z, T) = \tilde{P}_m + (\tilde{P}_c - \tilde{P}_m)V_f(z) - (\tilde{P}_c + \tilde{P}_m)P_d(z) \quad (3.3)$$

The ceramic and metal material properties are denoted by  $\tilde{P}_c$  and  $\tilde{P}_m$  separately. The term  $\tilde{P}(z, T)$  is the general term to represent Young's modulus  $E(z, T)$ , density

$\rho(z, T)$  and thermal expansion coefficient ( $\alpha$ ) of plate constituent materials across the thickness are given.  $P_d(z)$  denotes porosity distribution function across the thickness, and depends upon the kind of porosity distribution.

Table 3.1 Various layer schemes of FGSPs (Daikh and Zenkour (2019))

Sl. No.	Layer schemes	$h_0$	$h_1$	$h_2$	$h_3$
1.	1-2-1	$-h/2$	$-h/4$	$+h/4$	$+h/2$
2.	1-1-1	$-h/2$	$-h/6$	$+h/6$	$+h/2$
3.	2-1-2	$-h/2$	$-h/10$	$+h/10$	$+h/2$
4.	1-0-1	$-h/2$	$0$	$0$	$+h/2$
5.	2-2-1	$-h/2$	$-h/10$	$+3h/10$	$+h/2$
6.	2-1-1	$-h/2$	$0$	$+h/4$	$+h/2$

$V_f(z)$  denotes the volume fraction of the ceramic material at any point along the  $z$ -direction. For single-layer FG plate is given by Eq. (3.4). The variations of volume fraction of ceramic material along the dimensionless thickness of single-layer FGM plates for different volumes fraction exponent is shown in Fig. 3.2.

$$V_f(z) = \left( \frac{z}{h} + \frac{1}{2} \right)^n, \quad h_0 \leq z \leq h_3 \quad (3.4)$$

The term  $n$  denotes the volume fraction exponent. The volume fraction can be varied to obtain power law or sigmoidal function-based plates.

### 3.2.1 Power Law Functionally Graded Sandwich Plate (PFGSP)

A fundamental power law-based material idealization technique is considered in the

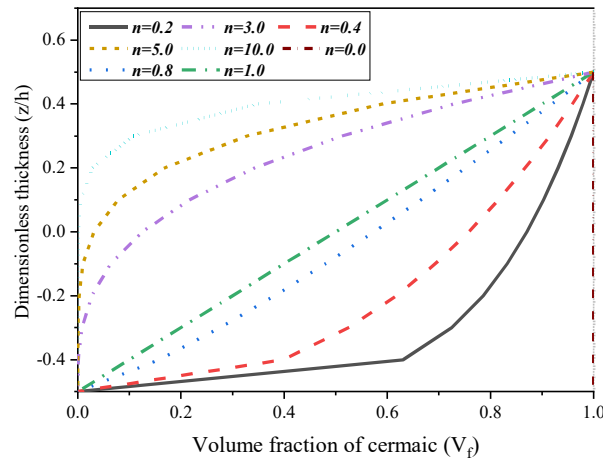


Fig. 3.2 Variations of volume fraction of ceramic material along the dimensionless thickness of single layer FGM plates for different volumes fraction exponent

current study to describe the variation in material properties across  $h$ . The volume fraction of bottom, core, and top sheets along the thickness direction is expressed as  $V_f^b(z)$ ,  $V_f^{co}(z)$  and respectively (also shown in Eq. (3.5)). Further, the term  $z$  represents the distances of any points from the mid surfaces along the  $z$ - directions. The variations of the volume fraction of ceramic material along the dimensionless thickness of FCF PFGSP for different volumes fraction exponent are displayed in Fig. 3.3(a).

$$\begin{aligned}
 V_f^b(z) &= \left( \frac{z-h_0}{h_1-h_0} \right)^n, & h_0 \leq z \leq h_1 \\
 V_f^{co}(z) &= 1, & h_1 \leq z \leq h_2 \\
 V_f^t(z) &= \left( \frac{z-h_3}{h_2-h_3} \right)^n, & h_2 \leq z \leq h_3
 \end{aligned} \tag{3.5}$$

### 3.2.2 Sigmoidal-Based Functionally Graded Sandwich Plate (SFGSP)

Compared to the stresses produced by power law, sigmoidal FGM reduces the stress concentration.(Chung and Chi (2001)). Here the variation of volume fraction based on the sigmoid function in the  $z$ -direction is given by Eq. (3.6). The variations of volume fraction of ceramic material along the dimensionless thickness of FCF SFGSP for different volume fraction exponents are displayed in Fig. 3.3(b).

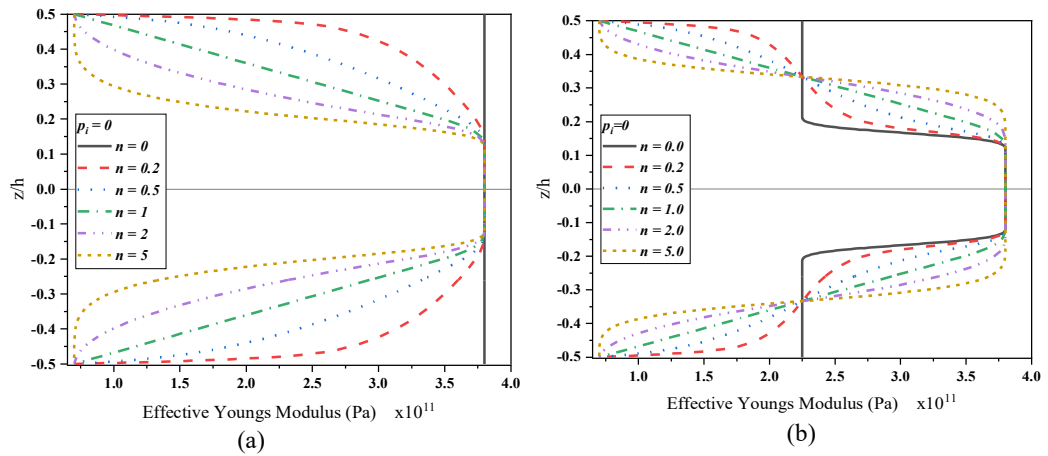


Fig. 3.3 Effective Young's modulus versus dimensionless thickness of FCF (a) PFGSP (b) SFGSP for several volume fraction exponent ( $n$ )

$$\begin{aligned}
V_f^b(z) &= \frac{1}{2} \left( \frac{z-h_0}{h_m-h_0} \right)^n, & h_0 \leq z \leq h_m & \quad V_f^t(z) = 1 - \frac{1}{2} \left( \frac{z-h_2}{h_n-h_2} \right)^n, & h_2 \leq z \leq h_n \\
V_f^t(z) &= 1 - \frac{1}{2} \left( \frac{z-h_1}{h_m-h_1} \right)^n, & h_m \leq z \leq h_1 & \quad V_f^b(z) = \frac{1}{2} \left( \frac{z-h_3}{h_n-h_3} \right)^n, & h_n \leq z \leq h_3 \\
V_f^{co}(z) &= 1, & h_1 \leq z \leq h_2 & 
\end{aligned} \quad (3.6)$$

Where  $h_m = (h_0 + h_1)/2$  and  $h_n = (h_2 + h_3)/2$  indicates the middle surface positions of the lower and upper face sheets correspondingly. Eq. (3.5) and Eq. (3.6), which correspond to FCF sandwich plates, can be modified accordingly for MFC and MFM sandwich plates (Singh and Harsha (2020a)).

Due to the absence of symmetry, FG plates' neutral surface may not coincide with their middle surface. By setting the origin of the coordinate system on the neutral surface, FG plate problems can be treated with the homogenous isotropic plate theories. Two distinct planes,  $z_{ms}$  and  $z_{ns}$  are taken into consideration to determine the location of the neutral surface of the FG sandwich plate, as illustrated in Fig. 3.4. Thus, the shift of neutral surface  $d$  can be obtained as given in Eq. (3.7).

$$d = \frac{\int_{h_0}^{h_1} E(z_{ms})z_{ms} dz + \int_{h_1}^{h_2} E(z_{ms})z_{ms} dz + \int_{h_2}^{h_3} E(z_{ms})z_{ms} dz}{\int_{h_0}^{h_1} E(z_{ms}) dz + \int_{h_1}^{h_2} E(z_{ms}) dz + \int_{h_2}^{h_3} E(z_{ms}) dz} \quad (3.7)$$

Where  $E_m$  is the effective Youngs modulus given by Eq. (3.3),  $z_{ms}$  and  $z_{ns}$  are the  $z$  coordinates based on the middle and neutral surface of the FGM constraining layers, respectively.

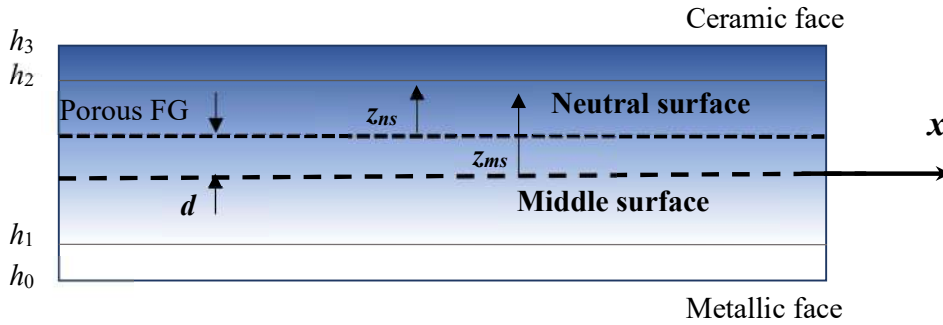


Fig. 3.4 The position of the middle surface and neutral surface for FGSP

### 3.3 POROSITY DISTRIBUTION MODELS

The porosity defect can appear as micro voids during the FGSP manufacturing process due to significant differences in the solidification temperature of FGM constituents. In certain instances, the difference in temperature between the die and the material being poured causes the percentage of porosity to be more significant at the surface. In other instances, the longer solidification times cause the porosity distribution to be higher near the core of the samples (Vynnycky (2020)). The mechanical strength of FGM can vary due to different porosity distributions. Therefore, it becomes essential to study the effect of varying porosity distribution and percentage of porosity during the analysis phase. To address this issue, several porosity distributions are modelled using the mathematical function varying across thickness as listed in Table 3.2, Table 3.3, and Table 3.4 for single-layer FGM, FCF FGSPs, and MFC FGSPs, respectively. Here porosity index is represented by  $p_i$ . Fig. 3.5 and Fig. 3.6 show the schematic representation of porosity distributions across the thickness direction in FCF and MFC FGSP, respectively. Here  $P_d^t$  and  $P_d^b$  refers to the top and bottom sheet porosity distribution, respectively

Table 3.2 Porosity models and corresponding distribution functions for single layer FGM plate (Kiran et al. (2018))

Description	Porosity distribution functions
1. U-D: In this model, the pores are distributed uniformly along with the plate thickness.	$P_d^t(z) = P_d^b(z) = \frac{p_i}{2}$
2. X-D: In this case, the porosity is distributed such that porosity concentration is high at the top portion but low at the mid-height of the plate.	$P_d^b(z) = \frac{p_i}{2} \left[ \frac{ 2z }{h} \right]$
3. O-D: In this case, the concentration of porosities is high at the mid-height of the plate and low at the top and bottom portions.	$P_d^b(z) = \frac{p_i}{2} \left[ 1 - \frac{ 2z }{h} \right]$
4. V-D: In this case, the porosity concentration is high at the top portion of the plate and low at the bottom portion.	$P_d^b(z) = \frac{p_i}{2} \left[ 1 + \frac{ 2z }{h} \right]$

Table 3.3 Porosity models and corresponding distribution functions for FCF ((Daikh and Zenkour (2019))

Description	Porosity distribution functions
1. U-D: In this model, the pores are distributed uniformly along with the plate thickness.	$P_d^t(z) = P_d^b(z) = \frac{p_i}{2}, h_0 \leq z \leq h_3$
2. X-D: In this case, the porosity is distributed such that porosity concentration is high at the outer surface and interface but low at the middle thickness of face sheets.	$P_d^b(z) = \frac{p_i}{2} \left[ \frac{ 2z - (h_0 + h_1) }{h_1 - h_0} \right], \quad h_0 \leq z \leq h_1$ $P_d^t(z) = \frac{p_i}{2} \left[ \frac{ 2z - (h_3 + h_2) }{h_3 - h_2} \right], \quad h_2 \leq z \leq h_3$
3. O-D: In this case, the porosity concentration is high at the middle thickness of face sheets and low at the outer surfaces and interface.	$P_d^b(z) = \frac{p_i}{2} \left[ 1 - \frac{ 2z - (h_0 + h_1) }{h_1 - h_0} \right], \quad h_0 \leq z \leq h_1$ $P_d^t(z) = \frac{p_i}{2} \left[ 1 - \frac{ 2z - (h_3 + h_2) }{h_3 - h_2} \right], \quad h_2 \leq z \leq h_3$
4. Log O-D: In this case, porosity concentration varies logarithmically across the thickness of face sheets.	$P_d^b(z) = \log\left(1 + \frac{p_i}{2}\right) \left[ 1 - \frac{ 2z - (h_0 + h_1) }{h_1 - h_0} \right], \quad h_0 \leq z \leq h_1$ $P_d^t(z) = \log\left(1 + \frac{p_i}{2}\right) \left[ 1 - \frac{ 2z - (h_3 + h_2) }{h_3 - h_2} \right], \quad h_2 \leq z \leq h_3$
5. V1-D: In this case, the concentration of porosity in face sheets is high at the interface and low at the outer surfaces.	$P_d^b(z) = \frac{p_i}{2} \left[ 1 - \frac{z - h_1}{h_0 - h_1} \right], \quad h_0 \leq z \leq h_1$ $P_d^t(z) = \frac{p_i}{2} \left[ \frac{z - h_3}{h_2 - h_3} \right], \quad h_2 \leq z \leq h_3$
6. V2-D: In this case, the porosity concentration in the face sheets is low at the interface positions and high at the outer surfaces.	$P_d^b(z) = \frac{p_i}{2} \left[ \frac{z - h_1}{h_0 - h_1} \right], \quad h_0 \leq z \leq h_1$ $P_d^t(z) = \frac{p_i}{2} \left[ 1 - \frac{z - h_3}{h_2 - h_3} \right], \quad h_2 \leq z \leq h_3$

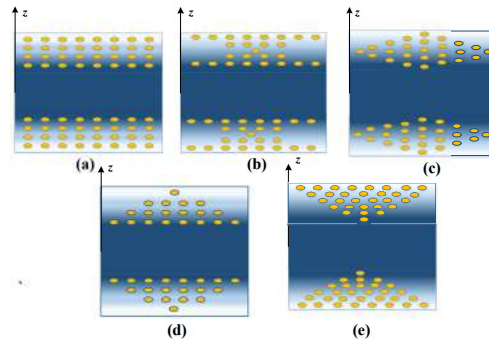


Fig. 3.5 Schematic cross-section of 1-1-1 FCF FGSP with porosity distribution (a)U-D (b)X-D (c) O-D (d) V1-D (e) V2-D

Table 3.4 Porosity models and corresponding distribution functions for MFC

Description	Porosity distribution functions
1. U-D: This model distributes pores uniformly with plate thickness.	$P_d^{co}(z) = \frac{p_i}{2}, h_1 \leq z \leq h_2$
2. X-D: The porosities are less concentrated at the center portion and highly concentrated at the interface.	$P_d^{co}(z) = \frac{p_i}{2} \left[ \frac{ 2z - h_1 - h_2 }{h_2 - h_1} \right], h_1 \leq z \leq h_2$
3. O-D: The porosities are highly concentrated at the center portion and less concentrated at the interface of the FG core.	$P_d^{co}(z) = \frac{p_i}{2} \left[ 1 - \frac{ 2z - h_1 - h_2 }{h_2 - h_1} \right], h_1 \leq z \leq h_2$
4. V1-D In this case, the concentration of porosity is high at the top interface positions and low at the bottom interface.	$P_d^{co}(z) = \frac{p_i}{2} \left( \frac{z - h_1}{h_2 - h_1} \right), h_1 \leq z \leq h_2$
5. V2-D In this case, the concentration of porosity is low at the top interface positions and high at the bottom interface.	$P_d^{co}(z) = \frac{p_i}{2} \left[ 1 - \left( \frac{z - h_1}{h_2 - h_1} \right) \right], h_1 \leq z \leq h_2$

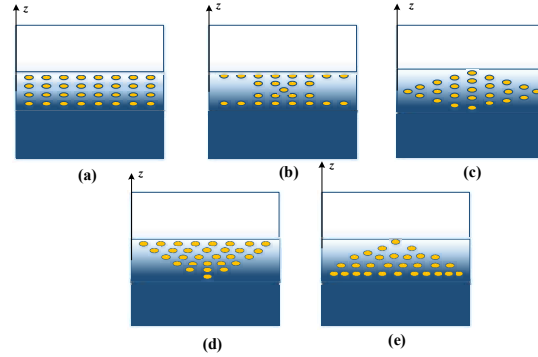


Fig. 3.6 Schematic cross-section of 1-1-1 MFC FGSP with porosity distribution (a)U-D (b)X-D (c)O-D (d)V1-D (e)V2-D

### 3.4 GEOMETRY OF SANDWICH PLATE

FGSPs with a circular shaped cutout with diameter ‘ $d$ ’, length ‘ $a$ ’, width ‘ $b$ ’ and thickness ‘ $h$ ’ along with a positive set of the coordinate system with respect to  $x$ ,  $y$ , and  $z$  directions are as exemplified in Fig. 3.7. The terms  $u_0, v_0, w_0$  are the components of displacements along the coordinate’s directions  $x$ ,  $y$  and  $z$  respectively of an arbitrary point on the planes  $z = 0$  (mid-planes). Further, the rotations of the normal to the mid planes about  $y$ - and  $x$ -axes are represented by  $\theta_x$  and  $\theta_y$ , respectively.

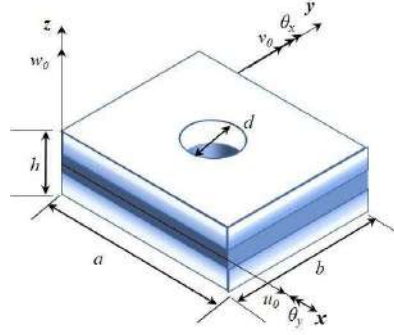


Fig. 3.7 Schematic of FGSP with a circular cutout

### 3.5 DISPLACEMENT MODEL

In this work, FGSP is used based on a neutral surface as a reference plane, and Reissner-Mindlin first-order shear deformation theory (Whitney and Pagano (1972)) is adopted in this examination centred on the assumption that the normal to the midplane remain straight and need not to be perpendicular to the mid plane after bending so that the displacement field in deformable shear plate is shown in Eq. (3.8)

$$\begin{aligned} u(x, y, z) &= u_0(x, y) + z\theta_x(x, y), \\ v(x, y, z) &= v_0(x, y) + z\theta_y(x, y), \\ w(x, y, z) &= w_0(x, y). \end{aligned} \quad (3.8)$$

### 3.6 STRAIN-DISPLACEMENTS RELATION

Green-Lagrange's type of strain displacement relation is incorporated for this analysis. The elastic stiffness matrix is determined by considering the linear component of strain, while the geometric stiffness matrix is derived by considering the nonlinear component of strain. By substitution of the displacements field given by Eq. (3.8) in strain terms, strain displacements relations are obtained as in Eq. (3.9). The linear strain displacement relations are:

$$\begin{aligned} \left\{ \varepsilon_x \quad \varepsilon_y \quad \gamma_{xy} \quad \gamma_{yz} \quad \gamma_{xz} \right\}^T &= \left\{ \frac{\partial u_0}{\partial x} \quad \frac{\partial v_0}{\partial y} \quad \frac{\partial u_0}{\partial y} + \frac{\partial v_0}{\partial x} \quad \theta_y + \frac{\partial w_0}{\partial y} \quad \theta_x + \frac{\partial w_0}{\partial x} \right\}^T \\ &+ z \left\{ \frac{\partial \theta_x}{\partial x} \quad \frac{\partial \theta_y}{\partial y} \quad \frac{\partial \theta_x}{\partial y} + \frac{\partial \theta_y}{\partial x} \quad 0 \quad 0 \right\}^T \end{aligned} \quad (3.9)$$

the terms  $\varepsilon_x$ ,  $\varepsilon_y$  and  $\gamma_{xy}$  are linear in-plane normal, and shear strains at a point in the plate with references to the FG plates axes, respectively. The terms  $\gamma_{yz}$  and  $\gamma_{xz}$  are

transverse shear strains. Further, the nonlinear parts of the strains are selected to evaluate the geometrics stiffness matrix by using strain energy owing to in-plane axial stress and nonlinear strain (Bathe (2014)) and are expressed as Eq. (3.10).

$$\begin{aligned}
\varepsilon_{xnl} &= \frac{1}{2} \left\{ \left( \frac{\partial u}{\partial x} \right)^2 + \left( \frac{\partial v}{\partial x} \right)^2 + \left( \frac{\partial w}{\partial x} \right)^2 + z^2 \left[ \left( \frac{\partial \theta_x}{\partial x} \right)^2 + \left( \frac{\partial \theta_y}{\partial x} \right)^2 \right] \right\} \\
\varepsilon_{ynl} &= \frac{1}{2} \left\{ \left( \frac{\partial u}{\partial y} \right)^2 + \left( \frac{\partial v}{\partial y} \right)^2 + \left( \frac{\partial w}{\partial y} \right)^2 + z^2 \left[ \left( \frac{\partial \theta_x}{\partial y} \right)^2 + \left( \frac{\partial \theta_y}{\partial y} \right)^2 \right] \right\} \\
\gamma_{xynl} &= \left( \frac{\partial u}{\partial x} \frac{\partial u}{\partial y} \right) + \left( \frac{\partial v}{\partial x} \frac{\partial v}{\partial y} \right) + \left( \frac{\partial w}{\partial x} \frac{\partial w}{\partial y} \right) + z^2 \left[ \frac{\partial \theta_x}{\partial x} \frac{\partial \theta_x}{\partial y} + \frac{\partial \theta_y}{\partial x} \frac{\partial \theta_y}{\partial y} \right]
\end{aligned} \tag{3.10}$$

The terms  $\varepsilon_{xnl}$ ,  $\varepsilon_{ynl}$  and  $\gamma_{xynl}$  indicate nonlinear normal and shear strains at an arbitrary point in the plate with reference to the FG plate axes, respectively. The nonlinear strains are used in the strain energy equation, and the geometric stiffness matrix is obtained (Cook et al. (1989)).

### 3.7 CONSTITUTIVE RELATIONSHIP

The FGM plate linear constitutive relation can be stated as in Eq. (3.11) (Singh and Harsha (2020a))

$$\begin{Bmatrix} \sigma_x \\ \sigma_y \\ \tau_{xy} \\ \tau_{yz} \\ \tau_{xz} \end{Bmatrix} = \begin{bmatrix} Q_{11} & Q_{12} & 0 & 0 & 0 \\ Q_{12} & Q_{22} & 0 & 0 & 0 \\ 0 & 0 & Q_{44} & 0 & 0 \\ 0 & 0 & 0 & Q_{55} & 0 \\ 0 & 0 & 0 & 0 & Q_{66} \end{bmatrix} \begin{Bmatrix} \varepsilon_x - \alpha(z)\Delta T \\ \varepsilon_y - \alpha(z)\Delta T \\ 0 \\ 0 \\ 0 \end{Bmatrix} \tag{3.11}$$

where,

$$Q_{11} = Q_{22} = \frac{E(z, T)}{(1 - \nu^2)}; \quad Q_{12} = Q_{21} = \frac{\nu E(z, T)}{(1 - \nu^2)}; \quad Q_{33} = Q_{44} = Q_{55} = \frac{E(z, T)}{2(1 + \nu)}$$

Where  $(\sigma_x, \sigma_y, \tau_{xy}, \tau_{yz}, \tau_{xz})$  are stresses and  $(\varepsilon_x, \varepsilon_y, \gamma_{xy}, \gamma_{yz}, \gamma_{xz})$  are strains with respects to plate reference axes. While  $E(z, T)$  signifies the temperature-dependent Young's modulus at any point along the  $z$ -direction.

The total in-plane force resultants and moments, produced due to temperature rise are defined as

$$\begin{bmatrix} N_x^T & M_x^T \\ N_y^T & M_y^T \\ N_{xy}^T & M_{xy}^T \end{bmatrix} = \begin{bmatrix} N^T & M^T \end{bmatrix} = \int_{-h/2}^{+h/2} \begin{Bmatrix} \sigma_x \\ \sigma_y \\ \tau_{xy} \end{Bmatrix} (1, z) dz, \quad \begin{bmatrix} Q_x \\ Q_y \end{bmatrix} = \int_{-h/2}^{+h/2} \begin{bmatrix} \tau_{xz} \\ \tau_{yz} \end{bmatrix} dz$$

The thermal force and moment resultants  $\{M^T\}$  can also be represented as

$$\begin{aligned} \{N^T\} &= \int_{-h/2}^{+h/2} \{\beta\} \Delta T dz \\ \{M^T\} &= \int_{-h/2}^{+h/2} \{\beta\} \Delta T z dz \end{aligned}$$

where,

$$\beta = \begin{Bmatrix} (Q_{11} + Q_{12}) \alpha \\ (Q_{12} + Q_{22}) \alpha \\ 0 \end{Bmatrix}$$

$$\begin{Bmatrix} N_i \\ M_i \\ Q_i \end{Bmatrix} = \begin{bmatrix} \bar{A}_{ij} & \bar{B}_{ij} & 0 \\ \bar{B}_{ij} & \bar{D}_{ij} & 0 \\ 0 & 0 & \bar{S}_{ij} \end{bmatrix} \begin{Bmatrix} \varepsilon_j \\ k_j \\ \gamma_j \end{Bmatrix} \quad (3.12)$$

In the abbreviated form, Eq. (3.12) is written as shown in Eq. (3.13)

$$\{N\} = [D] \{\varepsilon\} \quad (3.13)$$

The term,  $N_i = [N_x \ N_y \ N_{xy}]^T$  are in-plane stress resultants,  $M_i = [M_x \ M_y \ M_{xy}]^T$  are moments stress resultants, and  $Q_i = [Q_x \ Q_y]^T$  are transverse shear stress resultants; likewise are strains,  $k_j = [k_x \ k_y \ k_{xy}]^T$  are curvatures, and  $\gamma_j = [\gamma_{yz} \ \gamma_{xz}]^T$  are transverse shear strains. Further, the term  $\bar{A}_{ij}$  is extension-extension matrix,  $\bar{B}_{ij}$  is the extension-bending matrix,  $\bar{D}_{ij}$  is the bending-bending matrix, and can be written as Eqs. (3.14) and (3.15)

$$(\bar{A}_{ij}, \bar{B}_{ij}, \bar{D}_{ij}) = \int_{-h/2}^{+h/2} (1, z, z^2) Q_{ij} dz \quad i, j = 1, 2, 6 \quad (3.14)$$

$$\bar{S}_{ij} = \int_{-h/2}^{+h/2} k Q_{ij} dz \quad i, j = 4, 5 \quad (3.15)$$

The shear corrections factor is expressed by the term  $k$  and is incorporated in  $\bar{S}_{ij}$ .

### 3.8 LINEAR STRAIN-NODAL DISPLACEMENT MATRIX

The elemental displacements can be expressed into nodal displacements, as shown in Eq. (3.16). The strain field is expanded using shape functions as shown in Eq. (3.17):

$$\left\{ \begin{array}{l} \varepsilon_x \\ \varepsilon_y \\ \gamma_{xy} \\ k_x \\ k_y \\ k_{xy} \\ \gamma_{xz} \\ \gamma_{yz} \end{array} \right\} = \left[ \begin{array}{l} \frac{\partial u}{\partial x} \\ \frac{\partial v}{\partial y} \\ \frac{\partial u}{\partial y} + \frac{\partial v}{\partial x} \\ \frac{\partial \theta_x}{\partial x} \\ \frac{\partial \theta_y}{\partial y} \\ \frac{\partial \theta_x}{\partial y} + \frac{\partial \theta_y}{\partial x} \\ \frac{\partial w}{\partial x} + \theta_x \\ \frac{\partial w}{\partial y} + \theta_y \end{array} \right]_{i=1,8} \quad (3.16)$$

$$\begin{Bmatrix} \frac{\partial u}{\partial x} \\ \frac{\partial v}{\partial y} \\ \frac{\partial u}{\partial y} + \frac{\partial v}{\partial x} \\ \frac{\partial \theta_x}{\partial x} \\ \frac{\partial \theta_y}{\partial y} \\ \frac{\partial \theta_x}{\partial y} + \frac{\partial \theta_y}{\partial x} \\ \frac{\partial w}{\partial x} + \theta_x \\ \frac{\partial w}{\partial y} + \theta_y \end{Bmatrix} = \begin{bmatrix} \frac{\partial N_i}{\partial x} & 0 & 0 & 0 & 0 \\ 0 & \frac{\partial N_i}{\partial y} & 0 & 0 & 0 \\ \frac{\partial N_i}{\partial x} & \frac{\partial N_i}{\partial y} & 0 & 0 & 0 \\ 0 & 0 & 0 & \frac{\partial N_i}{\partial x} & 0 \\ 0 & 0 & 0 & 0 & \frac{\partial N_i}{\partial y} \\ 0 & 0 & 0 & \frac{\partial N_i}{\partial x} & \frac{\partial N_i}{\partial y} \\ 0 & 0 & \frac{\partial N_i}{\partial x} & N_i & 0 \\ 0 & 0 & \frac{\partial N_i}{\partial y} & 0 & N_i \end{bmatrix}_{i=1,8} \begin{Bmatrix} u_i \\ v_i \\ w_i \\ \theta_{xi} \\ \theta_{yi} \end{Bmatrix}_{i=1,8} \quad (3.17)$$

The strain-nodal displacement equation for  $j^{th}$  element can be abbreviated as shown in Eq. (3.18)

$$\{\varepsilon\}_j = [\mathbf{B}]\{d\}_j \quad (3.18)$$

Where  $[\mathbf{B}]$  is strain displacement matrix and  $\{d\}$  is displacement matrix

### 3.9 FINITE ELEMENT FORMULATION

A closed-form solution is tedious to solve complex problems in terms of geometry, loading, and boundary condition. Numerical technique such as FE provides an alternative in such case. In this study, vibration, buckling, and dynamic instability of FG plate with a cutout under in-plane loads and follower load are investigated using a FE approach.

#### 3.9.1 Iso-Parametric Element

In the present study, an 8-noded ‘serendipity’ element has been used to discretize the domain of the FG plate. Fig. 3.8 shows the schematic diagram of the isoparametric element.

In the current work, the FGM plate is discretized with the aid of eight noded isoparametric elements with 5 degrees of freedom per node viz.  $u$ ,  $v$ ,  $w$ ,  $\theta_x$  and  $\theta_y$  per

node is used. The generalized displacement vector and element geometry of the model at any point can be represented in terms of shape functions as expressed in Eq. (3.19).

$$\{d\}_j = N_i \{d_i\}, x = \sum_{i=1}^8 N_i x_i, y = \sum_{i=1}^8 N_i y_i \quad (3.19)$$

where  $\{d\} = \{u_i, v_i, w_i, \theta_{xi}, \theta_{yi}\}$  is displacement vector and  $u_i, v_i, w_i, \theta_{xi}$  and  $\theta_{yi}$  are the respective values at node  $i$ . Further,  $x_i$  and  $y_i$  are the cartesian coordinates of the  $i^{\text{th}}$  nodes. The interpolating (shape) function  $N_i$  in terms of the normalized coordinates  $\eta$  and  $\xi$  can be defined for 8-noded isoparametric element as Eqs. (3.20–3.22)

For corner nodes 1, 3, 5 and 7

$$N_i = \frac{1}{4}(1 + \xi\xi_i)(\xi\xi_i + \eta\eta_i - 1)(\eta\eta_i + 1) \quad (3.20)$$

For middle nodes 2 and 6

$$N_i = \frac{1}{2}(1 - \xi^2)(1 - \eta\eta_i) \quad (3.21)$$

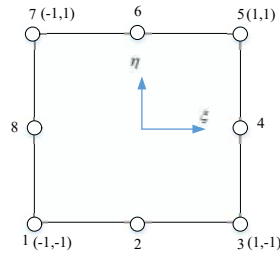


Fig. 3.8 Rectangular Element with natural coordinates and local node number

For middle nodes 4 and 8

$$N_i = \frac{1}{2}(1 + \xi\xi_i)(1 - \eta^2) \quad (3.22)$$

The derivatives of the shape functions concerning the global coordinate systems are related to their derivatives in the natural co-ordinates system as given in Eq. (3.23)

$$\begin{bmatrix} \frac{\partial N_i}{\partial x} \\ \frac{\partial N_i}{\partial y} \end{bmatrix} = [\mathbf{J}]^{-1} \begin{bmatrix} \frac{\partial N_i}{\partial \xi} \\ \frac{\partial N_i}{\partial \eta} \end{bmatrix} \quad (3.23)$$

Here  $[\mathbf{J}]$  is the Jacobian matrix and is used to map the natural coordinate system to the cartesian coordinate system is given by Eq. (3.24)

$$[\mathbf{J}] = \begin{bmatrix} \frac{\partial x}{\partial \xi} & \frac{\partial y}{\partial \xi} \\ \frac{\partial x}{\partial \eta} & \frac{\partial y}{\partial \eta} \end{bmatrix} \quad (3.24)$$

### 3.9.2 Elemental Stiffness Matrix

The strain energy  $U_l$  due to linear strains in the entire plate can be stated in terms of the stresses and linear strains below.

$$U_l = \frac{1}{2} \int_v \{\varepsilon_l\}^T \{\sigma\} dv \quad (3.25)$$

The strain energy in the  $j^{th}$  element can be obtained by substituting and Eq. (3.17) and Eq. (3.18) in Eq. (3.25).

$$U_{l,j} = \frac{1}{2} \int_A \{d\}_j^T [\mathbf{B}]_j^T [\mathbf{D}]_j [\mathbf{B}]_j \{d\}_j dA \quad (3.26)$$

The total strain energy of the overall plate can be found by summation of individual element strain energies as shown in Eq. (3.27)

$$U_l = \sum_{j=1}^m \frac{1}{2} \int_A \{d\}_j^T [\mathbf{B}]_j^T [\mathbf{D}]_j [\mathbf{B}]_j \{d\}_j dA \quad (3.27)$$

The above equation is alternatively stated as in Eq. (3.28)

$$U_l = \frac{1}{2} \sum_{j=1}^m \{d\}_j^T [\mathbf{K}]_j \{d\}_j \quad (3.28)$$

in which  $[\mathbf{K}]_j = \int_A [\mathbf{B}]_j^T [\mathbf{D}]_j [\mathbf{B}]_j dA$  is the stiffness matrix of the  $j^{th}$  element.

Where,  $[\mathbf{B}]$  is the linear strain-displacement matrix and  $[\mathbf{D}]$  is the matrix of stiffness. The finite element assemblage is done by adding the above elemental matrices, taking the global displacement vector of the nodes of the entire plate to be  $\{d\}$ , which results in the following relation. As shown in Eq. (3.29)

$$U_l = \frac{1}{2} \{d\}^T [\mathbf{K}] \{d\} \quad (3.29)$$

This point  $[\mathbf{K}]$  is called the global elastic stiffness matrix of the entire plate.

### 3.9.3 Geometric Stiffness Matrix

The plate loses its stiffness when acted upon by an in-plane edge load. The geometric stiffness matrix is used to take into account the loss of stiffness. Here Green-Lagrange's strain displacement relations, as shown in Eq. (3.10), is considered. The strain energy due to nonlinear strains arising from unit in-plane load can be expressed as in Eq. (3.30)

$$U_{nl} = \int_v \{\sigma^0\}^T \{\varepsilon_{nl}\} dv \quad (3.30)$$

Where  $\{\sigma^0\}$  is the initial in-plane stress field due to unit in-plane load computed at each point where Gaussian Quadrature has been performed to evaluate the integrals. Substituting Eq. (3.10) in Eq. (3.30), we obtain

$$\begin{aligned} U_{nl} = & \frac{1}{2} \int_v \sigma_x^0 \left\{ \left( \frac{\partial u}{\partial x} \right)^2 + \left( \frac{\partial v}{\partial x} \right)^2 + \left( \frac{\partial w}{\partial x} \right)^2 + z^2 \left[ \left( \frac{\partial \theta_x}{\partial x} \right)^2 + \left( \frac{\partial \theta_y}{\partial x} \right)^2 \right] \right\} dv + \\ & \frac{1}{2} \int_v \sigma_y^0 \left\{ \left( \frac{\partial u}{\partial y} \right)^2 + \left( \frac{\partial v}{\partial y} \right)^2 + \left( \frac{\partial w}{\partial y} \right)^2 + z^2 \left[ \left( \frac{\partial \theta_x}{\partial y} \right)^2 + \left( \frac{\partial \theta_y}{\partial y} \right)^2 \right] \right\} dv \\ & + \int_v \tau_{xy}^0 \left\{ \left( \frac{\partial u}{\partial x} \frac{\partial u}{\partial y} \right) + \left( \frac{\partial v}{\partial x} \frac{\partial v}{\partial y} \right) + \left( \frac{\partial w}{\partial x} \frac{\partial w}{\partial y} \right) + z^2 \left[ \frac{\partial \theta_x}{\partial x} \frac{\partial \theta_x}{\partial y} + \frac{\partial \theta_y}{\partial x} \frac{\partial \theta_y}{\partial y} \right] \right\} dv \end{aligned} \quad (3.31)$$

This equation can be integrated across thickness  $h$ , and the strain energy of a  $j^{th}$  element is:

$$U_{nl} = \frac{1}{2} \int_A \underbrace{\left[ \begin{array}{c} \frac{\partial u}{\partial x} \\ \frac{\partial u}{\partial y} \\ \frac{\partial v}{\partial x} \\ \frac{\partial v}{\partial y} \\ \frac{\partial w}{\partial x} \\ \frac{\partial w}{\partial y} \\ \frac{\partial \theta_x}{\partial x} \\ \frac{\partial \theta_x}{\partial y} \\ \frac{\partial \theta_y}{\partial x} \\ \frac{\partial \theta_y}{\partial y} \end{array} \right]^T}_{\text{d}A} \underbrace{\left[ \begin{array}{cccccccccccc} h\sigma_x^0 & h\tau_{xy}^0 & 0 & 0 & 0 & 0 & 0 & 0 & 0 & 0 & 0 & 0 \\ h\tau_{xy}^0 & h\sigma_y^0 & 0 & 0 & 0 & 0 & 0 & 0 & 0 & 0 & 0 & 0 \\ 0 & h\sigma_x^0 & h\tau_{xy}^0 & 0 & 0 & 0 & 0 & 0 & 0 & 0 & 0 & 0 \\ 0 & h\tau_{xy}^0 & h\sigma_y^0 & 0 & 0 & 0 & 0 & 0 & 0 & 0 & 0 & 0 \\ 0 & 0 & 0 & h\sigma_x^0 & h\tau_{xy}^0 & 0 & 0 & 0 & 0 & 0 & 0 & 0 \\ 0 & 0 & 0 & h\tau_{xy}^0 & h\sigma_y^0 & h\tau_{xy}^0 & h\sigma_y^0 & 0 & 0 & 0 & 0 & 0 \\ 0 & 0 & 0 & 0 & 0 & h\sigma_x^0 & h\tau_{xy}^0 & h\sigma_y^0 & 0 & 0 & 0 & 0 \\ 0 & 0 & 0 & 0 & 0 & h\tau_{xy}^0 & h\sigma_y^0 & h\tau_{xy}^0 & h\sigma_y^0 & 0 & 0 & 0 \\ 0 & 0 & 0 & 0 & 0 & 0 & 0 & 0 & 0 & h^3 \sigma_x^0 & h^3 \tau_{xy}^0 & 0 \\ 0 & 0 & 0 & 0 & 0 & 0 & 0 & 0 & 0 & h^3 \tau_{xy}^0 & h^3 \sigma_x^0 & 0 \\ 0 & 0 & 0 & 0 & 0 & 0 & 0 & 0 & 0 & h^3 \tau_{xy}^0 & h^3 \sigma_y^0 & 0 \\ 0 & 0 & 0 & 0 & 0 & 0 & 0 & 0 & 0 & 0 & 0 & h^3 \tau_{xy}^0 \\ 0 & 0 & 0 & 0 & 0 & 0 & 0 & 0 & 0 & 0 & 0 & h^3 \sigma_x^0 \\ 0 & 0 & 0 & 0 & 0 & 0 & 0 & 0 & 0 & 0 & 0 & h^3 \tau_{xy}^0 \\ 0 & 0 & 0 & 0 & 0 & 0 & 0 & 0 & 0 & 0 & 0 & h^3 \sigma_y^0 \\ 0 & 0 & 0 & 0 & 0 & 0 & 0 & 0 & 0 & 0 & 0 & h^3 \tau_{xy}^0 \\ 0 & 0 & 0 & 0 & 0 & 0 & 0 & 0 & 0 & 0 & 0 & h^3 \sigma_y^0 \end{array} \right]}_{\text{d}A} \quad (3.32)$$

The above Eq. (3.32) is abbreviated as

$$U_{nl} = \frac{1}{2} \int_A \{f\}^T [\mathbf{S}] \{f\} dA \quad (3.33)$$

where

$$\{f\} = \left[ \frac{\partial u}{\partial x} \quad \frac{\partial u}{\partial y} \quad \frac{\partial v}{\partial x} \quad \frac{\partial v}{\partial y} \quad \frac{\partial w}{\partial x} \quad \frac{\partial w}{\partial y} \quad \frac{\partial \theta_x}{\partial x} \quad \frac{\partial \theta_x}{\partial y} \quad \frac{\partial \theta_y}{\partial x} \quad \frac{\partial \theta_y}{\partial y} \right]^T \quad (3.34)$$

$$[\mathbf{S}] = \begin{bmatrix} [\mathbf{S}]_1 & 0 & 0 & 0 & 0 \\ 0 & [\mathbf{S}]_1 & 0 & 0 & 0 \\ 0 & 0 & [\mathbf{S}]_1 & 0 & 0 \\ 0 & 0 & 0 & [\mathbf{S}]_2 & 0 \\ 0 & 0 & 0 & 0 & [\mathbf{S}]_2 \end{bmatrix}$$

$$[\mathbf{S}]_1 = \begin{bmatrix} h\sigma_x^0 & h\tau_{xy}^0 \\ h\tau_{xy}^0 & h\sigma_y^0 \end{bmatrix} = \begin{bmatrix} N_x^0 & N_{xy}^0 \\ N_{xy}^0 & N_y^0 \end{bmatrix}$$

$$[\mathbf{S}]_2 = \begin{bmatrix} \frac{h^3}{12} \sigma_x^0 & \frac{h^3}{12} \tau_{xy}^0 \\ \frac{h^3}{12} \tau_{xy}^0 & \frac{h^3}{12} \sigma_y^0 \end{bmatrix} = \frac{h^2}{12} \begin{bmatrix} N_x^0 & N_{xy}^0 \\ N_{xy}^0 & N_y^0 \end{bmatrix}$$

Using shape functions defined in Eqs (3.20–3.22), the nonlinear strain vector  $\{f\}$ , defined in Eq. (3.34), can be expressed in terms of the nodal displacement  $\{d\}_j$  for the  $j^{\text{th}}$  element as

$$\begin{Bmatrix} \frac{\partial u}{\partial x} \\ \frac{\partial u}{\partial y} \\ \frac{\partial v}{\partial x} \\ \frac{\partial v}{\partial y} \\ \frac{\partial w}{\partial x} \\ \frac{\partial w}{\partial y} \\ \frac{\partial \theta_x}{\partial x} \\ \frac{\partial \theta_x}{\partial y} \\ \frac{\partial \theta_y}{\partial x} \\ \frac{\partial \theta_y}{\partial y} \end{Bmatrix} = \sum_{i=1}^8 \begin{Bmatrix} \frac{\partial N_i}{\partial x} u_i \\ \frac{\partial N_i}{\partial y} u_i \\ \frac{\partial N_i}{\partial x} v_i \\ \frac{\partial N_i}{\partial y} v_i \\ \frac{\partial N_i}{\partial x} w_i \\ \frac{\partial N_i}{\partial y} w_i \\ \frac{\partial N_i}{\partial x} \theta_{xi} \\ \frac{\partial N_i}{\partial y} \theta_{xi} \\ \frac{\partial N_i}{\partial x} \theta_{yi} \\ \frac{\partial N_i}{\partial y} \theta_{yi} \end{Bmatrix} = \begin{Bmatrix} \frac{\partial N_i}{\partial x} & 0 & 0 & 0 & 0 \\ \frac{\partial N_i}{\partial y} & 0 & 0 & 0 & 0 \\ 0 & \frac{\partial N_i}{\partial x} & 0 & 0 & 0 \\ 0 & \frac{\partial N_i}{\partial y} & 0 & 0 & 0 \\ 0 & 0 & \frac{\partial N_i}{\partial x} & 0 & 0 \\ 0 & 0 & \frac{\partial N_i}{\partial y} & 0 & 0 \\ 0 & 0 & 0 & \frac{\partial N_i}{\partial x} & 0 \\ 0 & 0 & 0 & \frac{\partial N_i}{\partial y} & 0 \\ 0 & 0 & 0 & 0 & \frac{\partial N_i}{\partial x} \\ 0 & 0 & 0 & 0 & \frac{\partial N_i}{\partial y} \end{Bmatrix} \begin{Bmatrix} u_i \\ v_i \\ w_i \\ \theta_{xi} \\ \theta_{yi} \end{Bmatrix}_{i=1 \text{ to } 8} \quad (3.35)$$

For the  $j^{\text{th}}$  isoparametric element, the previous relationship is abbreviated as,

$$\{f\}_j = [\mathbf{G}]_j \{d\}_j \quad (3.36)$$

Substituting Eq. (3.36) into Eq. (3.33), we obtain the energy due to nonlinear strains for the  $j^{\text{th}}$  element.

$$U_{nlj} = \frac{1}{2} \int_A \{d\}_j^T \{\mathbf{G}\}_j^T [\mathbf{S}]_j [\mathbf{G}]_j \{d\}_j dA \quad (3.37)$$

$$U_{nl} = \frac{1}{2} \{d\}_j^T [\mathbf{K}_{G.e}]_j \{d\}_j$$

where  $[\mathbf{K}_{G.e}]_j$  = Geometric or stress stiffness of the  $j^{\text{th}}$  element

$$[\mathbf{K}_{G.e}]_j = \int_A [\mathbf{G}]_j^T [\mathbf{S}]_j [\mathbf{G}]_j dA \quad (3.38)$$

As assembly over all the  $m$  elements will yield the total non-linear strain energy

$$U_{nl} = \frac{1}{2} \sum_{j=1}^m \{d\}_j^T [\mathbf{K}_{G.e}]_j \{d\}_j \quad (3.39)$$

$$U_{nl} = \frac{1}{2} \{d\}^T [\mathbf{K}_G] \{d\}$$

Where  $[\mathbf{K}_G]$  is the geometric stiffness matrix for the whole plate

### 3.10 ELEMENTAL MASS MATRIX

The plate in motion, dependent on time, has some kinetic energy. The displacements, in this case, are the functions of time. If  $\dot{u}$ ,  $\dot{v}$  and  $\dot{w}$  are the translational velocities and  $\dot{\theta}_x$  and  $\dot{\theta}_y$  are the rotational velocities of a differential portion of the plate, then the kinetic energy 'T' of a FGM plate can be written as

$$T = \frac{1}{2} \rho \int_{A-h/2}^{h/2} [\dot{U}^2 + \dot{V}^2 + \dot{W}^2] dz dA \quad (3.40)$$

In which  $\rho$  is mass per unit volume

$$T = \frac{1}{2} \rho \int_{A-h/2}^{h/2} [(\dot{u} + z\dot{\theta}_x)^2 + (\dot{v} + z\dot{\theta}_y)^2 + \dot{w}^2] dz dA \quad (3.41)$$

Simplifying the above and expressing it in matrix form, we get

$$T = \frac{1}{2} \rho \int_A \begin{Bmatrix} \dot{u} \\ \dot{v} \\ \dot{w} \\ \dot{\theta}_x \\ \dot{\theta}_y \end{Bmatrix}^T \begin{bmatrix} h & 0 & 0 & 0 & 0 \\ 0 & h & 0 & 0 & 0 \\ 0 & 0 & h & 0 & 0 \\ 0 & 0 & 0 & \frac{h^3}{12} & 0 \\ 0 & 0 & 0 & 0 & \frac{h^3}{12} \end{bmatrix} \begin{Bmatrix} \dot{u} \\ \dot{v} \\ \dot{w} \\ \dot{\theta}_x \\ \dot{\theta}_y \end{Bmatrix} dA \quad (3.42)$$

Considering the  $j^{th}$  element in the discretized plate (out of a total of 'm' number of elements), the velocity vector can be expressed in terms of shape functions and nodal velocity vectors of that element as

$$T = \frac{1}{2} \int_A \left\{ \dot{d} \right\}^T [\mathbf{I}] \left\{ \dot{d} \right\} dA \quad (3.43)$$

Where,

$$[\mathbf{I}] = \begin{bmatrix} \rho h & 0 & 0 & 0 & 0 \\ 0 & \rho h & 0 & 0 & 0 \\ 0 & 0 & \rho h & 0 & 0 \\ 0 & 0 & 0 & \frac{\rho h^3}{12} & 0 \\ 0 & 0 & 0 & 0 & \frac{\rho h^3}{12} \end{bmatrix}_{5 \times 5}$$

$$\begin{Bmatrix} \dot{u} \\ \dot{v} \\ \dot{w} \\ \dot{\theta}_x \\ \dot{\theta}_y \end{Bmatrix} = \begin{bmatrix} N_i & 0 & 0 & 0 & 0 \\ 0 & N_i & 0 & 0 & 0 \\ 0 & 0 & N_i & 0 & 0 \\ 0 & 0 & 0 & N_i & 0 \\ 0 & 0 & 0 & 0 & N_i \end{bmatrix} \begin{Bmatrix} \dot{u}_i \\ \dot{v}_i \\ \dot{w}_i \\ \dot{\theta}_{xi} \\ \dot{\theta}_{yi} \end{Bmatrix}_{i=1 \text{ to } 8}$$

The above equation is condensed as

$$\{\dot{d}\} = [\mathbf{N}]\{\dot{d}\}_j \quad (3.44)$$

The kinetic energy of the  $j^{\text{th}}$  element is arrived by substituting the above Eq. (3.44) into Eq. (3.43), to obtain

$$T = \frac{1}{2} \int_A \{\dot{d}\}_j^T [\bar{\mathbf{N}}]_j^T [\mathbf{I}]_j [\bar{\mathbf{N}}]_j \{\dot{d}\}_j dA \quad (3.45)$$

Therefore, the total kinetic energy in the entire plate panel is obtained by summing the energies of all the individual elements,

$$T = \sum_{j=1}^m \frac{1}{2} \int_A \{\dot{d}\}_j^T [\bar{\mathbf{N}}]_j^T [\mathbf{I}]_j [\bar{\mathbf{N}}]_j \{\dot{d}\}_j dA \quad (3.46)$$

The expression for kinetic energy is written in abbreviated form as

$$T = \frac{1}{2} \sum_{j=1}^m \{\dot{d}\}_j^T [\mathbf{m}]_j \{\dot{d}\}_j \quad (3.47)$$

Where  $\{m\}_j = \int_A [\bar{\mathbf{N}}]_j^T [\mathbf{I}]_j [\bar{\mathbf{N}}]_j dA$  is an elemental mass matrix of the  $j^{\text{th}}$  element.

An assembly over all the elements will yield the total kinetic energy of the entire plate as mentioned in Eq. (3.48), in which  $[\mathbf{M}]$  is called the mass matrix of the entire plate

$$T = \frac{1}{2} \{\dot{d}\}^T [\mathbf{M}] \{\dot{d}\} \quad (3.48)$$

### 3.10.1 Work Done by Follower Force

A rectangular cantilever plate acted upon by follower force at the free edge is illustrated in the Fig. 3.9. The follower force forms an angle of  $\varphi\theta_y$  with the plate's mid-plane. The

parameter  $\varphi$  is termed as the direction control parameter, and it has a value ranging from 0 to 1. When this parameter is set to 0, the system is conservative and only uses

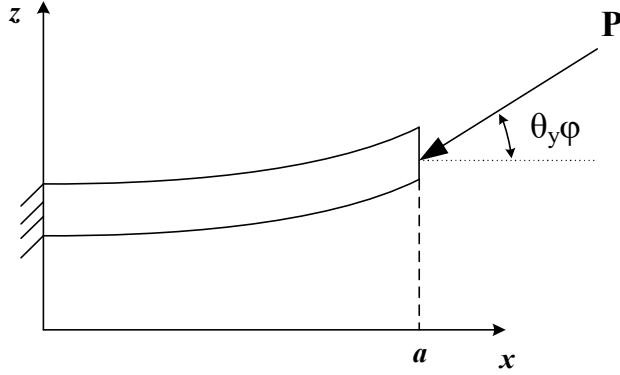


Fig. 3.9 Plate with tangential follower load

in-plane forces. When  $\varphi$  is set to 1, the system is completely dependent on follower force, hence making it a nonconservative problem.

Considering that the follower force acts on the  $n$  nodes, the variational work done by the follower force at the  $i^{th}$  node can be expressed in the form of the product of matrices as:

$$\delta W_f = \sum_{i=1}^n \delta W_{f,i} = \sum_{i=1}^n \delta w_{f,i} (-P_i \theta_{y,i}) \quad (3.49)$$

$$\delta W_{f,i} = \begin{Bmatrix} \delta u_i \\ \delta v_i \\ \delta w_i \\ \delta \theta_{x,i} \\ \delta \theta_{y,i} \end{Bmatrix}^T \begin{bmatrix} 0 & 0 & 0 & 0 & 0 \\ 0 & 0 & 0 & 0 & 0 \\ 0 & 0 & 0 & 0 & P_j \\ 0 & 0 & 0 & 0 & 0 \\ 0 & 0 & 0 & 0 & 0 \end{bmatrix} \begin{Bmatrix} u_i \\ v_i \\ w_i \\ \theta_{x,i} \\ \theta_{y,i} \end{Bmatrix} \quad (3.50)$$

$$= -\{\delta d\}_i^T [\mathbf{K}_{F,e}] \{d\}_i$$

$[\mathbf{K}_{F,e}]_i$  is an unsymmetric matrix corresponding to the change in the stiffness due to follower force. The global follower force stiffness matrix,  $[\mathbf{K}_F]$  is obtained by a finite element assembly of  $[\mathbf{K}_{F,e}]_i$ . The total variational work done by the follower force is given by

$$\delta W_f = -\{\delta d\}_i^T [\mathbf{K}_{F,e}] \{d\}_i \quad (3.51)$$

### 3.11 GOVERNING EQUATION

The various energies and the work done due to conservative and nonconservative forces have been formulated earlier and are summarised here for clarity.

The strain energy due to linear strains in the plate is  $U_l = \frac{1}{2} \{d\}^T [\mathbf{K}_e] \{d\}$

The strain energy due to non-linear strains in the plate is  $U_{nl} = \frac{1}{2} \{d\}^T [\mathbf{K}_G] \{d\}$

The kinetic energy in the plate is

$$T = \frac{1}{2} \{\dot{d}\}^T [\mathbf{M}] \{\dot{d}\}$$

The variational work done by the follower force is given by

$$\delta W_f = -\{\delta d\}_i^T [\mathbf{K}_{F,e}] \{d\}_i$$

Hamilton's principle, which traditionally considers work performed by conservative forces, can also be extended to include work performed by non-conservative forces as well. A modified form of Hamilton's principle representing a structure under a nonconservative loading system can be written as,

$$\int_{t_1}^{t_2} [\delta(T - U_l - PU_{nl}) + P\delta W_f] dt = 0 \quad (3.52)$$

$$\int_{t_1}^{t_2} \left[ \{\delta d\}^T [\mathbf{M}] \{\ddot{d}\} + [[\mathbf{K}_m] - P([\mathbf{K}_G] + [\mathbf{K}_F])] \{d\} \right] dt = 0 \quad (3.53)$$

Since all variations are arbitrary, Eq. (3.53) can be satisfied in general only when the term in square brackets vanishes, i.e., when

$$[\mathbf{M}] \{\ddot{d}\} + [[\mathbf{K}_m] - P([\mathbf{K}_G] + [\mathbf{K}_F])] \{d\} = 0 \quad (3.54)$$

Eq. (3.54) is the most general governing differential equation of motion for solving flutter problems under follower loading conditions.

The above-generalized equation can be reduced to represent the problem under a conservative loading system by substituting  $[\mathbf{K}_F] = 0$  in Eq. (3.54) to obtain:

$$[\mathbf{M}] \{\ddot{d}\} + [[\mathbf{K}_m] - P_{cr}[\mathbf{K}_G]] \{d\} = 0 \quad (3.55)$$

Eq. (3.55) represents governing differential equilibrium equation for the FGSP with cutouts subjected to mechanical in-plane edge load and thermal loads. The matrix  $[K_m]$  is a modified stiffness matrix, which is the function of temperature and is expressed as  $[K_m] = [K_e] - [K_G^T]$ . Here  $[K_e]$  denote the global structural elastic stiffness matrix, and  $[K_G^T]$  is the global geometric stiffness matrix due to temperature. While  $[M]$  represents global consistent mass matrix and  $[K_G]$  is geometrics stiffness matrix due to mechanical in-plane edge load. These matrices are found by assembling each individual corresponding element level matrices and are deposited in a skyline technique. Further, the terms  $\{d\}$  and  $\{\ddot{d}\}$  are displacement and acceleration. Further, to obtain a buckling load, the intensity of the load is increased; as the load increases, the natural frequency keeps on reducing and reaches zero. The P corresponding to zero frequency is the buckling load. This method of obtaining buckling loads is known as the dynamic approach.

### 3.12 CLASSIFICATION OF PROBLEMS

The governing Eq. (3.55) can be modified to arrive at several problems as follows:

- I. *Free vibration*: Here, during the absence of load, i.e.,  $P = 0$ , problem reduces to free vibration

$$[K_m]\{d\} - \omega^2\{d\}[M] = 0 \quad (3.56)$$

Eq. (3.56) represents the eigenvalue problem, where  $\omega^2$  is the eigenvalue yielding natural frequency and  $\{d\}$  depicts the eigenvector for different modes of the plate. The Lowest value of the eigenvalue denotes the fundamental natural frequency.

- II. *Vibration with in-plane load*: The plate vibrates harmonically with a given  $P$ , then Eq. (3.55) reduces to,

$$[[K_m] - P[K_G]]\{d\} - \omega^2\{d\}[M] = 0 \quad (3.57)$$

- III. *Static stability (buckling)*: Setting the load to be static and acceleration of the structure to be zero  $\{\ddot{d}\} = 0$ , in Eq. (3.55), we obtain

$$[[K_m] - P_{cr}[K_G]]\{d\} = 0 \quad (3.58)$$

The above Eq. (3.58) yields eigenvalues. The lowest eigenvalue is termed as the critical buckling load of the plate.

IV. *Follower force problem*: The equation reduces to

$$[\mathbf{M}]\{\ddot{\mathbf{d}}\} + \left[ [\mathbf{K}_m] - P_{cr}(\mathbf{K}_G + \mathbf{K}_F) \right] \{\mathbf{d}\} = 0 \quad (3.59)$$

The geometric stiffness matrix owing to follower loading is denoted as  $(\mathbf{K}_G + \mathbf{K}_F)$ . The magnitude of the applied follower load is denoted by  $P$ , while the nodal displacement vector is denoted by  $\{\mathbf{d}\}$  in Eq. (3.59). The  $[\mathbf{K}_G]$  matrix considers the applied load's total in-plane component, whereas the  $[\mathbf{K}_F]$  matrix considers the follower load's non-conservative component perpendicular to the plate undeformed mid-plane.

### 3.13 SUPPORT CONDITIONS

In the present investigation, for each support condition, two sets of boundary conditions are considered. In string used to describe any support conditions, the letters 'S', 'C', and 'F' designates simply support, clamped, and free end conditions, respectively. The first two terms in the support condition string represent the right and left side support condition, while the last two terms denote the top and bottom support condition of the plate. The first set of boundary conditions is for the static analysis to determine pre-buckling stresses, and the second set of boundary conditions is for the buckling analysis. For the geometry of the FGM plate shown in Fig. 3.1, the boundary conditions at the plate edges corresponding to a few support conditions considered are represented in Fig. 3.10.

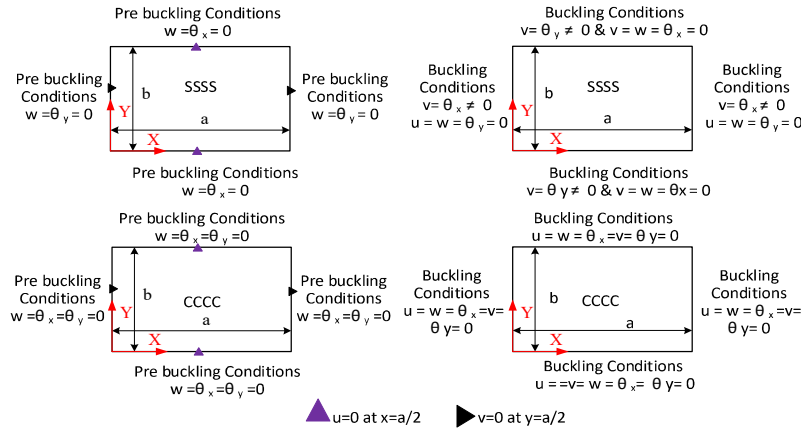


Fig. 3.10 Support conditions considered in the current study

### **3.14 COMPUTER IMPLEMENTATION**

The computer implementation of the present FE formulation is executed by developing a suitable computer code in MATLAB R2012b environment. Different programs are built for various analyses, viz., free vibration, buckling, and dynamic instability. The execution for MATLAB codes of different analyses are performed using a laptop with the specification of Intel(R) Core (TM) i5-2600 CPU @ 3.4GHz, 8.00GB RAM, 64-bit Operating system.

### **3.15 CLOSURE**

In this chapter, detailed theoretical formulations and solution methodology for the free vibration, buckling, and dynamic stability analyses of FGM plates based on FSDT are presented. The effective material properties of the FGM are evaluated through Voigt's micromechanical model through the power-law and sigmoidal function-based distribution. Four types of sandwich configurations and different types of porosity distribution models considered are presented. The properties of FGM are assumed to be temperature-dependent and graded along the thickness direction. The domain is discretized using suitable finite element steps through an eight-noded quadrilateral isoparametric Lagrange element. In the following chapter, the numerical results obtained and a discussion of various plate problems using the above techniques are presented.



## CHAPTER 4

### VIBRATION AND BUCKLING ANALYSIS OF POROUS FG SANDWICH PLATE WITH/WITHOUT CUTOUT SUBJECTED TO LOCALISED IN-PLANE EDGE LOADS

#### 4.1 PRELIMINARY REMARKS

FGM plate members, which finds a place in the application of spacecraft (Noda (1999)) and thrust chamber of rockets (Udupa et al. (2014)), are usually idealization of a smaller portion of much larger and more complicated built-up or stiffened structure exposed to the thermal and mechanical loads. The applied loads are exerted on the smaller portion by the adjacent plates, and hence uniform load is meager, as the force transferred between the plate members depends on their relative stiffness. These forces vary from one structure to another and cannot be computed without complex analysis. It becomes essential to analyze the structure assuming different types of in-plane edge load distributions. These loads can be uniform, linearly varying, nonlinearly varying, localised, or concentrated. In a few circumstances, localised edge loads arise from adjoining and connected plate members during the operational condition and also due to the reaction from the supports. In addition, such loads occur due to the partial failure of connection components. The non-uniformity in the stress due to in-plane load will further increase due to the formation of porosity and cutouts, significantly affects the vibration and buckling response of FGSPs.

Hence, this chapter attempts to analyze and discuss the vibration and buckling characteristics of FGSP with/without cutout under localised in-plane edge loads. To do so, a general formulation, as presented in Chapter 3, has been developed by taking Green-Lagrange type nonlinear kinematics, and it is utilized to compute the desired responses. Because the stress distribution within the plate element is significantly non-uniform, a dynamic technique was employed to solve the buckling problems, with two sets of boundary conditions, one for pre-buckling stresses and another for buckling load calculations. The effects of various geometrical, material parameters and the support conditions on vibration and buckling response of FGSP under different localised in-

plane edge loads are studied. Finally, this chapter is summarised with the concluding remarks in chapter 8.

## 4.2 PROBLEM DESCRIPTION

In the present investigation, different types of in-plane edge loads acting on two opposite sides of the plate are considered for the study are discussed in detail. The localised uniformly distributed in-plane edge load from one end is referred to as Type-I (Fig. 4.1 (a)), localised uniformly distributed in-plane edges load from both ends is referred to as Type-II (Fig. 4.1 (b)). The localised uniformly distributed in-plane edge load from the center of the plate is referred to as Type-III (Fig. 4.1 (c)), and concentrated load from one end of the plate is referred to as Type-IV (Fig. 4.1 (d)). The term  $c$  represents the width of the load in case of uniformly distributed edge load (Type-I, Type-II, Type-III), and for Type-IV, it is the distances of the concentrated loads from the lower edges of the plate along the width. While  $b$  is the total widths of the plates. To compare the effect of each loading condition, the total load ( $P_0c$ ) is kept constant irrespective of the position and width of edge loads. Further,  $P_0$  represents load intensity (i.e., load magnitude/ $c$ ) in the cases of Type-I, II, and III. In cases of Type-IV, where  $P$  represents the magnitude of the concentrated load. The percentage shown in Fig. 4.1 denotes the portion of the width over which the load is acting for e.g., 100% denotes that the edge load is acting over the entire width of the plate.

In the current study, single-layer FGM, FCF, and MFM sandwich configurations, as shown in Fig. 3.1 are incorporated. In addition, in this investigation, U-D, O-D, X-D and V-D porosity for single-layer FGM plates, as mentioned in Chapter 4, are considered. While for FCF and MFM sandwich configurations, U-D and V-D porosity are incorporated to study the vibration and buckling response of FGM plate with/without cutout under localised in-plane edge loads.

## 4.3 RESULTS AND DISCUSSION

The vibration and buckling responses are obtained using a developed mathematical formulation and an in-house MATLAB code that can be extended for any general case. The convergence study of the FGSP with cutout under localised in-plane edge load is performed for various geometrical and material configurations.

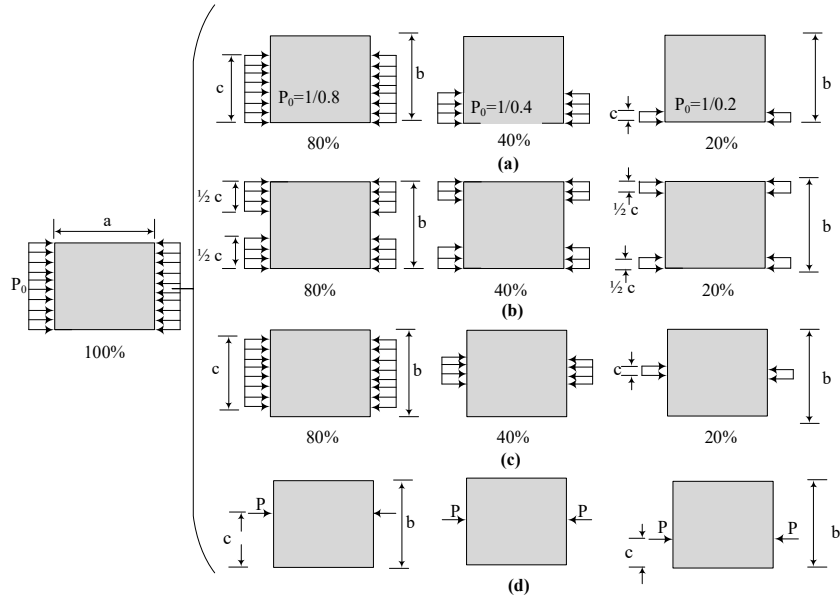


Fig. 4.1 Representation of loading cases (a) Type-I, (b) Type-II, (c) Type-III, (d) Type-IV

Consequently, a variety of examples is solved for validation purposes by comparing the present results with those available in published literature. After the exhaustive evaluation of the present model, an inclusive parametric study of FGSP under localised in-plane edge is performed. Here, the vibration and buckling response of FGSPs is analyzed various geometrical and material parameters and support conditions. The material properties of FGM constituents used throughout the analysis are taken the same as in Table 4.1. If not stated otherwise, critical buckling loads ( $P_{cr}$ ) and natural frequencies ( $\omega$ ) are represented in non-dimensional form as

$$\bar{P}_{cr} = P_{cr} b^2 / D, \quad D = E_c h^3 / 12(1 - \nu^2)$$

$$\bar{\omega} = \omega b^2 \sqrt{\rho_c / E_c h^2}$$

where  $\rho_c$  is the material density of ceramic,  $D = E_c h^3 / 12(1 - \nu^2)$  is the flexural rigidity of the plates.

### 4.3.1 Convergence and Validation Studies

**Example 1:** In this example, a single layer FGM square thin plate with side-to-thickness ratio ( $b/h$ ) of 100 under the application of load Type-III with  $c/b = 0.2$  and  $n = 1.0$  is considered, and the numerical results are tabulated in Table 4.2. The ceramic and metal material properties of the plate are presented in Table 4.1. The results are presented for buckling analysis of the plate with SSSS and CCCC support conditions.

Table 4.1 Materials Properties used in FGM plate (Hosseini-hashemi et al. (2010))

Materials	Properties		
	E (GPa)	$\rho$ (kg/m <sup>3</sup> )	$\nu$
Aluminium (Al)	70	2707	0.3
Zirconia (ZrO <sub>2</sub> )	151	3000	0.3

For vibration analysis, SSSS plates are considered without in-plane load ( $P/\bar{P}_{cr} = 0.0$ ) and with in-plane load ( $P/\bar{P}_{cr} = 0.5$ ). It is noticed from Table 4.2 that the buckling, as well as vibration results, converge well at a 10 x 10 mesh size. Henceforth, analysis in the consequent numerical studies is carried out considering these mesh sizes.

**Example 2:** Subsequently, the comparison study is carried out by considering localised edge loads (Type- III), and the results are tabularized sideways with the results presented by Sundaresan et al. (1998) in Table 4.3. The  $\bar{P}_{cr}/\bar{P}_{cr}^*$  ( $\bar{P}_{cr} = P_{cr}b^2/Eh^3$ ;  $\bar{P}_{cr}^* = P_{cr}^*b^2/Eh^3$ , where  $P_{cr}$  and  $P_{cr}^*$  are the critical buckling load due to localised edge load and uniformly distributed in-plane edge load respectively,  $E$  is Young's modulus of isotropic material) obtained for isotropic thin square plate ( $b/h = 100$ ) agree well with the literature as percentage error is appreciably less ( $< 0.74\%$ ). The appreciable similarity in results between the literature and the current study demonstrates the correctness of the formulation of several stiffness matrices involved. It is also noted that  $\bar{P}_{cr}/\bar{P}_{cr}^*$  increases with an increase in the % loaded edge length.

**Example 3:** This example is carried out for a single-layer FGM thin plate ( $b/h = 100$ ) subjected to Type-IV load with SSSS and CSCS support condition. The present  $\bar{P}_{cr}$  ( $\bar{P}_{cr} = P_{cr}b/D_{ce}$ ;  $D_{ce} = E_{ce}h^3/12(1 - \nu^2)$ ) are compared with results reported by Chen and Liew (2004), considering plates with an aspect ratio ( $a/b$ ) equal to 0.5, 1.0 and load width ratio ( $c/b$ ) equal to 0.5, 0.25 and 1.0. The material properties considered for the present comparison study are shown in Table 4.1. The volume fraction exponent ( $n$ ) considered is 1.0. It is perceived from Table 4.4 that the non-dimensional critical buckling load for plates with SSSS and CSCS support conditions decrease as the concentrated load move towards the centre of the plate with  $a/b = 0.5$  and 1.0. It is evident from Table 4.4 that the present outcomes are in good agreement with the literature.

Table 4.2 Convergences of non-dimensional critical buckling loads ( $\bar{P}_{cr}$ ) and non-dimensional natural frequencies ( $\bar{\omega}$ ) of thin square single layer FGM plate subjected to load Type-III with  $c/b = 0.2$ .

Mesh division	Non-dimensional critical buckling load ( $\bar{P}_{cr}$ )		Non-dimensional Frequency ( $\bar{\omega}$ ) SSSS	
	SSSS	CCCC	P/ $\bar{P}_{cr} = 0.0$	P / $\bar{P}_{cr} = 0.5$
2 x 2	68.773	83.677	8.328	4.021
4 x 4	21.996	93.620	5.103	3.858
6 x 6	19.887	54.846	5.064	3.675
8 x 8	19.257	49.553	5.064	3.620
10 x 10	18.966	47.992	5.061	3.594
12 x 12	18.968	47.981	5.061	3.592

Table 4.3 Variation of  $\bar{P}_{cr} / \bar{P}_{cr}^*$  for an isotropic thin square plate ( $a/h = 100$ ) subjected to Types-III load

% Loaded edge length	SSSS			CCCC		
	Present	Sundaesan et al. (1998)	% Error	Present	Sundaesan et al. (1998)	% Error
20	0.668	0.667	0.12	0.691	0.688	0.33
40	0.721	0.719	0.36	0.754	0.749	0.75
60	0.804	0.804	0.08	0.840	0.836	0.53
80	0.905	0.905	0.04	0.924	0.917	0.73
100	1.000	1.000	0.00	1.000	1.000	0.00

**Example 4:** The validation study is further continued by considering moderately thick ( $b/h = 10$ ) FCF square FGSP subjected to uniformly distributed in-plane edge load. In the current example, the effect of different layer schemes and volume fraction exponent is calculated, and buckling results are tabularized in Table 4.5 along with the results from Adhikari et al. (2020), Zenkour (2005) and Swaminathan and Naveenkumar (2014). The FGM sandwich plate is made of Aluminium ( $E_m = 70$  GPa,  $\rho_m = 2702$  kg/m<sup>3</sup>) and Alumina ( $E_{ce} = 380$  GPa,  $\rho_{ce} = 3800$  kg/m<sup>3</sup>). The Poisson's ratio ( $\nu$ ) is considered 0.3 for both metal and ceramic materials. The sandwich plates with various layer schemes, as mentioned in Table 3.1, are considered for the analysis. The non-dimensional critical buckling load ( $\bar{P}_{cr} = P_{cr} a^2 / 100 E_0 h^3$ ,  $E_0 = 1$  GPa) obtained from the current FE model shows the minimal difference with the results presented in the literature. Swaminathan and Naveenkumar (2014) and Zenkour (2005) have obtained  $\bar{P}_{cr}$  using closed-form solution with HSDT-12 and sinusoidal shear deformation theory respectively while, Adhikari et al. (2020) employed the FE

Table 4.4 Comparison of non-dimensional critical buckling load ( $\bar{P}_{cr} = P_{cr}b/D_{ce}$ ;  $D_{ce} = E_{ce}h^3/12(1 - \nu^2)$ ) of SSSS and CSCS single-layer FGM (Al/ZrO<sub>2</sub>) plate subjected to Type-IV load

<i>a/b</i>	<i>c/b</i>	SSSS		CSCS	
		Present	Chen and Liew (2004)	Present	Chen and Liew (2004)
0.5	0.1	56.656	55.986	95.137	91.455
	0.25	26.891	27.093	62.381	62.547
	0.5	21.356	21.39	57.796	58.136
1	0.1	35.111	36.723	45.749	46.286
	0.25	26.271	25.96	42.109	42.374
	0.5	18.5	18.429	33.721	33.891

Table 4.5 Comparison of non-dimensional critical buckling load ( $\bar{P}_{cr} = P_{cr} a^2/100E_0h^3$ ,  $E_0 = 1 \text{ GPa}$ ) of simply supported FCF FGM (Al/Al<sub>2</sub>O<sub>3</sub>) sandwich plate subjected to uniformly distributed uniaxial compressive load

<i>n</i>	Source	Sandwich Layer schemes					
		1-0-1	2-1-2	2-1-1	1-1-1	2-2-1	1-2-1
0	Adhikari et al. (2020)	13.005	13.005	13.005	13.005	13.005	13.005
	Zenkour (2005)	13.004	13.004	13.004	13.004	13.004	13.004
	Swaminathan and Naveenkumar (2014)	12.953	12.953	-	12.953	-	12.953
	Present	12.816	12.816	12.816	12.816	13.729	13.729
0.5	Adhikari et al. (2020)	7.364	7.941	8.224	8.437	8.810	9.217
	Zenkour (2005)	7.337	7.913	8.200	8.437	8.787	9.195
	Swaminathan and Naveenkumar (2014)	7.333	7.912	-	8.406	-	9.184
	Present	7.228	7.796	8.078	8.285	8.656	9.059
1	Adhikari et al. (2020)	5.166	5.839	6.193	6.464	6.949	7.507
	Zenkour (2005)	5.142	5.814	6.170	6.465	6.926	7.484
	Swaminathan and Naveenkumar (2014)	5.148	5.819	-	6.443	-	7.482
	Present	5.065	5.726	6.076	6.342	6.821	7.372
5	Adhikari et al. (2020)	2.653	3.036	3.394	3.575	4.107	4.734
	Zenkour (2005)	2.638	3.023	3.385	3.559	4.092	4.714
	Swaminathan and Naveenkumar (2014)	2.642	3.025	-	3.563	-	4.720
	Present	2.599	2.976	3.331	3.505	4.028	4.643

method using HSDT-9. The difference in results is due to the different techniques for solution and displacement fields considered in the literature, which require more computation effort than the present method involving FSDT.

**Example 5:** In this example, the non-dimensional natural frequencies ( $\bar{\omega} = \omega \left(\frac{a^2}{h}\right) \sqrt{\rho_0/E_0}$ ,  $E_0 = 1 \text{ GPa}$ ,  $\rho_0 = 1 \text{ kg/m}^3$ ) of SSSS FCF moderately thick ( $a/h = 10$ ) FGSP are obtained by considering various  $n$  and layer schemes. The FGSP is made of Aluminium ( $E_m = 70 \text{ GPa}$ ,  $\rho_m = 2707 \text{ kg/m}^3$ ) and Alumina ( $E_{ce} = 380 \text{ GPa}$ ,  $\rho_{ce} = 3800 \text{ kg/m}^3$ ). The Poisson's ratio ( $\nu$ ) is considered 0.3 for both metal and ceramic materials. A sandwich plate with various layer schemes, as mentioned in Table 3.1, is considered for the analysis. The results found are compared with those obtained analytically by Zenkour (2005), as shown in Table 4.6. The close agreement between the present study and the literature show the correctness of the mass matrix in the formulation.

**Example 6:** The comparison study is further continued to ascertain the exactness of the present formulation for the plate with porosity imperfection. Towards this, the non-dimensional natural frequencies ( $\bar{\omega} = \omega \left(\frac{a^2}{h}\right) \sqrt{\rho_0/E_0}$ ,  $E_0 = 1 \text{ GPa}$ ,  $\rho_0 = 1 \text{ kg/m}^3$ ) of simply supported square porous FGM sandwich plates is obtained and compared with results presented in the research article by Daikh and Zenkour (2019). The sandwich plate is moderately thick ( $a/h = 10$ ) with  $n = 2.0$ . The FGM sandwich plate is made of Aluminium ( $E_m = 70 \text{ GPa}$ ,  $\rho_m = 2707 \text{ kg/m}^3$ ) and Alumina ( $E_{ce} = 380 \text{ GPa}$ ,  $\rho_{ce} = 3800 \text{ kg/m}^3$ ). The Poisson's ratio ( $\nu$ ) is considered 0.3 for both metal and ceramic materials. The authors have incorporated simple higher orders shears deformation theory to perform free vibrational analysis. Here, the FCF FGM sandwich plate is considered with U-D type porosity distribution. The porosity index  $p_i = 0.1$  and  $0.2$  is considered. A sandwich plate with various layer schemes, as mentioned in Table 3.1, is considered for the present analysis. It is perceived from Table 4.7 that non-dimensional natural frequencies decrease with an increase in the porosity index irrespective of the layer schemes. The comparison is presented in Table 4.7, and the presented results are convincingly close to those available in the literature in terms of accuracy.

**Example 7:** Lastly, the comparison study is continued to ascertain the exactness of the present formulation for  $\bar{P}_{cr}$  ( $\bar{P}_{cr} = P_{cr} a^2 / 100 E_0 h^3$ ,  $E_0 = 1 \text{ GPa}$ ) of the plate with porosity imperfection. Towards this, the non-dimensional critical buckling load of

Table 4.6 Comparison of non-dimensional natural frequency ( $\bar{\omega} = \omega \left(\frac{a^2}{h}\right) \sqrt{\rho_0/E_0}$ ,  $E_0 = 1 \text{ GPa}$ ,  $\rho_0 = 1 \text{ kg/m}^3$ ) of simply supported FCF FGM (Al/Al<sub>2</sub>O<sub>3</sub>) sandwich plate.

$n$	Source	Sandwich Layer schemes					
		1-0-1	2-1-2	2-1-1	1-1-1	2-2-1	1-2-1
0.0	Zenkour (2005)	1.825	1.825	1.825	1.825	1.825	1.825
	Present	1.825	1.825	1.825	1.825	1.825	1.825
0.5	Zenkour (2005)	1.442	1.482	1.510	1.517	1.545	1.573
	Present	1.442	1.482	1.505	1.517	1.545	1.573
1.0	Zenkour (2005)	1.243	1.300	1.349	1.353	1.408	1.439
	Present	1.240	1.297	1.332	1.351	1.394	1.437
5.0	Zenkour (2005)	0.946	0.982	1.074	1.045	1.147	1.174
	Present	0.943	0.979	1.030	1.042	1.108	1.172

simply supported square porous FGSP is obtained and compared with results presented in the research article by Daikh and Zenkour (2019) (Closed form solution) and Vinh and Huy (2021) (FE technique). The sandwich plate considered is moderately thick ( $a/h = 10$ ) with volume fraction exponent  $n = 2.0$ . The FGM sandwich plate is made of Aluminium ( $E_m = 70 \text{ GPa}$ ,  $\rho_0 = 2707 \text{ kg/m}^3$ ) and Alumina ( $E_{ce} = 380 \text{ GPa}$ ,  $\rho_{ce} = 3800 \text{ kg/m}^3$ ) The plate is subjected to uniform compressive in-plane edge load. The Poisson's ratio ( $\nu$ ) is considered 0.3 for both metal and ceramic materials. Here, FCF FGM sandwich plate is considered with U-D type porosity distribution. The porosity index  $p_i = 0.1$  &  $0.2$  is considered. Sandwich plate with various layer schemes as mentioned in Table 3.1 is considered for the present analysis. It is perceived from Table 4.8 that non-dimensional critical buckling load decrease with increase in the porosity index irrespective of the layer schemes. The comparison is presented in Table 4.8, and the presented results are convincingly close to those available in literature in terms of accuracy.

### 4.3.2 Parametric Studies

A comparative study of the results obtained from current formulation with literature results are carried out in section 4.1. After the comparative study, parametric studies are carried out to examine the influence of porosity on vibration and buckling responses of FGM single layer and FGSP exposed to localised edge load by varying volume fraction exponent, porosity distribution, porosity indices, side-to-thickness ratio, load width ratio, aspect ratio and support condition.

Table 4.7 Comparisons of non-dimensional natural frequency ( $\bar{\omega} = \frac{\omega a^2}{h} \sqrt{\rho_0/E_0}$ ,  $E_0 = 1 \text{ GPa}$ ,  $\rho_0 = 1 \text{ kg/m}^3$ ) of simply supported square FCF FGM (Al/Al<sub>2</sub>O<sub>3</sub>) sandwich plate with porosity

$p_i$	Source	Sandwich Layer schemes					
		1-0-1	1-1-1	1-2-1	2-1-2	2-2-1	2-1-1
0.1	Daikh and Zenkour (2019)	0.9825	1.1207	1.2493	1.0471	1.1819	1.0935
	Present	0.9885	1.1272	1.255	1.0536	1.1895	1.102
0.2	Daikh and Zenkour (2019)	0.8786	1.0420	1.1915	0.9549	1.1105	1.0055
	Present	0.8914	1.0551	1.2027	0.9685	1.1249	1.0218

Table 4.8 Comparison of non-dimensional critical buckling load  $\bar{P}_{cr}$  ( $\bar{P}_{cr} = P_{cr} a^2 / 100 E_0 h^3$ ,  $E_0 = 1 \text{ GPa}$ ) of simply supported square FCF (Al/Al<sub>2</sub>O<sub>3</sub>) sandwich plate with porosity and subjected to uniform compressive in-plane edge loads.

$p_i$	Source	Sandwich Layer schemes					
		1-0-1	1-1-1	1-2-1	2-1-2	2-2-1	2-1-1
0.1	Present	1.357	1.989	2.606	1.659	2.260	1.841
	Daikh and Zenkour (2019)	1.362	1.997	2.622	1.665	2.272	1.849
	Vinh and Huy (2021)	1.343	1.969	2.586	1.641	2.240	1.822
0.2	Present	0.973	1.620	2.272	1.278	1.892	1.450
	Daikh and Zenkour (2019)	0.960	1.605	2.265	1.262	1.881	1.436
	Vinh and Huy (2021)	0.946	1.582	2.234	1.244	1.854	1.415

#### 4.3.2.1 Vibration behaviour of single layer FGM and FGSP with and without Porosity under localised edge loads

The FGM plates with different sandwich configurations, sandwich layer schemes, types of porosity distributions, and porosity index to investigate the influence of the free vibration characteristics are considered for the analysis. The effect of initial stresses on the variation in non-dimensional natural frequencies of single layer FGM plate is examined by choosing load Type-III. The outcomes are displayed in Figs. 4.2(a) and (b). Initially, a square plate with the volume fraction exponent and porosity index  $n = 1.0$  and  $p_i = 0.0$  is considered to study the effect of load width ratio (Fig. 4.2(a)). The load width ratio is varied from 0.2 to 1.0. The results represented in Fig. 4.2 indicate that for any given load width ratio, the non-dimensional natural frequency decreases with increase in the intensity of edge load and reaches zero frequency at the onset of critical load. Also, for a certain non-dimensional load  $P$ , the frequency increases with increase in the load width ratio. The reason behind such behaviour is due to the increase

in the effect of support restraints as the load width increases. Hence, the natural frequency of plate is increased with an increase in load width ratio.

Further, a similar study is examined by considering different volume fraction exponents ( $n$ ) and the consequences are shown in Fig. 4.2(b). The plate is subjected to localised edge loads with  $c/b = 0.6$ . It is perceived from Fig. 4.2(b) that for a specified non-dimensional load, the non-dimensional natural frequency decreases with the rise in volume fraction exponents ( $n$ ) and is found to be maximum for  $n = 1.0$  and least for  $n = 100.0$ . In an FGM plate with a lesser volume fraction exponent, ceramic content is greater than that of metal. The Young's modulus of ceramic material is higher than metal; the plate with lesser volume fraction exponent exhibit higher natural frequency due to increased stiffness as the ceramic material content is high. Likewise, an increase in the volume fraction exponent results in an increase in the metal content and hence the natural frequency of the FGM plate decreases.

The study is extended to understand the influence of different porosity distributions on the vibration behaviour of single layer FGM plate, as shown in Fig. 4.3(a).

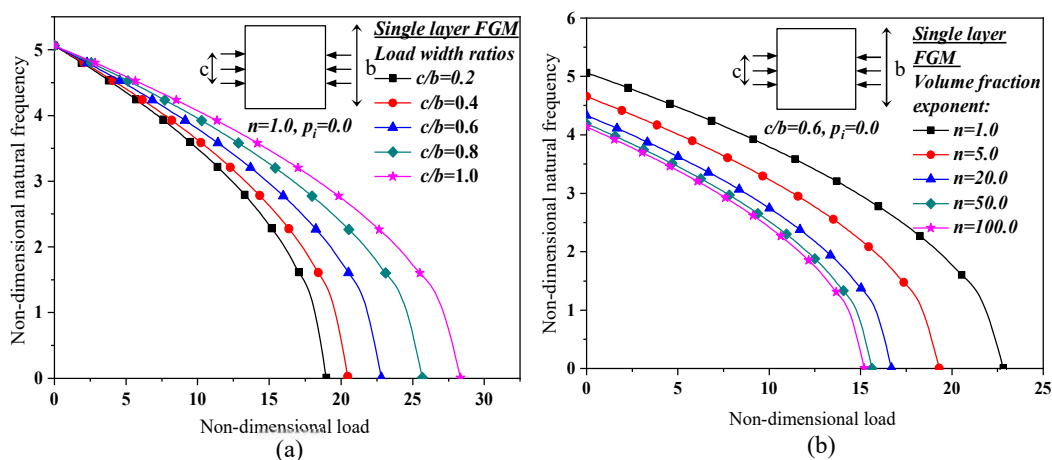


Fig. 4.2 Variation of non-dimensional natural frequency of single layer FGM plate for different (a) load width ratios (b) volume fraction exponents

The porosity index and volume fraction exponent are chosen as  $p_i = 0.2$  and  $n = 1.0$  respectively. The plates are subjected to Type- III loading with  $c/b = 0.2$ . Here four types of porosity distributions, as mentioned in section 4.2 are considered for the study. Fig. 4.3(a). shows that with an increase in the initial stress, the frequency parameter decreases and approaches zero irrespective of the type of porosity distribution. Fig.

4.3(a) also depicts that O-D type of porosity distribution exhibits the highest natural frequency amongst all the porosity distribution in the order of O-D > X-D > U-D > V-D. A similar trend is observed as the initial stresses resulting from the localised edge loads increases. The physical reason behind higher natural frequency for plates with O-D type distribution is due to the concentration of pores close to mid surface of the plate. As the pores are close to the mid surface, reduction in stiffness is not significant, hence O-D type exhibits higher natural frequency as compared to other porosity distributions.

The investigation is further extended by considering FCF FGSP with porosity, and the outcomes are exemplified in Fig. 4.3(b) by considering different sandwich layer schemes. The U-D type porosity with a porosity index,  $p_i = 0.2$ , volume fraction exponent,  $n = 5$  and load width ratio,  $c/b = 0.2$  are considered for the study. It is inferred from Fig. 4.3(b) that the non-dimensional natural frequencies decrease with the increment in the intensity of the applied load and attain a value of zero at the respective critical buckling loads. However, the difference in natural frequency of the plate with different layer schemes is minimal when the initial stresses are absent, but the effect gradually increases with the introduction of initial stresses.

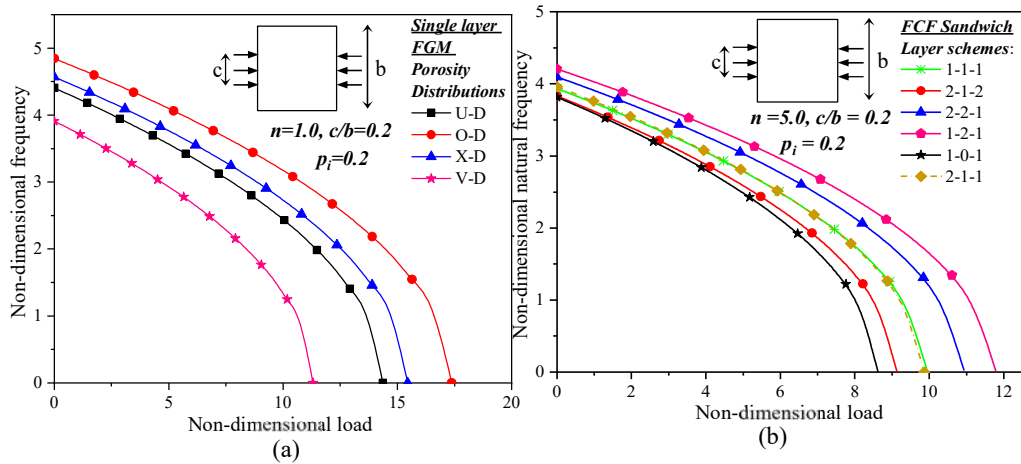


Fig. 4.3 Variation of non-dimensional natural frequency for plates subjected to load Type-III and different (a) porosity distributions (Single layer FGM) and (b) layer schemes (FCF sandwich).

It can be comprehended that the sandwich with 1-2-1 and 1-0-1-layer scheme give maximum and minimum non-dimensional natural frequency, irrespective of initial stresses. For 1-2-1 layer scheme, the increased non-dimensional natural frequency is due to the increased stiffness contributed by the higher thickness of the ceramic core

sheet. Likewise, the sandwich plate with a 1-0-1 scheme exhibits a lesser non-dimensional natural frequency due to the presence of only porous FGM face sheets and the absence of stiffer core sheets. The effect of porosity indices on the non-dimensional natural frequency of FCF and MFM square thin ( $b/h = 50$ ) sandwich (1-2-1) plates subjected to Type-II localised edge loads is studied, and the outcomes are presented in Fig. 4.4. In this study, U-D type of porosity is selected with  $p_i = 0.0, 0.1, 0.2, 0.3, 0.4$  and  $0.5$ . The volume fraction exponent and load width ratio are selected as  $0.5$  and  $0.6$ , respectively. It is observed from Figs. 4.4(a) and (b) that the non-dimensional natural frequency reduces with an increase in the porosity indices for both FCF and MFM sandwich plates at certain non-dimensional loads. The reason behind such behaviour is due to the reduction in the stiffness of the sandwich plate with an increase in the porosity indices. Further, it can also be noticed that the amount of reduction in non-dimensional natural frequency with an increase in porosity indices is more significant in FCF sandwich plates with two porous face sheets as compared to MFM sandwich plates with the single porous core.

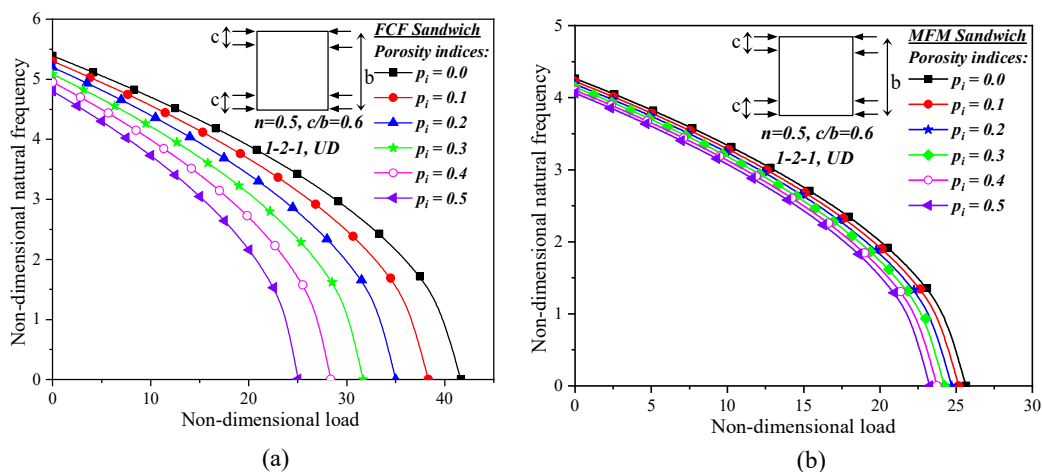


Fig. 4.4 Variation of non-dimensional natural frequency with porosity indices for (a) FCF and (b) MFM 1-2-1 sandwich plates having U-D type of porosity under load Type-II with  $c/b = 0.6$ .

The influence of the type of localised edge loads on the non-dimensional natural frequency of FCF and MFM square sandwich plates (1-2-1) with V-D type porosity is illustrated in Figs. 4.5(a) and (b), respectively. It is observed that for a certain non-dimensional load, the non-dimensional natural frequency is maximum for plate subjected to Type-II localised edge load, followed by Type-I, Type-IV and Type-III

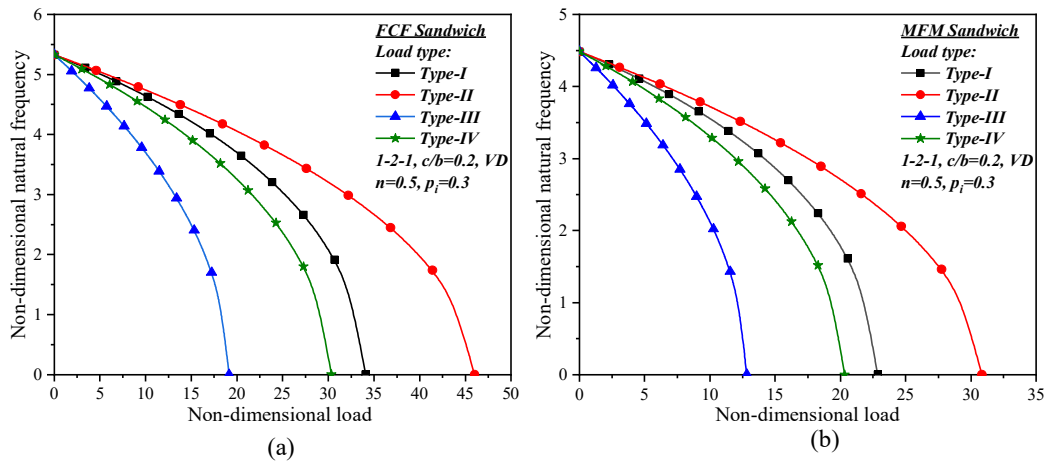


Fig. 4.5 Variation of non-dimensional natural frequency for (a) FCF and (b) MFM 1-2-1 FGSP having V-D porosity distribution subjected to different types of localised edge load with  $c/b = 0.2$ .

loads. The reason behind the increased non-dimensional natural frequency of plates subjected to Type-II is due to the fact that the loads are located at the stiffer region of the plates i.e., close to supports. Due to this, the plate remains stiff, which in turns increases the non-dimensional natural frequency.

#### 4.3.2.2 Buckling characteristics of single layer FGM plate without porosity under load Type-I and Type-II

The buckling responses of single layer FGM square plates without porosity subjected to localised edge load from one end of the plate (Type-I) is analyzed in these sections, and the outcomes are projected in Figs. 4.6(a) and (b). It is witnessed from Fig. 4.6 (a) that the non-dimensional critical buckling load ( $\bar{P}_{cr}$ ) reduces with the rise in load width ratio up to a  $c/b$  of around 0.6 and subsequently increases with the further rise in  $c/b$  regardless of volume fraction exponents. The non-dimensional critical buckling load ( $\bar{P}_{cr}$ ) is also observed to be much higher when loading is close to the edges of the FGM plate. It might be owing to the influence of edge constraints, where the stiffness of the FGM plate is considerably higher in comparison with the central region of the single layer FGM plates. It is essential to note that for a given  $c/b$ , the variation in the value of  $\bar{P}_{cr}$  is insignificant at higher volume fraction exponents as compared to that of lesser volume fraction exponents. The non-dimensional critical buckling load variation with various aspect ratios ( $a/b$ ) is further studied by selecting volume fraction exponent,  $n = 1.0$  and outcomes are illustrated in Fig. 4.6(b).

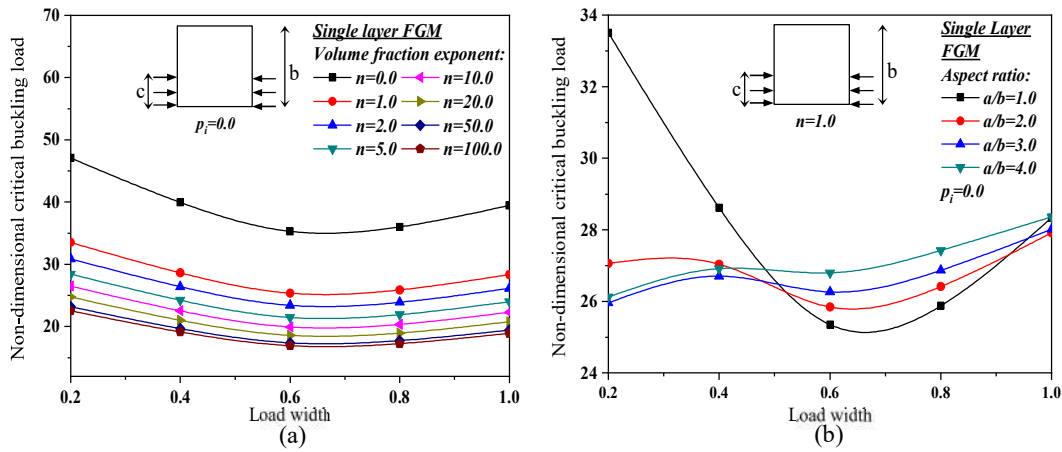


Fig. 4.6 Variation of non-dimensional critical buckling load with load width ratio for single layer FGM plates without porosity subjected to Type -I loading (a) Influence of various volume fraction exponents (b) Influence of different aspect ratio of the plates

As it is observed from Fig. 4.6(b) at lower load width ratio ( $c/b$ ) the variation in the non-dimensional critical buckling load for FGM plate with different aspect ratios is significantly large, while at higher  $c/b$  the non-dimensional critical buckling load variation is relatively less, especially at  $c/b = 0.5$  &  $1.0$ . It is further noticed that with increase in  $a/b$ , non-dimensional critical buckling load of single layer FGM plate decreases only till certain  $c/b$  (i.e.,  $c/b \leq 0.4$ ) and with increase in  $c/b$  the buckling behaviour changes, i.e., the buckling resistance of single layer FGM plate increases with the rise in the aspect ratios ( $a/b$ ) of FGM plate.

This variation in behaviour may be due to the change in the amplitude of buckling mode shapes particularly at the stiffer region of the plate, which can be seen in Fig. 4.7 at  $c/b = 0.2$  and  $0.6$ . It is essential to observe that the value of  $\bar{P}_{cr}$  remains constant irrespective of  $a/b$  at around  $c/b = 0.45$ . It may be due to closely constant amplitude of buckling modes shapes in any aspect ratios of the FGM plate, which can be observed in Fig. 4.7 for  $c/b = 0.45$ . In addition, a similar study is continued by considering Type-II load and results are depicted in Figs. 4.8(a) and (b). From Fig.4.8(a), it can be witnessed that the buckling resistance of the single layer FGM plate gradually decreases as the load width ratio ( $c/b$ ) increases irrespective of volume fraction exponent ( $n$ ). This behaviour is because of the reduction in the influence of edge restraints with the increase in the load width ratio ( $c/b$ ). Also, when the load width ratio ( $c/b$ ) approaches the extreme value, the single layer FGM plates are prone to buckling at significantly lesser non-dimensional critical buckling load as compared to

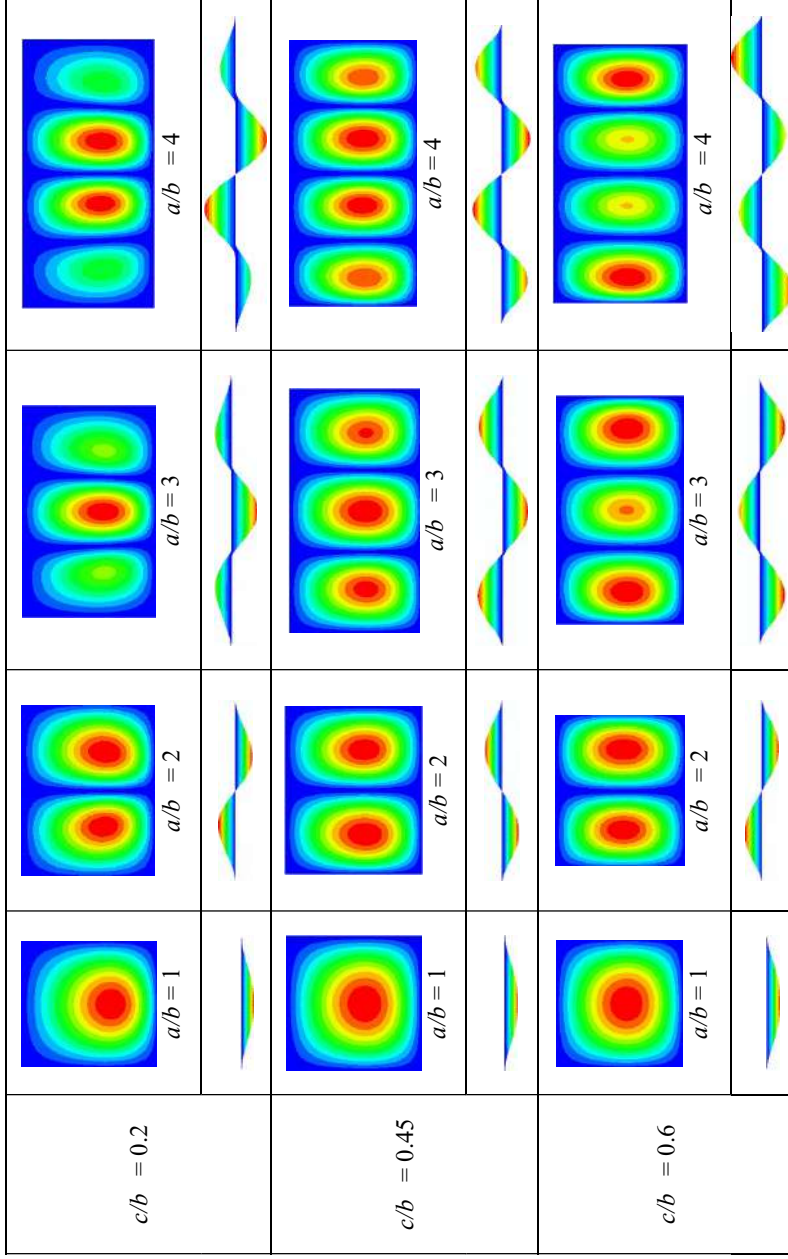


Fig. 4.7 Modes shapes for various aspect ratios of single layer FGM plates without porosity and  $n = 1$  under load Type-I

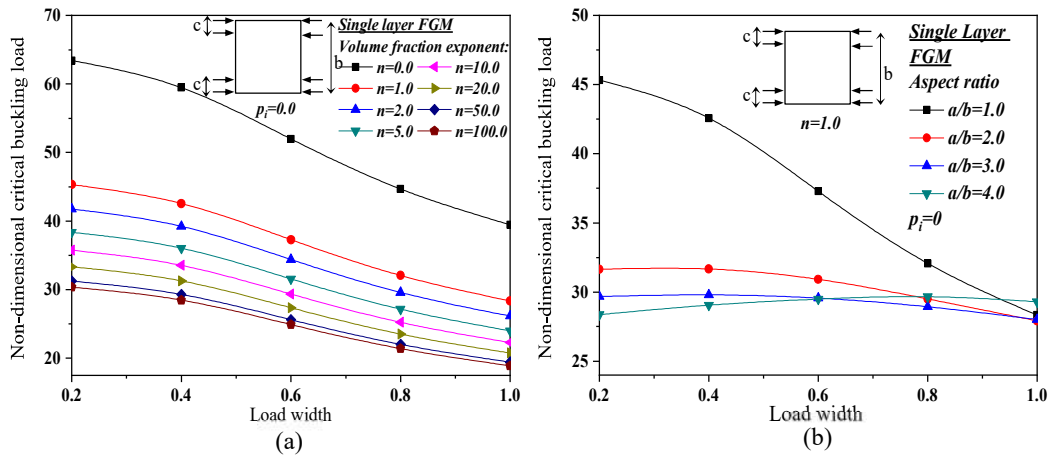


Fig. 4.8 Variation of non-dimensional critical buckling load with load width ratio for single layer FGM plates without porosity subjected to Type-II loadings (a) Influence of various volume fraction exponent (b) Influence of various aspect ratio of the plate

the corresponding non-dimensional critical buckling load at minimum load width ratio ( $c/b$ ). Considering the volume fraction exponent  $n = 1.0$ , the influence of different aspect ratios of single layer FGM plate on the buckling behaviour ( $\bar{P}_{cr}$ ) is investigated by considering load Type-II, and the results are illustrated in Fig. 4.8(b). The graphical representation indicates that with the rise in aspect ratios ( $a/b$ ) of single layer FGM plate, the buckling strength of the plate decreases and is found to be extreme and least at  $a/b = 1$  and 4, respectively. It can also be understood from the graph that the difference in the value of  $\bar{P}_{cr}$  with  $a/b$  is found to be substantial at lower load width ratio ( $c/b$ ) and trivial at higher load width ratio ( $c/b$ ).

#### 4.3.2.3 Buckling characteristics of different cases of FGM plate with porosity under load Type-I and Type-II

The effect of various volumes fraction exponent and porosity index on the buckling characteristics of single layer simply supported FGM square plates is investigated and the outcomes are tabularized (Table 4.9). The non-dimensional critical buckling loads are obtained here using Type-I and Type-II localised edge loads with  $c/b = 0.2$ . It can be noted that for any given porosity index, the non-dimensional critical buckling load decreases with increase in volume fraction exponent. It is worth nothing that for any volume fraction exponent, the buckling resistance of the FGM plate decreases with an increase in the value of porosity index ( $p_i$ ). Further, for V-D porosity type the effective

Table 4.9 Effect of volume fraction exponent and porosity index on the non-dimensional critical buckling load ( $\bar{P}_{cr}$ ) of single layer FGM plates subjected to Type-I and Type-II localised edge loads ( $c/b = 0.2$ )

$n$	$p_i$	Type of Loading									
		Type-I					Type-II				
		Pure FG*	U-D	O-D	X-D	V-D	Pure FG*	U-D	O-D	X-D	V-D
0.1	0.1	36.796	33.267	35.893	34.174	30.636	49.623	44.864	48.406	46.087	41.316
	0.2	36.796	29.720	34.987	31.547	24.427	49.623	40.080	47.184	42.545	32.942
	0.3	36.796	26.147	34.075	28.916	18.135	49.623	35.262	45.955	38.996	24.456
	0.4	36.796	22.538	33.159	26.280	-	49.623	30.395	44.719	35.441	-
	0.5	36.796	18.875	32.236	23.637	-	49.623	25.455	43.474	31.876	-
0.5	0.1	32.888	29.274	31.946	30.226	26.592	44.353	39.479	43.082	40.763	35.862
	0.2	32.888	25.617	30.994	27.554	20.179	44.353	34.548	41.799	37.160	27.214
	0.3	32.888	21.899	30.031	24.872	13.554	44.353	29.534	40.501	33.543	18.279
	0.4	32.888	18.090	29.056	22.177	-	44.353	24.396	39.186	29.908	-
	0.5	32.888	14.133	28.066	19.467	-	44.353	19.060	37.851	26.253	-
1.0	0.1	30.148	26.480	29.181	27.461	23.763	40.659	35.711	39.354	37.034	32.046
	0.2	30.148	22.745	28.199	24.760	17.189	40.659	30.674	38.030	33.392	23.181
	0.3	30.148	18.909	27.201	22.043	10.229	40.659	25.500	36.685	29.727	13.795
	0.4	30.148	14.908	26.183	19.305	-	40.659	20.105	35.312	26.035	-
	0.5	30.148	10.611	25.141	16.542	-	40.659	14.311	33.906	22.309	-
2.0	0.1	27.977	24.376	27.042	25.322	21.696	37.731	32.874	36.469	34.150	29.259
	0.2	27.977	20.717	26.095	22.656	15.244	37.731	27.940	35.193	30.555	20.559
	0.3	27.977	16.964	25.134	19.976	8.374	37.731	22.878	33.897	26.940	11.293
	0.4	27.977	13.036	24.155	17.278	-	37.731	17.581	32.577	23.301	-
	0.5	27.977	8.729	23.153	14.557	-	37.731	11.772	31.226	19.631	-

\*All the values shown in this column are for FGM plates without porosity ( $p_i = 0.0$ )

Young's modulus becomes negative for  $p_i \geq 0.4$  in case of  $n = 0.5$ . And for volume fraction exponent  $n = 1.0, 2.0, 5.0$  the effective Young's modulus becomes negative for  $p_i \geq 0.3$  as shown in Fig. 4.9. The negative value for effective Young's modulus is not possible in actual conditions. Hence for V-D porosity type,  $\bar{P}_{cr}$  is obtained by limiting the porosity index to 0.3.

Table 4.10 depicts the effect of different porosity indices on the non-dimensional critical buckling load ( $\bar{P}_{cr}$ ) of FCF and MFM type of FGM FGSP subjected to Type-I and Type-II localised edge loads. In this study, four different types of FGM layer schemes are considered with U-D type porosity. The porosity index is chosen as  $p_i = 0.1, 0.2$  and  $0.3$ . Here, the localised edge loads with load width ratio  $c/b = 0.2, 0.4$  and  $0.6$  are considered. Few of the results generated are also compared with the results from the ABAQUS software tool, and results show good comparison. In the FE software, the FGM plate is modelled by considering shell elements made up of a number of layers and varying the effective material properties of each layer according to a modified power law. For FCF, FGSP with 1-2-1 and 2-1-2 layer scheme show maximum and minimum buckling strength irrespective of porosity indices. While for MFM FGSP 2-1-2 and 1-2-1, layer scheme with porosity show maximum and minimum buckling strength irrespective of porosity indices. But for non-porous MFM FGM sandwich plate, 1-2-1 and 2-2-1 layer scheme exhibits maximum and minimum buckling strength, respectively. However, the non-dimensional critical buckling load variation among different layer schemes for a particular porosity index in an MFM type sandwich is negligible as compared to that of non-dimensional critical buckling load

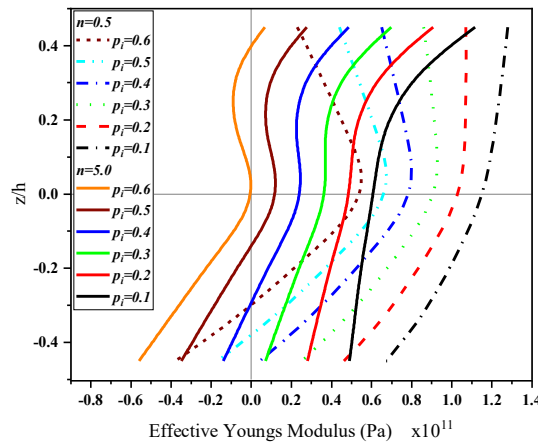


Fig. 4.9 Variation of effective Young's modulus through the thickness of single-layer FGM plates with V-D type porosity distribution

Table 4.10 Effect of porosity index on the non-dimensional critical buckling load ( $\bar{P}_{cr}$ ) of square simply supported FCF and MFM FGM sandwich plate with porosity subjected to Type-I and Type-II localised edge loads (U-D,  $n = 5.0$   $b/h = 100$ )

Type of load	$c/b$	$p_i$	Sandwich Configuration							
			FCF			MFM				
			1-1-1	2-1-2	2-2-1	1-2-1	1-1-1	2-1-2	2-2-1	1-2-1
Type-I	0	0	24.354 (24.371)	23.114 (23.106)	25.924 (25.938)	27.057 (27.064)	21.828 (21.844)	21.815 (21.829)	22.028 (22.036)	21.868 (21.888)
		0.1	21.039	19.699	22.733	24.045	21.700	21.786	21.655	21.437
		0.2	17.724	16.284	19.508	21.033	21.571	21.758	21.262	21.005
	0.3	0	14.408 (14.418)	12.868 (12.852)	16.241 (16.249)	18.021 (18.021)	21.442 (21.454)	21.729 (21.741)	20.845 (20.845)	20.573 (20.588)
		0.1	20.669	19.617	22.002	22.963	18.527	18.516	18.696	18.561
		0.2	17.855	16.718	19.293	20.406	18.418	18.492	18.380	18.195
	0.4	0.1	15.041	13.819	16.555	17.849	18.309	18.468	18.047	17.829
		0.2	12.227	10.920	13.783	15.292	18.200	18.444	17.693	17.462
		0.3	18.271	17.340	19.448	20.298	16.377	16.367	16.407	16.407
0.6	0.1	15.783	14.778	17.054	18.038	16.281	16.346	16.248	16.084	
	0.2	13.296	12.215	14.634	15.778	16.185	16.325	15.953	15.760	
	0.3	10.808	9.653	12.183	13.518	16.088	16.304	15.640	15.436	
Type-II	0	0	32.844	31.171	34.961	36.489	29.438	29.419	29.707	29.492
		0.1	28.373	26.566	30.657	32.427	29.264	29.381	29.205	28.910
		0.2	23.902	21.960	26.308	28.364	29.091	29.343	28.675	28.328
	0.3	0	19.431	17.353	21.903	24.301	28.917	29.305	28.112	27.745
		0.1	30.780	29.213	32.765	34.196	27.590	27.573	27.842	27.640
		0.2	26.590	24.896	28.730	30.389	27.428	27.537	27.372	27.095
	0.4	0	22.400	20.580	24.654	26.581	27.266	27.502	26.876	26.550
		0.1	18.208	16.262	20.525	22.773	27.103	27.466	26.348	26.005
		0.2	26.905	25.535	28.639	29.890	24.116	24.102	24.337	24.161
0.6	0.1	23.242	21.762	25.113	26.562	23.975	24.071	23.926	23.684	
	0.2	19.579	17.988	21.549	23.234	23.833	24.040	23.492	23.208	
	0.3	15.915	14.214	17.941	19.905	23.691	24.009	23.031	22.731	

Values in the bracket are obtained from ABAQUS

variation among FCF sandwich types. Subsequently, it is worth taking note that the buckling strength offered by FCF type of sandwich plate is greater than MFM type of sandwich plates at porosity index  $p_i = 0.0$ . At higher porosity index (i.e.,  $p_i = 0.3$ ) MFM type of sandwich plate offers slightly higher buckling strength than FCF type of sandwich plate irrespective of layer schemes. The higher buckling strength of FCF type sandwich plates in comparison with MFM type of sandwich plates at  $p_i = 0.0$  is due to the stiffer core of ceramic material and non-porous FGM face sheets in FCF type of sandwich plate which contribute together for better buckling resistance. While at porosity index  $p_i = 0.3$ , the effects of porosity in reducing the buckling strength is more prominent in sandwich plates with two porous FGM faces sheets and non-porous ceramic cores (FCF) in comparison with MFM type of sandwich plates having only one layer of porous FGM core and nonporous homogenous metal face layers.

The investigations are further carried out to understand the influence of porosity index, and the type of porosity distribution on buckling behaviour of single layer FGM plate subjected to Type-I and Type-II localised edge load. The load width ratio considered for this investigation is 0.2. Fig.4.10 represents the effect of porosity distribution, and porosity index on the buckling behaviour of simply supported square single layer FGM plate. It can be observed that with the increase in the porosity index, the non-dimensional critical buckling load decreases for all types of porosity distribution considered. It also be perceived that the effect of the increase in porosity index on a decrease of buckling strength of plates with O-D type of porosity are marginal compared to the plates with the remaining type of porosity distributions considered, while the rate of decrease in non-dimensional critical buckling load with the increase in porosity index is significant for V-D type of porosity. And also, for V-D type of porosity, non-dimensional critical buckling load is found up to porosity index,  $p_i = 0.4$ . The reason behind this consideration is discussed earlier.

#### *4.3.2.4 Buckling characteristics of single layer FGM plates without porosity under load Type-III and Type-IV*

The case of localised edge loads from the centre of the plates (Type-III) is considered in this subdivision, and the buckling variation of single layer FGM plates is shown in Fig. 4.11(a) by considering different volume fractions exponent ( $n$ ). It can be

comprehended from Fig. 4.11(a) that the non-dimensional critical buckling load ( $\bar{P}_{cr}$ ) increases as the load width ratio ( $c/b$ ) increases irrespective of volumes fraction exponent ( $n$ ) and found to be maximum at  $c/b = 1.0$  and least at  $c/b = 0.2$ . In this load case, the plate is primarily loaded at lower stiffness region, i.e., at the mid-portion of FGM plate and as the load width increases, it progressively transfers towards the higher stiffness area (i.e., edges of the FGM plate), wherein the considerable compressive zone gets extended over a wide plate area of supports at the edges. Therefore, this provides reason for the above-mentioned behaviour. Nevertheless, this behaviour is completely inverted in the load Type-II. It is vital to note that for a given  $c/b$ , the variation in the value of  $\bar{P}_{cr}$  is significantly higher at lower volume fraction exponents as compared to that of higher volume fraction exponents.

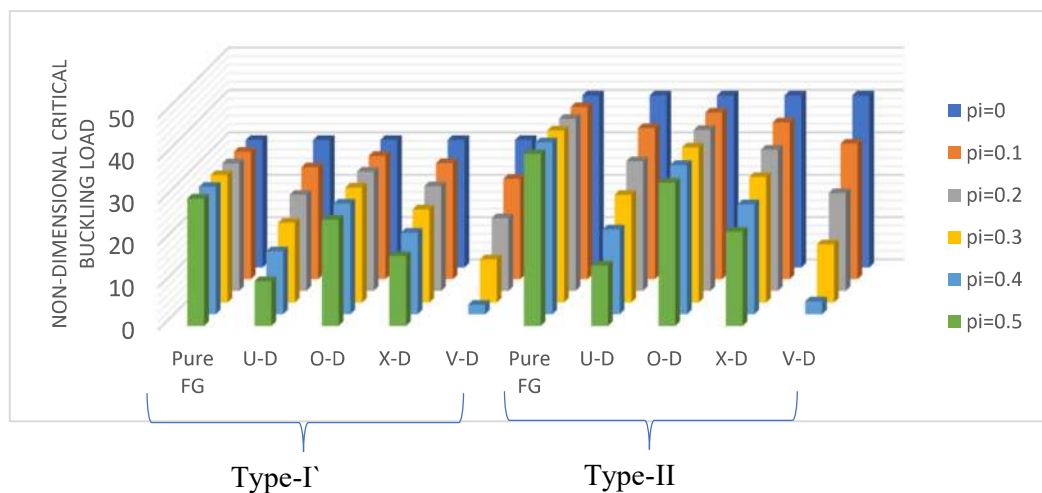


Fig. 4.10 Variation in the non-dimensional critical buckling load ( $\bar{P}_{cr}$ ) of simply supported single layer FGM plates under localised edge load with porosity index and porosity distribution (Type-I and Type-II,  $n = 2.0$ ,  $c/b = 0.2$ ,  $b/h = 100$ )

Subsequently, a similar study is carried out further to study the effect of different aspect ratio of single layer FGM plate by considering volume fraction exponent,  $n = 1.0$ . The outcomes are exemplified in Fig. 4.11(b). It is apparent from Fig. 4.11(b) that the value of  $\bar{P}_{cr}$  increases with the increase in plate aspect ratio irrespective of load width ratio except at  $c/b = 1.0$ , wherein the value of  $\bar{P}_{cr}$  is found to be nearly constant for all aspect ratios of the plate. It is also witnessed from the figure that for any given  $c/b$ , the buckling strength of the single layer FGM plate increases with the increase in aspect ratio ( $a/b$ ) and is observed to be least at  $c/b = 0.2$  and maximum at  $c/b = 1.0$ . It is worth

to note that the variation in the value of  $\bar{P}_{cr}$  among different  $a/b$  is found to be maximum when the load are concentrated towards the centre of the panel ( $c/b = 0.2$ ) and this variation reduces as the  $c/b$  increases. At  $c/b = 1.0$  the variation in  $\bar{P}_{cr}$  is found to be negligible.

The effect of different position of concentrated edge load (Type-IV) on the buckling characteristics of single layer porous FGM plate with different volume fraction exponents ( $n$ ) is studied in this section, and the outcomes are demonstrated in Fig. 4.12(a). It can be seen from Fig. 4.12(a) that the buckling resistance of the FGM plate decrease as the load moves towards the middle edge portion of single layer FGM plate, i.e.,  $c/b = 0.1$  to 0.5. The physical reason behind this behaviour may be due to the reduction in the effect of edge restraints.

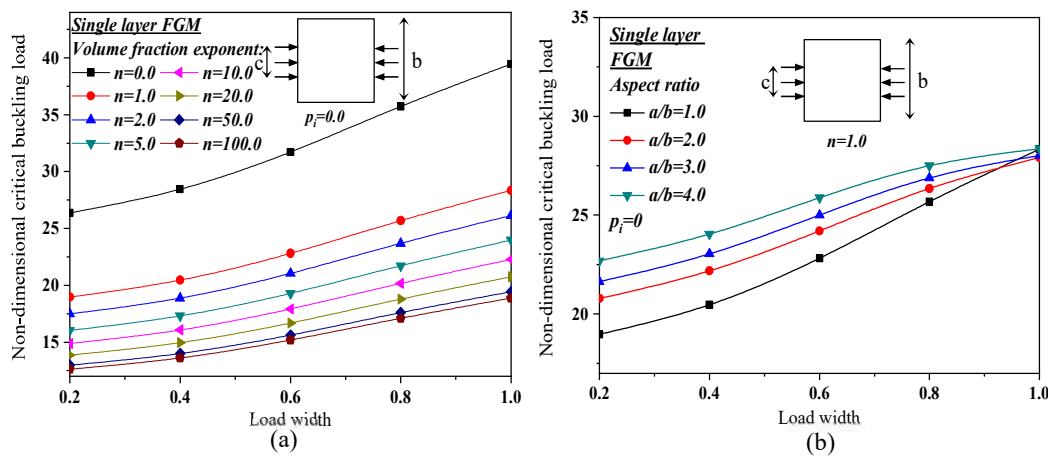


Fig. 4.11 Variation of non-dimensional critical buckling load with load width ratios of single layer FGM plates without porosity subjected to Type-III loading (a) Effect of volume fraction exponent (b) Effect of aspect ratio of the plates.

By considering single layer FGM plate with  $n = 1$ , the analysis is carried out to examine the effect of plate aspect ratio and the results are showcased in Fig 4.12(b). It is noticed from Fig. 4.12(b) that the value of  $\bar{P}_{cr}$  decreases with the increase in the plate aspect ratio ( $a/b$ ) only up to  $c/b \approx 0.2$ , and thereafter asymmetric behaviour is observed, wherein the values of  $\bar{P}_{cr}$  increases with the increases in the FGM plates aspect ratios. This behaviour is almost similar to that of the plate under load Type-I, and hence the reason which holds good for the plate with load Type-I also draws out to plates with load Type-IV.

#### 4.3.2.5 Buckling behaviour of different cases of FGM plate with porosity under load Type-III & Type-IV

The influence of volume fraction exponent and porosity index on non-dimensional critical buckling load of single layer FGM plate subjected to Type-III and Type-IV localised edge loads is studied. Here, load width ratio,  $c/b = 0.2$  is considered for the analysis and results are tabulated (Table 4.11). It can be seen from Table 4.11 that the non-dimensional critical buckling load decreases with increased porosity index irrespective of the type of porosity distribution. Also, the O-D type of porosity exhibits maximum buckling resistance, and V-D type of porosity distribution offers minimum buckling resistance irrespective of the volume fraction exponent, porosity index, and type of localised edge loading.

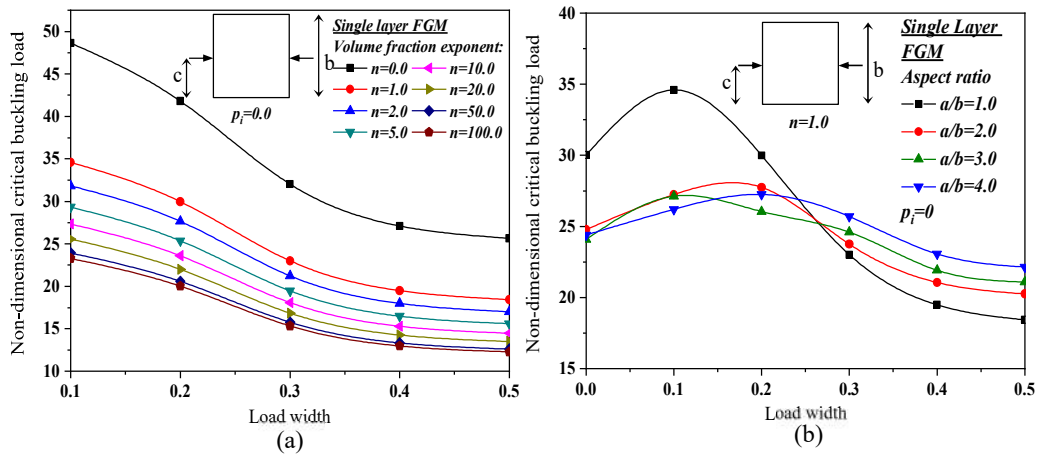


Fig. 4.12 Variation of non-dimensional critical buckling load with load width ratio for single layer FGM plates without porosity subjected to Type-IV loadings (a) Effect of volumes fraction exponents (b) Effect of aspect ratio of the plate

As discussed earlier, for V-D type porosity with volume fraction exponent  $n = 5.0$ , the porosity index is restricted to  $p_i = 0.3$ , since the effective Young's modulus tends to become negative for  $p_i = 0.4$  as shown in Fig. 4.9.

The effect of the porosity index and the layer scheme on the buckling behaviour is studied in this section by considering Type-III and Type-IV localised edge loads. The obtained numerical values are tabulated in Table 4.12 for the FCF & MFM configuration of sandwich plates. In consistent with the discussion in the last section, trends are similar for different layer schemes and porosity indices. However, for FCF sandwich configuration, the plate with 1-2-1 layer scheme offers the highest buckling

Table 4.1.1 Effect of volume fraction exponent and porosity index on non-dimensional critical buckling load of single layer FGM plates subjected to Type-III and Type-IV localised edge loads ( $c/b = 0.2$ )

$n$	$p_i$	Type of Loading									
		Type-III					Type-IV				
		Pure FG*	U-D	O-D	X-D	V-D	Pure FG*	U-D	O-D	X-D	V-D
0.5	0.1	20.630	18.651	20.124	19.159	17.176	38.001	34.356	37.068	35.293	31.640
	0.2	20.630	16.662	19.616	17.686	13.694	38.001	30.693	36.132	32.581	25.228
	0.3	20.630	14.659	19.105	16.211	10.166	38.001	27.003	35.190	29.864	18.730
	0.4	20.630	12.636	18.591	14.733	-	38.001	23.276	34.243	27.142	-
	0.5	20.630	10.582	18.074	13.251	-	38.001	19.494	33.290	24.413	-
1.0	0.1	18.439	16.413	17.910	16.946	14.909	33.965	30.233	32.991	31.216	27.463
	0.2	18.439	14.362	17.377	15.448	11.313	33.965	26.456	32.008	28.457	20.841
	0.3	18.439	12.278	16.838	13.944	7.599	33.965	22.617	31.014	25.688	14.000
	0.4	18.439	10.142	16.291	12.433	-	33.965	18.682	30.007	22.905	-
	0.5	18.439	7.923	15.736	10.913	-	33.965	14.597	28.984	20.107	-
2.0	0.1	16.903	14.846	16.361	15.396	13.323	31.135	27.346	30.135	28.360	24.541
	0.2	16.903	12.752	15.811	13.882	9.637	31.135	23.489	29.121	25.571	17.752
	0.3	16.903	10.601	15.251	12.358	5.735	31.135	19.528	28.091	22.765	10.565
	0.4	16.903	8.358	14.681	10.823	-	31.135	15.396	27.039	19.938	-
	0.5	16.903	5.949	14.097	9.274	-	31.135	10.959	25.962	17.085	-
5.0	0.1	15.686	13.667	15.162	14.198	12.164	28.892	25.173	27.925	26.151	22.405
	0.2	15.686	11.616	14.631	12.703	8.547	28.892	21.394	26.947	23.398	15.743
	0.3	15.686	9.511	14.093	11.200	4.694	28.892	17.518	25.954	20.630	8.648
	0.4	15.686	7.309	13.544	9.687	-	28.892	13.462	24.943	17.844	-
	0.5	15.686	4.894	12.983	8.161	-	28.892	9.014	23.908	15.034	-

\*All the values shown under this column are for FGM plates without porosity ( $p_i = 0.0$ )

resistance amongst all the other layer schemes plates without porosity in the order of 1-2-1 > 2-2-1 > 1-1-1 > 2-1-2 irrespective of load width ratios ( $c/b$ ) under Type-III and Type-IV loading condition.

Similarly, in the MFM type of sandwich the higher buckling resistance is in the order 2-2-1 > 1-2-1 > 1-1-1 > 2-1-2 for non-porous plate and it is in the order of 2-1-2 > 1-1-1 > 2-2-1 > 1-2-1 for any kind of porosity indices, irrespective of load width ratios ( $c/b$ ) under Type III and Type IV. As discussed earlier, among FCF and MFM types of sandwich plate, the MFM type of sandwich shows the highest buckling resistance only for higher porosity index irrespective of sandwich layer schemes. But this is not true for plates without porosity, where FCF type sandwich plates show the highest buckling resistance irrespective of layer schemes.

Moreover, for MFM sandwich configuration plates, 2-1-2 layer scheme shows less sensitivity towards the decrease in non-dimensional critical buckling load with increase in porosity index and also exhibits maximum buckling resistance. The poor sensitivity in buckling behaviour of behaviour the (2-1-2) layer scheme plate is due to the smaller thickness of porous FGM core sheet and larger thickness of non-porous metal face sheets (i.e., 0.32% decrease in non-dimensional critical buckling load with a decrease in porosity index from 0.1 to 0.3, for Type-III loads with  $c/b = 0.2$ ). Along the same lines, 1-2-1 layer scheme of MFM porous FGM sandwich plate having a greater thickness of porous FGM core sheet portrays higher variation of critical buckling load with the change in porosity index (i.e., 4.14% decrease in non-dimensional critical buckling load with a decrease in porosity index from 0.1 to 0.3). Also, the study is carried out to examine the effect of porosity distribution and porosity index on the buckling behaviour of a simply supported square single layer FGM plate subjected to Type-III and Type-IV localised edge loads. The results obtained are graphically presented in Fig 4.13. Here the porosity indices are chosen as  $p_i = 0.1, 0.2, 0.3, 0.4$  and  $0.5$ . As mentioned in the discussion for similar studies on the plate under Type-I and Type-II loading, the non-dimensional critical buckling load decreases with increase in the porosity index for all the types of porosity distributions. It can be perceived that the decrease in porosity index is significant in the case of V-D porosity distribution and

Table 4.12 Effect of porosity index on the non-dimensional critical buckling load ( $\bar{P}_{cr}$ ) of square simply supported FCF and MFM FGM sandwich plate with porosity subjected to Type-III and Type-IV localised edge loads (U-D,  $n = 5.0$ ,  $b/h = 100$ )

Type of Load	$c/b$	$p_t$	Sandwich Configuration							
			FCF			MFM				
			1-1-1	2-1-2	2-2-1	1-2-1	1-1-1	2-1-2	2-2-1	1-2-1
Type-III	0	0	13.653	12.958	14.533	15.168	12.238	12.230	12.350	12.260
		0.1	11.794	11.043	12.743	13.479	12.166	12.215	12.141	12.019
		0.2	09.935	09.128	10.935	11.790	12.094	12.199	11.921	11.777
		0.3	08.076	07.213	09.104	10.101	12.022	12.183	11.687	11.535
	0.4	0	14.729	13.979	15.679	16.364	13.203	13.195	13.323	13.227
		0.1	12.724	11.913	13.748	14.542	13.125	13.178	13.098	12.966
		0.2	10.719	09.848	11.797	12.720	13.048	13.161	12.861	12.705
		0.3	08.713	07.782	09.821	10.897	12.970	13.144	12.609	12.445
	0.6	0	16.423	15.587	17.482	18.246	14.721	14.712	14.856	14.748
		0.1	14.187	13.284	15.329	16.214	14.635	14.694	14.605	14.458
		0.2	11.951	10.980	13.154	14.183	14.549	14.675	14.340	14.167
		0.3	09.715	08.676	10.951	12.150	14.462	14.656	14.059	13.876
Type-IV	0	0	16.586	15.742	17.656	18.427	14.867	14.857	15.003	14.894
		0.1	14.329	13.416	15.482	16.376	14.779	14.838	14.749	14.600
		0.2	12.071	11.090	13.286	14.324	14.692	14.819	14.481	14.306
		0.3	09.812	08.764	11.061	12.272	14.604	14.799	14.197	14.012
	0.4	0	14.033	13.319	14.938	15.591	12.579	12.571	12.694	12.602
		0.1	12.123	11.351	13.099	13.855	12.505	12.555	12.479	12.353
		0.2	10.212	09.383	11.240	12.119	12.431	12.539	12.253	12.105
		0.3	08.301	07.414	9.358	10.382	12.356	12.522	12.012	11.856
	0.5	0	13.281	12.605	14.137	14.755	11.904	11.897	12.013	11.926
		0.1	11.473	10.742	12.396	13.112	11.834	11.882	11.810	11.691
		0.2	09.665	08.879	10.638	11.469	11.764	11.866	11.596	11.456
		0.3	07.856	07.017	08.856	09.826	11.694	11.851	11.368	11.220

minimal in the case of O-D type porosity.

#### 4.3.2.6 Effect of side-to-thickness and support conditions on different cases of FGM sandwich plate with porosity

Table 4.13 presents the effect of side-to-thickness ratios, support condition and porosity distributions on the non-dimensional critical buckling loads ( $\bar{P}_{cr}$ ) of single layer FGM plates with SSSS and CCCC support conditions subjected to various types of localised edge loads. In this study, the load width ratio is chosen as 0.2 for all types of localised edge loads. The volume fraction exponent and porosity index are considered as 2.0 and 0.1, respectively. The increase in the side-to-thickness ratio led to an increase in non-dimensional critical buckling load irrespective of the type of porosity distribution.

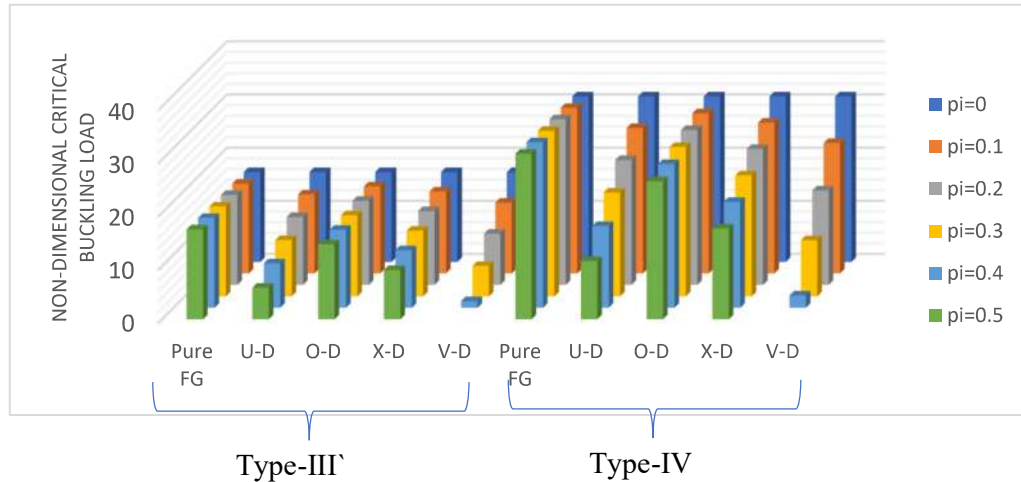


Fig. 4.13 Variation of non-dimensional critical buckling load ( $\bar{P}_{cr}$ ) for simply supported single layer FGM plates subjected to localised edge load with different porosity indices and porosity distribution (Type-III and Type-IV,  $n = 2.0$ ,  $c/b = 0.2$ )

In thick plates ( $b/h = 5$ ) the change in non-dimensional critical buckling loads with the porosity distribution is negligible for both SSSS and CCCC support conditions compared to that of thin plate configuration. The thick and moderately thick plates witness a sudden increase in the non-dimensional critical buckling loads with the increase in the side to thickness ratio. Further, there is a steady increase in the buckling load in thin plates (i.e.,  $b/h \geq 50$ ). Also, there is a large difference in critical buckling load between SSSS and CCCC support conditioned thin plates. But this is not followed in the case of thick plates, wherein critical buckling load differences between SSSS and

Table 4.13 Non-dimensional critical buckling loads ( $\bar{P}_{cr}$ ) of SSSS and CCCC supported single layer FG plates with varying side-to-thickness ratio ( $c/b = 0.2$ ,  $n = 2.0$ ,  $p_i = 0.1$ ).

Type of loading	Porosity distribution	Support condition									
		SSSS					CCCC				
		100	50	20	10	5	100	50	20	10	5
Type-I	Pure FG	30.148	30.028	29.224	26.489	7.097	61.409	60.077	54.508	28.644	7.154
	U-D	26.480	26.375	25.670	23.264	6.269	53.942	52.773	47.902	25.368	6.333
	O-D	29.181	29.062	28.268	25.537	6.686	59.418	58.121	52.625	27.007	6.744
	X-D	27.461	27.354	26.638	24.210	6.681	55.959	54.754	49.800	27.005	6.743
	V-D	23.763	23.670	23.055	20.960	5.850	48.432	47.390	43.140	23.727	5.922
Type-II	Pure FG	40.659	40.520	39.608	31.908	7.930	87.910	86.749	81.594	32.132	8.028
	U-D	35.711	35.589	34.790	28.203	6.997	77.218	76.198	71.689	28.460	7.110
	O-D	39.354	39.217	38.317	30.066	7.469	85.074	83.941	78.850	30.298	7.570
	X-D	37.034	36.910	36.098	30.045	7.460	80.093	79.044	74.461	30.295	7.569
	V-D	32.046	31.940	31.240	26.318	6.523	69.313	68.407	64.475	26.622	6.650
Type-III	Pure FG	16.903	16.865	16.602	15.713	11.726	43.991	43.354	39.998	31.449	11.825
	U-D	14.846	14.813	14.583	13.806	10.247	38.640	38.081	35.144	27.659	10.356
	O-D	16.361	16.323	16.063	15.184	11.024	42.573	41.948	38.637	30.232	11.122
	X-D	15.396	15.362	15.129	14.341	10.951	40.077	39.506	36.518	28.875	11.060
	V-D	13.323	13.293	13.094	12.418	9.446	34.682	34.190	31.623	25.054	9.567

CCCC edged plates are almost negligible, irrespective of porosity distributions and localised edge loads.

Additionally, Table 4.14 represents the influence of side-to-thickness ratio, support condition and layer schemes on the buckling characteristics of FCF and MFM FGM sandwich plates. Here, the plate are subjected to Type-I localised edge load with  $c/b = 0.2$ . Also, U-D and V-D types of porosity distributions are considered with a porosity index of  $p_i = 0.2$ . It can be noticed from Table 4.14 that the sandwich plates with V-D type of porosity distributions yield a higher buckling load as compared to that of plates with U-D type of porosity distributions. Hence, U-D type of porosity distribution is more dangerous than V-D type of porosity distribution for the same percentages of porosity imperfection. This observation can be described on the basis of the distribution of pore concentration from the mid surface. In the U-D type pores are distributed away from the mid surface; hence the buckling load decreases. The non-dimensional critical buckling loads increases with an increase in sides-to-thickness ratio irrespective of the type of porosity distributions. This unforeseen behaviour is due to the non-dimensional critical buckling load term, which contains the thickness parameter of the plate ( $h$ ) in the numerator. This behaviour stands for all the FGM layer schemes. It is also observed that a 1-2-1 layer scheme offers higher buckling resistance for porous FCF FGM sandwich plates. As observed in the earlier section, variation between non-dimensional critical buckling loads of SSSS and CCCC support thick plate is almost negligible irrespective of layer scheme.

#### *4.3.2.7 Buckling characteristics of FGSP with porosity and cutout under load Type-I and Type-II*

The influence of cutout ratio on the bucking characteristics of square simply supported porous FCF PFGSP ( $b/h = 100$ ) subjected to Type-I and Type- II localised edge loads has been examined in this section, and the outcomes are illustrated in Fig. 4.14 (a) and (b), respectively. In this study, FCF PFGSP with U-D, porosity index,  $p_i = 0.2$  and volume fraction exponent,  $n = 5.0$  is considered. From Fig. 4.14(a) it can be noticed that the nondimensional critical buckling decreases with increase in  $c/b$  ratio up to  $c/b$  of around 0.6, and further increases with increase in the load width ratio irrespective of cutout ratio. The rigidity of the FGM plate is noticeably lower in this area of the mid-

Table 4.14 Non-dimensional critical buckling loads ( $\bar{P}_{cr}$ ) of SSSS and CCCC support condition FCF and MFM FGM sandwich plate with varying side-to-thickness ratio subjected to load Type-I ( $c/b = 0.2, n = 2.0, p_1 = 0.2$ ).

Type of Sandwich	BC	b/h	Type of porosity distribution												
			U-D						V-D						
			1-1-1	2-1-2	2-2-1	1-2-1	2-1-1	1-1-1	2-1-2	2-2-1	1-2-1	2-1-1	1-1-1		
FCF	SSSS	5	7.415	6.665	7.756	8.353	6.912	7.960	7.319	8.261	8.762	7.542	7.960	7.319	
		10	18.776	17.201	20.321	21.817	18.334	22.547	21.322	23.898	24.983	22.346	22.547	21.322	
	CCCC	20	20.140	18.468	21.842	23.438	19.720	24.330	23.047	25.826	26.970	24.184	24.330	23.047	
		50	20.547	18.846	22.295	23.922	20.133	24.863	23.562	26.402	27.563	24.733	24.863	23.562	
	MFM	CCCC	100	20.609	18.903	22.364	23.996	20.196	24.943	23.640	26.489	27.653	24.816	24.943	23.640
			5	7.415	6.665	7.782	8.353	6.938	7.960	7.319	8.276	8.762	7.555	7.960	7.319
FCF	SSSS	10	29.662	26.660	31.142	33.414	27.765	31.841	29.275	33.112	35.048	30.226	31.841	29.275	
		20	38.491	35.261	41.673	44.724	37.601	46.220	43.711	49.005	51.216	45.824	46.220	43.711	
	CCCC	50	41.338	37.907	44.837	48.110	40.483	49.947	47.315	53.024	55.367	49.656	49.947	47.315	
		100	42.212	38.708	45.786	49.127	41.340	51.004	48.318	54.148	56.539	50.710	51.004	48.318	
	MFM	CCCC	5	5.298	5.249	5.322	5.358	5.268	5.570	5.413	5.648	5.767	5.471	5.570	5.413
			10	19.150	19.234	19.121	18.862	19.270	19.393	19.324	19.611	19.511	19.524	19.393	19.324
FCF	SSSS	20	21.009	21.125	20.968	20.651	21.162	21.215	21.179	21.449	21.298	21.399	21.215	21.179	
		50	21.566	21.691	21.520	21.186	21.728	21.760	21.734	21.999	21.832	21.960	21.760	21.734	
	CCCC	100	21.649	21.776	21.603	21.266	21.813	21.841	21.818	22.082	21.913	22.044	21.841	21.818	
		5	5.298	5.249	5.322	5.358	5.268	5.570	5.413	5.649	5.767	5.472	5.570	5.413	
	MFM	CCCC	10	21.191	20.998	21.288	21.433	21.070	22.281	21.652	22.595	23.067	21.887	22.281	21.652
			20	39.280	39.456	39.220	38.685	39.529	39.773	39.634	40.221	40.010	40.047	39.773	39.634
FCF	CCCC	50	43.168	43.408	43.081	42.425	43.484	43.582	43.514	44.063	43.747	43.966	43.582	43.514	
		100	44.113	44.362	44.023	43.349	44.439	44.528	44.464	45.020	44.691	44.926	44.528	44.464	

edge length portion as compared to the edge region of the single-layer FGM plates, which may be due to the effect of edge restraints. For Type- II localised edge load it can be witnessed from Fig. 4.14 (b) that the buckling resistance of the FCF FGM plate gradually decreases as the load width ratio ( $c/b$ ) increases irrespective of cutout ratio. This behaviour is because of the reduction in the influence of edge restraints with the increase in the load width ratio ( $c/b$ ). Further it can be noticed that, with increase in the cutout ratio the buckling load decrease at higher load width ratios, but at lower  $c/b$  i.e., at  $c/b < 0.45$  buckling resistance increases. The reason for the increase in buckling resistance may due to diffusion of stresses to stiffer region of plates with cutout that occurs when loads are acting at edges of the plate (i.e., lower load with ratio)

#### 4.3.2.8 Buckling characteristics of FGSP with porosity and cutout under load Type-III and Type-IV

Fig. 4.15 (a) and (b) depicts the effect of cutout ratios on  $\bar{P}_{cr}$  of square simply supported porous FCF PFGSP ( $b/h = 100$ ) subjected to Type-III and Type-IV localised edge load. Here, the load  $c/b$  is varied. Also, U-D of porosity distributions are considered with a porosity index of  $p_i = 0.2$  and volume fraction exponent,  $n = 5.0$ . It can be observed from Fig. 4.15(a) that the nondimensional critical buckling load increases with increase in  $c/b$  ratio as discussed earlier. Further, with increase in the cutout ratio the nondimensional critical buckling load decrease irrespective of load width ratio. The decrease in the nondimensional critical buckling due to increase in the cutout ratio may be due to increase in the stresses in vicinity of the cutout portion. Further, as noticed in

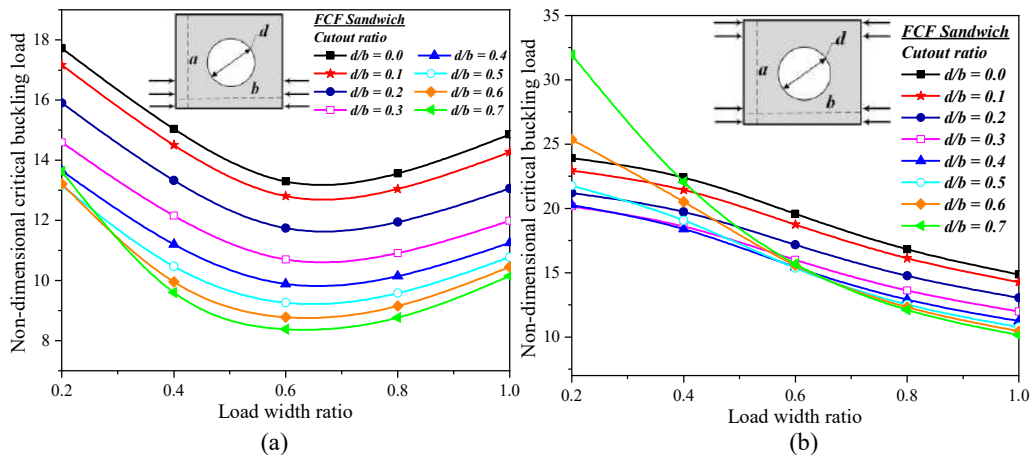


Fig. 4.14 Variation of nondimensional critical buckling load with load width ratios for FCF FGM plates with porosity and varying cutout ratio subjected to (a) Type-I (b) Type-II

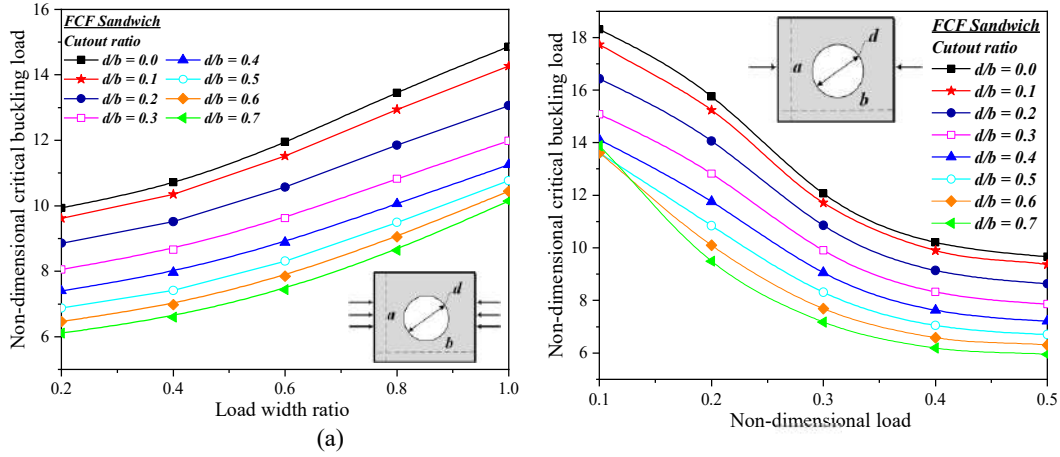


Fig. 4.15 Variation of nondimensional critical buckling load with load width ratios for FCF FGM plates with porosity and varying cutout ratio subjected to (a) Type-III (b) Type-IV

Fig. 4.15(b), the nondimensional critical buckling load of the plate subjected to Type-IV decreases as the load moves towards middle edge portion of the plate and this behaviour is due to reduction in the effect of edge restraints near the middle edge portion of the plate. In continuation, it is seen from Fig. 4.15(b) that the nondimensional critical buckling load of the plate decrease with increase in cutout ratio for all load width ratio, except for  $d/b = 0.7$ , for which that the nondimensional critical buckling load slightly increase at  $c/b < 0.2$ . This behaviour may be due to diffusion of stress towards the edges, i.e., higher stiffness regions.

#### 4.4 CLOSURE

This chapter uses the FE method to study the vibration and buckling response of porous FGSP with and without cutout subjected to localised inplane edge loads. The effective properties of the FGSP are evaluated using power law-based homogenization technique. Four types of porosity distribution models are explored, and the porosity imperfections are modelled as the criteria of stiffness reduction. The current study incorporates two distinct kinds of sandwich configuration in such a way that there is no material mismatch along the thickness direction. The application of different cases of localised loads on the plate with/without cutouts leads to the development of nonuniform stresses. Hence a novel dynamic approach has been proposed to evaluate buckling loads by implementing two sets of boundary conditions. The results obtained from current FE formulations are compared with results obtained from analytical

solution and numerical methods available in the literature. After establishing the accuracy wide variety of numerical or parametric studies have been carried out and useful conclusions are drawn from the analysis. Following chapter investigates extensively the vibration and buckling characteristics of porous FGSP with cutout under NIELs.



## CHAPTER 5

### VIBRATION AND BUCKLING ANALYSIS OF POROUS FG SANDWICH PLATES WITH AND WITHOUT CUTOUT UNDER NONUNIFORM IN-PLANE EDGE LOADS

#### 5.1 PRELIMINARY REMARKS

The FGSPs are a small portion of a complicated built up-structure, and the load transfer between these plates takes place in the form of in-plane loads through the plate edges, and these in-plane loads are rarely uniform due to the relative stiffness of adjacent members, support restraints and external loading conditions. The non-uniformity in the stress due to in-plane load will further increase due to the formation of porosity and cutouts, which significantly affects the vibration and buckling response of FGSPs. Hence, this chapter attempts to analyze and discuss the effect of porosity on vibration and buckling characteristics of FGSP with cutout under nonuniform loads. In order to do so, a general formulation, as presented in Chapter 3 has been developed by taking Green-Lagrange strains displacement relation, and it is utilized to compute the desired responses. Because the stress distribution within the plate element is significantly non-uniform, a dynamic technique was employed to solve the buckling problems, with two sets of boundary conditions, one for pre-buckling stresses and another for buckling load calculations. The effects of various geometrical and material parameters and the support conditions on vibration and buckling response of porous FGSP under different NIELs are investigated in this chapter. In the end, this chapter is summed up in chapter 8 with some useful conclusions.

#### 5.2 PROBLEM DESCRIPTION

In the present study, different cases of uniaxial in-plane loads acting on the opposite edge of FGSPs considered are discussed in detail in this section. Two sets of NIELs are considered; they are linearly and nonlinearly varying in-plane edge loads. In this analysis, seven different cases of linearly and nonlinearly varying in-plane edge loads that can occur in practical conditions are chosen as displayed in Fig. 5.1 and Fig. 5.2, respectively. The term  $P_0$  signifies the maximum intensity of load per unit length. The

loading patterns are represented using a mathematical equation in Table 5.1. The term  $\eta$  represents  $y/b$  and  $P_y$  denote the loading parameters for NIEL acting on the edges parallel to the  $y$ -axis of the plate.

In the present study, FCF and MFC sandwich configurations as shown in Fig. 3.1 are considered. These sandwich configurations with U-D, O-D, Log O-D, and V1-D porosity distributions, as mentioned in Chapter 3, are considered to study the vibration and buckling response of FGSP with cutout under NIELs. Firstly, the accuracy of the solution obtained is established by comparing the present results with those available in the literature. After verifying the accuracy, parametric studies have been carried out extensively.

### 5.3 RESULTS AND DISCUSSION

The vibration and buckling responses are obtained using developed mathematical formulation through an inhouse MATLAB code that can extend for any general case. The convergence study of the FGSP under nonuniform load is performed for various geometrical and material configurations.

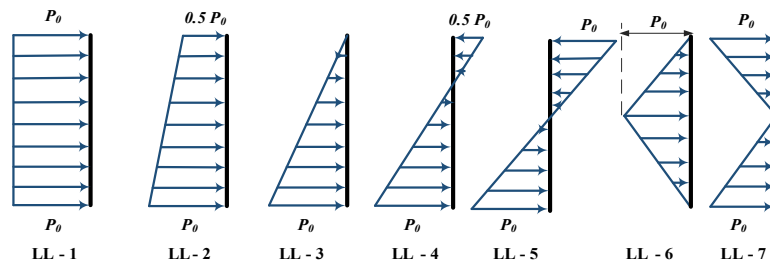


Fig. 5.1 Various cases of linearly varying in-plane edge loads

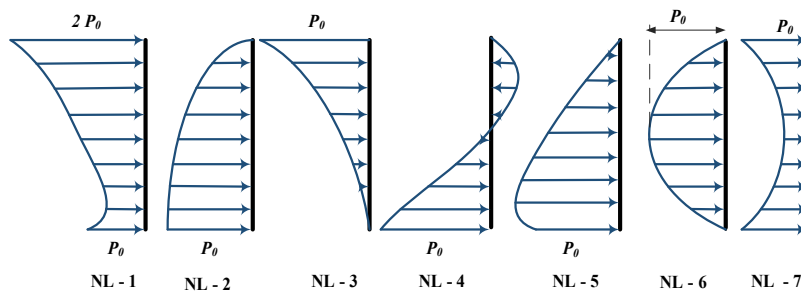


Fig. 5.2 Various cases of nonlinearly varying in-plane edge loads

Table 5.1 Loading Equations

Sl. No.	Linearly varying load case	Loading equation	Nonlinearly varying load case	Loading equation
1.	LL - 1	$P_y = P_0$	NL - 1	$P_y = P_0 \left(1 - \eta + 2\eta^2\right)$
2.	LL - 2	$P_y = P_0 (1 - 0.5\eta)$	NL - 2	$P_y = P_0 \left(1 - \eta^2\right)$
3.	LL - 3	$P_y = P_0 (1 - \eta)$	NL - 3	$P_y = P_0 \left(\eta^2\right)$
4.	LL - 4	$P_y = P_0 (1 - 1.5\eta)$	NL - 4	$P_y = P_0 \left(1 - 3\eta + 2\eta^2\right)$
5.	LL - 5	$P_y = P_0 (1 - 2\eta)$	NL - 5	$P_y = P_0 \left(1 + \eta - 2\eta^2\right)$
6.	LL - 6	$P_y = P_0 (2\eta) \quad 0 \leq y \leq b/2$ $P_y = 2P_0 (1 - \eta) \quad b/2 \leq y \leq b$	NL - 6	$P_y = 4P_0 \left(\eta - \eta^2\right)$
7.	LL - 7	$P_y = P_0 (1 - 2\eta) \quad 0 \leq y \leq b/2$ $P_y = P_0 (2\eta - 1) \quad b/2 \leq y \leq b$	NL - 7	$P_y = P_0 \left(1 - 2\eta + 2\eta^2\right)$

Consequently, a variety of examples are solved for validation purposes by comparing the present results with those available in published literature. After the exhaustive testing of the present model, an inclusive parametric study of FGSP under nonuniform load is performed. Here, the vibration and buckling response of FGSPs are analysed for various geometrical parameters, material parameters and support conditions.

The material properties of constituent materials considered in the current study are  $E_m = 70$  GPa,  $E_c = 380$  GPa,  $\rho_m = 2707$  kg/m<sup>3</sup>,  $\rho_c = 3800$  kg/m<sup>3</sup> and Poisson's ratio  $\nu = 0.3$ . In continuation, the effects of different parameters on the vibration and buckling response of porous FGSP with cutout are discussed in detail. If not stated otherwise, critical buckling loads ( $P_{cr}$ ) and natural frequencies ( $\omega$ ) are represented in non-dimensional form as

$$\bar{P}_{cr} = P_{cr} a^2 / E_m h^3$$

$$\bar{\omega} = (\omega a^2 / h) \sqrt{\rho_0 / E_0}, E_0 = 1 \text{ GPa}, \rho_0 = 1 \text{ kg / m}^3$$

A refined mesh pattern implemented in this work can be noticed in Fig. 5.3, along with a non-uniform loading pattern. The terms  $n_x$ ,  $n_y$ ,  $n_{xl}$ ,  $n_{yl}$  and  $n_h$  are the mesh control

parameters in the respective directions, and detailed mesh specifications are discussed in the subsequent section, 5.3.1, containing convergence and validation studies.

### 5.3.1 Convergence and Validation Studies

**Example 1:** Here, the convergence study is performed by choosing finer mesh near the surrounding area of the cutout and coarser mesh away from the cutout portion, as shown in Fig. 5.3. The mesh control parameters,  $n_x = n_y$ ,  $n_{x1} = n_{y1}$ ,  $n_h$  are also depicted in Fig. 5.3. The  $\bar{P}_{cr}$  are evaluated for simply supported square single layer FG plate with  $n = 1$  and 2 and subjected to LL-1 by varying the mesh size. The properties of the constituent materials (Al/Al<sub>2</sub>O<sub>3</sub>) incorporated are mentioned in Section 5.3. The mesh size is varied by changing the mesh control parameters. The  $\bar{P}_{cr}$  results are evaluated for  $d/b$  ratios 0.3 and 0.5, and outcomes are listed in Table 5.2 for different mesh sizes. It can be inferred from the table that for  $d/b = 0.3$ , 184 elements give good convergence. While plates with  $d/b = 0.5$  require 196 elements. Finally, it is concluded that the convergence criterion has been satisfied for plates with circular cutouts. After meeting the convergence criteria, comparison studies were conducted to validate the buckling and vibration response of the FGSPs. To validate and check the effectiveness of the foregoing FE formulation, results arrived are compared with results existing in the previously published literature as mentioned in the examples below.

**Example 2:** The critical buckling loads of FCF PFGSP acted upon by LL-6 are found and compared with results published by Adhikari et al. (2020) as mentioned in Table 5.3. The  $\bar{P}_{cr}$  ( $\bar{P}_{cr} = P_{cr}a^2/100E_0h^3$ ,  $E_0 = 1 \text{ GPa}$ ) are found for FCF PFGSP having U-D type of porosity with  $p_i = 0.3$ .

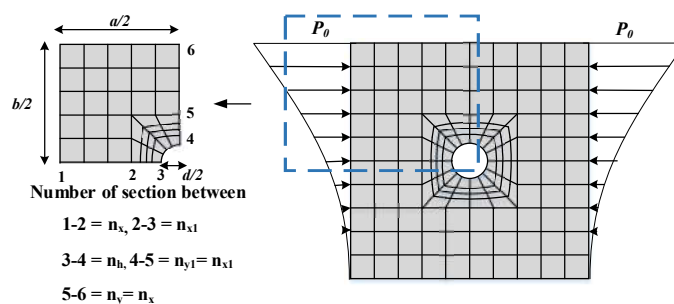


Fig. 5.3 Detailed Mesh pattern over full plate featuring a circular shaped cutout acted by NIELs

Table 5.2 Convergence of  $\bar{P}_{cr}$  for a simply supported single layer FG plate with a central circular cutout under the action of LL-1

Cutout ratio ( $d/b$ )	Mesh order			Number of elements	$\bar{P}_{cr}$	
	$n_x = n_y$	$n_{x1} = n_{x2}$	$n_h$		$n = 1$	$n = 2$
0.3	2	2	24	112	7.8919	6.1580
	2	3	24	136	7.8872	6.1543
	2	4	24	160	7.8865	6.1538
	2	5	24	184	7.8865	6.1537
	1	2	32	100	7.0914	5.5332
0.5	1	3	32	132	7.0867	5.5296
	1	4	32	164	7.0857	5.5288
	1	5	32	196	7.0854	5.5286

Table 5.3 Comparison of  $\bar{P}_{cr}$  for FCF PFGSP (Al/Al<sub>2</sub>O<sub>3</sub>) with U-D porosity distributions and subjected to LL-6.

Support condition	$b/h$	Sandwich Layer scheme					
		2-1-1		1-1-1		1-2-1	
		Adhikari et al. (2020)	Present	Adhikari et al. (2020)	Present	Adhikari et al. (2020)	Present
SSSS	20	1.517	1.511	2.177	2.169	4.524	4.507
	50	1.520	1.520	2.182	2.181	4.541	4.539
	100	1.521	1.521	2.183	2.183	4.544	4.54
CCCC	20	3.934	3.882	5.638	5.568	11.651	11.511
	50	3.966	3.966	5.690	5.690	11.825	11.831
	100	3.973	4.001	5.701	5.735	11.862	11.908

The volume fraction exponent of the sandwich plates with  $n = 5$  is considered. The properties of the constituent materials (Al/Al<sub>2</sub>O<sub>3</sub>) incorporated in this example are mentioned in Section 5.3. The  $\bar{P}_{cr}$  are obtained for plates with  $b/h = 20, 50,$  and  $100$ . The buckling loads are found for plates with SSSS and CCCC support conditions. It is evident from Table 5.3 that the results are in good agreement for different  $b/h$  and support conditions.

**Example 3.** In this instance, the free vibration and buckling study for all sides simply supported square moderately thick ( $a/h = 10$ ) PFGSP and SFGSP with porosity has been performed. The properties of the constituent materials (Al/Al<sub>2</sub>O<sub>3</sub>) incorporated are mentioned in Section 5.3. The  $\bar{\omega}$  and  $\bar{P}_{cr}$  are found for FCF plates having U-D and O-D type of porosity with porosity indices  $p_i = 0.1$  and  $0.2$ . The volume fraction exponent of the sandwich plates with  $n = 2$  is considered. Fig. 3.1 shows a few sandwich layer schemes considered in this example. Here, uniaxial compressive in-plane edge load is considered to check the validity of the current formulation for the buckling

problem. The Non-dimensional fundamental frequencies  $\bar{\omega} = (\omega a^2/h)\sqrt{\rho_0/E_0}$ ,  $E_0 = 1 \text{ GPa}$ ,  $\rho_0 = 1 \text{ kg/m}^3$  and non-dimensional critical buckling load  $\bar{P}_{cr}$  ( $\bar{P}_{cr} = P_{cr}a^2/100E_0h^3$ ,  $E_0 = 1 \text{ GPa}$ ) obtained are presented along with analytical solutions given by Daikh and Zenkour (2019) in Table 5.4 and Table 5.5. Here the  $\bar{\omega}$  and  $\bar{P}_{cr}$  for PFGSP with U-D porosity distributions are also compared with results presented by VanVinh and Huy (2021) (FE-based solution). Table 5.4 and Table 5.5 show that the outcomes obtained are in good harmony for different porosity distributions, porosity indices, and FGSPs with two other material idealization techniques.

**Example 4.** Finally, in this instance,  $\bar{P}_{cr}$  of thin ( $a/h = 100$ ) square isotropic plates with cutout is calculated and verified by comparison with outcomes of Abolghasemi et al. (2019), Sabir and Chow (1986) and El-Sawy and Nazmy (2001) considering different cutout ratios and support conditions. Abolghasemi et al. (2019) have obtained analytical solutions for buckling problems of plates with SSSS and CCCC. At the same time, Sabir and Chow (1986) and El-Sawy and Nazmy (2001) have employed the FE method to compute  $\bar{P}_{cr}$  for SSSS. The present authors have arrived at a critical buckling load using FSDT. In this example, a structural steel material plate with 200 GPa as Young's modulus and 0.3 as Poisson's ratio is considered. The  $\bar{P}_{cr}$  considered for the analysis is taken as  $\bar{P}_{cr} = P_{cr}b^2/\pi^2D$ . The obtained results are presented in the Table 5.6. It is apparent from the comparison study that the current outcomes are in decent harmony with those present in the literature and thus validating the current formulation for plates with cutouts. It is noticed that  $\bar{P}_{cr}$  reduces with rise in the cutout ratio, irrespective of the support conditions.

### 5.3.2 Parametric studies

In the preceding section, it is noticed that the current outcomes using FE formulations are in good concurrence with the results existing in the literature. Thus, in the subsequent subsections, the vibration and buckling responses of the FGSPs are examined by considering several parameters such as volume fraction exponent, support condition, nonuniform load case, plate aspect ratio, porosity distribution, sandwich layer scheme, cutout ratio, etc.

Table 5.4 Comparison of  $\bar{\omega}$  for FCF PFGSP and SFGSP (Al/Al<sub>2</sub>O<sub>3</sub>) simply supported porous sandwich plate of various types of porosity distributions and porosity indices.

Material idealization technique	Porosity distribution	$P_i$	Sandwich Layer schemes												
			$\bar{\omega}$						2-1-1						
			1-1-1		1-2-1		2-2-1		2-1-1		2-1-1		2-1-1		
PFGSP	U-D	0.1	1.127	1.121	1.121	1.121	1.255	1.249	1.250	1.190	1.182	1.183	1.102	1.094	1.094
		0.2	1.055	1.042	1.042	1.203	1.191	1.192	1.125	1.110	1.110	1.111	1.022	1.005	1.006
		0.1	1.160	1.158	-	1.279	1.277	-	1.219	1.216	-	-	1.139	1.135	-
	O-D	0.2	1.131	1.125	-	1.256	1.251	-	1.193	1.186	-	-	1.110	1.102	-
		0.1	1.268	1.260	-	1.379	1.372	-	1.320	1.311	-	-	1.235	1.226	-
		0.2	1.217	1.201	-	1.340	1.326	-	1.274	1.258	-	-	1.181	1.164	-
SFGSP	U-D	0.1	1.290	1.288	-	1.397	1.394	-	1.340	1.337	-	-	1.259	1.257	-
		0.2	1.269	1.263	-	1.380	1.373	-	1.321	1.314	-	-	1.237	1.232	-
	O-D	0.1	1.290	1.288	-	1.397	1.394	-	1.340	1.337	-	-	1.259	1.257	-
		0.2	1.269	1.263	-	1.380	1.373	-	1.321	1.314	-	-	1.237	1.232	-

Table 5.5 Comparison of  $\bar{P}_{cr}$  for FCF PFGSP and SFGSP (Al/Al<sub>2</sub>O<sub>3</sub>) simply supported porous sandwich plate of various types of porosity distributions and porosity indices.

Material idealization technique	Porosity distribution	Sandwich Layer schemes												
		$p_i$	1-1-1						2-2-1					
			Present		Daikh and Zenkour (2019)		Van Vinh and Huy (2021)		Present		Daikh and Zenkour (2019)		Van Vinh and Huy (2021)	
PFGSP	U-D	0.1	1.989	1.997	1.969	2.606	2.622	2.586	2.260	2.272	2.240	1.841	1.849	1.822
		0.2	1.620	1.605	1.582	2.272	2.265	2.234	1.892	1.881	1.854	1.450	1.436	1.415
	O-D	0.1	2.180	2.206	-	2.775	2.810	-	2.448	2.479	-	2.047	2.072	-
		0.2	2.003	2.013	-	2.611	2.631	-	2.273	2.289	-	1.867	1.878	-
SFGSP	U-D	0.1	2.614	2.622	-	3.236	3.250	-	2.881	2.893	-	2.422	2.429	-
		0.2	2.247	2.222	-	2.904	2.886	-	2.523	2.503	-	2.040	2.018	-
	O-D	0.1	2.799	2.833	-	3.401	3.440	-	3.061	3.099	-	2.614	2.651	-
		0.2	2.618	2.634	-	3.237	3.256	-	2.885	2.906	-	2.428	2.455	-

Table 5.6 Comparison of  $\bar{P}_{cr}$  for isotropic square simply supported plate with various cutout ratios and support conditions.

$d/b$	Support condition					
	SSSS				CCCC	
	Source				Source	
	Abolghasemi et al. (2019)	Sabir and Chow (1986)	El-Sawy and Nazmy (2001)	Present	Abolghasemi, et al. (2019)	Present
0	3.986	-	4.000	3.997	9.914	10.071
0.1	3.924	3.691	3.859	3.837	9.723	9.464
0.2	3.571	3.445	3.531	3.513	8.958	8.778
0.3	3.23	3.185	3.24	3.23	8.735	8.589
0.4	3.023	3.049	3.04	3.026	8.381	8.520
0.5	2.89	2.84	2.914	2.896	7.801	8.208
0.6	2.818	-	2.829	2.806	7.099	7.774

The loading cases considered here are given in Fig. 5.1 and Fig. 5.2. The loading case shown here is compressive in nature. The parametric studies related to vibration and buckling characteristics are discussed in the successive sub-sections.

### 5.3.2.1 Vibration characteristics of porous FGSPs with cutouts subjected to NIELs

The investigation is carried out to comprehend the impact of different cases of nonlinearly varying NIELs on the variation of the  $\bar{\omega}$  due to an increase in the non-dimensional in-plane edge load for square simply supported porous FCF PFGSP ( $b/h = 100$ ,  $n = 1.0$ ) with cutout ratio ( $d/b = 0.2$ ) as displayed in Fig. 5.4. The porosity distribution U-D and  $p_i = 0.2$  is chosen. It is noteworthy to observe that plates subjected to NL-4 show highest  $\bar{\omega}$  with an increase in the non-dimensional in-plane load in

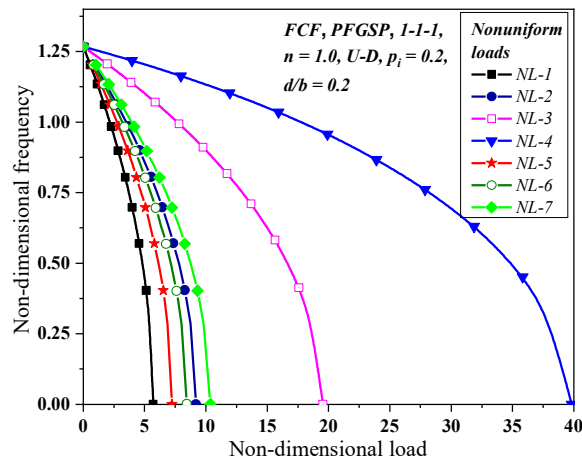


Fig. 5.4 Variation of  $\bar{\omega}$  for square porous FCF PFGSP with cutout subjected to nonlinearly varying loads

comparison with  $\bar{\omega}$  of plates subjected to other cases of nonlinearly varying loads. The reason behind such behaviour is mainly due to the existence of a tensile portion of the loads along with compressive loads, as in NL-4. These tensile loads cause a stretching effect, which leads to an increase in the stiffness of the plate and hence the  $\bar{\omega}$  increases. Similarly, LL-5 exhibits the highest  $\bar{\omega}$  among several linearly varying loads due to the existence of tensile loads along with compressive loads. For the sake of brevity, only the variation of the non-dimensional frequencies of plates subjected to nonlinearly varying loads are presented. Thus, the type of NIELs significantly impact the  $\bar{\omega}$  of the porous FGSPs with cutout. Further, the impact of various sandwich layer schemes and cutout ratios on the  $\bar{\omega}$  of square simply supported porous FCF PFGSP ( $b/h = 100$ ,  $n = 1.0$ ) subjected to NL-1 with  $d/b = 0.2$  is investigated, and the outcomes are depicted in Fig. 5.5 and Fig. 5.6, respectively. The porosity distribution U-D and  $p_i = 0.2$  is chosen. It is witnessed from Fig. 5.5 that the PFGSP with 1-2-1 and 1-0-1 sandwich layer schemes shows the maximum and minimum non-dimensional frequencies, respectively. The higher  $\bar{\omega}$  for 1-2-1 sandwich layer scheme is due to the larger thickness of the ceramic core sheet compared to thin face sheets, which offer higher stiffness to the plate. It is worthwhile to mention that for a certain non-dimensional in-plane edge load, the  $\bar{\omega}$  increases with the increase in the volume of the material at the core portion of the FCF PFGSP. Furthermore, it is comprehended from Fig. 5.6 that the  $\bar{\omega}$  of the square simply supported porous FCF PFGSP ( $b/h = 100$ ,  $n = 1.0$ ) subjected to NL-1 increases with the

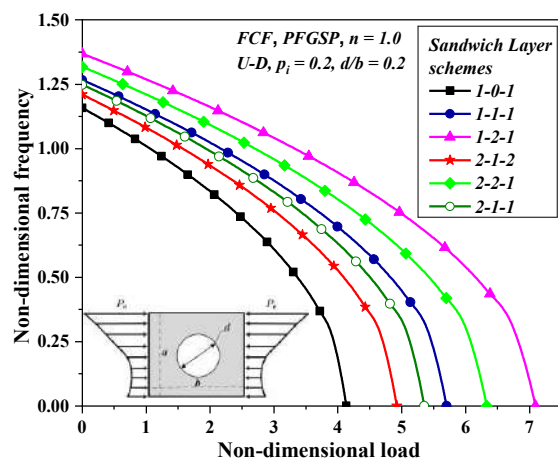


Fig. 5.5 Variation of  $\bar{\omega}$  for square porous FCF PFGSP with cutout subjected to NL-1 for different sandwich layer schemes

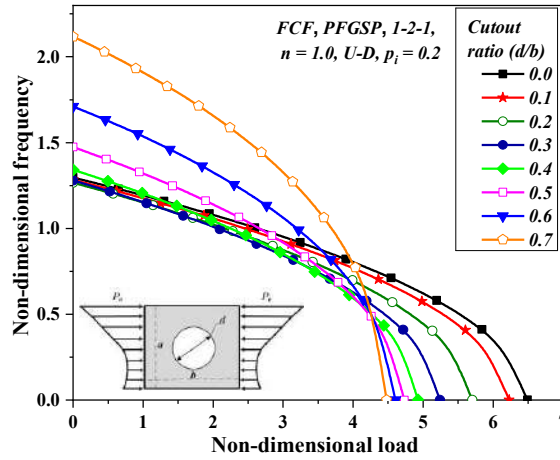


Fig. 5.6 Variation of  $\bar{\omega}$  for square porous FCF PFGSP with cutout for different cutout ratios

increase in cutout ratio only up to certain non-dimensional loads, and thereafter, the reverse response is noticed. It also perceived that for any cutout size, the  $\bar{\omega}$  decreases with an increase in the non-dimensional load and approaches zero at a particular non-dimensional load. Thus, the non-dimensional load corresponding to the zero-frequency parameter gives the  $P_{cr}$  of the plate. This method of deriving  $P_{cr}$  for a plate member acted upon by in-plane edge load is known as the dynamic approach. This approach is adopted in the current study to determine the critical buckling loads for porous FGSPs with cutouts acted upon by NIELs. The effect of the type of material idealization technique on the variation of  $\bar{\omega}$  due to the increase in the non-dimensional load of square simply supported porous FCF PFGSP and SFGSP ( $b/h = 50$ ,  $n = 0.5$ ) with cutout ( $d/b = 0.4$ ) is illustrated in Fig. 5.7 considering  $p_i = 0.1$  and different porosity distributions. The plate is acted upon by NL- 3. It can be revealed that at any non-dimensional load, the  $\bar{\omega}$  for the PFGSP is greater than that of SFGSP irrespective of the porosity distribution at a given  $n = 0.5$ . The SFGSP shows a lesser  $\bar{\omega}$  because of the fact that the stiffness of SFGSP is less than that of PFGSP at  $n = 0.5$ , but as the  $n$  increases, the behaviour reverses due to the variation of the material distribution pattern across the thickness of the plate, which leads to change in the stiffness of the plate. Next, the influence of porosity distribution and porosity indices on the variation of  $\bar{\omega}$  due to the increase in the non-dimensional load on square simply supported porous FCF SFGSP ( $b/h = 50$ ,  $n = 2.0$ ) with cutout ( $d/b = 0.6$ ) subjected to NL-5 are studied, and outcomes are depicted in Fig. 5.8. It is perceived that V1-D porosity distribution exhibits higher  $\bar{\omega}$  followed by Log O-D, O-D, and U-D.

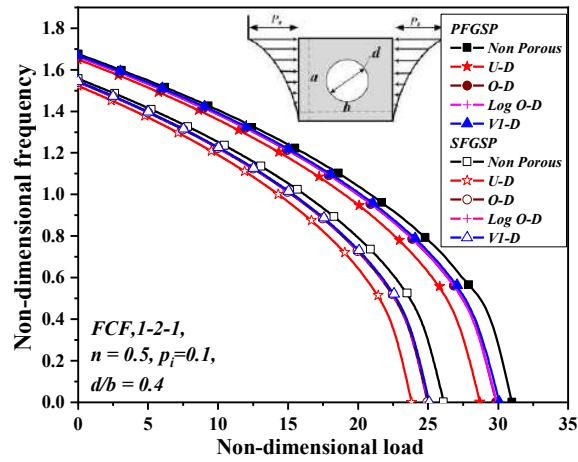


Fig. 5.7 Variation of  $\bar{\omega}$  for square porous FCF PFGSP and SFGSP with cutout for different porosity distributions

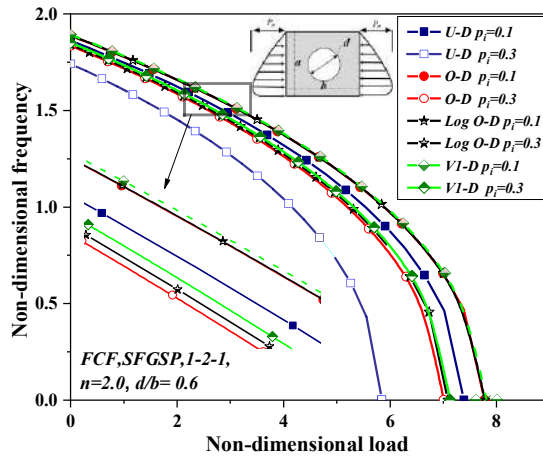


Fig. 5.8 Variation of  $\bar{\omega}$  for square porous FCF SFGSP with cutout for different porosity distributions and porosity indices

Subsequently, it can be observed that plates with PT-1 are more sensitive, while V1-D is least affected by the change in porosity indices in terms of  $\bar{\omega}$  regardless of the load. Thus, it can be decided that the porosity distribution plays a significant role in the free vibration response of FGSPs with cutouts.

The influence of different  $n$  on the variation of  $\bar{\omega}$  is studied for square simply supported porous FCF SFGSP ( $b/h = 50$ ) with cutout ratios ( $d/b = 0.2$  and  $0.6$ ), and outcomes are exemplified in Fig. 5.9. The porosity distribution U-D and  $p_i = 0.2$  is chosen. The plate is acted upon by NL- 3. It is clearly perceived that at any non-dimensional load, the  $\bar{\omega}$  decreases with an increase in the volume fraction exponent due to the increase in the metal content in the FGSPs, which in turn results in the decrease of the stiffness of the

plate irrespective of the cutout ratios. Also, the decrease in  $\bar{\omega}$  due to an increase in the  $n$  is not substantial at higher volume fraction exponents.

### 5.3.2.2 Effect of different cases of NIELs and cutout ratios on buckling characteristics of porous FGSPs

The influence of linearly and nonlinearly varying NIELs on the buckling characteristics of square simply supported porous FCF PFGSP ( $b/h = 100$ ) with cutouts have been examined in this section, and the outcomes are illustrated in Figs. 5.10(a) and (b), respectively, by considering different cutouts ratios. In this study, FCF PFGSP with U-D, porosity index,  $p_i = 0.2$ , and volume fraction exponent,  $n = 1.0$ , is considered. It is seen from Fig. 5.10(a) that the  $\bar{P}_{cr}$  decreases with the increase in  $d/b$ , irrespective of linearly varying edge load cases except for the case LL-5 (i.e., pure bending case), wherein a slight increase in  $\bar{P}_{cr}$  is detected for higher cutout ratios. It is also noticed that the  $\bar{P}_{cr}$  is observed to be maximum for LL-5 (i.e., pure bending case) and minimum for LL-1 (uniform load case). It is to be noted that among various linearly varying loads, LL-4 & LL-5 provide higher buckling resistance for all the cutout ratios.

The reason for such behaviour is the presence of both tensile and compressive loads that act at the same edges of the plate. Thus, high-intensity stresses are developed at the top and bottom regions of the plate, as observed in in-plane stress distribution plots, as shown in Fig. 5.11. The in-plane stress contours in Fig. 5.11 are obtained through ABAQUS (Version 2021) FEM software package.

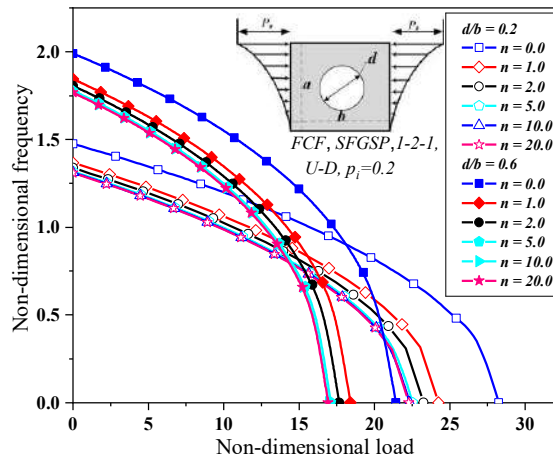


Fig. 5.9 Variation of  $\bar{\omega}$  for square porous FCF SFGSP with cutout for different cutout ratios and volume fraction exponent

The increase in buckling resistance of the plate in the case of such loading is due to the phenomena of stress diffusion, where the stresses try to move towards the stiffer region of the plate, i.e., towards edges of the plate or away from the less stiff region of the plate (i.e., the region surrounding the cutouts). Similar behaviour can also be observed in the case of a plate subjected to load cases LL-7, as high stress is formed at the top and bottom edges of the plate, as noticed in Fig. 5.11. Further, for load cases LL-1, 2, 3, and 6, high stresses are formed at the vicinity of the cutouts, which is the lesser stiffness zone in the plate; therefore, the buckling resistance of the plate is relatively less. Further, consistent with the discussion from the previous paragraph, FCF PFGSP subjected to NL-4 with a combination of tensile and compressive loads on the plate edges shows higher buckling resistance amongst various nonlinearly varying loads regardless of the cutout ratios, as observed in Fig. 5.10(b). The In-plane stress distribution for NL-4 shows the formation of high stress at the top edges of the plate, clearly due to the loading profile, and stress diffusion leads to the increase in the buckling resistance of the plate.

Furthermore, plates subjected to load case NL-3 offer higher buckling resistance as high stresses are formed at the top edge of the plates. While for the rest of the nonlinearly varying edge load cases, the buckling resistance of the plate is seen to be relatively less as the high stresses are formed in the vicinity of the cutouts, which is the less stiff region in the plate, as shown in Fig. 5.11.

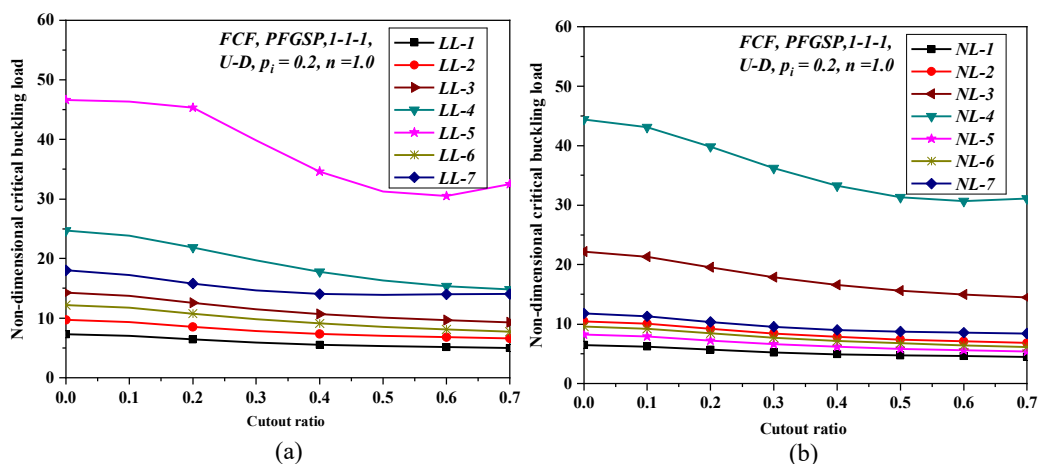


Fig. 5.10 Effect of different cases of NIELs and cutout ratio on  $\bar{P}_{Cr}$  of FCF PFGSP subjected to (a) Linearly varying loads, (b) Nonlinearly varying loads

Therefore, the different types of NIELs significantly affect the buckling characteristics of porous FGSPs with varying cutout ratios and must be considered during the analytical and experimental investigation phases to simulate most of the possible loading cases occurring during the practical conditions to know the plate behaviour. Previously the study was carried out considering constant porosity distributions and porosity indices. In order to understand the buckling behaviour of plates acted upon by NIELs due to the variation in porosity, the current investigation is carried out.

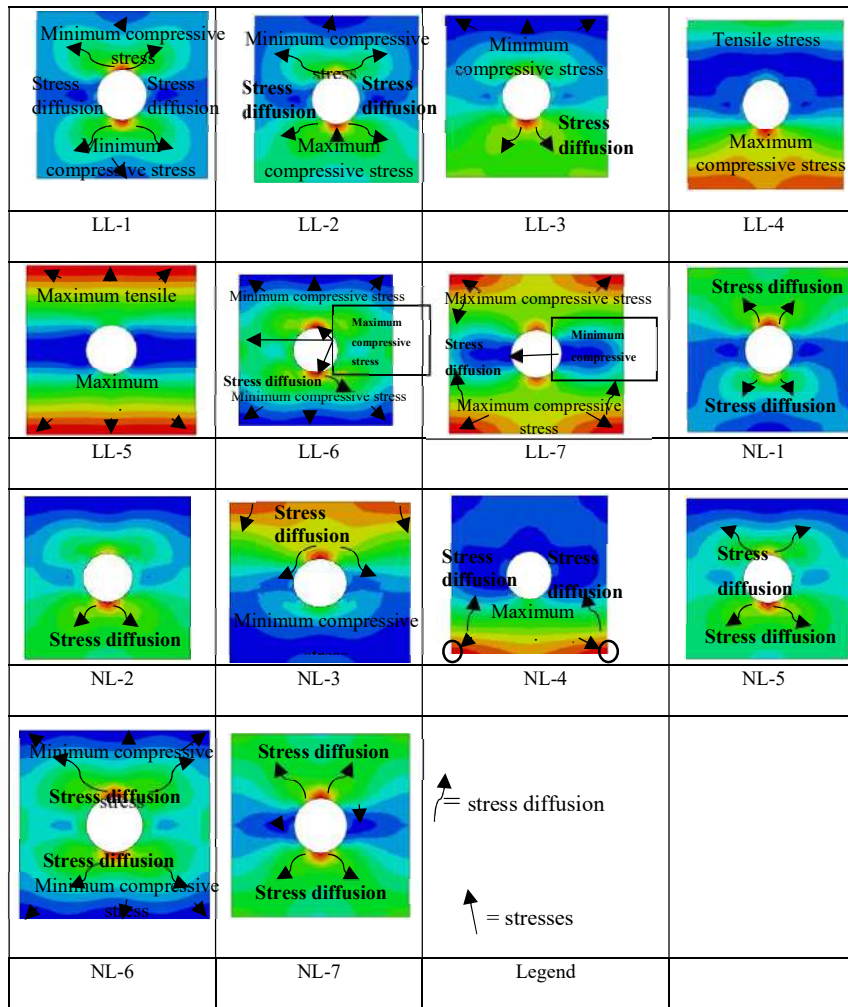


Fig. 5.11 In-plane stress contours for FCF PFGSP subjected to uniaxial linearly and nonlinearly varying in-plane edge loads

In this study, linearly varying loads LL-4, LL-5, LL-7 and NL-3, NL-4, NL-7 are considered as these loads provide the highest critical buckling loads among the several cases of nonuniform loads and cutout ratios considered, as noticed from Fig. 5.10. Also,

the behaviour of plates under such loads is noticeably different as compared to other cases of loads. For this study square simply supported FCF PFGSP ( $b/h = 20$ ,  $d/b = 0.5$ ,  $n = 0.5$ ) with four types of porosity distributions and porosity indices varying from 0.0 to 0.4 are chosen. The critical buckling load outcomes are presented in Figs. 5.12(a) and (b) for PFGSP with cutouts subjected to linearly varying and nonlinearly varying nonuniform loads, respectively. As seen, the non-dimensional buckling load reduces as the porosity indices increase due to the reduction in the plate's stiffness caused by the removal of materials due to the occurrence of the pores. Similar results can be observed for plates subjected to different cases of NIELs and porosity distribution types. It is worth mentioning that plates acted upon by LL-5 and NL-4 show a significant reduction in buckling resistance with an increase in the porosity indices as compared to other cases of nonuniform loads. This behaviour may be attributed to a significant decline in the stiffness of the plate under both the compressive and tensile nature of loading on the plate edge as the porosity indices increase. Thus, porosity plays a significant role in the buckling response of plates acted upon by different cases of NIELs.

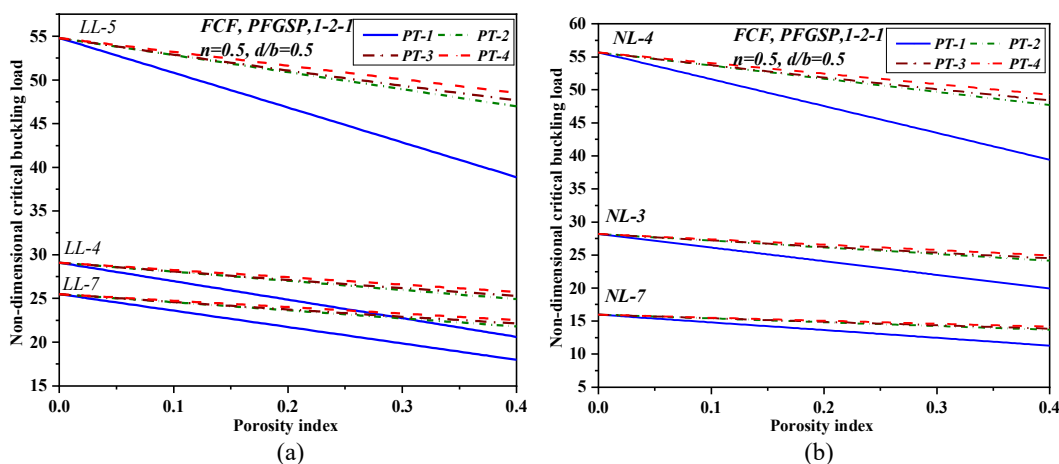


Fig. 5.12 Effect of porosity on  $\bar{P}_{cr}$  of FCF PFGSP subjected to (a) Linearly varying loads (b) Nonlinearly varying loads

### 5.3.2.3 Effect of material idealization technique on buckling characteristics of porous FGSPs with cutouts

Figs. 5.13(a) and (b) exhibit plots of  $\bar{P}_{cr}$  variation with volume fraction exponent for power law and sigmoid function based square simply supported FCF and MFC FGSPs ( $b/h = 100$ ) with cutouts, respectively. The plate consists of cutouts with  $d/b = 0.2$ , and the plate is considered to be acted upon by nonlinearly varying in-plane edge load case

NL-6. The  $p_i$  is chosen as 0.2, and the sandwich layer scheme considered is 1-1-1. As mentioned in section 5.2, four types of porosity distributions are considered for the investigation. It can be noticed that the material idealization technique has a substantial impact on the buckling characteristics of the two different configurations of FGSPs. In Fig. 5.13(a) and (b), it can be detected that an increase in  $n$  results in a decrease of  $\bar{P}_{cr}$  values regardless of the porosity distribution model and material idealization technique. However, for FCF sandwich configuration, it can be noticed from Fig. 5.13(a) that there is a rapid decrease in the  $\bar{P}_{cr}$  with an increase in the  $n$  from 0 to 2, and thereafter the variation is found to be gradual in the case of FCF PFGSP, while in the case of FCF SFGSP, the reduction is observed to be gradual from  $n = 0.0$  to 2.0 and thereafter the reduction is found to be minimal as compared to that of FCF PFGSP.

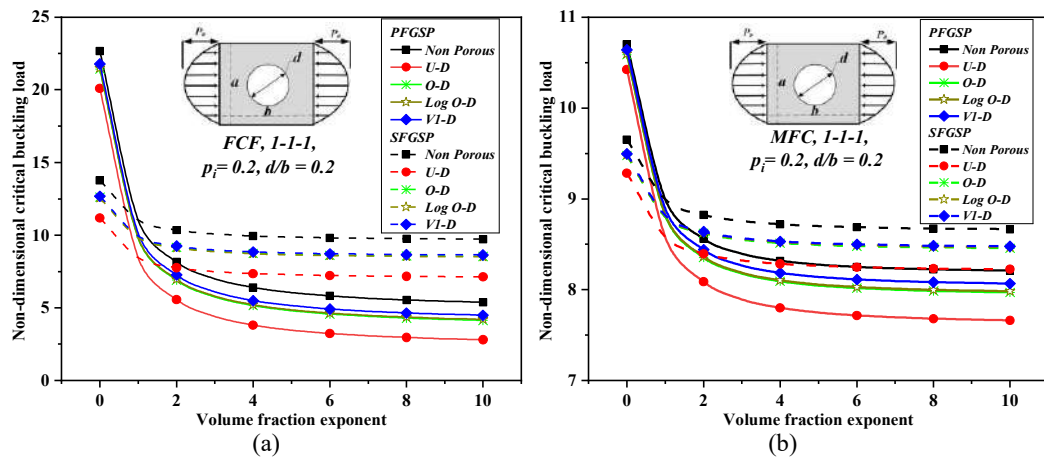


Fig. 5.13 Effect of type of material idealization technique on  $\bar{P}_{cr}$  of PFGSP and SFGSP (a) FCF (b) MFC with cutouts subjected to load NL-6

Also, the  $\bar{P}_{cr}$  of FCF PFGSP reduced by 86.08 % due to a reduction in  $n$  from 0.0 to 10.0, whereas it is 36.18 % for FCF SFGSP with U-D porosity and subjected to nonuniform loading conditions. Further, a similar trend in variation of  $\bar{P}_{cr}$  with respect to the increase in volume fraction exponent is observed for MFC PFGSP and MFC SFGSP with the cutouts, as demonstrated in Fig. 5.13(b). Here, the reduction in  $\bar{P}_{cr}$  with an increase in the  $n$  is perceived to be 26.49% and 11.

38% for MFC PFGSP and MFC SFGSP, respectively. Therefore, it can be noted that SFGSP behaves better by exhibiting a smaller percentage of decrease in buckling

resistance with the increase in  $n$ , irrespective of the type of sandwich configuration and porosity distribution models.

#### 5.3.2.4 Effect of porosity distribution on buckling characteristics of porous FGSPs with cutouts

Table 5.7 depicts the effect of porosity distribution models on  $\bar{P}_{cr}$  of square simply supported porous FCF SFGSP ( $b/h = 100$ ) with various volume fraction exponent, sandwich layer schemes, and cutout ratios. The plate is considered to be subjected to NL-2 case loading conditions. The  $p_i$  is restricted to 0.3, as the effective Young's modulus across the thickness of FCF SFGSP becomes negative for porosity distribution model U-D and O-D when  $p_i = 0.4$  and  $n = 5.0$ . In support of this, the variation of effective Young's modulus for different porosity indices of FCF SFGSP along with different volume fraction exponent, is plotted in Fig. 5.14. It is interesting to notice from Fig. 5.14 that the effective Young's modulus becomes negative for U-D and O-D, while for other porosity distributions, the effective Young's modulus remains positive. Hence, this can be labelled as the limiting criteria of U-D and O-D porosity distribution models. Table 5.7 implies that the porosity distribution models significantly affect the buckling characteristics of FGSPs with different cutout ratios and sandwich layer schemes. It is distinctly clear from this study that the  $\bar{P}_{cr}$  declines with an increase in the porosity index regardless of the porosity distribution model. It can be seen from Table 5.7 that sandwich plates with porosity distribution V1-D offer the highest buckling strength amongst all other porosity distribution models, and it is in the order of V1-D > Log O-D > O-D > U-D. It is noteworthy to mention that the reduction in  $\bar{P}_{cr}$  with porosity index is predominant in the case of U-D, whereas it is least in the case of V1-D regardless of the cutout ratio, sandwich layer scheme and volume fraction exponents. The reason for the increased buckling resistance of plates with V1-D can be attributed to the position of pore concentration, i.e., maximum porosity is concentrated close to either side of the neutral axis of the plate where the in-plane stresses are relatively low. However, for plates with U-D, pores are concentrated away from the neutral axis and show a noticeable change in the reduction of buckling strength of the plate with an increase in porosity indices. It can also be noticed that the difference in  $\bar{P}_{cr}$  of plates with Log O-D and O-D porosity distribution is small. It can also be

Table 5.7 Effect of porosity distribution on  $\bar{P}_{cr}$  for FCF SFGSP with cutouts subjected to nonlinearly varying in-plane edge load for various volume fraction exponent and sandwich layer schemes.

$d/b$	$n$	Sandwich Layer scheme	Non-Porous $p_i = 0.0$	U-D			O-D			Log O-D			VI-D		
				$p_i = 0.10$	$p_i = 0.30$	$p_i = 0.10$	$p_i = 0.10$	$p_i = 0.30$	$p_i = 0.10$	$p_i = 0.30$	$p_i = 0.10$	$p_i = 0.30$	$p_i = 0.10$	$p_i = 0.30$	
0.4	0.5	1-1-1	10.995	09.796	07.398	10.402	09.214	10.416	09.336	10.488	09.473				
		1-2-1	12.403	011.314	09.135	11.861	10.777	11.874	10.888	11.917	10.944				
		2-1-1	10.758	09.546	07.093	10.164	08.970	10.178	09.093	10.268	09.284				
		2-2-1	11.718	10.566	08.233	11.149	10.004	11.163	10.121	11.227	10.242				
	1.0	1-1-1	10.233	09.034	06.636	09.640	08.452	9.654	08.574	09.726	08.711				
		1-2-1	11.921	10.832	08.653	11.379	10.294	11.392	10.405	11.435	10.462				
		2-1-1	09.808	08.587	06.108	09.209	08.005	09.224	08.129	09.315	08.324				
		2-2-1	11.022	09.864	07.517	10.449	09.298	10.463	09.416	10.529	09.538				
	2.0	1-1-1	09.598	08.399	06.001	09.004	07.817	09.019	07.938	09.091	08.076				
		1-2-1	11.519	10.430	08.251	10.977	09.893	10.990	10.004	11.033	10.060				
		2-1-1	09.009	07.778	05.278	08.406	07.191	08.420	07.316	08.512	07.514				
		2-2-1	10.438	09.275	06.916	09.864	08.707	09.877	08.826	09.943	08.948				
0.6	0.5	1-1-1	09.145	07.945	05.547	08.551	07.363	08.565	07.485	08.637	07.622				
		1-2-1	11.232	10.143	07.964	10.690	09.605	10.703	09.716	10.746	09.773				
		2-1-1	08.433	07.196	04.679	07.827	06.605	07.841	06.731	07.934	06.930				
		2-2-1	10.020	08.853	06.485	09.443	08.282	09.457	08.402	09.523	08.524				
	1.0	1-1-1	09.962	08.877	06.707	09.425	08.350	09.438	08.460	09.503	08.584				
		1-2-1	11.236	10.251	08.280	10.746	09.765	10.758	09.865	10.796	09.917				
		2-1-1	09.746	08.649	06.429	09.208	08.128	09.221	08.239	09.302	08.412				
		2-2-1	10.616	09.573	07.463	10.101	09.065	10.113	09.171	10.172	09.280				
	2.0	1-1-1	09.273	08.188	06.018	08.736	07.661	08.749	07.771	08.814	07.896				
		1-2-1	10.801	09.815	07.844	10.310	09.329	10.322	09.430	10.361	09.481				
		2-1-1	08.888	07.782	05.539	08.346	07.256	08.359	07.368	08.441	07.544				
		2-2-1	09.987	08.939	06.815	09.469	08.427	09.481	08.534	09.540	08.644				
5.0	1-1-1	08.699	07.614	05.443	08.162	07.087	08.175	07.197	08.240	07.322					
	1-2-1	10.438	09.452	07.481	09.947	08.966	09.959	09.067	09.998	09.118					
	2-1-1	08.165	07.052	04.788	07.620	06.520	07.633	06.633	07.716	06.812					
	2-2-1	09.459	08.407	06.272	08.939	07.893	08.952	08.000	09.011	08.110					
5.0	1-1-1	08.289	07.204	05.033	07.752	06.677	07.765	06.787	07.830	06.911					
	1-2-1	10.178	09.193	07.221	09.688	08.707	09.700	08.807	09.738	08.858					
	2-1-1	07.645	06.525	04.246	07.096	05.990	07.109	06.104	07.193	06.284					
	2-2-1	09.081	08.025	05.883	08.560	07.509	08.572	07.617	08.632	07.728					

observed that the percentage decrease in  $\bar{P}_{cr}$  due to an increase in porosity indices rises with the increase in  $n$  regardless of porosity distribution, cutout ratio, and sandwich layer scheme.

### 5.3.2.5 Effect of different sandwich layer schemes on buckling characteristics of porous FGSPs with cutouts

The effect of the sandwich layer scheme on the  $\bar{P}_{cr}$  of square simply supported FCF, and MFC PFGSP ( $b/h = 100$ ) with cutouts has been analyzed in this section, and the outcomes are illustrated in Fig. 5.15(a) and (b), respectively, by selecting various porosity indices. Here,  $n = 2.0$  is chosen. The plate consists of a cutout with  $d/b = 0.2$  and is subjected to NL-5. The porosity distribution model U-D and O-D are considered for the present investigation. The porosity indices are varied from 0.0 to 0.4. It is perceived from Fig. 5.15 that the  $\bar{P}_{cr}$  for the plate with O-D is higher than U-D porosity, irrespective of the sandwich layer scheme, type of sandwich configuration, and porosity indices.

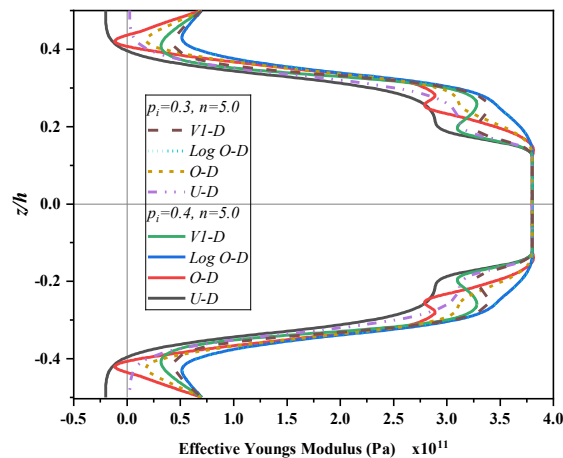


Fig. 5.14 Effective Young's modulus versus dimensionless thickness of FCF SFGSP with different porosity distribution model.

As discussed in an earlier section, it is perceived here that the  $\bar{P}_{cr}$  decreases with the increase in porosity indices. It is noticed from Fig. 5.15(a) that FCF PFGSP with a 1-2-1 layer scheme possesses maximum buckling strength amongst all other sandwich layer schemes in the order of  $1-2-1 > 2-2-1 > 1-1-1 > 2-1-1 > 2-1-2 > 1-0-1$  regardless of porosity distribution model and porosity indices. The highest buckling resistance in the case of a 1-2-1 sandwich layer scheme is due to the higher thickness of the core

sheet in comparison to the thickness of the face sheet, wherein the core sheet is made of ceramic material having a larger Young's modulus, which contributes to the rise in the stiffness. As the thickness of the core sheet in the sandwich plate decreases, the buckling resistance also decreases and is found to be the minimum for a 1-0-1 sandwich layer scheme, where the core sheet is absent. Further, it can be noticed from Fig. 5.15 (b) that the MFC FGSPs with a 1-2-1 layer scheme are more sensitive, and 2-1-1 is less sensitive to variation in the porosity indices. The reason behind such behaviour may be due to the higher thickness of the FG core sheet, which consists of porosity defects in comparison with the thickness of nonporous homogenous face sheets.

### 5.3.2.6 Effect of support conditions and side-to-thickness ratio on buckling characteristics of porous FGSPs with cutouts

The effect of support conditions and  $b/h$  ratio on the  $\bar{P}_{cr}$  of square FCF and MFC SFGSP with cutouts has been investigated, and the outcomes are tabulated in Table 5.8. Four combinations of support conditions are considered (SSSS, CCCC, SSCC, CCFF). The  $\bar{P}_{cr}$  is evaluated for the plate with  $d/b = 0.4$  and  $0.7$ ,  $n = 0.5$ . Also, the plate with a 1-2-1-layer scheme is considered to be subjected to NL-4 case. The porosity distribution model U-D, O-D, Log O-D, and V1-D are chosen with two porosity indices ( $p_i = 0.1$  and  $0.3$ ) for the investigation. It is noticed from Table 5.8 that SFGSP with CCCC support condition possesses the largest  $\bar{P}_{cr}$  as expected amid all the other support conditions considered in the order of  $CCCC > SSCC > SSSS > CCFF$  for all the types

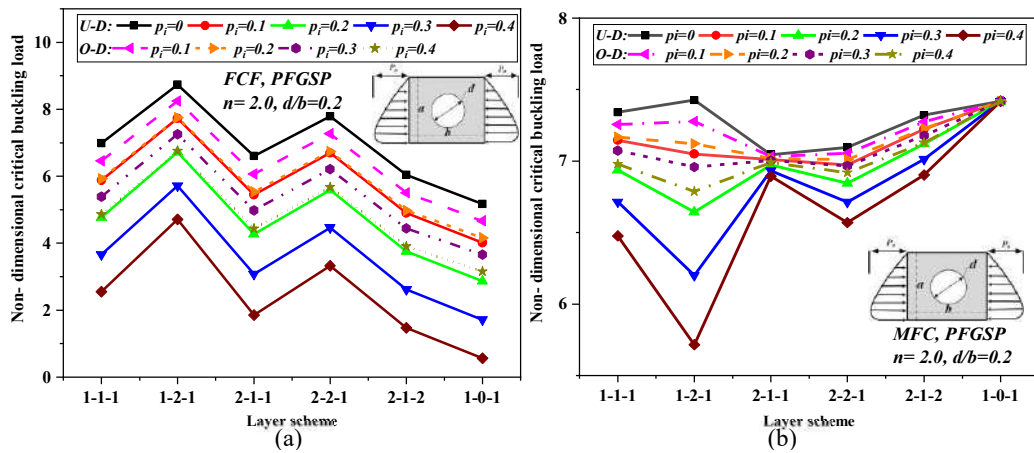


Fig. 5.15 Effect of sandwich layer scheme on  $\bar{P}_{cr}$  for (a) FCF (b) MFC PFGSP with cutout subjected to load NL-5.

Table 5.8 Effect of support conditions and  $b/h$  on  $\bar{P}_{cr}$  of porous FCF and MFC SFGSP with cutouts.

$d/b$	Support Condition	$b/h$	Sandwich Configurations											
			FCF				MFC							
			U-D	$p_i=0.1$	$p_i=0.3$	$p_i=0.1$	V1-D	U-D	$p_i=0.1$	$p_i=0.3$	$p_i=0.1$	O-D	$p_i=0.1$	$p_i=0.3$
0.4	SSSS	100	47.982	38.753	50.299	45.706	50.536	46.416	43.045	39.497	43.915	42.341	44.057	42.767
		50	47.624	38.479	49.919	45.369	50.153	46.071	42.584	39.064	43.447	41.884	43.587	42.304
		20	46.086	37.320	48.282	43.926	48.504	44.594	40.567	37.159	41.402	39.882	41.532	40.271
		10	41.981	34.221	43.916	40.074	44.107	40.651	35.390	32.248	36.159	34.741	36.264	35.053
	CCCC	100	108.214	87.620	113.382	103.136	113.905	104.708	95.301	87.404	97.238	93.725	97.547	94.653
		50	104.844	84.899	109.844	99.929	110.350	101.449	92.169	84.503	94.048	90.636	94.347	91.531
		20	94.435	77.053	98.768	90.165	99.194	91.453	81.905	74.845	83.636	80.460	83.883	81.199
		10	72.219	60.042	75.217	69.247	75.488	70.079	60.188	54.473	61.588	58.954	61.735	59.387
	SSCC	100	102.994	83.325	107.930	98.144	108.431	99.649	84.079	77.134	85.782	82.698	86.058	83.526
		50	100.399	81.271	105.195	95.685	105.681	97.145	82.373	75.545	84.048	81.012	84.316	81.818
		20	91.268	74.431	95.467	87.130	95.880	88.381	75.524	69.089	77.102	74.217	77.335	74.914
		10	71.115	59.069	74.083	68.174	74.353	69.001	58.776	53.242	60.129	57.587	60.276	58.017
CCFF	100	19.855	16.036	20.814	18.913	20.912	19.207	15.330	14.067	15.639	15.079	15.690	15.231	
	50	19.711	15.926	20.661	18.777	20.757	19.068	15.208	13.953	15.516	14.958	15.566	15.109	
	20	19.069	15.446	19.976	18.176	20.068	18.452	14.653	13.429	14.953	14.408	15.001	14.550	
	10	17.382	14.178	18.181	16.595	18.259	16.832	13.201	12.060	13.481	12.968	13.521	13.087	

Table 5.8 (Continued)

$d/b$	Support Condition	$b/h$	Sandwich Configurations											
			FCF				MFC				VI-D			
			U-D	O-D	$p_i = 0.1$	$p_i = 0.3$	U-D	O-D	$p_i = 0.1$	$p_i = 0.3$	U-D	O-D	$p_i = 0.1$	$p_i = 0.3$
			$p_i = 0.1$	$p_i = 0.3$	$p_i = 0.1$	$p_i = 0.3$	$p_i = 0.1$	$p_i = 0.3$	$p_i = 0.1$	$p_i = 0.3$	$p_i = 0.1$	$p_i = 0.3$	$p_i = 0.1$	$p_i = 0.3$
		100	41.989	33.953	44.005	40.008	44.210	40.623	32.610	29.914	33.271	32.073	33.378	32.394
	SSSS	50	40.919	33.127	42.872	38.999	43.070	39.593	31.727	29.089	32.374	31.200	32.477	31.509
		20	36.999	30.153	38.708	35.316	38.877	35.826	28.356	25.906	28.957	27.856	29.043	28.115
		10	28.534	23.653	29.737	27.342	29.847	27.680	20.318	18.194	20.838	19.844	20.881	19.965
	CCCC	100	95.405	78.031	99.756	91.124	100.182	92.407	73.712	67.473	75.245	72.438	75.466	73.103
		50	84.765	69.104	88.682	80.910	89.069	82.077	65.396	59.850	66.757	64.269	66.958	64.870
		20	65.563	54.144	68.389	62.768	68.653	63.574	49.450	44.946	50.553	48.499	50.688	48.899
0.7		10	32.670	30.146	33.301	32.039	33.301	32.039	23.691	21.141	24.327	23.056	24.329	23.062
	SSCC	100	94.252	77.034	98.564	90.010	98.988	91.285	72.845	66.688	74.357	71.589	74.577	72.250
		50	84.136	68.573	88.029	80.305	88.414	81.466	64.924	59.422	66.274	63.807	66.474	64.405
		20	65.338	53.948	68.157	62.550	68.421	63.354	49.297	44.812	50.396	48.351	50.531	48.750
		10	32.670	30.146	33.301	32.039	33.301	32.039	23.688	21.138	24.325	23.054	24.327	23.060
	CCFF	100	13.191	10.655	13.828	12.566	13.893	12.761	10.252	9.407	10.460	10.085	10.493	10.186
		50	13.085	10.573	13.715	12.466	13.780	12.659	10.165	9.325	10.370	9.998	10.404	10.098
		20	12.630	10.234	13.231	12.040	13.291	12.222	9.777	8.960	9.978	9.613	10.009	9.708
		10	11.450	9.346	11.974	10.933	12.026	11.089	8.772	8.013	8.958	8.617	8.985	8.696

of porosity distribution models and cutout ratios considered. This behaviour of CCCC plates can be attributed to the increase in the degree of the edge restraints. The  $\bar{P}_{cr}$  reduces with a decrease in the  $b/h$  of the plate, and this contrasting behaviour occurs due to the non-dimensional parameter considered, as mentioned in section 5.3. But in actual conditions an increase in plate thickness leads to an increase in flexural rigidity, which causes an increase in buckling resistance. Since the thickness parameter is in the denominator, as mentioned in section 5.3, it causes a reversal in response to  $\bar{P}_{cr}$  leading to a decrease in  $\bar{P}_{cr}$  with an increase in the thickness of the plate.

Further, it can be inferred from Table 5.8 that for both FCF and MFC SFGSP, the amount of reduction in the buckling resistance with the increase in the porosity indices is more evident in the case of plates with CCCC support conditions followed by SSCC, SSSS, and CCFF support condition for any porosity distribution model and cutout ratio. Furthermore, it is evident that the increase in the porosity indices from  $p_i = 0.1$  to  $p_i = 0.3$  leads to a reduction in buckling load, and this phenomenon is accentuated in the case of thinner plates than in thicker plates with cutouts. Lastly, the buckling resistance variation of plates with smaller cutout ratios is more sensitive to variation in porosity indices in comparison to plates featuring larger cutouts regardless of the porosity distribution model. Thus, porosity significantly influences plates with different support conditions and  $b/h$  ratios.

### *5.3.2.7 Effect of varying aspect ratio and cutout ratio on buckling characteristics of porous FGSPs*

In this segment, the coupled influence of varying aspect ratios and cutout ratios on  $\bar{P}_{cr}$  has been investigated by considering NL-7, and LL-6 loading cases and the consequences are portrayed in Figs. 5.16 (a) and (b), respectively. The simply supported porous FCF PFGSP ( $b/h = 100$ ) plate with a 1-1-1 layer scheme has been considered by keeping the width ( $b$ ) of the plate constant and varying the length ( $a$ ) of the plate. Here porosity distribution U-D with porosity indices  $p_i = 0.2$  and  $0.4$  and  $n = 0.5$  are selected. It can be noticed from Fig. 5.16(a) that the aspect ratio affects the  $\bar{P}_{cr}$  of FGSPs with cutouts significantly. It is witnessed that the buckling resistance of the plate decreases with an increase in  $d/b$  for plates with an aspect ratio  $a/b = 1.0$ , irrespective of porosity indices. However, the buckling behaviour of the plate changes with an

increase in the aspect ratio from  $a/b = 1.0$  to  $2.0$ , wherein the buckling resistance increases with an increase in  $d/b$ . This behaviour can also be witnessed in Fig. 5.16 (b), which shows the changes in  $\bar{P}_{cr}$  for porous FCF FGSPs with various aspect ratios and subjected to LL-6. The probable reason for such behaviour can also be explained by analysing the buckling mode shape pattern and in-plane stress distribution for various aspect ratios and cutout ratios of plates, as represented in Fig. 5.17. The decrease in the buckling strength of the plate with the rise in the  $d/b$  can be attributed to the increase in the magnitude of in-plane stress intensity as well as the distribution of high stresses around the locality of the cutouts, as seen in Fig. 5.17(a). Whereas, for plates with  $a/b = 2.0$ , the increase in the buckling strength with an increase in the  $d/b$ , as witnessed in Fig. 5.16, may be due to an increase in the number of buckling mode half waves as observed in Fig. 5.17(b). The In-plane stress distribution and buckling mode shapes, as in Fig. 5.17 were obtained through ABAQUS. Further, it can be noticed that  $\bar{P}_{cr}$  reduces with an increase in the porosity indices regardless of the  $a/b$  and  $d/b$ , but the amount of reduction in buckling strength can vary in plates with different aspect ratios. In addition, the buckling resistance for plates subjected to LL-6 is greater than for plates subjected to NL-7, as observed in Fig. 5.10.

#### *5.3.2.8 Effect of varying position of the cutouts and cutout ratio on buckling characteristics of porous FGSPs*

The present investigation is performed to analyze the influence of the position of the cutouts with varying cutout ratios ( $d/b$  ranging from  $0.1$  to  $0.7$ ) on the  $\bar{P}_{cr}$  of porous FCF PFGSP ( $b/h = 100$ ) with  $a/b = 1.0$  and  $a/b = 2.0$ , and the outcomes are shown in Figs. 5.18(a) and (b) respectively. For this study, the plate with porosity distribution U-D,  $p_i = 0.2$ , and  $n = 0.5$  are considered. The PFGSP is considered to be subjected to NL-5. The position of the cutout is represented as the ratio of the distance between the plate edge (loading edge) and the centre of the cutout ( $x_c$ ) to the length of the plate ( $a$ ), and the cutout position is varied in the  $x$ -direction along the line passing through the mid-width of the plate, keeping other parameters unchanged.

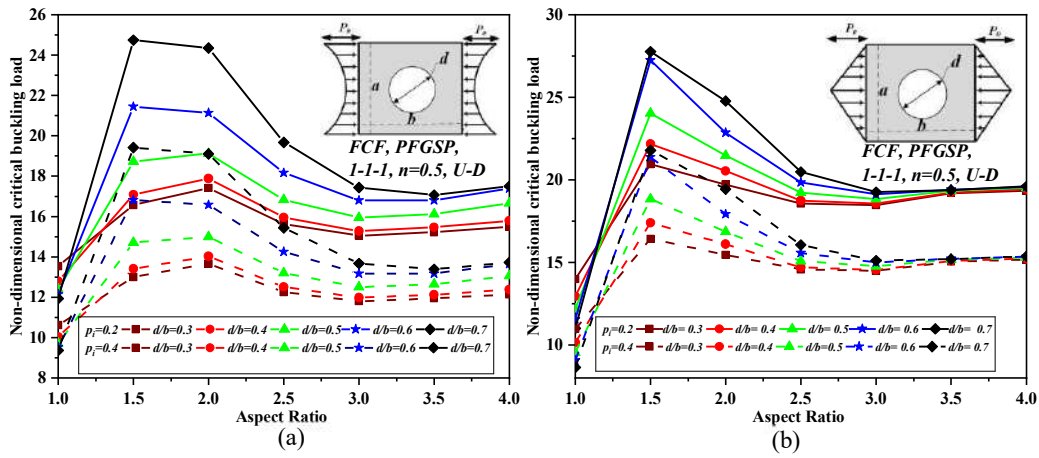


Fig. 5.16 Effect of  $a/b$  and  $d/b$  on  $\bar{P}_{Cr}$  of FCF PFGSP (1-1-1) subjected to (a) NL-7 (b) LL-6.

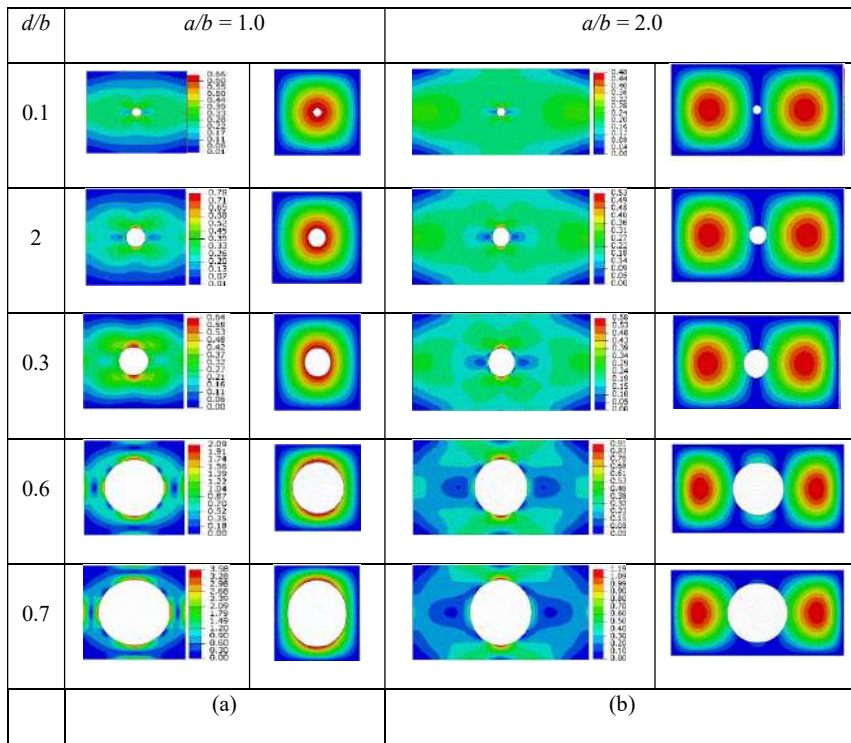


Fig. 5.17 In-plane stress distribution and buckling mode shapes for FCF PFGSP with various cutout ratios with (a)  $a/b = 1$  and (b)  $a/b = 2$  subjected to load NL-6

It is revealed from Fig. 5.18(a) that the  $\bar{P}_{Cr}$  for plates with  $a/b = 1.0$  increases as cutout moves towards the edge of the plate with  $d/b \leq 0.4$ , while for plates with  $d/b > 0.4$ ,  $\bar{P}_{Cr}$  decreases. The increase in  $\bar{P}_{Cr}$  as the cutout moves towards the edge of the plate may be due to the change in the position of cutouts towards the support region, wherein the

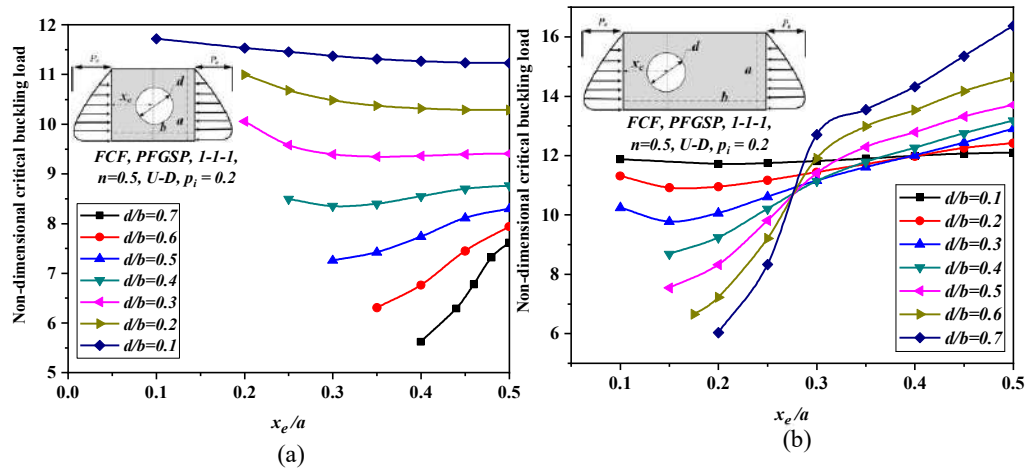


Fig. 5.18 Effect of position of cutout and cutout ratio on  $\bar{P}_{cr}$  of FCF PFGSP with (a)  $a/b = 1.0$   
(b)  $a/b = 2.0$

stiffness of the PFGSP is comparatively more than the middle region of the plate. Subsequently, it can be perceived from Fig. 5.18(b) that the  $\bar{P}_{cr}$  of porous FCF PFGSP with  $a/b = 2.0$  decreases as the position of the cutouts moves away from the centre of the plate for plates with  $d/b > 0.3$ . However, for the plate with  $d/b \leq 0.3$ , the  $\bar{P}_{cr}$  decreases initially as the cutouts move away from the centre up to  $x_e/a = 0.15$ , and then the  $\bar{P}_{cr}$  somewhat increases as the cutouts move towards the edge of the plate (decrease in  $x_e/a$ ). This behaviour can be described by studying the variation in the buckling mode shapes for plates with different cutout ratios and positions of the cutouts, as shown in Fig. 5.19. The In-plane stress distribution and buckling mode shapes, as in Fig. 5.19 were obtained through ABAQUS. It can be perceived from Fig. 5.19 that there is a decrease in the number of buckling mode half waves as the position of the cutouts is close to the edge of the plate, this may be the cause for a decrease in buckling resistance with a decrease in  $x_e/a$ . Further, it is noteworthy to mention that for plates having cutouts close to the centre of the plate, the buckling resistance of the plate increases with an increase in the  $d/b$ . This behaviour of the plate changes in an asymmetric manner as the cutout is positioned close to the edge of the plate. This may occur due to an increase in the number of buckling mode half-waves with the increase in the cutout ratio as the cutout is positioned close to the centre of the plate and vice-versa for plates with higher cutout ratios. The  $\bar{P}_{cr}$  for the plates with a smaller cutout

ratio is less affected by variation in the position of the cutout. Also, due to an increase in the porosity indices of the plate similar trend in the variation of  $\bar{P}_{cr}$  can be expected.

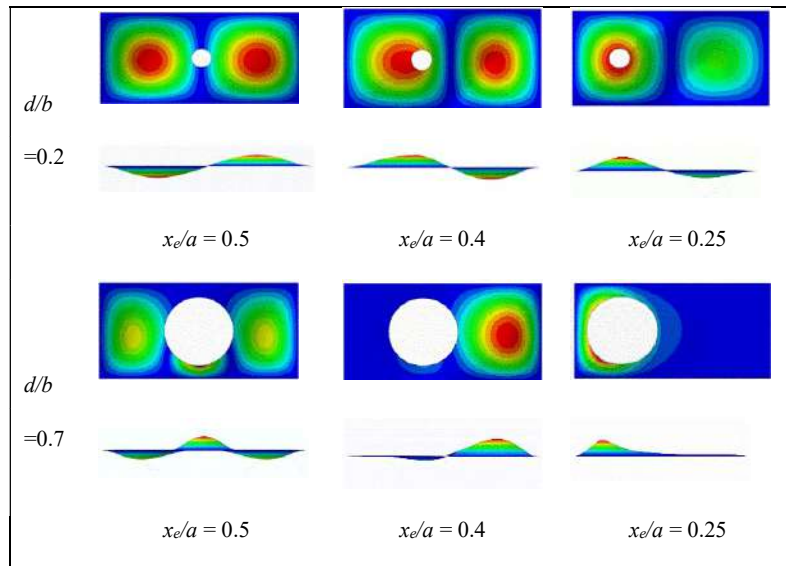


Fig. 5.19 Buckling mode shapes for FCF PFGSP of  $a/b = 2.0$  and subjected to load NL- 5

## 5.4 CLOSURE

This chapter investigates the vibration and buckling response of porous FGSP with cutout subjected to nonuniform loads using the FE method. The effective material properties of the FGSP are evaluated using power law and sigmoidal function-based homogenization technique. Four types of porosity distribution models are explored, and the porosity imperfections are modelled as the criteria of stiffness reduction. The current study incorporates two distinct kinds of sandwich configuration in such a way that there is no material mismatch along the thickness direction. The application of different cases of NIELs on the plate with cutouts leads to the development of nonuniform stresses. Hence a novel dynamic approach has been proposed to evaluate buckling loads by implementing two sets of boundary conditions. The results obtained from current FE formulations are compared with results arrived from analytical solutions and numerical methods available in the literature. After establishing the accuracy variety of parametric studies have been carried out. The subsequent chapter extensively investigates the vibration and buckling characteristics of porous FGSP with cutout under thermomechanical load.

## CHAPTER 6

### VIBRATION AND BUCKLING ANALYSIS OF POROUS FG SANDWICH PLATES WITH AND WITHOUT CUTOUT UNDER THERMO-MECHANICAL LOADS

#### 6.1 PRELIMINARY REMARKS

Thermal management plays a critical role in modern engineering applications, where efficient heat transfer and temperature control are essential for optimal performance, reliability, and longevity of components and systems. FGM composites offer unique advantages in addressing thermal management challenges by leveraging their inherent property gradients. In design life, along with thermal loads, the plates are under mechanical loads. Therefore, FGM needs to be modelled and investigated not only to the influence of mechanical but also thermal loads. Under combination of mechanical and thermal loads, the vibration and buckling behaviour of porous FGM plate with cutout is significantly affected. The complexity of the stress due to non-uniform in-plane mechanical edge loads will further increase due to the formation of porosity and cutouts, which significantly affects the vibration and buckling response of FGSPs in a thermal environment. Hence, this chapter attempts to analyze and discuss the vibration and buckling response of porous FGSP with cutout under thermomechanical loads. In order to do so, a mathematical formulation, as presented in Chapter 3, has been developed by taking Green-Lagrange type nonlinear strain, FSDT kinematics, and it is utilized to compute the response under thermomechanical loads.

Because the stress distribution within the plate element is significantly non-uniform, therefore a dynamic technique has been employed to solve the buckling problems, with two sets of boundary conditions applied, one for pre-buckling stresses and another for buckling load calculations. The effects of various geometrical and material parameters and the support conditions on the vibration and buckling response of porous FGSP with cutout under thermomechanical loads are extensively investigated. Finally, this chapter is summarised with the concluding remarks in Chapter 8. The FGM plate finds several applications in the thermal environment and is designed to perform efficiently in the thermal field.

## 6.2 PROBLEM DESCRIPTION

This section discusses in depth several examples of uniaxial in-plane load acting on the opposite edges of the FGSPs investigated in the current study. As depicted in Fig. 6.1, various cases of varying in-plane edge loads that can occur in reality are selected for this analysis. Here Load Case (LC), LC-1 is uniformly distributed across the full width of the plate and other cases are nonuniform in nature. The term  $P_0$  indicates the maximum intensity of loads per unit length. As seen in Fig. 6.1, the loading cases are expressed by a mathematical expression. The terms  $\eta$  represents  $y/b$  and  $P_y$  denotes the loading function for Nonuniform In-plane Edge Loads (NIELs) acting on the edges parallel to the y-axis of the plates. Further in this study, porosity distributions, as mentioned in Table 3.2 are considered.

The present study considers FCF and MFC sandwich configurations as illustrated in Fig. 3.1. The FCF and MFC FGSP are considered with U-D, X-D, O-D, V1-D, and V2-D porosity as discussed in Chapter 3 for the analysis of vibration and buckling behaviour of porous FGSP with/without cutout under thermo-mechanical loads. The accuracy of the solution obtained is evaluated by comparing the present results with those available in the literature. After verifying the accuracy of the formulation and solution, parametric studies have been carried out extensively.

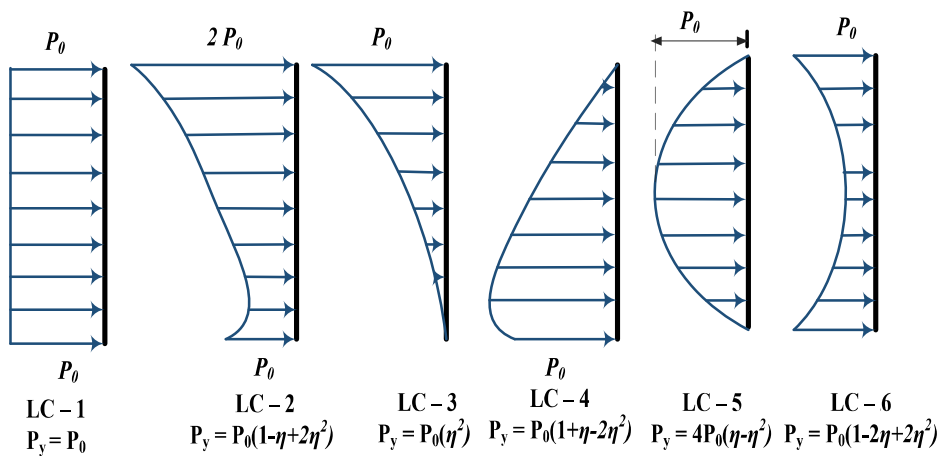


Fig. 6.1 Various cases of in-plane compressive edge load

### 6.3 RESULTS AND DISCUSSION

The vibration and buckling responses are obtained using developed mathematical formulation through an in-house MATLAB code that can extend for any general case. The convergence study of the FGSP under thermomechanical load is performed for various geometrical and material configurations. Consequently, a variety of examples is solved for validation purposes by comparing the present results with those available in published literature. After the exhaustive testing of the present formulation, an inclusive parametric study of FGSP under thermomechanical load is performed. Here, the vibration and buckling response of FGSPs is analyzed for various geometrical material parameters and support conditions. The temperature-dependent and independent material properties of constituent materials considered in the current study are mentioned in Table 6.1 and Table 6.2, respectively. Unless otherwise specified, plates made of Si<sub>3</sub>N<sub>4</sub>/SUS304 material are employed for convergence and parametric studies. Figs. 6.2(a) and (b) represents the variation of Young's modulus and thermal coefficient of expansion due to change in temperature. In continuation, the effects of different parameters on vibration and buckling response of porous FGSP with/without cutout under thermomechanical loads are performed and discussed. If not stated otherwise, critical buckling loads ( $\bar{P}_{cr}$ ) and natural frequencies ( $\omega$ ) are represented in non-dimensional form as

The non-dimensional critical buckling load is given as

$$\bar{P}_{cr} = P_{cr} a^2 / 100 E_0 h^3, E_0 = 1 \text{ GPa}$$

Table 6.1 Metal and ceramic material temperature-dependent physical properties (Reddy and Chin (1998))

Materials	Properties	$\bar{P}_0$	$\bar{P}_1$	$\bar{P}_2$	$\bar{P}_3$	$\bar{P}$ ( $T=300\text{K}$ )
Si <sub>3</sub> N <sub>4</sub>	E (Pa)	348.43×10 <sup>9</sup>	-3.07×10 <sup>-4</sup>	2.16×10 <sup>-7</sup>	-8.946×10 <sup>-11</sup>	322.271×10 <sup>9</sup>
	α (1/K)	5.872×10 <sup>-6</sup>	9.095×10 <sup>-4</sup>	0	0	7.4746×10 <sup>-6</sup>
	ρ (kg/m <sup>3</sup> )	2370	0	0	0	2370
SUS304	E (Pa)	201.04×10 <sup>9</sup>	3.079×10 <sup>-4</sup>	-6.534 ×10 <sup>-7</sup>	0	207.787×10 <sup>9</sup>
	α (1/K)	12.33×10 <sup>-6</sup>	8.086×10 <sup>-4</sup>	0	0	1.532×10 <sup>-5</sup>
	ρ (kg/m <sup>3</sup> )	8166	0	0	0	8166
ZrO <sub>2</sub>	E (Pa)	244.27×10 <sup>9</sup>	-1.371×10 <sup>-3</sup>	1.214×10 <sup>-6</sup>	-3.681×10 <sup>-10</sup>	168.063×10 <sup>9</sup>
	α (1/K)	12.766×10 <sup>-6</sup>	-1.491×10 <sup>-3</sup>	-1.006×10 <sup>-5</sup>	-6.778×10 <sup>-11</sup>	18.591×10 <sup>-6</sup>
	ρ (kg/m <sup>3</sup> )	3000	0	0	0	3000
Ti-Al <sub>6</sub> -4V	E (Pa)	122.56×10 <sup>9</sup>	-4.586 ×10 <sup>4</sup>	0	0	105.70 ×10 <sup>9</sup>
	α (1/K)	7.578 × 10 <sup>-6</sup>	6.638 ×10 <sup>-4</sup>	-3.147×10 <sup>-6</sup>	0	6.941 × 10 <sup>-6</sup>
	ρ (kg/m <sup>3</sup> )	4427	0	0	0	4427

Table 6.2 Temperature-independent material properties of metal and ceramic (Sah and Ghosh (2022b))

Materials	Properties			
	E (Pa)	$\alpha$ (1/K)	$\rho$ (kg/m <sup>3</sup> )	$\nu$
Aluminium (Al)	$70 \times 10^9$	$23 \times 10^{-6}$	2702	0.3
Alumina (Al <sub>2</sub> O <sub>3</sub> )	$380 \times 10^9$	$7.4 \times 10^{-6}$	3800	0.3
Titanium alloy (Ti-Al <sub>6</sub> -4V)	$66.20 \times 10^9$	$10.3 \times 10^{-6}$	4000	0.3
Zirconia (ZrO <sub>2</sub> )	$244.27 \times 10^9$	$12.766 \times 10^{-6}$	5700	0.3

The non-dimensional critical buckling temperature is given as

$$\bar{T}_{cr} = 10^{-3} \Delta T_{cr}$$

The non-dimensional natural frequencies are given as

$$\bar{\omega} = (\omega a^2 / h) \sqrt{\rho_0 / E_0}, E_0 = 1 \text{ GPa}, \rho_0 = 1 \text{ kg / m}^3$$

$$\tilde{\omega} = (\omega b^2 / \pi^2) \sqrt{h \rho / D_m}, D_m = E_m h^3 / (12(1 - \nu^2)), E_m (T_0 = 300K)$$

### 6.3.1 Convergence and Validation Studies

**Example 1:** The convergence study is essential for selecting the optimum mesh size to ensure the correct convergence of results while conducting a FE analysis. The mesh control parameters,  $n_x = n_y$ ,  $n_{xl} = n_{yl}$ ,  $n_h$  as indicated in Table 6.3, are explained well in Fig. 6.3. In this study simply supported square FCF PFGSP are considered to be made of Si<sub>3</sub>N<sub>4</sub>/SUS304 and the material properties are tabulated in Table 6.1. In this context, it can be inferred from the table that for  $d/b = 0.3$ , 184 elements give good convergence. While plates with  $d/b = 0.5$  require 196 elements. Lastly, circular cutout plates satisfy the convergence requirement. After achieving the convergence criteria, comparison studies were carried out to validate the vibration and buckling response of the porous FGSPs with cutout. To validate and check the effectiveness of the foregoing FE formulation, results arrived at are compared with results existing in the previously published literature, as mentioned in the examples below.

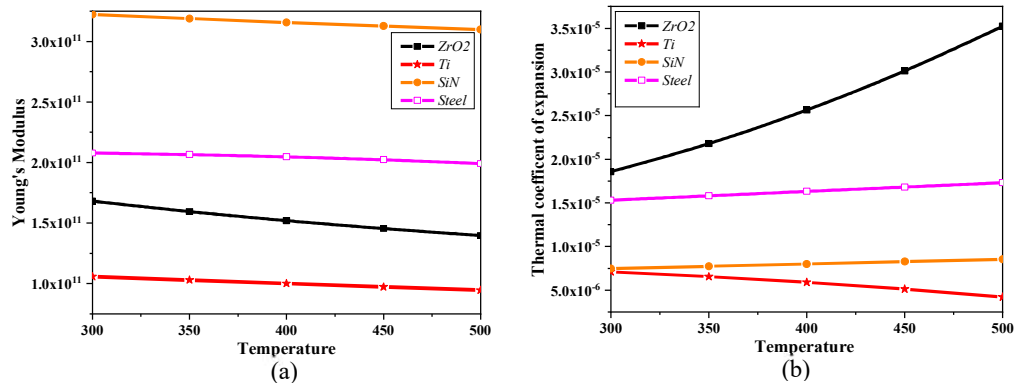


Fig. 6.2 Variation of temperature dependent properties (a) Young's Modulus (b) thermal coefficient of expansion with temperature

Table 6.3 Convergence of  $\bar{P}_{cr}$  for a square simply supported porous FCF PFGSP with a centrally situated circular cutouts under the actions of LC-1 and uniform temperature rise  $\Delta T = 100$  ( $b/h = 10$ , 1-1-1, U-D,  $p_i = 0.3$ )

Cutout ratio ( $d/b$ )	Mesh order			Number of elements	$\bar{P}_{cr}$		
	$n_x = n_y$	$n_{x1} = n_{x2}$	$n_h$		$n = 1$	$n = 2$	$n = 5$
0.3	2	2	24	112	4.1074	4.0221	3.9051
	2	3	24	136	4.1139	4.0144	3.9471
	2	4	24	160	4.1138	4.0143	3.9470
	2	5	24	184	4.1138	4.0142	3.9470
0.5	1	2	32	100	3.5341	3.4491	3.3921
	1	3	32	132	3.5339	3.4488	3.3919
	1	4	32	164	3.5337	3.4486	3.3917
	1	5	32	196	3.5336	3.4485	3.3916

**Example 2:** This instance is executed for the square and rectangular moderately thick ( $b/h = 10.0$ ) clamped supported  $\text{Si}_3\text{N}_4/\text{SUS304}$  FGM plate. The temperature-dependent material property of constituent material is mentioned in Table 6.1. In Table 6.4, five modes of natural frequencies are obtained considering  $n = 1.0, 2.0$ , and  $5.0$ . It is observed that the outcomes from the current formulation are in close conformity with the results of Li et al. (2009) as tabulated in Table 6.4. It can be seen that the natural frequency parameters decrease as the  $n$  increases.

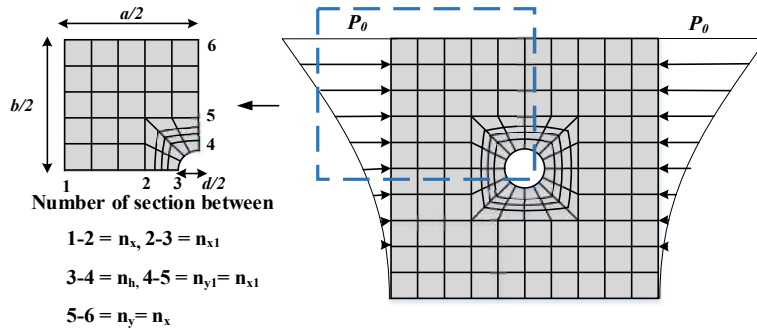


Fig. 6.3 Detailed Mesh pattern over full plate featuring a circular shaped cutout acted by NIELs

Table 6.4: Natural frequency parameters ( $\tilde{\omega}$ ) for CCCC rectangular  $\text{Si}_3\text{N}_4/\text{SUS304}$  FGM plates exposed to uniform temperature rise  $\Delta T = 300$  K

$a/b$	$n$	Source	Modes				
			$\omega_1$	$\omega_2$	$\omega_3$	$\omega_4$	$\omega_5$
1.0	1.0	Present	4.0983	8.0509	8.0509	11.4045	13.5231
		Li et al. (2009)	4.2110	8.2429	8.2429	11.6602	13.7916
	2.0	Present	3.6433	7.1690	7.1690	10.1593	12.0457
		Li et al. (2009)	3.7202	7.3010	7.3010	10.3348	12.2256
	5.0	Present	3.2780	6.4570	6.4570	9.1511	10.8469
		Li et al. (2009)	3.3267	6.5424	6.5424	9.2647	10.9594
0.5	1.0	Present	10.1537	12.7848	17.2301	22.1609	22.5669
		Li et al. (2009)	10.3932	13.0762	17.5982	22.4803	22.6024
	2.0	Present	9.0380	11.3824	15.3429	19.7071	19.9219
		Li et al. (2009)	9.2111	11.5890	15.5999	19.9043	20.0234
	5.0	Present	8.1337	10.2442	13.8074	17.7031	17.7466
		Li et al. (2009)	8.2568	10.3868	13.9819	17.8183	17.9309

**Example 3:** The existing outcomes are compared with experimental results that are available in the literature to determine whether the current FE formulation is acceptable in determining the fundamental frequencies of the plate with cutout. Here the experimental results for laminated plates are considered for comparison as there is a lack of experimental results pertaining to FGM plates with cutout. The frequencies of Carbon Fiber reinforced (CFR) laminated plates with cutout obtained using the developed FE formulation is compared with experimental results from Zang et al. (2021) ( $E_{11} = 150.0$ ,  $E_{22} = 9.0$  GPa,  $G_{12} = 5.12$  GPa,  $\nu_{12} = 0.24$ , density =  $1650 \text{ kg/m}^3$ ,

$[0/90^\circ]_{10}$ ,  $a = 0.160$  m,  $b = 0.08$  m,  $h = 0.004$  m, free on all sides) as shown in Fig. 6.4(a).

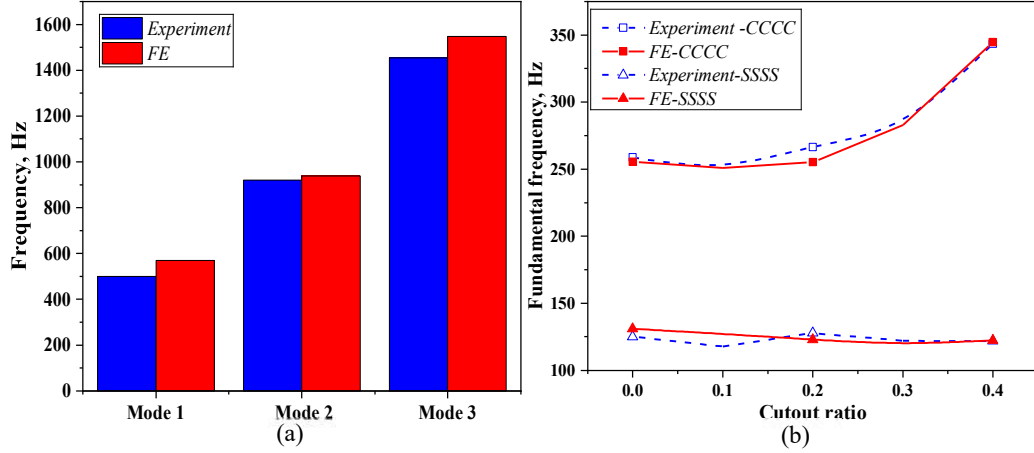


Fig. 6.4 Comparison of frequency of (a) CFR (b) GFR laminated composite plate with cutout

In addition, the frequencies obtained for varying cutout ratios from present formulations are compared with experimental results of Glass Fibre Reinforced (GFR) laminated composite plates from Sinha et al. (2021) ( $E_{11} = E_{22} = 16.07$  GPa,  $G_{12} = G_{13} = G_{23} = 2.814$  GPa,  $\nu_{12} = 0.25$ , density =  $1664$  kg/m<sup>3</sup>,  $[0/90^\circ]_{2s}$ ,  $a = b = 0.235$  m,  $h = 0.0028$  m) as illustrated in Fig. 6.4(b). The outcomes of the present FE formulation are in excellent accordance with the experiment data, as can be seen from Fig. 6.4.

**Example 4.** In this instance, the validation is executed for all sides simply supported square MFC PFGSP. The properties of the constituent materials (Ti-Al<sub>6</sub>-4V/ZrO<sub>2</sub>) incorporated here are mentioned in Table 6.2. The FGSP with  $n = 0.5$  is chosen. Table 3.1 provides details of the sandwich layer schemes evaluated in this scenario. To evaluate the efficacy of the current formulation for the thermal buckling problem, uniform temperature rise across the thickness is taken into account here. The  $\bar{T}_{cr} = 10^{-3} \Delta T_{cr}$  obtained from current FE formulations are presented along with analytical solutions given by Daikh and Megueni (2018). Table 6.5 reveals that the findings obtained for various thickness ratios and sandwich layer schemes are in satisfactory correlation.

**Example 5:** The accurateness of the existing FE formulation in obtaining  $\bar{P}_{cr}$  of the plate exposed to thermomechanical loads is presented in this example. Here FCF PFGSP ( $b/h = 10$ ,  $a/b = 1.0$ ) plates with all sides simply support having  $n = 0.5$  and  $2.0$

and several sandwich layer schemes are considered. The properties of the constituent materials (Ti-Al<sub>6</sub>-4V/ZrO<sub>2</sub>) incorporated in this instance are recorded in Table 6.2.

Table 6.5 Comparison of MFC PFGSP (Ti-Al<sub>6</sub>-4V/ZrO<sub>2</sub>) square simply supported FGSP of different sandwich layer schemes and thickness ratio.

Sandwich layer Schemes	Source	$b/h = 10$	$b/h = 15$	$b/h = 25$	$b/h = 50$
1-1-1	Present	0.7359	0.3373	0.1234	0.0310
	Daikh and Megueni (2018)	0.7468	0.3395	0.1237	0.0310
1-2-1	Present	0.7565	0.3469	0.127	0.0319
	Daikh and Megueni (2018)	0.7676	0.3492	0.1272	0.0319
2-2-1	Present	0.7892	0.3622	0.1326	0.0334
	Daikh and Megueni (2018)	0.8008	0.3646	0.1329	0.0334

In the analytical solutions presented by Li et al. (2021) 50% of the  $\bar{T}_{cr}$  increment is applied through uniform temperature rise to find out the nondimensional mechanical load ( $\bar{P}_{cr(T/2)}$ ). Table 6.6 presents a comparison of critical buckling load due to mechanical load  $\bar{P}_{cr(T=0)}$ , critical buckling temperature ( $\bar{T}_{cr}$ ) and critical buckling load due to thermomechanical loads  $\bar{P}_{cr(T/2)}$  of current and literature results. It is apparent that the outcomes from the existing FE formulations are in appreciable concord with results obtained through analytical solutions, as furnished in Table 6.6.

**Example 6:** The  $\bar{T}_{cr}$  for FCF porous PFGSP and SFGSP ( $a/b = 1.0$ ) resting on simply supports are evaluated and compared in Table 6.7 with a set of outcomes based on an analytical solution by Sah and Ghosh (2022b). In this example uniform porosity distribution (U-D) is considered with porosity index 0.1 and 0.2. The FGSP with  $n = 2.0$  is assumed. The properties of the constituent materials (Ti-Al<sub>6</sub>-4V/ZrO<sub>2</sub>) incorporated are mentioned in Table 6.2. The  $\bar{T}_{cr}$  obtained in the current study are in decent congruence with available results for various  $p_i$ , sandwich layer schemes, and FGSPs with two distinct material homogenization techniques.

**Example 7:** The present example is carried out to present the usefulness of the established FE formulation in calculating the  $\bar{T}_{cr}$  of FG plate with cutout. They are obtained for simply supported square FG plates with cutouts and are mentioned alongside those mentioned in the work of Yu et al. (2016) in Table 6.8. The constituent materials (Al/Al<sub>2</sub>O<sub>3</sub>) properties incorporated are mentioned in Table 6.2.

The computed  $\bar{T}_{cr}$  from the current FE formulation are consistent with those evaluated in Yu et al. 2016 as shown in Table 6.8.

Table 6.6 Comparison of  $\bar{P}_{cr(T=0)}$ ,  $\bar{T}_{cr}$  and  $\bar{P}_{cr(T/2)}$  of simply supported FCF PFGSP ( $a/b = 1.0$ ,  $b/h = 10.0$ ) (Ti-Al<sub>6</sub>-4V/ZrO<sub>2</sub>) of various sandwich layer schemes and  $n$ .

Sandwich layer scheme	$n$	Source	$\bar{P}_{cr(T=0)}$	$\bar{P}_{cr(T/2)}$	$\bar{T}_{cr}$
1-1-1	0.5	Present	2.8189	1.4089	0.7808
		Li et al. (2021)	2.8696	1.4348	0.7946
	2	Present	1.7956	0.8975	0.6298
		Li et al. (2021)	1.8321	0.9161	0.6424
1-2-1	0.5	Present	3.0408	1.5198	0.7959
		Li et al. (2021)	3.0933	1.5466	0.8093
	2	Present	2.1285	1.0440	0.6546
		Li et al. (2021)	2.1692	1.0846	0.6669
2-1-2	0.5	Present	2.6783	1.3386	0.7782
		Li et al. (2021)	2.7275	1.3638	0.7922
	2	Present	1.6134	0.8065	0.6375
		Li et al. (2021)	1.6474	0.8237	0.6508

### 6.3.2 Parametric studies

#### 6.3.2.1 Vibration characteristics of porous FGSPs with cutouts subjected to thermomechanical loads

The current study is carried out to understand the vibration characteristics of porous FGSP with cutouts exposed to thermomechanical loads. The plate is subjected to several types of NIELs. Initially, the impact of various cutout ratio on the  $\bar{\omega}$  of simply supported porous FCF SFGSP ( $a/b = 1$ ,  $b/h = 10$ ,  $n = 0.5$ ) exposed to LC -1 and  $\Delta T = 100$  is investigated, and the outcomes are depicted in Fig. 6.5. Fig. 6.5 shows that the increase in cutout ratio causes the  $\bar{\omega}$  of the FCF PFGSP subjected to LC-1 to increase. This trend is observed up to a certain intensity of non-dimensional in-plane loads, after which the response tends to reverse. The decrease in  $\bar{\omega}$  with an increase in the cutout ratio at the lower magnitude of in-plane edge load is due to the fact that the decrease in mass is more significant than the reduction of stiffness of the plate due to increase in the size of cutout. According to observation, the frequency of the plate with any cutout size drops as the non-dimensional load increases and eventually approaches zero at a specific non-dimensional load. Thus, the  $\bar{P}_{cr}$  of the plate is given by the non-dimensional load.

Table 6.7 Comparison of  $\bar{T}_c$  for porous FCF PFGSP and SFGSP simply supported square plate ( $b/h = 10.0, n = 2.0$ ) subjected to uniform temperature rise across the thickness.

$p_i$	Source	Material Idealization technique																			
		PFGSP						SFGSP													
		1-1-1	1-2-1	1-1-2	2-1-2	2-2-1	2-2-1	1-1-1	1-2-1	1-1-2	2-1-2	2-2-1	2-2-1								
	Present with NS	0.2877	0.2994	0.2985	0.2912	0.2970	0.3036	0.3214	0.2893	0.2959	0.3214	0.2877	0.2994	0.2985	0.2912	0.2970	0.3036	0.3214	0.2893	0.2959	0.3214
0	Present with MS	0.2877	0.2994	0.2990	0.2912	0.2974	0.3036	0.3214	0.3044	0.2959	0.3138	0.2877	0.2994	0.2990	0.2912	0.2974	0.3036	0.3214	0.3044	0.2959	0.3138
	Sah and Ghosh (2022b)	0.2928	0.3048	0.3038	0.2964	0.3024	0.3091	0.3275	0.3199	0.3053	0.3194	0.2928	0.3048	0.3038	0.2964	0.3024	0.3091	0.3275	0.3199	0.3053	0.3194
	Present with NS	0.2743	0.2857	0.2882	0.2819	0.2835	0.2974	0.3132	0.2853	0.2940	0.3168	0.2743	0.2857	0.2882	0.2819	0.2835	0.2974	0.3132	0.2853	0.2940	0.3168
0.1	Present with MS	0.2743	0.2857	0.2889	0.2819	0.2841	0.2974	0.3132	0.3018	0.2940	0.3073	0.2743	0.2857	0.2889	0.2819	0.2841	0.2974	0.3132	0.3018	0.2940	0.3073
	Sah and Ghosh (2022b)	0.2789	0.2907	0.2931	0.2867	0.2884	0.3026	0.3189	0.3066	0.2991	0.3124	0.2789	0.2907	0.2931	0.2867	0.2884	0.3026	0.3189	0.3066	0.2991	0.3124
	Present with NS	0.2537	0.2675	0.2687	0.2631	0.2635	0.2859	0.3010	0.2763	0.2861	0.3076	0.2537	0.2675	0.2687	0.2631	0.2635	0.2859	0.3010	0.2763	0.2861	0.3076
0.2	Present with MS	0.2537	0.2675	0.2697	0.2631	0.2642	0.2859	0.3010	0.2931	0.2861	0.2957	0.2537	0.2675	0.2697	0.2631	0.2642	0.2859	0.3010	0.2931	0.2861	0.2957
	Sah and Ghosh (2022b)	0.2577	0.2719	0.2730	0.2673	0.2677	0.2907	0.3063	0.2973	0.2908	0.3003	0.2577	0.2719	0.2730	0.2673	0.2677	0.2907	0.3063	0.2973	0.2908	0.3003

NS: Neural surface; MS: Middle surface.

Table 6.8 Comparisons of  $\bar{T}_c$  for simply supported square FGM plate consisting cutout ( $d/b = 0.2$ ) exposed to temperature load.

Source	$n$		
	0	1	5
Present	11.932	7.187	5.961
Yu et al. (2016)	11.737	7.140	6.297

corresponding to the zero-frequency parameter. This technique of arriving at critical buckling load for a plate member acted upon by in-plane edge load is identified as the dynamic approach. This method is used in the existing investigation to establish the  $\bar{P}_{cr}$  for thermomechanical loaded FGSFs with porosity and cutouts.

To show the effect of NIELs on  $\bar{\omega}$  of porous FCF SFGSPs ( $b/h = 10, n = 2.0, p_i = 0.2$ ) having cutout ( $d/b = 0.2$ ) in thermomechanical environment, the natural frequency for square plate is plotted against the non-dimensional load as shown in Fig. 6.6. It is detected from Fig. 6.6 that for any type of load, the value natural frequency decreases with increase in non-dimensional load. Nevertheless, for any given non-dimensional in-plane load the plates subjected to LC-3 and LC-6 shows the highest  $\bar{\omega}$ , whereas plates with LC-2 exhibits a lesser  $\bar{\omega}$ . The higher  $\bar{\omega}$  obtained in the case of plates with LC-3 and LC-6 may be due to the formation of tensile stress along with compressive stress due to the profile of load. These, tensile stresses stabilize the plate and cause the increase in  $\bar{\omega}$ . On the other hand, plates subjected to LC-1 and LC-2 shows lower  $\bar{\omega}$  as majority of compressive stresses are concentrated near the central portion of the plate where stiffness is less due to cutout.

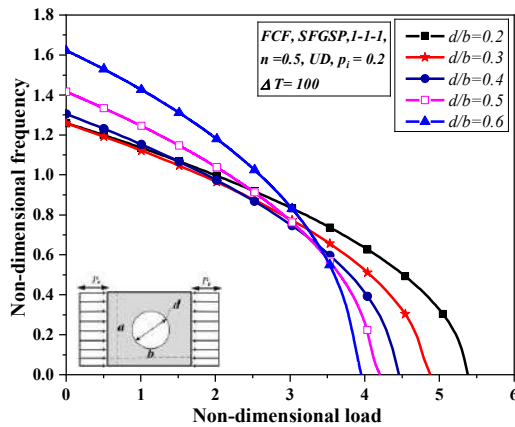


Fig. 6.5 Effect of cutout ratio on  $\bar{\omega}$  of square porous FCF SFGSP ( $a/b = 1.0$ ) subjected to in-plane load and  $\Delta T = 100$ .

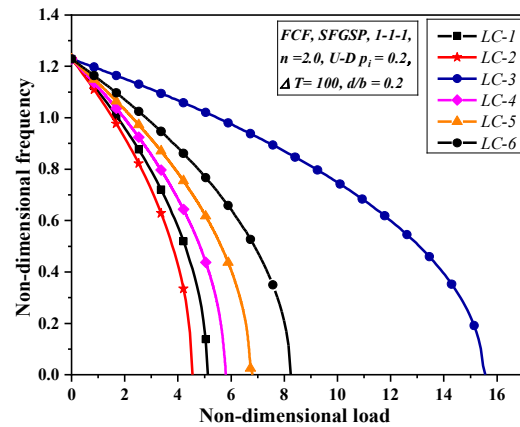


Fig. 6.6 Effect of different NIEL on  $\bar{\omega}$  for porous FCF SFGSP ( $a/b = 1.0$ ) with cutout under  $\Delta T = 100$

Fig. 6.7 depicts the impact of porosity distributions on the variation of  $\bar{\omega}$  owing to an increase in non-dimensional in-plane load of simply supported FCF SFGSP ( $a/b = 1.0$ ) with cutout. The plate is considered to be subjected to LC-1. It is noticed that at particular non-dimensional in-plane load, the plates with U-D porosity exhibit the

lowest natural frequency followed by V2-D, X-D, O-D and V1-D. The plates U-D and V2-D have porosity concentration away from the neutral surface, thus causing larger reduction in stiffness, thus showing lower frequency.

Further, the consequence of porosity indices and temperature rise on variation of  $\bar{\omega}$  of porous FCF and MFC PFGSPs ( $b/h = 10$ ,  $n = 2.0$ ) with cutouts ( $d/b = 0.2$ ) exposed to inplane edge loads in thermal environment are studied and results are illustrated in Fig. 6.8. Here plates with U-D porosity are considered and is subjected to LC-1. It is observed that the  $\bar{\omega}$  decreases with increase in temperature due to the stiffness degradation irrespective of porosity indices. Also, with increase in porosity indices the natural frequencies also reduce irrespective of temperature rise. The difference in natural frequencies due to increase in porosity indices increases with increase in the magnitude of in-plane loads in case of FCF PFGSP.

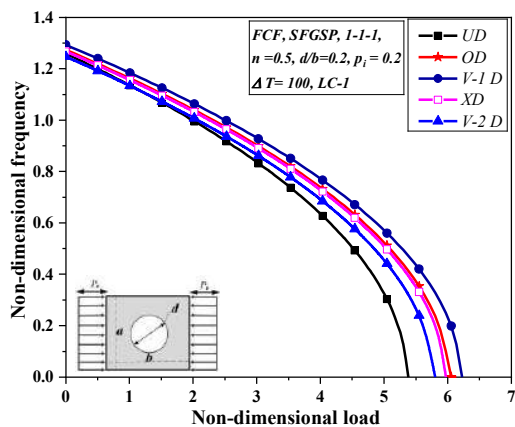


Fig. 6.7 Effect of porosity distribution on  $\bar{\omega}$  for porous FCF SFGSP ( $a/b = 1.0$ ) with cutout under inplane load and  $\Delta T = 100$

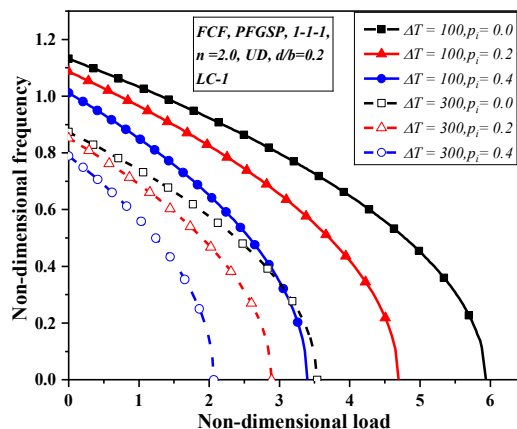


Fig. 6.8 Effect of  $p_i$  and temperature rise on  $\bar{\omega}$  of porous FCF PFGSP ( $a/b = 1.0$ ) under inplane load.

Further, the impact of porosity and temperature rise on natural frequency variation of MFC PFGSPs ( $b/h = 10$ ,  $n = 2.0$ ) having cutouts ( $d/b = 0.2$ ) exposed to inplane edge loads in thermal environment is investigated and outcomes are plotted in Fig. 6.9. The LC-1 is applied to the plate in this study and U-D porosity is considered. Here, it is noticed that  $\bar{\omega}$  of MFC plates decreases with rise in  $p_i$  and significant decrease is observed in plates under higher temperature rise. Also, it is well known and can be noticed in Fig. 6.9 that the plate  $\bar{\omega}$  reduces with upsurge in the temperature rise, due to the loss of stiffness at higher temperature. For MFC PFGSPs it is observed from Fig.

6.9 that at lower temperature, the natural frequency of plate is less sensitive to change in porosity. But at higher temperature, noticeable change in  $\bar{\omega}$  is observed owing to the change in porosity. The effects of boundary condition on natural frequencies variation of FCF PFGSPs ( $b/h = 10, n = 2.0$ ) having cutouts ( $d/b = 0.3$ ) exposed to LC-1 inplane edge loads in a thermal environment is investigated, and outcomes are plotted in Fig. 6.10. It can be observed from Fig. 6.10 that  $\bar{\omega}$  of FCF plate with CCCC support conditions possess the highest  $\bar{P}_{cr}$  amongst all the other supports conditions in the orders of CCCC > CCSS > CCFF > SSSS, irrespective of the sandwich layers scheme, temperature and cutouts ratios. Due to the effect of edge restraints, CCCC plates exhibit maximum buckling resistance compared to plates with other support conditions. With the decrease in the edge restraints, the natural frequency of the plate reduces, as noticed for CCSS, CCFF and SSSS plates.

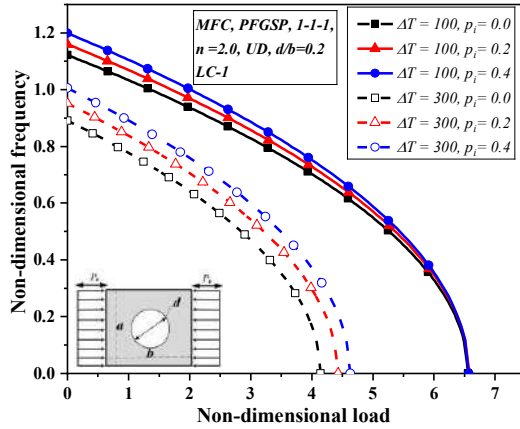


Fig. 6.9 Effect of  $p_i$  and temperature rise on  $\bar{\omega}$  of porous MFC PFGSPs ( $a/b = 1.0$ ) under inplane load

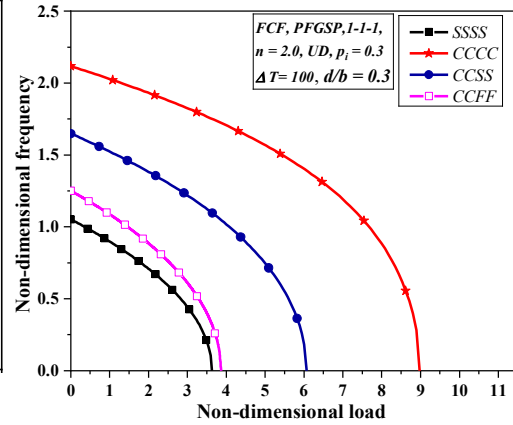


Fig. 6.10 Effect of different boundary condition on  $\bar{\omega}$  of porous FCF PFGSPs ( $a/b = 1.0$ ) under inplane load and  $\Delta T = 100$

### 6.3.2.2 Effect of cutout size, temperature and nonuniform loads on buckling response of porous FGSPs under thermomechanical loads

The consequence of cutout size, temperature and NIELs on  $\bar{P}_{cr}$  of simply supported porous (U-D,  $p_i = 0.2$ ) FCF SFGSP ( $b/h = 10, 1-1-1, n = 2.0$ ) with cutout has been exhibited in Figs. 6.11(a) and (b). It is detected that increase in cutout size leads to decrease in  $\bar{P}_{cr}$  for all the types of loading cases and thermal environment ( $\Delta T = 50, \Delta T = 150$ ). The second examination consist of exploration of effect of temperature on buckling load. As observed, the buckling load reduces with increase in temperature for

all the cutout sizes and loading cases. Fig. 6.11 reveals that the highest  $\bar{P}_{cr}$  is obtained for plates subjected to LC-3 loading amongst all the other loading pattern in the order of LC-3 >LC-6 > LC-5 >LC-4 >LC-1 >LC-2 irrespective of temperature and cutout size. It is evident that type of mechanical loading case plays important role in buckling behaviour of FGSP with cutout. The same behaviour can be seen in detail in the form of histogram for different temperature rise as shown in Fig. 6.11(b).

### 6.3.2.3 Effect of cutout size and porosity on buckling response of porous FGSPs under thermomechanical loads

Fig. 6.12 shows the consequence of cutout size and porosity on buckling characteristics of square simply supported porous (U-D) FCF SFGSP ( $b/h = 10, 1-1-1$ ). The plate is considered to be subjected to LC-1 loads. It is shown that  $\bar{P}_{cr}$  decreases with an increase in  $p_i$  due to reduction of the stiffness of the plate member under thermomechanical environment. In line with the explanation in the previous section  $\bar{P}_{cr}$  reduces as the size of the cutout increases. The decrease in  $\bar{P}_{cr}$  with a rise in  $p_i$  is more noticeable in plates with smaller cutout sizes than the plates with larger cutout ratios. To have a clear understanding the variation in  $\bar{P}_{cr}$  is also represented in the form of the histogram as shown in Fig. 6.12(b).

### 6.3.2.4 Effect of porosity indices and volume fraction exponent on buckling response of porous FGSPs under thermomechanical loads

The consequence of  $p_i$  and  $n$  on the  $\bar{P}_{cr}$  of simply supported square porous (U-D) FCF PFGSP and SFGSP ( $b/h = 10, 1-1-1$ ) having cutout ( $d/b = 0.3$ ) exposed to LC-1 for several temperature rises is displayed in Fig. 6.13. Three different temperature rises ( $\Delta T = 50, 200, 300$ ) are considered. As stated in Table 6.1, the material properties are considered temperature dependent. These figures can be used to generate three levels of analysis: (a) It can be found that the increasing of  $\Delta T$  decreases the  $\bar{P}_{cr}$  of the considered plates, (b) the rise in  $n$  leads to decrease in the  $\bar{P}_{cr}$ . Also, the decrease in  $\bar{P}_{cr}$  with an increase in  $n$  is significant in the case of PFGSP in comparison with SFGSP, (c) the increase in the  $p_i$  from 0.0 to 0.4 leads to decrease of the  $\bar{P}_{cr}$ . Also, the decrease in  $\bar{P}_{cr}$  of both PFGSP and SFGSP with increase in the  $p_i$  is observed to be more significant at lower temperature rise as compared to the decrease seen at higher

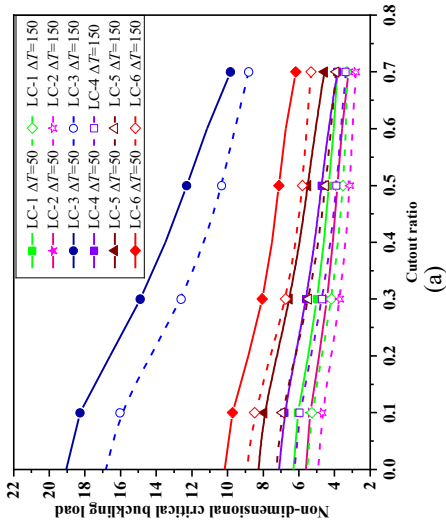


Fig. 6.11 Effect of various cutout ratio, temperature and nonuniform loading on  $\bar{P}_{cr}$  of square simply supported porous FCF SFGSP under thermomechanical loading (a) Graphical line plot (b) Histogram

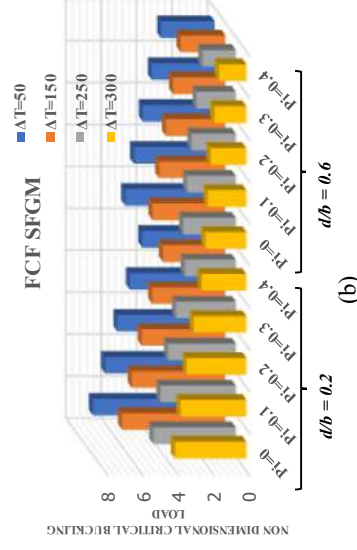
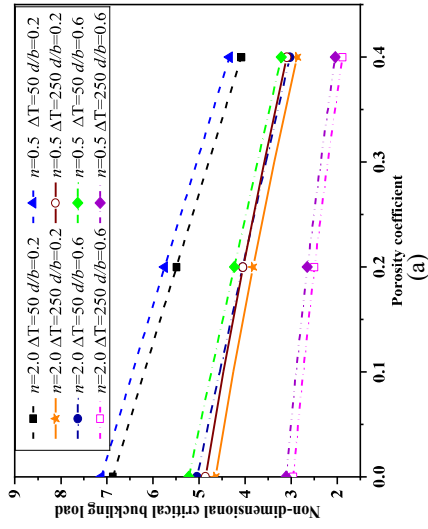
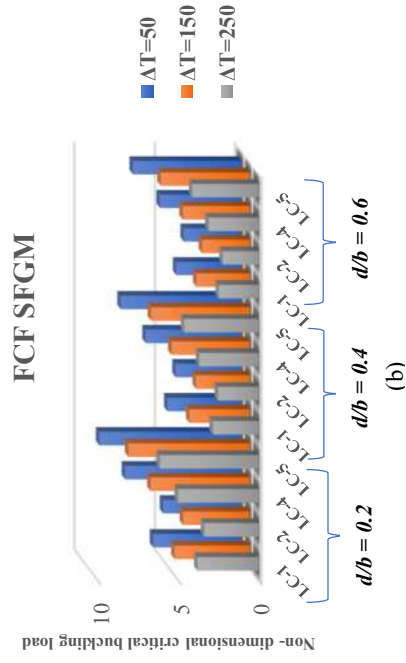


Fig. 6.12 Coupled influence of porosity, cutout size and temperature on  $\bar{P}_{cr}$  of square simply supported FCF SFGSP porous plates under thermomechanical loading. (a) Graphical line plot (b) Histogram

temperature difference (rise). Further, the effect of  $p_i$  and  $n$  on the  $\bar{P}_{cr}$  of porous simply supported (U-D) MFC PFGSP and SFGSP ( $a/b = 1$ ,  $b/h = 10$ , 1-1-1) with cutout ( $d/b = 0.3$ ) subjected to LC-1 in different temperature environment is analyzed and observations are displayed in Fig. 6.14. In consistent from discussion from the above section it can be noticed that the  $\bar{P}_{cr}$  decreases with increase in  $n$ . Also, the decrease in  $\bar{P}_{cr}$  with  $n$  is significant for PFGSP as compared to SFGSP, especially during the increase in  $n$  from 0.0 to 2.0. With further increase in  $n$ , the decrease in the  $\bar{P}_{cr}$  is not significant. In addition, it is noteworthy to mention that at lower temperature, the  $\bar{P}_{cr}$  decrease with increase in the porosity index, while at higher temperature the  $\bar{P}_{cr}$  increases with increase in the  $p_i$ . This unexpected increase in  $\bar{P}_{cr}$  at higher temperature rise is due to the reduction in effective coefficient of thermal expansion due to increase in porosity index, which increases the thermal load-bearing capacity, contrasting to  $\bar{P}_{cr}$  at lower temperature which decreases with increase in  $p_i$  due to a reduction in effective Young's modulus. Parenthetically, in comparison with MFC, the FCF FGSP shows significant variation in  $\bar{P}_{cr}$  with increase in the  $n$  irrespective of material idealization technique considered.

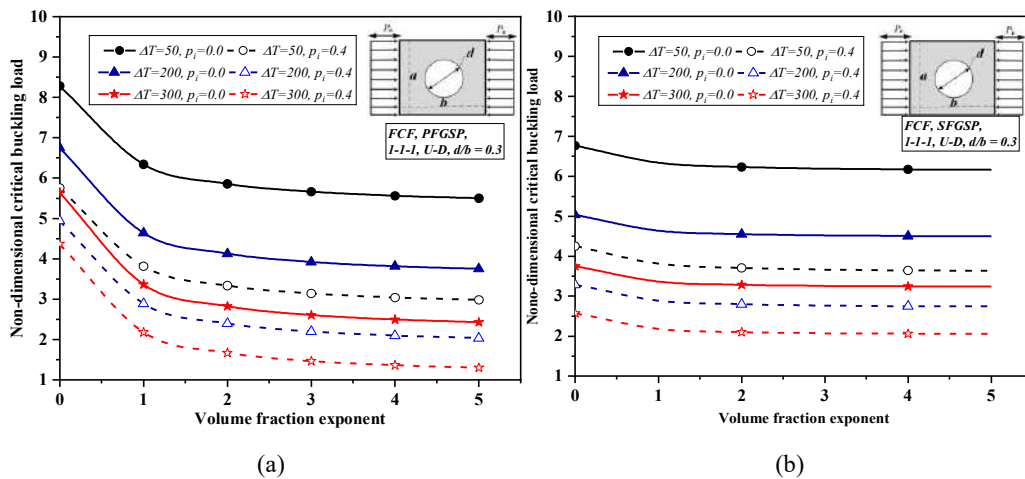


Fig. 6.13 Effect of  $p_i$  and  $n$  on  $\bar{P}_{cr}$  of porous FCF a) PFGSP b) SFGSP under uniform temperature environment

### 6.3.2.5 Effect of porosity distributions and sandwich configurations on buckling response of porous FGSPs under thermomechanical loads

Table 6.9 describes the impact of porosity distribution, temperature and sandwich layer schemes on  $\bar{P}_{cr}$  of simply supported square FCF SFGSP ( $a/b = 1$ ,  $b/h = 10$ ,  $n = 2.0$ ) with

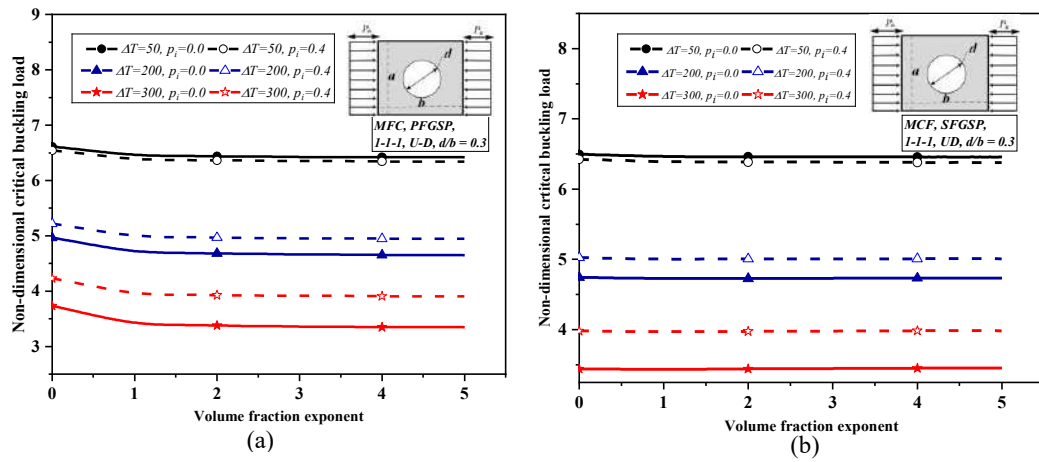


Fig. 6.14 Effect of  $p_i$  and  $n$  on  $\bar{P}_{cr}$  of MFC a) PFGSP b) SFGSP under uniform temperature environment cutout ( $d/b = 0.2$  and  $0.5$ ). The plate is under LC-1 case of mechanical loading condition. Three different uniform temperature rises ( $\Delta T = 50, 200, 300$ ) are considered. The plate is analyzed using various porosity distribution functions as mentioned in Table 3.3 and Table 3.4. For more clarity the outcomes are also exemplified in Fig. 6.15 (a). In consistent with discussion in the previous section the  $\bar{P}_{cr}$  for FCF plate decreases with increase in the  $p_i$ . It can be noted from Table 6.9 that plate with U-D porosity distribution possess lowest  $\bar{P}_{cr}$  amongst all the other porosity distribution in the order of  $U-D < V2-D < X-D < O-D < V1-D$  irrespective of the sandwich layer scheme, temperature and cutout ratio.

Among all the porosity distribution, V1-D type of porosity shows maximum  $\bar{P}_{cr}$  irrespective of temperature and porosity index as maximum pores are distributed close to the neutral surface of the plate. This effect is stronger with U-D pores than with irregularly distributed pores, demonstrating once more how the distribution of pores can enhance the buckling response of PFGSP. Therefore, the distribution of pores has a notable impact on the elastic modulus of FGSP and, consequently, the buckling behaviour of these structural components. Thus, in the design and experimentation phases of aeroelastic, automotive, and reactor components in thermomechanical environment, this parameter is crucial.

A similar study is carried out considering MFC SFGSP ( $b/h = 10, n = 2$ ) having cutout ( $d/b = 0.2$  and  $0.5$ ) and results are tabulated in Table 6.10. To have insightfully view the results are also illustrated in Fig. 6.15 (b). It can be observed that the variation in

$\bar{P}_{cr}$  of MFC plates due to increase in porosity index is not pronounced as compared to FCF plates. The reason for such behaviour is owing to the presence of porous FGM core close to the neutral surface of the sandwich plate. At lower temperature rise  $\bar{P}_{cr}$  decreases with increase in  $p_i$  but with increase in temperature rise  $\bar{P}_{cr}$  increases with increases in porosity index due to effect of reduction in effective thermal expansion coefficient as noticed in earlier section. It is noticed that at  $\Delta T=50$  plates with U-D type exhibits significant reduction in  $\bar{P}_{cr}$  and has the lowest  $\bar{P}_{cr}$ , while plates with V-D type shows least variation in  $\bar{P}_{cr}$  (showing highest  $\bar{P}_{cr}$ ). The reason for such phenomena is owing to the fact that at lower temperature rise Young's modulus governs the change in  $\bar{P}_{cr}$  due to change in  $p_i$  and hence plate with U-D and X-D distribution in which pores are distributed away from neutral surface shows significant reduction in  $\bar{P}_{cr}$  (and lowest). Also, plates with V2-D porosity shows lesser  $\bar{P}_{cr}$ , as maximum porosity is distributed near bottom interface of plate which has metal content. Further at higher temperature rise ( $\Delta T=200$  and  $300$ ) due the role of thermal expansion coefficient, the  $\bar{P}_{cr}$  increases with increase in porosity index. And U-D demonstrates significant variation (also highest  $\bar{P}_{cr}$ ) amongst the several other porosity distributions considered irrespective of cutout ratio. While plate with other porosity distributions such as X-D, O-D, V1-D and V2-D shows small variation in  $\bar{P}_{cr}$  with increase in the  $p_i$ .

The influence of sandwich layer schemes on the buckling behaviour of FCF and MFC SFGSP is now investigated using the results tabularized in Table 6.9 and Table 6.10 respectively. For more clarity the results are also displayed in Figs. 6.16 (a) and (b) for  $\Delta T = 50$  and  $\Delta T = 300$  respectively. Table 6.9 also presents the  $\bar{P}_{cr}$  values of FCF SFGSP for different sandwich layer schemes. The plates with 1-2-1 layer scheme hold highest  $\bar{P}_{cr}$  amid all the layer scheme in the order of  $1-2-1 > 2-2-1 > 1-1-1 > 2-1-1 > 2-1-2$  irrespective of the temperature rise. In consistent with discussion in the above section the  $\bar{P}_{cr}$  decreases with increase in the porosity index in case of all the sandwich layer schemes, however the decrease in the  $\bar{P}_{cr}$  is prominent in case of lesser temperature (i.e.,  $\Delta T = 50$ ). Among plates with several layer scheme, plates with 2-1-2 layer scheme is sensitive to variation in porosity index as it contains larger thickness of porous face sheets irrespective of porosity distribution, cutout ratio and temperature rise. However, the plate with layer scheme 1-2-1 exhibits less variation in  $\bar{P}_{cr}$  with

increase in the porosity index as it contains lesser thickness of porous layers/larger thickness of nonporous core. In continuation with previous discussion,  $\bar{P}_{cr}$  variation of MFC plates of different sandwich configuration plates is observed in Table 6.10 and Fig. 6.16(b). It is noticed that plates with 1-2-1 layer scheme exhibits noticeable variation in  $\bar{P}_{cr}$  with increase in porosity index as it contains larger thickness of porous FG core. While plate with 2-1-2 layer scheme shows least variation in  $\bar{P}_{cr}$ . Additionally, it can be highlighted that at lower temperature the  $\bar{P}_{cr}$  of the plate decreases with the upsurge in  $p_i$ , while at higher temperature rises the  $\bar{P}_{cr}$  increases owing to dissimilarity in thermal expansion coefficient of the constituent materials.

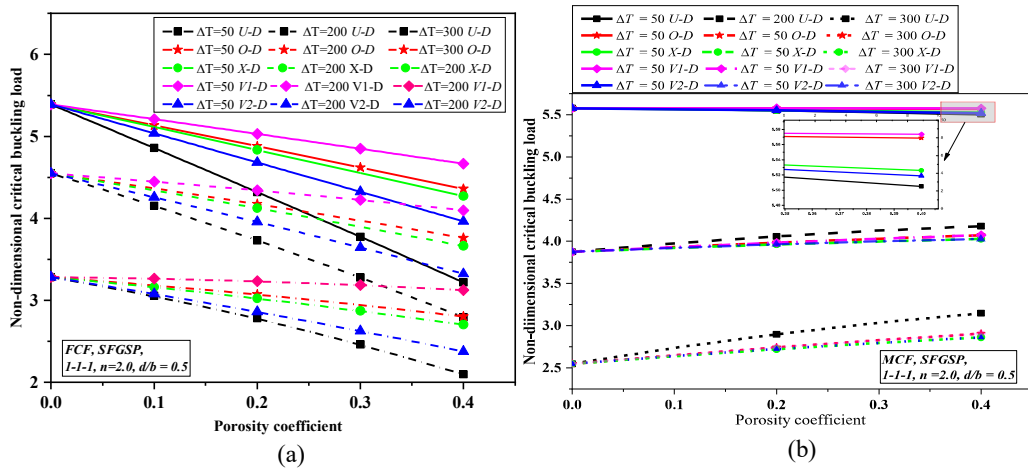


Fig. 6.15 Effects of porosity distribution on the  $\bar{P}_{cr}$  of (a) FCF SFGSP (b) MFC SFGSP under a thermomechanical environment ( $n=2, b/h=10, d/b = 0.5$ ).

### 6.3.2.6 Effect of support condition on buckling response of porous FGSPs under thermomechanical loads

The impact of different support condition on  $\bar{P}_{cr}$  of porous (U-D) simply supported square FCF SFGSPs is inspected and results are tabularized in Table 6.11. Irrespective of porosity index, temperature, volume fraction exponent and cutout ratio it is noticed that plates with CCCC and SSSS support condition provides the highest and lowest  $\bar{P}_{cr}$  respectively. While the  $\bar{P}_{cr}$  of plates with CCSS falls in between  $\bar{P}_{cr}$  of SSSS and CCCC plate. The reason for increase in  $\bar{P}_{cr}$  for CCCC plates is due to the increase in the edge restrains, as the edge restrains decrease the  $\bar{P}_{cr}$  decreases as observed in case of plates with CCSS and SSSS. It can be also observed that plates with CCCC and SSSS show

Table 6.9 Effects of porosity distribution and sandwich layer scheme on the  $\bar{P}_{cr}$  of square simply supported FCF SFGSP under thermal environment ( $n = 2, b/h = 10$ ).

d/b	$\Delta T$	Sandwich Layer scheme	Porosity distribution																		
			Non Porous			U-D			X-D			O-D			V1-D			V2-D			
			$p_i=0.0$	$p_i=0.1$	$p_i=0.4$	$p_i=0.1$	$p_i=0.4$	$p_i=0.1$	$p_i=0.4$	$p_i=0.1$	$p_i=0.4$	$p_i=0.1$	$p_i=0.4$	$p_i=0.1$	$p_i=0.4$	$p_i=0.1$	$p_i=0.4$	$p_i=0.1$	$p_i=0.4$		
0.2	50	1-1-1	6.870	6.184	4.082	6.514	5.431	6.542	5.544	6.639	5.933	6.417	5.039	5.703	4.820	5.312	4.636	3.835	4.433	3.667	4.100
		1-2-1	7.253	6.624	4.700	6.933	5.962	6.945	6.009	7.009	6.267	6.869	5.703	4.820	5.312	4.636	3.835	4.433	3.667	4.100	4.100
		2-1-2	6.764	6.092	4.027	6.407	5.331	6.450	5.481	6.568	5.969	6.288	4.820	5.312	4.636	3.835	4.433	3.667	4.100	4.100	4.100
		2-2-1	7.048	6.404	4.434	6.719	5.731	6.734	5.767	6.830	6.172	6.622	5.312	4.636	3.835	4.433	3.667	4.100	4.100	4.100	4.100
		2-1-1	6.628	5.929	3.782	6.255	5.120	6.304	5.314	6.424	5.794	6.135	4.636	3.835	4.433	3.667	4.100	4.100	4.100	4.100	4.100
		1-1-1	5.243	4.774	3.200	4.997	4.205	5.024	4.314	5.116	4.682	4.906	4.636	3.835	4.433	3.667	4.100	4.100	4.100	4.100	4.100
	200	1-2-1	5.661	5.198	3.680	5.425	4.677	5.437	4.723	5.497	4.965	5.365	4.433	3.667	4.100	4.100	4.100	4.100	4.100	4.100	4.100
		2-1-2	5.113	4.681	3.199	4.879	4.124	4.920	4.265	5.028	4.716	4.771	3.667	4.100	4.100	4.100	4.100	4.100	4.100	4.100	4.100
		2-2-1	5.429	4.980	3.486	5.200	4.472	5.214	4.503	5.301	4.873	5.112	4.100	4.100	4.100	4.100	4.100	4.100	4.100	4.100	4.100
		2-1-1	4.973	4.530	3.005	4.731	3.939	4.778	4.128	4.891	4.581	4.618	4.100	4.100	4.100	4.100	4.100	4.100	4.100	4.100	4.100
		1-1-1	4.025	3.714	2.526	3.860	3.280	3.714	2.526	3.974	3.740	3.771	2.924	2.924	2.924	2.924	2.924	2.924	2.924	2.924	2.924
		1-2-1	4.475	4.133	2.913	4.301	3.716	4.133	2.913	4.370	3.994	4.244	3.483	3.483	3.483	3.483	3.483	3.483	3.483	3.483	3.483
300	2-1-2	3.876	3.619	2.563	3.732	3.211	3.619	2.563	3.872	3.771	3.631	2.792	2.792	2.792	2.792	2.792	2.792	2.792	2.792	2.792	
	2-2-1	4.221	3.914	2.768	4.064	3.526	3.914	2.768	4.159	3.899	3.983	3.187	3.187	3.187	3.187	3.187	3.187	3.187	3.187	3.187	
	2-1-1	3.730	3.475	2.403	3.584	3.043	3.475	2.403	3.738	3.663	3.475	2.603	2.603	2.603	2.603	2.603	2.603	2.603	2.603	2.603	
	1-1-1	5.389	4.858	3.220	5.113	4.272	5.135	4.360	5.211	4.666	5.037	3.963	3.963	3.963	3.963	3.963	3.963	3.963	3.963	3.963	
	1-2-1	5.696	5.208	3.705	5.448	4.691	5.457	4.729	5.507	4.931	5.397	4.488	4.488	4.488	4.488	4.488	4.488	4.488	4.488	4.488	
	2-1-2	5.302	4.783	3.176	5.027	4.191	5.060	4.308	5.152	4.690	4.933	3.791	3.791	3.791	3.791	3.791	3.791	3.791	3.791	3.791	
0.5	50	2-2-1	5.530	5.032	3.494	5.276	4.508	5.288	4.535	5.363	4.852	5.200	4.180	4.180	4.180	4.180	4.180	4.180	4.180	4.180	4.180
		2-1-1	5.195	4.655	2.985	4.907	4.025	4.945	4.178	5.039	4.554	4.812	3.644	3.644	3.644	3.644	3.644	3.644	3.644	3.644	3.644
		1-1-1	4.550	4.155	2.795	4.342	3.662	4.367	3.763	4.451	4.099	4.258	3.324	3.324	3.324	3.324	3.324	3.324	3.324	3.324	3.324
		1-2-1	4.940	4.542	3.212	4.738	4.086	4.748	4.128	4.804	4.350	4.683	3.864	3.864	3.864	3.864	3.864	3.864	3.864	3.864	3.864
		2-1-2	4.425	4.069	2.805	4.232	3.591	4.269	3.720	4.367	4.131	4.133	3.178	3.178	3.178	3.178	3.178	3.178	3.178	3.178	3.178
		2-2-1	4.723	4.343	3.047	4.528	3.902	4.541	3.930	4.621	4.267	4.449	3.566	3.566	3.566	3.566	3.566	3.566	3.566	3.566	3.566
	200	2-1-1	4.296	3.933	2.635	4.096	3.426	4.139	3.599	4.242	4.014	3.992	3.007	3.007	3.007	3.007	3.007	3.007	3.007	3.007	3.007
		1-1-1	3.283	3.055	2.098	3.161	2.703	3.185	2.801	3.266	3.124	3.080	2.377	2.377	2.377	2.377	2.377	2.377	2.377	2.377	2.377
		1-2-1	3.710	3.438	2.416	3.571	3.089	3.582	3.130	3.635	3.343	3.518	2.875	2.875	2.875	2.875	2.875	2.875	2.875	2.875	2.875
		2-1-2	3.139	2.968	2.149	3.040	2.645	3.075	2.767	3.167	3.155	2.949	2.270	2.270	2.270	2.270	2.270	2.270	2.270	2.270	2.270
		2-2-1	3.467	3.237	2.304	3.349	2.921	3.361	2.944	3.435	3.258	3.276	2.618	2.618	2.618	2.618	2.618	2.618	2.618	2.618	2.618
		2-1-1	3.003	2.838	2.016	2.904	2.497	2.946	2.667	3.046	3.066	2.804	2.094	2.094	2.094	2.094	2.094	2.094	2.094	2.094	2.094

Table 6.10 Consequence of porosity distribution and sandwich layer scheme on the  $\bar{P}_{cr}$  of MFC SFGSP exposed to thermal environment ( $n=2.0, b/h=10$ ).

$d/b$	$\Delta T$	Sandwich Layer scheme	Porosity distribution											
			Non Porous		U-D		X-D		O-D		V1-D		V2-D	
			$p_i=0.0$	$p_i=0.1$	$p_i=0.4$	$p_i=0.1$	$p_i=0.4$	$p_i=0.1$	$p_i=0.4$	$p_i=0.1$	$p_i=0.4$	$p_i=0.1$	$p_i=0.4$	
0.2	50	1-1-1	7.120	7.102	7.022	7.105	7.051	7.119	7.106	7.120	7.112	7.103	7.041	
		1-2-1	7.129	7.051	6.772	7.067	6.869	7.114	7.055	7.109	7.037	7.071	6.873	
		2-1-2	7.064	7.054	7.000	7.056	7.026	7.062	7.049	7.052	7.008	7.066	7.067	
		2-2-1	7.068	7.032	6.892	7.038	6.941	7.062	7.036	7.038	6.934	7.062	7.037	
		2-1-1	7.117	7.116	7.102	7.115	7.107	7.118	7.119	7.120	7.125	7.114	7.100	
		1-1-1	5.444	5.524	5.678	5.478	5.555	5.492	5.608	5.492	5.610	5.478	5.550	
	200	1-2-1	5.444	5.514	5.591	5.458	5.459	5.504	5.639	5.497	5.616	5.464	5.470	
		2-1-2	5.347	5.410	5.534	5.377	5.445	5.382	5.467	5.372	5.423	5.387	5.488	
		2-2-1	5.351	5.435	5.580	5.383	5.444	5.406	5.536	5.381	5.432	5.408	5.543	
		2-1-1	5.447	5.505	5.630	5.475	5.544	5.478	5.556	5.479	5.559	5.475	5.541	
		1-1-1	4.204	4.355	4.675	4.275	4.444	4.288	4.496	4.288	4.497	4.275	4.440	
		1-2-1	4.198	4.375	4.705	4.268	4.411	4.312	4.586	4.306	4.564	4.273	4.420	
300	2-1-2	4.087	4.205	4.459	4.144	4.284	4.150	4.306	4.139	4.263	4.155	4.327		
	2-2-1	4.089	4.260	4.613	4.166	4.343	4.188	4.433	4.164	4.331	4.190	4.439		
	2-1-1	4.212	4.313	4.537	4.262	4.387	4.265	4.398	4.266	4.400	4.262	4.384		
	1-1-1	5.576	5.565	5.505	5.565	5.526	5.576	5.569	5.577	5.574	5.564	5.519		
	1-2-1	5.582	5.525	5.311	5.536	5.386	5.573	5.530	5.569	5.516	5.539	5.390		
	2-1-2	5.524	5.517	5.477	5.518	5.497	5.523	5.515	5.515	5.482	5.526	5.529		
0.5	50	2-2-1	5.527	5.503	5.395	5.506	5.434	5.525	5.507	5.506	5.428	5.525	5.509	
		2-1-1	5.573	5.575	5.566	5.573	5.569	5.576	5.578	5.577	5.582	5.572	5.564	
		1-1-1	3.875	3.976	4.179	3.921	4.029	3.932	4.072	3.932	4.071	3.921	4.027	
		1-2-1	3.872	3.982	4.160	3.911	3.980	3.947	4.125	3.942	4.103	3.916	3.991	
		2-1-2	3.781	3.859	4.021	3.819	3.909	3.824	3.927	3.815	3.890	3.828	3.945	
		2-2-1	3.785	3.896	4.108	3.833	3.938	3.852	4.012	3.831	3.926	3.853	4.019	
	200	2-1-1	3.880	3.949	4.099	3.914	3.998	3.916	4.007	3.917	4.008	3.914	3.996	
		1-1-1	2.547	2.737	3.147	2.639	2.862	2.650	2.905	2.649	2.904	2.639	2.862	
		1-2-1	2.536	2.779	3.264	2.643	2.885	2.680	3.030	2.674	3.007	2.649	2.897	
		2-1-2	2.428	2.575	2.898	2.501	2.681	2.506	2.700	2.496	2.661	2.511	2.719	
		2-2-1	2.430	2.649	3.115	2.533	2.781	2.552	2.855	2.531	2.767	2.554	2.864	
		2-1-1	2.559	2.681	2.956	2.620	2.774	2.623	2.783	2.623	2.783	2.620	2.774	

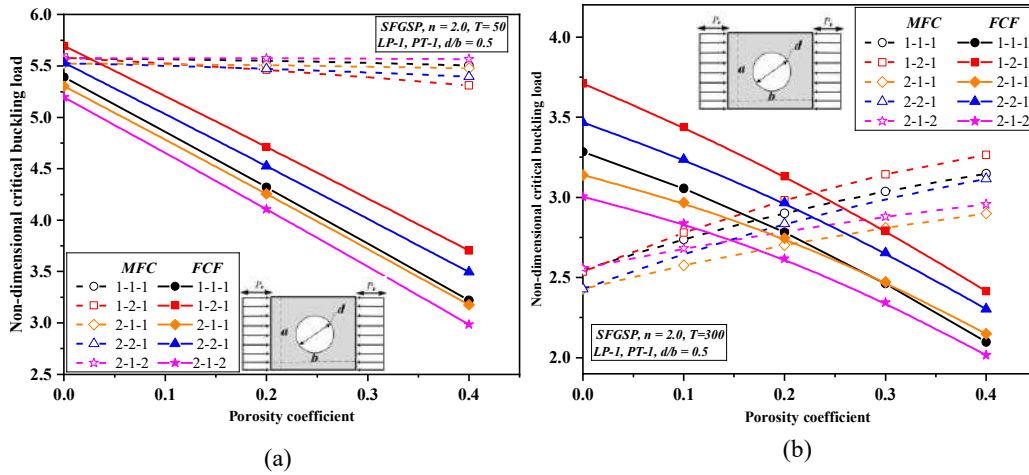


Fig. 6.16 Effects of sandwich layer scheme and porosity distribution on the  $\bar{P}_{cr}$  of FCF and MFC SFGSP ( $\text{Si}_3\text{N}_4/\text{SUS304}$ ) (a)  $\Delta T = 50$  (b)  $\Delta T = 300$  under thermomechanical environment. ( $b/h = 10$ )

maximum and minimum decrease in  $\bar{P}_{cr}$  due to the increase in porosity index irrespective of cutout ratio and temperature rise while decrease in  $\bar{P}_{cr}$  for plates with CCSS support condition lies in between.

### 6.3.2.7 Effect of material thermal expansion coefficient on buckling response of porous FGSPs under thermomechanical loads

Figure 6.17 (a) and (b) are plotted to study the effect of material thermal expansion coefficient on  $\bar{P}_{cr}$  on porous MFC SFGSP ( $a/b = 1$ ,  $b/h = 10$ ) having cutout ( $d/b = 0.1$ ) and simply support. Two set of material combinations ( $\text{Si}_3\text{N}_4/\text{SUS304}$  and  $\text{ZrO}_2/\text{SUS304}$ ) are carefully chosen in this study and their temperature dependent properties are mentioned in Table 6.1. It is to be noted that for  $\text{Si}_3\text{N}_4/\text{SUS304}$ ,  $\alpha_c < \alpha_m$  and for  $\text{ZrO}_2/\text{SUS304}$ ,  $\alpha_m < \alpha_c$ . The plate is subjected to LP-1 and U-D form of porosity is considered for the current study. It can be perceived from Figs. 6.17(a) and (b) that  $\bar{P}_{cr}$  of MFC plates made of  $\text{Si}_3\text{N}_4/\text{SUS304}$  decrease with increase in  $n$ , while the  $\bar{P}_{cr}$  increase with increase in  $n$  for plates made up of  $\text{ZrO}_2/\text{SUS304}$ . The basis for the upsurge in  $\bar{P}_{cr}$  with increase in  $n$  is due the lesser in the value of  $\alpha_m$  as compared to that of  $\alpha_c$  in case of  $\text{ZrO}_2/\text{SUS304}$ . In both  $\bar{P}_{cr}$  type of plate materials considered, the  $\bar{P}_{cr}$  decrease with rise in  $p_i$  at lower temperature rise, while in case of higher temperature rise,  $\bar{P}_{cr}$  increases with increase in the  $p_i$ . The physical basis for such behaviour is due to fact that at lower temperature, the reduction in effective Young's modulus governs,

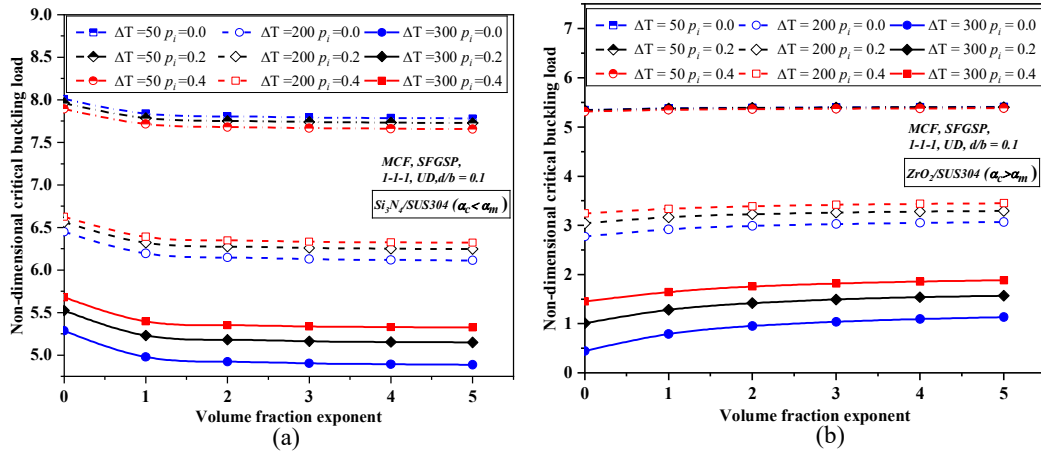


Fig. 6.17 Impact of material,  $n$  and porosity on the  $\bar{P}_{cr}$  of MFC SFGSP (a)  $\text{Si}_3\text{N}_4/\text{SUS304}$  (b)  $\text{ZrO}_2/\text{SUS304}$  under thermomechanical loads ( $b/h=10$ )

Table 6.11 Effect of support condition and temperature on  $\bar{P}_{cr}$  of FCF SFGSP under thermomechanical load ( $b/h=10, n=2$ )

Support Conditions	$n$	$d/b$	$\Delta T$							
			50		150		250		300	
			$p_i=0.1$	$p_i=0.4$	$p_i=0.1$	$p_i=0.4$	$p_i=0.1$	$p_i=0.4$	$p_i=0.1$	$p_i=0.4$
SSSS	0.5	0.2	6.439	4.341	5.502	3.749	4.471	3.090	3.923	2.738
		0.4	5.399	3.646	4.422	3.028	3.328	2.332	2.740	1.955
		0.6	4.733	3.215	3.902	2.684	2.899	2.045	2.331	1.683
	2.0	0.2	6.184	4.082	5.270	3.512	4.255	2.871	3.714	2.526
		0.4	5.185	3.429	4.229	2.832	3.153	2.154	2.573	1.786
		0.6	4.552	3.029	3.736	2.513	2.745	1.888	2.183	1.533
CCSS	0.5	0.2	10.080	6.840	9.212	6.285	8.238	5.655	7.714	5.314
		0.4	8.307	5.674	7.603	5.218	6.795	4.691	6.352	4.401
		0.6	5.865	4.050	5.446	3.775	4.957	3.452	4.684	3.271
	2.0	0.2	9.706	6.454	8.858	5.919	7.895	5.301	7.374	4.961
		0.4	8.011	5.364	7.321	4.923	6.520	4.404	6.078	4.115
		0.6	5.672	3.843	5.261	3.577	4.773	3.256	4.500	3.075
CCCC	0.5	0.2	14.253	9.761	13.323	9.155	12.264	8.457	11.687	8.074
		0.4	11.872	8.258	11.278	7.859	10.584	7.388	10.196	7.123
		0.6	8.188	5.807	7.895	5.606	7.558	5.371	7.372	5.241
	2.0	0.2	13.758	9.240	12.848	8.654	11.795	7.963	11.215	7.577
		0.4	11.504	7.856	10.920	7.469	10.224	6.997	9.831	6.727
		0.6	7.972	5.560	7.684	5.365	7.345	5.128	7.156	4.993

while at higher temperature reduction in effective thermal expansion coefficient governs due to the increase in porosity. Therefore, type of constituent material significantly effects the  $\bar{P}_{cr}$  of porous FGSP in thermomechanical environment. As FGMs has vast applications in thermal environment, the type of constituent material is to be chosen appropriately.

### 6.3.2.8 Stability region

Fig. 6.18 shows  $\bar{P}_{cr}$  variation with temperature of FCF SFGSP ( $b/h = 100, n = 2.0$ ) having cutout and porosity subjected to various loading pattern. Six types of loading cases as mentioned in Fig. 6.1 are considered.

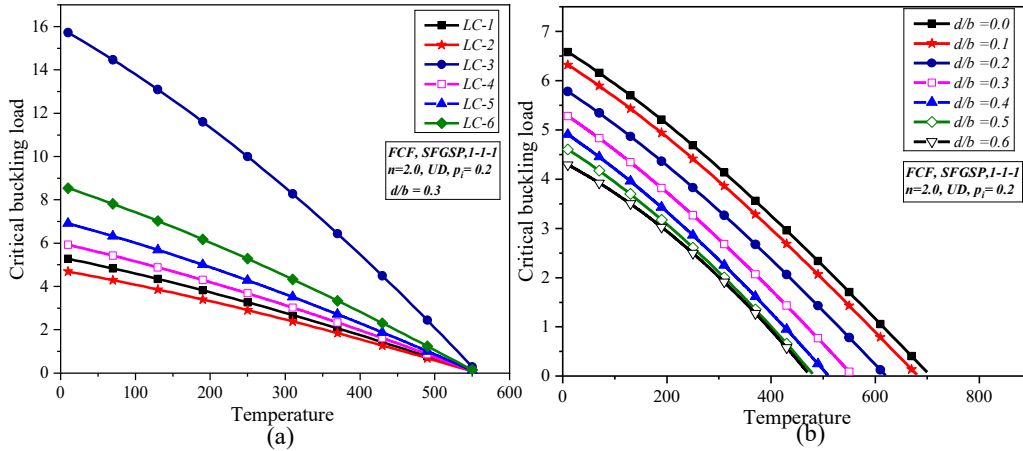


Fig. 6.18 Influence of (a) loading pattern (b)  $d/b$  on the stability region of FCF SFGSP under thermomechanical environment.

As expected, the  $\bar{P}_{cr}$  decreases with increase in the temperature for all the cases of load due to the stiffness degradation of plate with increase in temperature. LC-2 and LC-3 have the smallest and largest stability regions, respectively, among the different loading cases. The plates with LC-3 exhibits largest stability region as tensile stresses are developed in the plate with cutout due the loading variation across the width of the plate. Additionally, at lesser temperature rise, significant difference in  $\bar{P}_{cr}$  can be observed with change of the loading pattern, while the difference reduces with increase in the magnitude of temperature rise. Further, as observed in Fig. 6.18 (b) the stability region decreases as the cutout ratio increases from 0.0 to 0.6. The largest stability region is observed for the plate smaller cutouts. And as  $d/b$  increases the area of stability region decreases.

## 6.4 CLOSURE

This chapter investigates the vibration and buckling response of porous FGSP with cutout subjected to thermomechanical loads using FE method. The effective temperature dependent material properties of the FGSP are evaluated using power law and sigmoidal function-based homogenization technique. Four types of porosity

distribution models are explored, and the porosity imperfections are modelled as the criteria of stiffness reduction. The current study incorporates two distinct kinds of sandwich configuration in such a way that there is no material mismatch along the thickness direction. Here, a novel dynamic approach has been proposed to evaluate buckling loads by implementing two sets of boundary conditions. The results obtained from current FE formulations are compared with results obtained from analytical solutions and numerical methods available in the literature. After establishing the accuracy, a wide variety of numerical or parametric studies have been carried out to arrive at useful conclusions. The following chapter discusses the dynamic instability characteristics of porous FGSP with and without cutout under nonconservative forces localised and non-uniform in nature.



## **CHAPTER 7**

### **DYNAMIC INSTABILITY ANALYSIS OF POROUS FG SANDWICH PLATE WITH/WITHOUT CUTOUT**

#### **7.1 PRELIMINARY REMARKS**

The FGSPs may frequently fail due to a loss of stability rather than severe stresses that exceed the material's strength. The type of structural component instability is determined by the nature of the forces exerted on the structure. Static instability is commonly generated when the type of in-plane loading is conservative. In case of conservative force, the work done by the force depends on the initial and final position of the point of application only. On the other side of the coin, if the work performed is a function of the path that a force takes to get from its beginning condition to its final state, then that force is nonconservative. Nonconservative force 'follow' the direction of deflection, thereby changing its orientation as the structure deforms. Nonconservative forces are therefore called as follower forces. Research from the past shows that when these elements lose their stability because of follower forces, it could be because of either divergence (static instability) or flutter (dynamic instability). Failure by dynamic instability is when the loss of stability is caused by a unidirectional unbounded motion. These follower forces can be localised or nonuniform in nature. Hence, this chapter attempts to perform dynamic instability analysis of porous FGSP with/without cutout under localised and nonuniform edge loads. In order to do so, a general formulation, as presented in Chapter 3 has been developed by taking Green-Lagrange strains displacement relation, and it is employed to calculate the anticipated responses. The consequence of various geometrical and material parameters on dynamic instability analysis of porous FGSP with/without cutout under different localised and NIEL is investigated in this chapter.

#### **7.2 PROBLEM DESCRIPTION**

In this analysis, several cases of uniaxial localised edge loads and NIELs loads acting on the opposite edge of FGSPs as portrayed in Fig. 7.1 and Fig. 7.2 respectively are considered. Further, in the present study, FCF and MFC sandwich configurations, as

shown in Fig. 3.1 are incorporated. In the current study, U-D, O-D, X-D, V1-D and V2-D porosity distributions, as mentioned in Chapter 3, are considered to study the dynamic instability analysis of porous FGSP with cutout. To begin with, the correctness of the solution obtained is established by associating the present results with those existing in the literature. After verifying the accuracy, parametric studies have been carried out extensively.

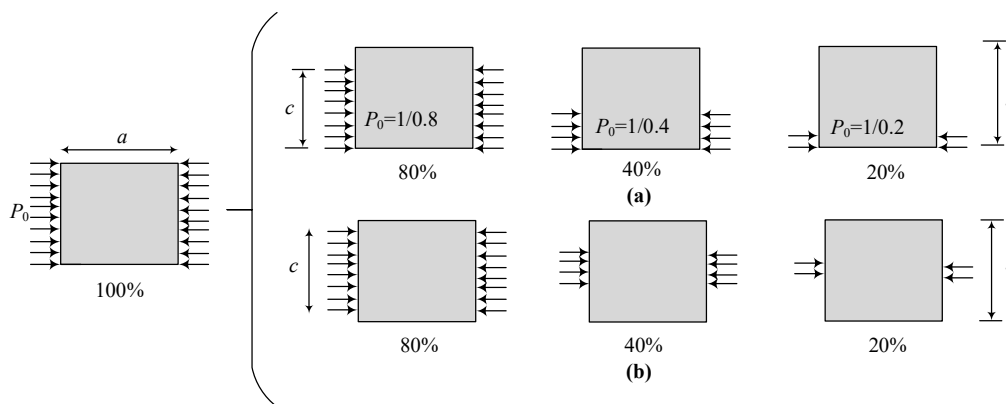


Fig. 7.1 Representation of loading cases (a) Type-I, (b) Type-III

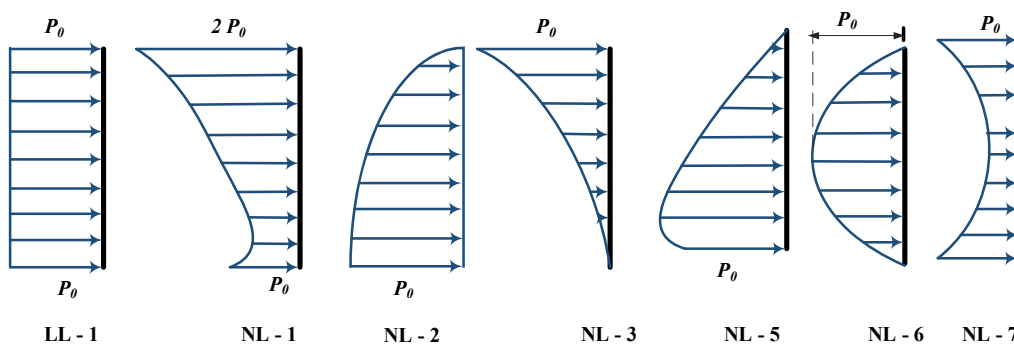


Fig. 7.2 Various cases of in-plane edge loads

### 7.3 RESULTS AND DISCUSSION

The dynamic instability characteristics are attained using established mathematical formulation through an in-house MATLAB code that can cover for any general case.

The convergence study of the porous FGSP under localised edge loads and nonuniform load is executed for numerous material and geometrical configurations. In continuation, numerous instances have been solved for validation purposes by comparing the current

findings with those found in published research literature. After the complete validation of the existing formulation, an inclusive parametric study of porous FGSP under localised edge loads and nonuniform load is performed. Here, dynamic instability analysis of porous FGSP with/without cutout under different localised edge loads and NIELs are analysed for various geometrical parameters and support conditions. If not stated otherwise, flutter loads and frequencies are represented in non-dimensional form as

$$\lambda_{cr} = \lambda a^2 / 100 E_0 h^3, E_0 = 1 \text{ GPa}$$

$$\gamma_{cr} = (\gamma a^2 / h) \sqrt{\rho_0 / E_0}, E_0 = 1 \text{ GPa}, \rho_0 = 1 \text{ kg / m}^3$$

### 7.3.1 Validation studies

**Example 1:** The accuracy of the present FE formulation for follower load formulation is determined by comparing the flutter loads and flutter frequencies to those previously published. Table 7.1 compares non-dimensional flutter loads and flutter frequencies of CFSS isotropic plates with various aspect ratios to those published by Adali (1982), Kumar et al. (2003), Datta and Deolasi (1996). According to the comparison results tabulated in Table 7.1, the obtained results were in accordance with the published results.

Table 7.1 Comparison of flutter load and flutter frequencies for a SSSS edged isotropic plate ( $b/h = 100, \nu = 0.3$ ) subjected to uniform follower loading

$a/b$	Present		Adali (1982)		Kumar et al. (2003)		Datta and Deolasi (1996)	
	$\lambda_{cr}$	$\gamma_{cr}$	$\lambda_{cr}$	$\gamma_{cr}$	$\lambda_{cr}$	$\gamma_{cr}$	$\lambda_{cr}$	$\gamma_{cr}$
1	51.64	16.677	51.65	16.67	51.651	16.685	52.06	16.33
0.5	26.897	49.471	27.11	49.58	26.923	49.567	27.20	49.30

**Example 2:** The current example is carried out to establish the accuracy of present FE formulation to predict the flutter load and frequencies of the plate subjected to localised type of follower forces. Here, antisymmetric angle-ply composite laminate ( $\theta/- \theta/ \theta/- \theta$ ) for various orientations, considering  $a/b = 1.0, b/h = 100$  and for varying load width. Due to deficiency of literatures reported on evaluating the flutter loads and frequencies of FG plate subjected to follower forces the verification of the FE formulation is carried

out with the flutter results of laminates as evaluated in Kumar et al. (2003) are presented in Table 7.2. The comparison discloses that the current results are consistent with those found in the open literature.

**Example 3:** In this example cross ply laminates (0/90, 0/90/0, 0/90/90/0) subjected to localised load from one edge is considered to predict the accuracy of current formulation. It is noticed that the load width ratio, i.e., position of the localised edge load significantly affects the flutter characteristic of the plate under follower force. Table 7.3 shows the comparison of flutter load and flutter frequencies of plate from present formulation subjected to localised edge loads with those obtained by Kumar et al. (2003). As observed in Table 7.3 the results obtained from current formulation are in satisfactory correlation.

### 7.3.2 Parametric studies

In the preceding section, it is noticed that the current outcomes using FE formulations are in good concurrence with the results existing in the literature. Thus, in this section investigations are carried out by considering several parameters such as volume fraction exponent, non-uniform load case, plate aspect ratio, porosity distribution, sandwich layer scheme, cutout ratio, etc. The loading cases considered here are given in Fig. 7.1 and Fig. 7.2. The loading case shown here is compressive in nature. The parametric studies related to dynamic instability characteristics of porous FGSPs with and without cutout are discussed in the successive sub-sections.

#### 7.3.2.1 Effect of volume fraction exponent

In this section the influence of volume fraction exponent on the flutter behaviour of porous FCF FGSP ( $a/b = 1.0$ ,  $b/h = 100$ ) under LL-1 are analysed and discussed. Here plates with 1-1-1 sandwich layer scheme with U-D type of porosity distribution with  $p_i = 0.2$  is incorporated for the study. Fig. 7.3 depicts the variation of real and imaginary part of natural frequency ( $\gamma$ ) and follower force ( $\lambda$ ) for plate with different volume fraction exponents. Here  $\gamma_1$  and  $\gamma_2$  are 1<sup>st</sup> and 2<sup>nd</sup> modes of natural frequency. It is perceived that volume fraction exponent significantly affects the flutter characteristics of the porous FGSPs. It is noticed that flutter load and frequencies decrease with

increase in the volume fraction exponent. With increase in the  $n$  the metal content in plate increases and causes decrease in the stiffness of the plate and hence flutter load flutter frequency of the plate decreases.

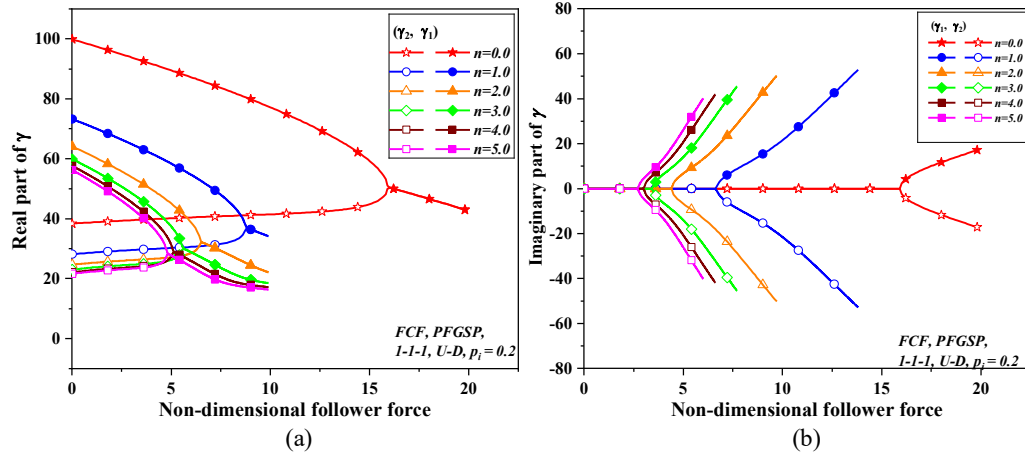


Fig. 7.3 Influence of volume fraction exponent on variation of non-dimensional natural frequency (a) real and (b) imaginary part with non-dimensional follower force for CFSS FGSP

### 7.3.2.2 Effect of porosity distribution

The consequence of different porosity distribution on flutter response of porous FCF FGSP ( $a/b=1.0$ ,  $b/h=100$ ) under LL-1 is investigated in this instance and is presented in Fig. 7.4. The plate with 1-1-1 sandwich layer scheme and  $n=2.0$  is incorporated with  $p_i=0.2$ . The several porosity distributions considered for the present investigation are mentioned in Table. 3.3. Fig. 7.4 depicts the variation of real and imaginary part of  $\gamma$  and  $\lambda$  of plates with different porosity indices. It is understood that the influence of porosity distribution on flutter behaviour of FGSP is obvious. As can be seen among the various porosity distributions considered plates with U-D and V1-D porosity shows lowest and highest flutter load and frequencies respectively. The reason for such behaviour lies in the pattern of the porosity distribution and distance of pore concentration from the neutral surface across the thickness of the plate. The V1-D porosity has maximum pores distributed close to the neutral surface, as compared to U-D distribution, therefore the flutter load and frequencies are more as reduction in stiffness of the plate is less in V1-D distribution. While in case of plates with U-D porosity the pores are concentrated throughout the plate and results in maximum

reduction in stiffness of the plate. Therefore, the pattern of pore distribution seriously affects the stiffness of the plate as result the flutter characteristics of the plate.



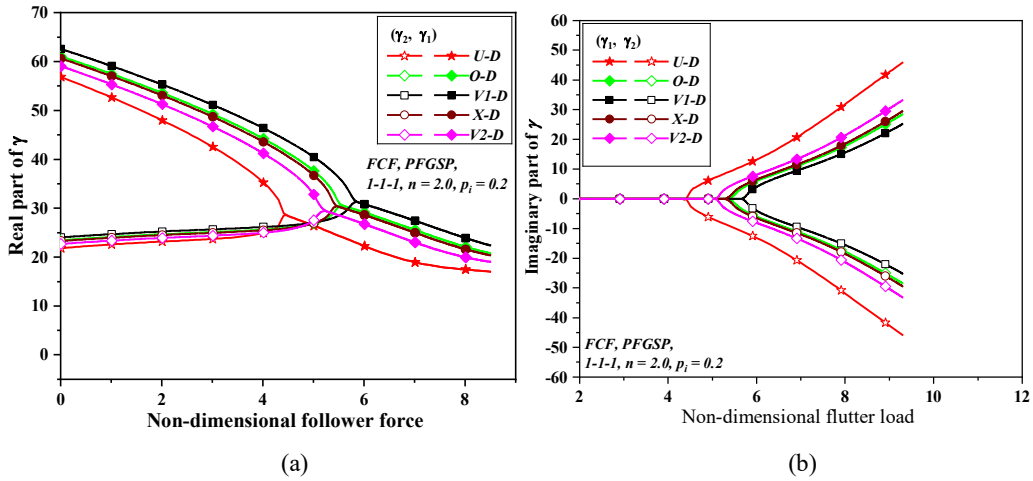


Fig. 7.4 Influence of porosity distribution on variation of non-dimensional natural frequency (a) real and (b) imaginary part with non-dimensional follower force for CFSS FGSP

### 7.3.2.3 Effect of porosity index

The investigation is continued to study the impact of porosity index on flutter characteristics of porous FCF FGSP ( $a/b = 1.0, b/h = 100$ ) subjected to LL-1. For this study U-D type of porosity distribution and 1-1-1 sandwich layer scheme is incorporated. The CFSS support condition is considered. Here, CFSS support condition plates are considered. Fig. 7.5 depicts the variation of real and imaginary part of  $\gamma$  and  $\lambda$  for different porosity indices. The flutter type of instability occurs when two real parts of the frequencies of the plate combine together. It is clearly noticed that porosity index substantially affects the flutter response of FGSPs. The results illustrated in Fig. 7.5 indicates that the flutter load and frequencies decreases with increase in the porosity index. The physical reason behind such behaviour is due to stiffness degradation of the plate with increase in the porosity content.

### 7.3.2.4 Effect of sandwich layer scheme

The impact of various sandwich layer scheme on flutter behaviour of porous FCF FGSP ( $a/b = 1.0, b/h = 100$ ) is examined in this section. For this study plates with U-D type of porosity ( $p_i = 0.2$ ) and  $n = 2.0$  is incorporated. The CFSS support condition is considered for the plate. Both symmetric and non-symmetric sandwich layer schemes as mentioned in Table 3.1 are considered for the current study. It can be noticed from Fig. 7.6 that plates with layer scheme 1-2-1 exhibits highest flutter load and frequency

in the order of 1-2-1 > 2-2-1 > 1-1-1 > 2-1-1 > 2-1-2. The FGSP with 1-2-1-layer scheme has larger thickness of the core which contributes towards increase in the stiffness and hence possess higher flutter load and frequency.

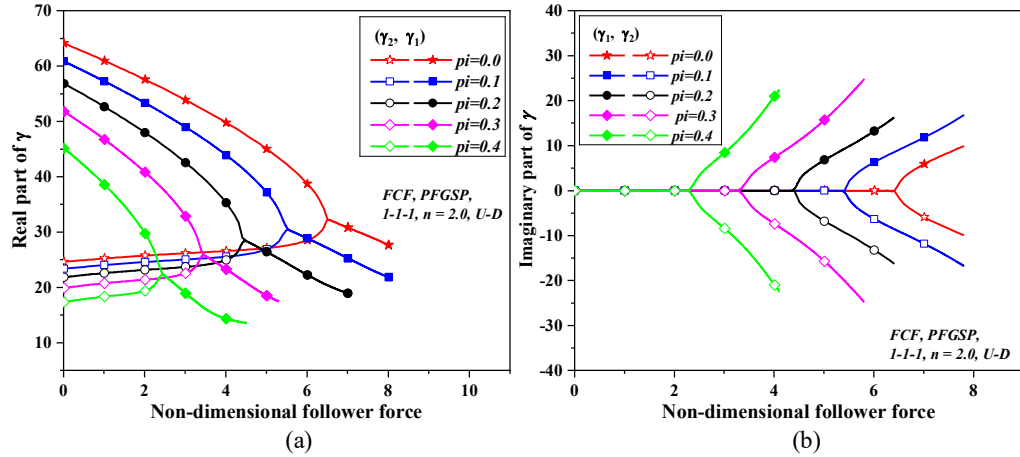


Fig. 7.5 Influence of porosity index on variation of non-dimensional natural frequency (a) real and (b) imaginary part with non-dimensional follower force for CFSS FGSP.

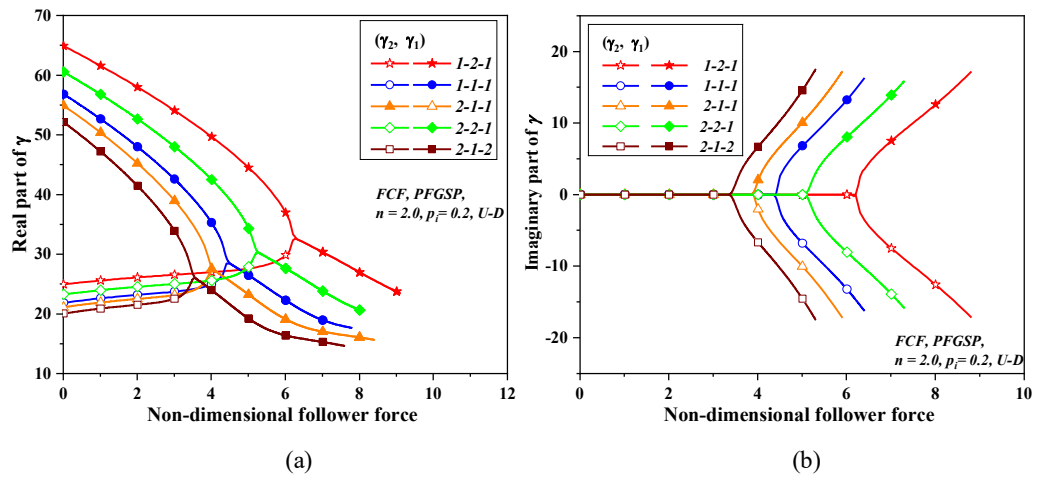


Fig. 7.6 Influence of sandwich layer scheme on variation of non-dimensional natural frequency (a) real and (b) imaginary part with non-dimensional follower force for CFSS FGSP.

### 7.3.2.5 Effect of load control parameter under uniform follower load.

The follower forces act at an  $\varphi \theta_x$  at the boundary, where the term  $\varphi$  denotes the directional control parameter (CP).  $\varphi$  can take up value between 0 to 1.0.  $\varphi = 0$  signifies that plate undergoes divergence type of instabilities. For CFSS boundary conditions, Figs. 7.7(a) and (b) illustrates how control parameter influences the load

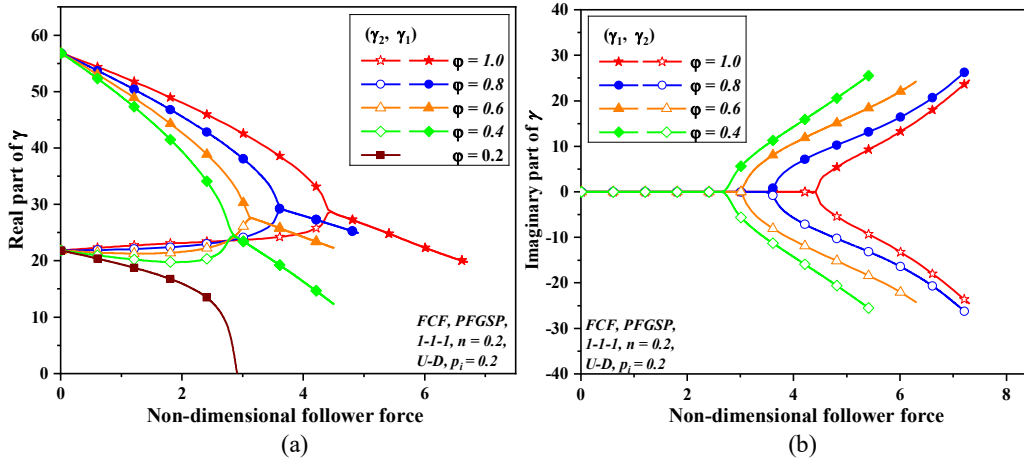


Fig. 7.7 Influence of load control parameter on variation of non-dimensional natural frequency (a) real and (b) imaginary part with non-dimensional follower force for CFSS FGSP.

versus frequency responses of the FCF PFGSP ( $a/b=1.0$ ,  $b/h = 100$ ,  $n = 2.0$ ). The plate is subjected to LL-1. The control parameter considered here ranges from 0.2 to 1.0. From the figures, it is observed that the controlled parameter plays key role on instability behaviour of FGSP. The plate undergoes divergence instabilities at lower control parameter values, as shown in the Fig. 7.7(a) The plates subjected to follower forces having  $\phi > 0.2$  undergoes flutter.

### 7.3.2.6 Effect of different non-uniform follower loads.

The effect of different nonuniform loads on flutter behaviour of porous FCF FGSP ( $a/b = 1.0$ ,  $b/h = 100$ ) is examined in this section. In current investigation plates with U-D type of porosity ( $p_i = 0.2$ ) and  $n = 2.0$  is incorporated. Here plates with CFSS support condition subjected to several loads as mentioned in section 7.2 (Fig. 7.2) is considered. It is observed from Fig. 7.8 that plates subjected to NL-3 exhibits maximum flutter load and frequency, while plates with NL-6 have minimum flutter load and frequency. The load patter of NL-3 is such that it results in tensile stresses in some portion of the plate along with compressive stress. The tensile stresses cause stretching effect and therefore additional load is required to cause the flutter. But in case of plates subjected to NL-3 load, only compressive stresses are formed in the entire plate and thus shows minimum flutter load. Therefore, type of in-plane edge load plays significant role in flutter behaviour of FGSP.

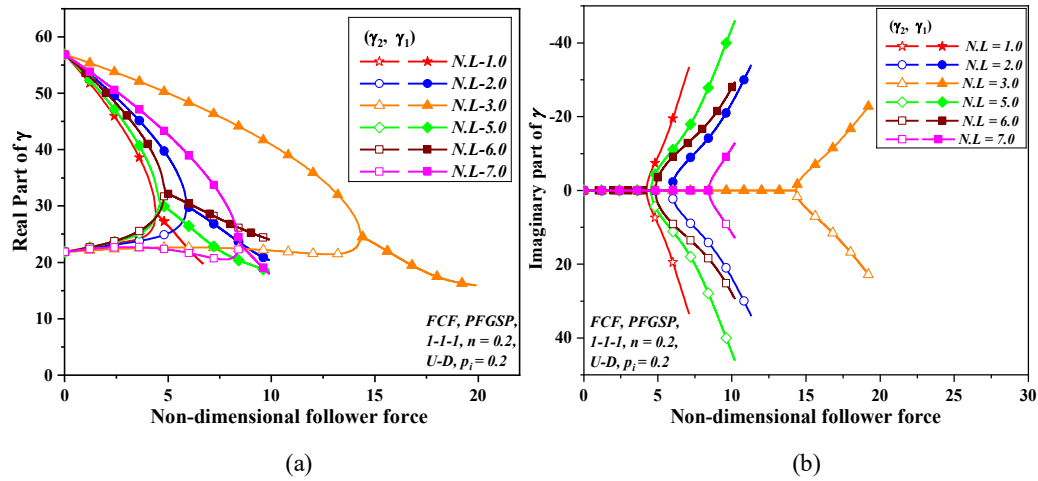


Fig. 7.8 Influence of non-uniform loads on variation of non-dimensional natural frequency (a) real and (b) imaginary part with non-dimensional follower force for CFSS FGSP.

### 7.3.2.7 Effect of aspect ratio

Figs. 7.9 (a) and (b) are plotted to understand the influence of aspect ratio on flutter frequency and loads. Here LL-1 type of in-plane edge loads is considered. For the current study porous FCF PFSP ( $b/h = 100, n = 2.0$ ) with 1-1-1 sandwich configuration and U-D porosity is incorporated. It is clearly observed that the flutter frequency and load are significantly affected by variation of aspect ratio of the plate as observed in Fig. 7.9. It can be discerned from Fig. 7.9 that the flutter load of the plate decreases with increase in the plate aspect ratio. In addition, it is clearly noticed that flutter frequency of the plate is reduced with increase in the aspect ratio of the plate.

### 7.3.2.8 Effect of cutout ratio

The effect of cutout ratio on variation of nondimensional flutter load and frequency is plotted in Fig. 7.10 for porous FCF PFSP ( $a/b = 1.0, b/h = 100, n = 2.0$ ) subjected to LL-1. Here plates with CFSS support condition and 1-1-1 sandwich configuration is considered. The selected plate is having U-D porosity and  $p_i = 0.2$ . As observed in Fig. 7.10(a), the flutter load of the plate decreases with increase in the cutout ratio, due to the decrease in the stiffness of the plate with increase in the cutout ratio. Also, the imaginary part of natural frequency decrease with increase in cutout ratio as noticed in Fig. 7.10(b).

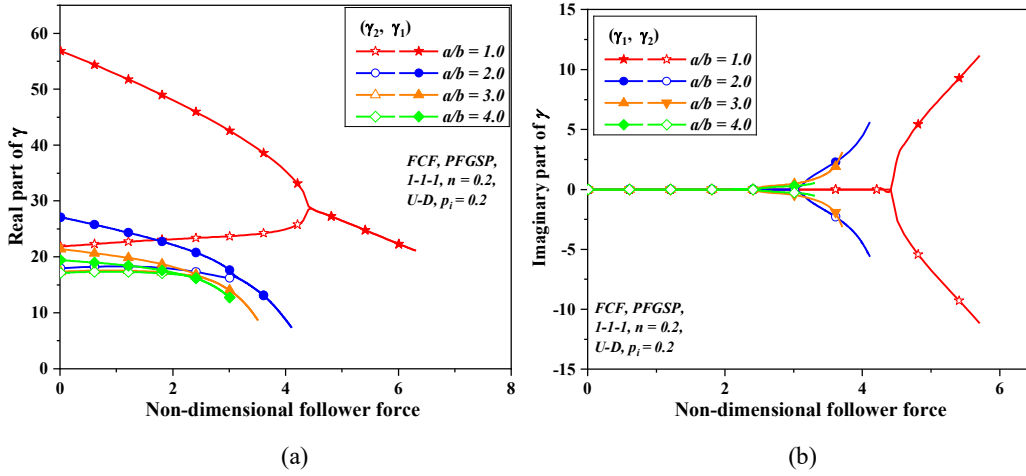


Fig. 7.9 Influence of aspect ratio on variation of non-dimensional natural frequency (a) real and (b) imaginary part with non-dimensional follower force for CFSS FGSP.

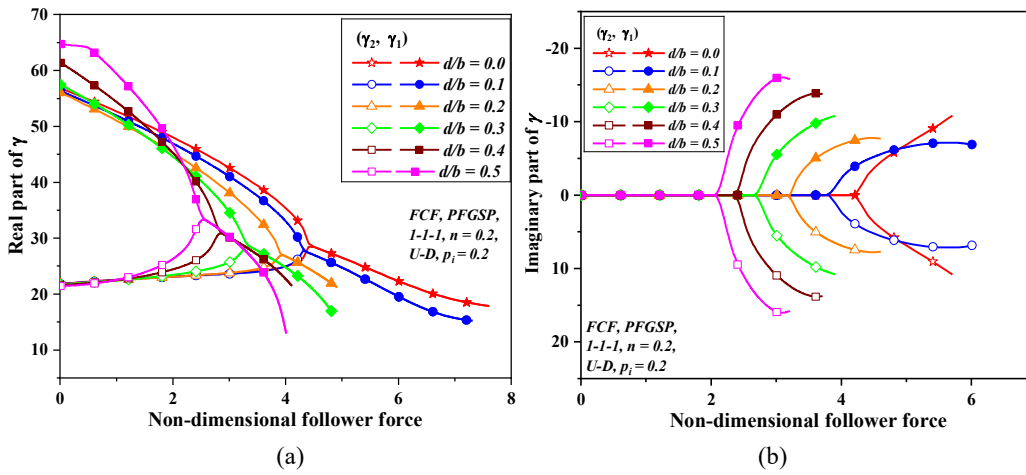


Fig. 7.10 Influence of cutout ratio on variation of non-dimensional natural frequency (a) real and (b) imaginary part with non-dimensional follower force for CFSS FGSP.

### 7.3.2.9 Effect sandwich configuration and material idealization technique

In this section, the influence of sandwich configuration and material idealization technique on flutter loads of porous FGSP with cutout is investigated. For this study FGSP with FCF and MFC sandwich configuration made of power law and sigmoidal function-based material idealization technique is considered. The volume fraction exponents of plate considered here are 0.5, 2.0 and 5.0. Also plates with five different types of porosity distributions (U-D, O-D, X-D, V1-D, V2-D) are considered with 0.1 and 0.4 porosity indices. The plate consists of cutout with  $d/b = 0.3$  and is subjected nonuniform load NL-6. It is noticed from Table 7.4 that with increase in volume fraction exponent and porosity indices the flutter load of the plates was noticed to

decrease. The variation in non-dimensional flutter load due to the increase in the volume fraction exponent is less in case of SFGSP as compared to PFGSPs. For plates

Table 7.4 Influence of sandwich configuration and material idealization technique on non-dimensional flutter load for a CFSS edged FGSP ( $b/h = 100$ ) subjected to NL-6.

Sandwich configuration	Porosity Distribution	$p_i$	Non-dimensional Flutter load						
			PFGSP			SFGSP			
			$n$						
			0.5	2	5	0.5	2	5	
MFC	U-D	0.1	6.071	5.411	5.211	5.841	5.591	5.511	
		0.4	5.691	4.911	4.641	5.461	5.141	5.051	
	O-D	0.1	6.141	5.501	5.301	5.911	5.671	5.591	
		0.4	5.981	5.291	5.071	5.781	5.481	5.401	
	X-D	0.1	6.131	5.481	5.291	5.891	5.651	5.571	
		0.4	5.921	5.211	5.001	5.711	5.421	5.341	
	V1-D	0.1	6.161	5.521	5.331	5.861	5.621	5.541	
		0.4	6.081	5.391	5.191	5.551	5.301	5.221	
	V2-D	0.1	6.101	5.451	5.261	5.861	5.621	5.541	
		0.4	5.831	5.101	4.871	5.551	5.301	5.221	
	FCF	U-D	0.1	8.581	4.461	3.091	6.861	5.881	5.571
			0.4	6.061	1.941	0.571	4.341	3.371	3.051
O-D		0.1	9.011	4.901	3.521	7.301	6.321	6.001	
		0.4	7.801	3.691	2.311	6.091	5.111	4.791	
X-D		0.1	8.981	4.871	3.491	7.261	6.291	5.971	
		0.4	7.671	3.561	2.181	5.961	4.981	4.661	
V1-D		0.1	9.121	5.011	3.641	7.411	6.431	6.121	
		0.4	8.251	4.141	2.761	6.541	5.561	5.241	
V2-D		0.1	8.871	4.751	3.381	7.151	6.171	5.861	
		0.4	7.221	3.111	1.731	5.511	4.531	4.211	

(1-1-1,  $p_i = 0.1$ ) with U-D porosity and FCF configuration the percentage decrease in flutter load is noticed to be 63.9% and 18.8% for PFGSP and SFGSP respectively due to variation in  $n$  from 0.5 to 5.0. And in case of MFC plates the variation is 14.16% and 5.64%. In investigation concerning to sandwich configuration the flutter load is maximum for FCF PFGSP in comparison to MFC PFGSP at lower volume fraction index, but for plates with higher volume fraction exponent flutter load of MFC is greater than FCF plates. At higher  $n$  FCF plates has maximum amount of ceramic as compared to ceramic content in MFC plate as it has central ceramic core sheet. Also, it is observed that for both FCF and MFC plates U-D porosity results in least flutter load in the order

of  $U-D < V2-D < X-D < O-D < V1-D$ , due the distance of pore concentration from the neutral surface plane. The plates with  $U-D$  and  $V2-D$  porosity are noticed to be critical as the maximum variation in flutter load is observed due to increase in porosity indices. Whereas for plates with  $V1-D$  and  $O-D$  in which pores are concentrated close to neutral surface exhibits minimum variation in flutter load.

In addition, it is noticed that reduction in flutter load caused by the increase in porosity indices is greatest in case of FCF plates as compared to MFC plates regardless of material idealisation technique. The reason for such behaviour is due to fact that FCF plates include two layers of porous sheets. For plates with 1-1-1 sandwich layer scheme,  $n = 2.0$  and  $U-D$  porosity, the percentage decrease in flutter load is observed to be 56.48 % and 9.24% in case of FCF and MFC PFGSP. Also, it is inferred from Table 7.4 that the decrease in flutter load with increase in porosity is significant in plates with at higher volume fraction exponent.

#### *7.3.2.10 Effect of localised edge loads and cutout ratio*

The influence of localised edge loads and cutout ratio on variation of flutter load is studied in the present section by considering FCF PFGSP ( $a/b=1.0$ ,  $b/h = 100$ ,  $n = 2.0$ ). The support condition selected for the plate is CFSS. Here sandwich layer scheme of the selected plate is 1-1-1 with  $U-D$  porosity and  $p_i = 0.2$  is considered. For this study plate is considered to be subjected to Type -I and Type-III localised edge loads as illustrated in Fig. 7.1 and cutout ratio is varied from 0.0 to 0.7. The flutter load variation for various load width ratios is plotted in Fig. 7.11. It is noticed from Fig. 7.11 (a) that for lower  $c/b$ , i.e., when the loads are concentrated towards the edge of the plate, the flutter load is maximum. Further it is evident that the flutter load of the plate decreases with increase in  $c/b$  and reaches a minimum for  $c/b = 0.6$ ; thereafter the flutter load increase with  $c/b$  irrespective of the cutout ratio. It is also clear that with increase in the  $d/b$  the flutter load of the plate reduces.

Further, for plate subjected to Type- III load i.e., load applied at central portion of the plate edge, the flutter load increase with increase in the load width ratio regardless of cutout ratio. The flutter load of plate is least when the load width ratio is minimum and highest for  $c/b = 1.0$  (load applied over fully length of the edge). At lower  $c/b$  the load is applied at the central portion of the plate which is less stiff, and hence the flutter load

is less. With increase in the  $c/b$  the load spreads over the higher stiffness zone of the plate the plate resulting from the effect of support restraints and therefore the flutter load is observed to increase.

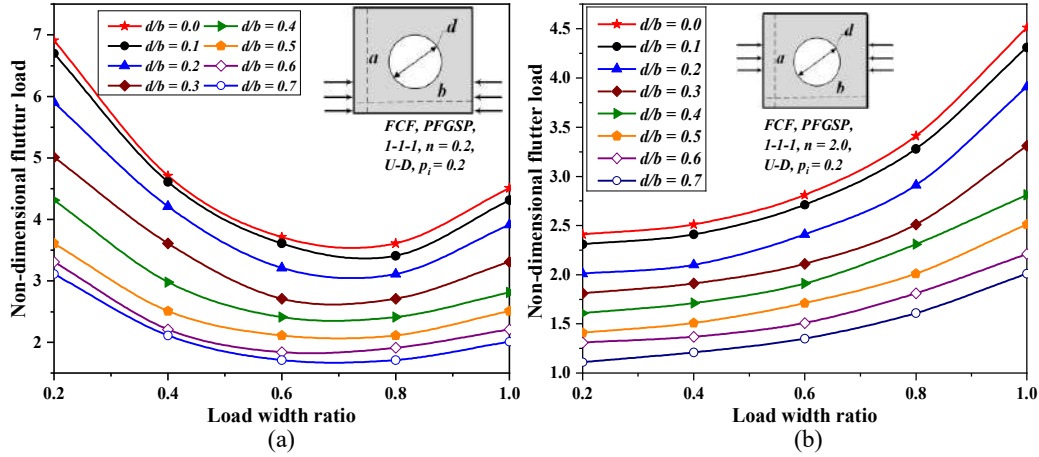


Fig. 7.11 Influence of cutout ratio and load width ratio on variation of non-dimensional flutter load of FCF PFGSP subjected to (a) Type-I and (b) Type-III follower force.

## 7.4 CLOSURE

The dynamic instability analysis results of porous FGSP with/without cutout subjected to localised and NIELs in non-thermal environment using FE method is presented in this chapter. The effective material properties of the FGSP are evaluated using power law and sigmoidal function-based homogenization techniques. The analysis is performed considering FCF and MFC sandwich configurations plates with different type of porosity distributions. The discussion obtained from the analysis are focused to study the influence of porosity, volume fraction exponent, sandwich configuration, different types of in-plane edge loads, cutout and aspect ratio on dynamic instability response of FGSP. The general conclusions based on the several numerous examples and the numerical discussion, suggestions for future research are presented in the following chapter.



## CHAPTER 8

### CONCLUSION

#### 8.1 GENERAL

The present study investigates the vibration and buckling behaviour of porous Functionally Graded Sandwich Plates (FGSP) with and without cutouts subjected to Non-uniform Inplane Edge Loads (NIELs) and localised in-plane edge loads in non-thermal (mechanical) and thermal environment (thermo-mechanical) using Finite Element (FE) method. In addition, the dynamic instability of the FGSP is also studied under a non-thermal environment. The accuracy of current formulation in predicting the natural frequencies and critical buckling loads is established by comparing the numerical results with the available analytical, numerical and experimental solutions in the literature.

On the basis of the analysis carried out and the numerical results obtained through numerous parametric studies, the following conclusions are arrived.

#### **a) Vibration and buckling characteristics of porous FG sandwich plate with/without cutout subjected to localised in-plane edge loads**

1. The results show some significant differences between the vibration and buckling behaviour of the porous FGM plate subjected to localised symmetrical load and that of uniform compressive load. When the applied load was at the centre portion of the edge, the buckling strength dramatically decreased. Therefore, an extra measure must be taken to avoid the elastic buckling of plates when localised edge loading is applied at the centre portion of the plate edge and similarly when concentrated loading is applied at the mid-width of the plate. The plate is less vulnerable to buckling when the localised edges loads are located near the edges of plates.
2. In the case of an FGM plate subjected to Type-III load, the buckling resistance of the plate increases with the increase in the plate aspect ratios. This behaviour is found to be reversed in the case of load Type-II, regardless of load width ratio.

However, it is a combination of the prior behaviour for Type-I and Type-IV loads, both of which are affected by the load width ratio.

3. The increase in volume fraction exponent reduces the buckling strength and natural frequency of the FGM plates due to the passage of material from ceramic to metal where the stiffness of the plate declines.
4. The increase in the porosity indices causes an increase in the porosity concentration, which leads to a reduction in the buckling resistances and natural frequency of the FGM plate due to the reduction in the effective stiffness of the plate.
5. The types of porosity distribution, which is based on the position of the pore concentration, play an essential role in the vibration and buckling behaviour of the FGM plate. The natural frequency and buckling resistance of plates with pores concentrated away from the mid-surface is relatively more affected than those with pores distributed close to the mid-surface. Hence, the influence of U-D type porosity distribution where pores are distributed away from the mid surface on buckling characteristics of FGM sandwich plates (FCF and MFM) is more critical compared to V-D type porosity distribution.
6. For the constant thickness, FCF sandwich configuration with a higher face to core thickness ratio is more affected to change in the porosity indices than MFM sandwich plates in terms of non-dimensional critical buckling load. The higher variation in the former type of sandwich plates is due to the higher thickness of porous sheets than the thickness of sheets without porosity.
7. The buckling resistance offered by the FCF sandwich configuration plates is higher than the MFM sandwich configuration plates with less and no porosity, while for the plates with higher porosity ( $p_i \geq 0.3$ ), MFM offers higher buckling resistance than FCF sandwich configuration irrespective of sandwich layer scheme, load width ratio and type of localised edge loads.
8. Non-dimensional critical buckling load of moderately thick and thick plates have less influence on the various types of porosity distributions.
9. The buckling resistance of FGSP with cutout and subjected to localised edge loads from both end decrease with increase in cutout ratio only when load is acting on complete width of the plate irrespective of  $d/b$ , whereas the buckling resistance

increases as the localised edge load is placed close to two edges of plate with larger  $d/b$ . For plates with cutout and subjected to localised edge loads from center, buckling load decreases with increase in cutout irrespective of load width ratio.

**b) Vibration and buckling analysis of porous FG sandwich plates with/without cutout under non-uniform in-plane edge loads**

1. The NIELs significantly affect the buckling characteristics of porous FGSPs with cutouts. The  $\bar{P}_{cr}$  for simply supported FGSPs with any porosity acted upon by NIELs exhibits decreasing trend with the increase in cutout ratio, except for plates subjected to compressive loads with tensile loads in some portion of the plate edge (i.e., for LL- 5 and NL-4), which shows increase in buckling resistance at larger cutout ratio, i.e., after  $d/b = 0.6$ . Also, plates under LL-5 and NL-4 are more sensitive to a reduction in buckling strength due increase in porosity indices as compared to other cases of load.
2. The rise in the volume fraction exponent for porous FGSPs with different cutouts ratios shows reductions in  $\bar{\omega}$  as well as  $\bar{P}_{cr}$  because of the rise in the amount of metal components in the FG plate. Further, the reductions in buckling resistance with an increase in volume fraction exponent is substantial in the case of PFGSP as compared to SFGSP with any cutout ratio.
3. The impact of variation in porosity indices on  $\bar{\omega}$  and  $\bar{P}_{cr}$  of FGSPs with the cutouts is more pronounced in the plate with large amount of metal composition, whereas the effect of variation in porosity indices reduces as the ceramic percentage increases irrespective of non-uniform loading cases and cutout ratios.
4. Plates with V1-D porosity having pores near the mid-surface exhibits the highest buckling load, whereas plates with U-D have the least buckling resistance as the position of pore concentration is away from the mid-surface. Also, U-D shows a noticeable decrease in  $\bar{P}_{cr}$  and  $\bar{\omega}$  due to the increase in porosity indices compared to V1-D regardless of cutout ratio and nonuniform load cases.
5. The porosity distribution models (U-D and O-D) can result in negative Young's modulus of FGSPs with/without cutouts beyond certain porosity indices ( $p_i > 0.3$ ) and volume fraction exponent, which is not possible in actual practice. This indicates the limitation of those models. Also, the influence of porosity distribution

models U-D and O-D on buckling characteristics is more critical than counterparts for the same percentage of porosity.

6. For constant plate thickness, the thickness of the porous face/core sheet significantly affects the buckling strength of FGSPs. The MFC with a thicker core and thinner face sheet is more susceptible to variation in porosity indices, while in the case of FCF, it's vice versa, regardless of the nonuniform loading case and cutout ratio.
7. Compared to the position of the cutouts with a lower cutout ratio, variations in the position of the cutouts with a higher cutout ratio along the loading direction have a substantial impact on the buckling strengths of FGSPs with porosity and subjected to NIELs.
8. The buckling resistance of FGSPs with cutout reduces with an increase in the cutout ratio in the case of a square plate. The variation in buckling resistance for rectangular plate, i.e., aspect ratio  $a/b > 1.0$ , follows a reverse trend regardless of porosity indices and nonuniform loading case.
9. The CCCC plates show a noticeable reduction in buckling resistance with an increase in porosity indices, followed by plates with SSCC, SSSS and CCFF support conditions.

### **c) Vibration and buckling analysis of porous FG sandwich plates with/without cutout under thermo-mechanical loads**

1. The plate with NIELs distributed towards the corner along the edges of the plate (i.e., LC-3 and LC-6) exhibits higher  $\bar{\omega}$  and  $\bar{P}_{cr}$  as compared to the plates with equivalent uniformly distributed load case (i.e., LC-1 and LC-2) irrespective of cutout size, temperature rise and porosity.
2. The  $\bar{P}_{cr}$  of simply supported FGSP decreases with an increase in cutout ratio, irrespective of the sandwich configuration, loading pattern, porosity and temperature rise considered. While  $\bar{\omega}$  of the FGSP increases with the increase in cutout ratio for plates without any in-plane edge load, and the trend reverses as the magnitude of in-plane edge load increases.

3. The V2-D porosity with the concentration of pores away from the neutral surface significantly affects the vibration and buckling characteristics of the plate under thermomechanical loads. At the same time, O-D porosity has the least effect.
4. The variation of  $\bar{P}_{cr}$  due to change in porosity index and volume fraction exponent is more substantial in FGSP modelled with power law function than the plates with sigmoidal function.
5. The  $\bar{P}_{cr}$  decreases with an increase in porosity index in the case of FCF FGSP, irrespective of temperature rise. While for MFC FGSP, the  $\bar{P}_{cr}$  decreases with an increase in porosity index at a lower temperature rise but increases at a higher temperature. Also, FCF FGSP displays more significant variation in  $\bar{P}_{cr}$  with volume fraction exponent than MFC FGSP regardless of material idealization.
6. The  $\bar{\omega}$  and  $\bar{P}_{cr}$  of plate decrease with increase in the temperature irrespective of porosity and cutout ratio. The variation in  $\bar{P}_{cr}$  with an increase in porosity index is prominent in the case of plates subjected to smaller temperature rise irrespective of cutout ratio and porosity distribution.
7. With the increase in edge constraints at the plate boundaries, the thermomechanical load required to buckle the plate increases in the order SSSS < CCSS < CCCC. The buckling load of CCCC plates are more sensitive to changes in porosity indices, followed by CCSS and SSSS plates.
8. Compared to plates with a higher cutout ratio, plates with a lower cutout ratio show a more significant decline in  $\bar{P}_{cr}$  when the porosity index increases.
9. In MFC FGSP subjected to thermomechanical loads,  $\bar{P}_{cr}$  decreases with an increase in volume fraction exponent for plates with  $\alpha_m > \alpha_c$ , while for plates with  $\alpha_c > \alpha_m$ , the  $\bar{P}_{cr}$  increases. Therefore, the constituent materials must be carefully selected for FGSP under thermomechanical loads.

**d) Dynamic instability analysis of porous FG sandwich plate with/without cutout**

1. The flutter load and frequency of the FGSP decrease with the volume fraction exponent increase.
2. The FGSP with cutout undergo divergence instability at the lower load control parameter, and the plate experiences flutter when the control parameter increases.

3. The flutter load and frequency of the FGSP decreases with an increase in the porosity index.
4. The FGSP with layer scheme 1-2-1 exhibit the highest flutter load and frequency in the order of 1-2-1 > 2-2-1 > 1-1-1 > 2-1-1 > 2-1-2.
5. The porosity distribution significantly affects the flutter behaviour of FGSP. The plates with U-D and V1-D porosity show the lowest and highest flutter load and frequency respectively and the order is given by UD < V2-D < X-D < O-D < V1-D.
6. The flutter load of FGSP decreases with increase in the cutout size.
7. The FGSP subjected to non-uniform loads NL-3 and NL-1 exhibits highest and least flutter load respectively.
8. The flutter load and frequency of FGSP decreases with increase in the aspect ratio of the plate.
9. In comparison to PFGSP, plates with SFGSP show less decrease in flutter load as the volume fraction exponent rises. FCF PFGSP has a higher flutter load than MFC PFGSP for lower volume fraction exponent, whereas MFC plates have a higher flutter load at higher volume fraction exponents.
10. Regardless of material idealisation process, the reduction in flutter load produced by a rise in porosity indices is greatest in case of FCF plates in comparison to MFC plates.
11. In case of plates subjected to Type-III (i.e., load at center portion) follower force, the flutter load is minimum when localised in-plane edge load is concentrated at central portion of the plate edge. While for plates with Type-I follower force (i.e., load at edge portion) the flutter load is maximum when the load is concentrated only at one edge portion. Here, flutter load decreases and then increases with increase in load width ratio, irrespective of cutout ratio.

## 8.2 SUGGESTIONS FOR FUTURE WORK

- i. The present study is concerned with the vibration, buckling and dynamic instability responses of flat FGM plates. It can be extended to folded plates, shells, variable thickness and skewed structures.

- ii. The proposed formulation is limited to the First-order Shear Deformation Theory (FSDT). It has the potential to be expanded to include improved Higher order Shear Deformation Theories (HSDT).
- iii. The vibration, buckling and dynamic instability analysis can be performed in hygrothermomechanical environment by considering linear and nonlinear temperature distribution across the thickness of the FGSP.



## REFERENCE

- Abolghasemi, S., Eipakchi, H. and Shariati, M. (2019). “An analytical solution for buckling of plates with circular cutout subjected to non-uniform in-plane loading.” *Arch. Appl. Mech.*, 89(12), 2519–2543.
- Adali, S. (1982). “Stability of a rectangular plate under nonconservative and conservative forces.” *Int. J. Solids Struct.*, 18(12), 1043–1052.
- Addou, F. Y., Meradjah, M., Bousahla, A. A., Benachour, A., Bourada, F., Tounsi, A. and Mahmoud, S. R. (2019). “Influences of porosity on dynamic response of FG plates resting on Winkler/Pasternak/Kerr foundation using quasi 3D HSDT.” *Comput. Concr.*, 24(4), 347–367.
- Adhikari, B., Dash, P. and Singh, B. N. (2020). “Buckling analysis of porous FGM sandwich plates under various types nonuniform edge compression based on higher order shear deformation theory.” *Compos. Struct.*, 251, 112597.
- Akbaş, Ş. D. (2017). “Vibration and static analysis of functionally graded porous plates.” *J. Appl. Comput. Mech.*, 3(3), 199–207.
- Atmane, H. A., Bedia, E. A. A., Bouazza, M., Tounsi, A. and Fekrar, A. (2016). “On the thermal buckling of simply supported rectangular plates made of a sigmoid functionally graded Al/Al<sub>2</sub>O<sub>3</sub> based material.” *Mech. Solids*, 51, 177–187.
- Bakoura, A., Bourada, F., Bousahla, A. A., Tounsi, A., Benrahou, K. H., Tounsi, A., Al-Zahrani, M. M. and Mahmoud, S. R. (2021). “Buckling analysis of functionally graded plates using HSDT in conjunction with the stress function method.” *Comput. Concr.*, 27(1), 73–83.
- Bansal, G., Gupta, A. and Katiyar, V. (2020a). “Vibration of porous functionally graded plates with geometric discontinuities and partial supports.” *Proc. Inst. Mech. Eng. Part C J. Mech. Eng. Sci.*, 234(21), 4149–4170.
- Bansal, G., Gupta, A. and Katiyar, V. (2020b). “Influence of geometric discontinuities and geometric/microstructural defects on the temperature-dependent vibration response of functionally graded plates on elastic foundation.” *J. Brazilian Soc. Mech. Sci. Eng.*, 42, 1–24.

- Bathe, K. J. (2014). "Finite Element Procedures.", 2<sup>nd</sup> Edition, *Klaus-Jurgen Bathe*, Massachusetts.
- Bekkaye, T. H. L., Fahsi, B., Bousahla, A. A., Bourada, F., Tounsi, A., Benrahou, K. H., Tounsi, A. and Al-Zahrani, M. M. (2020). "Porosity-dependent mechanical behaviours of FG plate using refined trigonometric shear deformation theory." *Comput. Concr.*, 26(5), 439–450.
- Biswas, S., Datta, P. K. and Kong, C. D. (2012). "Buckling, vibration, and flutter behaviour of laminated composite panels with flaws subjected to nonuniform follower forces." *J. Eng. Mech.*, 138(4), 347–357.
- Bodaghi, M., and Saidi, A. R. (2011). "Stability analysis of functionally graded rectangular plates under nonlinearly varying in-plane loading resting on elastic foundation." *Arch. Appl. Mech.*, 81, 765–780.
- Burlayenko, V. N. and Sadowski, T. (2020). "Free vibrations and static analysis of functionally graded sandwich plates with three-dimensional finite elements." *Meccanica*, 55(4), 815–832.
- Chaabani, H., Mesmoudi, S., Boutahar, L. and Bikri, K. E. (2022). "Buckling of porous FG sandwich plates subjected to various non-uniform compressions and resting on Winkler–Pasternak elastic foundation using a finite element model based on the high-order shear deformation theory." *Acta Mech.*, 233(12), 5359–5376.
- Chakraverty, S. and Pradhan, K. K. (2014). "Free vibration of exponential functionally graded rectangular plates in thermal environment with general boundary conditions." *Aerosp. Sci. Technol.*, 36, 132–156.
- Chen, D., Yang, J. and Kitipornchai, S. (2019). "Buckling and bending analyses of a novel functionally graded porous plate using Chebyshev-Ritz method." *Arch. Civ. Mech. Eng.*, 19(1), 157–170.
- Chen, X. L. and Liew, K. M. (2004). "Buckling of rectangular functionally graded material plates subjected to nonlinearly distributed in-plane edge loads." *Smart Mater. Struct.*, 13(6), 1430–1437.

- Chung, Y. L. and Chi, S. H. (2001). “The residual stress of functionally graded materials.” *J. Chinese Inst. Civ. Hydraul. Eng.*, 13, 1–9.
- Cook, R. D., Malkus, D. S., and Plesha, M. E. (1989). “Concepts and applications of finite element analysis.” 3<sup>rd</sup> Edition, *John Wiley and Sons*, New York.
- Daikh, A. A. and Megueni, A. (2018). “Thermal buckling analysis of functionally graded sandwich plates.” *J. Therm. Stress.*, 41(2), 139-159.
- Daikh, A. A. and Zenkour, A. M. (2019). “Free vibration and buckling of porous power-law and sigmoid functionally graded sandwich plates using a simple higher-order shear deformation theory.” *Mater. Res. Express*, 6(11), 115707.
- Datta, P. K. and Biswas, S. (2011). “Aeroelastic behaviour of aerospace structural elements with follower force: A review.” *Int. J. Aeronaut. Sp. Sci.*, 12(2), 134–148.
- Datta, P. K. and Deolasi, P. J. (1996). “Dynamic instability characteristics of plates subjected to partially distributed follower edge loading with damping.” *Proc. Inst. Mech. Eng. Part C J. Mech. Eng. Sci.*, 210(5), 445–452.
- El-Sawy, K. M. and Nazmy, A. S. (2001). “Effect of aspect ratio on the elastic buckling of uniaxially loaded plates with eccentric holes.” *Thin-Walled Struct.*, 39(12), 983–998.
- Garg, A., Belarbi, M. O., Chalak, H. D. and Chakrabarti, A. (2021). “A review of the analysis of sandwich FGM structures.” *Compos. Struct.*, 258, 113427.
- Ghiasian, S. E., Kiani, Y., Sadighi, M. and Eslami, M. R. (2014). “Thermal buckling of shear deformable temperature dependent circular/annular FGM plates.” *Int. J. Mech. Sci.*, 81, 137–148.
- Gupta, A. and Talha, M. (2018a). “Influence of porosity on the flexural and free vibration responses of functionally graded plates in thermal environment.” *Int. J. Struct. Stab. Dyn.*, 18(1), 1850013.
- Gupta, A. and Talha, M. (2018b). “Influence of initial geometric imperfections and porosity on the stability of functionally graded material plates.” *Mech. Based Des. Struct. Mach.*, 46(6), 693–711.
- Hosseini-hashemi, S., Damavandi, H. R., Akhavan, H. and Omidi, M. (2010). “Free vibration of functionally graded rectangular plates using first-order shear deformation

plate theory.” *Appl. Math. Model.*, 34(5), 1276–1291.

Huang, X. L. and Shen, H. S. (2004). “Nonlinear vibration and dynamic response of functionally graded plates in thermal environments.” *Int. J. Solids Struct.*, 41(9–10), 2403–2427.

Hussein, O. S. and Mulani, S. B. (2018). “Optimization of in-plane functionally graded panels for buckling strength: Unstiffened, stiffened panels, and panels with cutouts.” *Thin-Walled Struct.*, 122, 173–181.

Jaberzadeh, E., Azhari, M. and Boroomand, B. (2013). “Thermal buckling of functionally graded skew and trapezoidal plates with different boundary conditions using the element-free Galerkin method.” *Eur. J. Mech. / A Solids*, 42, 18–26.

Jalali, S. K., Naei, M. H. and Poorsolhjoui, A. (2010). “Thermal stability analysis of circular functionally graded sandwich plates of variable thickness using pseudo-spectral method.” *Mater. Des.*, 31(10), 4755–4763.

Jha, D. K., Kant, T. and Singh, R. K. (2013a). “A critical review of recent research on functionally graded plates.” *Compos. Struct.*, 96, 833–849.

Jha, D. K., Kant, T. and Singh, R. K. (2013b). “Free vibration response of functionally graded thick plates with shear and normal deformations effects.” *Compos. Struct.*, 96, 799–823.

Jin, G., Su, Z., Shi, S., Ye, T., and Gao, S. (2014). “Three-dimensional exact solution for the free vibration of arbitrarily thick functionally graded rectangular plates with general boundary conditions.” *Compos. Struct.*, 108(1), 565–577.

Kaddari, M., Kaci, A., Bousahla, A. A., Tounsi, A., Bourada, F., Tounsi, A., Bedia, E. A. A. and Al-Osta, M. A. (2020). “A study on the structural behaviour of functionally graded porous plates on elastic foundation using a new quasi-3D model: Bending and free vibration analysis.” *Comput. Concr.*, 25(1), 37–57.

Kim, J. H. and Kim, H. S. (2000). “Study on the dynamic stability of plates under a follower force.” *Comput. Struct.*, 74(3), 351–363.

Kiran, M. C., Kattimani, S. C. and Vinyas, M. (2018). “Porosity influence on structural behaviour of skew functionally graded magneto-electro-elastic plate.” *Compos. Struct.*,

191, 36–77.

Kumar, L. R., Datta, P. K. and Prabhakara, D. L. (2003). “Dynamic instability characteristics of laminated composite plates subjected to partial follower edge load with damping.” *Int. J. Mech. Sci.*, 45(9), 1429–1448.

Kumar H. S. N., Kattimani, S. and Nguyen-Thoi, T. (2021). “Influence of porosity distribution on nonlinear free vibration and transient responses of porous functionally graded skew plates.” *Def. Technol.*, 17(6), 1918–1935.

Kumar, V., Singh, S. J., Saran, V. H. and Harsha, S. P. (2021). “Vibration characteristics of porous FGM plate with variable thickness resting on Pasternak’s foundation.” *Eur. J. Mech. A/Solids*, 85, 104124.

Lanhe, W. (2004). “Thermal buckling of a simply supported moderately thick rectangular FGM plate.” *Compos. Struct.*, 64(2), 211–218.

Lal, R., and Saini, R. (2013). “Buckling and vibration of non-homogeneous rectangular plates subjected to linearly varying in-plane force.” *Shock Vib.*, 20(5), 879–894.

Lee, Y. H., Bae, S. I. and Kim, J. H. (2016). “Thermal buckling behaviour of functionally graded plates based on neutral surface.” *Compos. Struct.*, 137, 208–214.

Leipholtz, H. H. E. and Pfenndt, F. (1983). “Application of extended equations of galerkin to stability problems of rectangular plates with free edges and subjected to uniformly distributed follower forces.” *Comput. Methods Appl. Mech. Eng.*, 37(3), 341–365.

Li, Q., Iu, V. P., and Kou, K. P. (2009). “Three-dimensional vibration analysis of functionally graded material plates in thermal environment.” *J. Sound Vib.*, 324(3–5), 733–750.

Li, D., Zhu, H., and Gong, X. (2021). “Buckling analysis of functionally graded sandwich plates under both mechanical and thermal loads.” *Materials (Basel)*, 14(23).

Logan, D. L. (2016). “A first course in the finite element method.” 5<sup>th</sup> Edition, *Cengage learning*, Stanford.

Matsunaga, H. (2009). “Thermal buckling of functionally graded plates according to a 2D higher-order deformation theory.” *Compos. Struct.*, 90(1), 76–86.

- Merdaci, S., Adda, H. M., Hakima, B., Dimitri, R. and Tornabene, F. (2021). “Higher-order free vibration analysis of porous functionally graded plates.” *J. Compos. Sci.*, 5(11), 305.
- Natarajan, S., Chakraborty, S., Ganapathi, M. and Subramanian, M. (2014). “A parametric study on the buckling of functionally graded material plates with internal discontinuities using the partition of unity method.” *Eur. J. Mech. A/Solids*, 44, 136–147.
- Natarajan, S., and Manickam, G. (2012). “Bending and vibration of functionally graded material sandwich plates using an accurate theory.” *Finite Elem. Anal. Des.*, 57, 32–42.
- Noda, N. (1999). “Thermal Stresses in Functionally Graded Materials.” *J. Therm. Stress.*, 22(4–5), 477–512.
- Pandey, S. and Pradyumna, S. (2015). “Free vibration of functionally graded sandwich plates in thermal environment using a layerwise theory.” *Eur. J. Mech. / A Solids*, 51, 55–66.
- Park, S. H. and Kim, J. H. (2000). “Dynamic stability of a completely free circular cylindrical shell subjected to a follower force.” *J. Sound Vib.*, 231(4), 989–1005.
- Prakash, T., Singha, M. K. and Ganapathi, M. (2008). “Thermal postbuckling analysis of FGM skew plates.” *Eng. Struct.*, 30(1), 22–32.
- Prakash, T., Singha, M. K., and Ganapathi, M. (2009). “Influence of neutral surface position on the nonlinear stability behaviour of functionally graded plates.” *Comput. Mech.*, 43(3), 341–350.
- Rasool, M. and Singha, M. K. (2019). “Stability of variable stiffness composite laminates under compressive and shearing follower forces.” *Compos. Struct.*, 225, 111003.
- Reddy, B. S., Kumar, J. S., Reddy, C. E. and Reddy, K. V. K. (2013). “Buckling analysis of functionally graded material plates using higher order shear deformation theory.” *J. Compos.*, 2013.
- Reddy, B. S., Kumar, J. S., Reddy, C. E., & Reddy, V. K. (2014). “Free vibration behaviour of functionally graded plates using higher-order shear deformation theory.”

*J. Appl. Sci. Eng.*, 17(3), 231–241.

Reddy, J. N., and Chin, C. D. (1998). “Thermomechanical analysis of functionally graded cylinders and plates.” *J. Therm. Stress.*, 21(6), 593–626.

Rezaei, R., Shaterzadeh, A. R. and Abolghasemi, S. (2015). “Buckling analysis of rectangular functionally graded plates with an elliptic hole under thermal loads.” 7(1), 41–57.

Rezaei, A. S., Saidi, A. R., Abrishamdari, M., and Mohammadi, M. H. P. (2017). “Natural frequencies of functionally graded plates with porosities via a simple four variable plate theory: An analytical approach.” *Thin-Walled Struct.*, 120, 366–377.

Ruan, M., Wang, Z. M. and Wang, Y. (2012). “Dynamic stability of functionally graded materials skew plates subjected to uniformly distributed tangential follower forces.” *JVC/Journal Vib. Control*, 18(7), 913–923.

Sabir, A. B. and Chow, F. Y. (1986). “Elastic buckling of plates containing eccentrically located circular holes.” *Thin-Walled Struct.*, 4(2), 135–149.

Sah, S. K. and Ghosh, A. (2022a). “Influence of porosity distribution on free vibration and buckling analysis of multi-directional functionally graded sandwich plates.” *Compos. Struct.*, 279, 114795.

Sah, S. K. and Ghosh, A. (2022b). “Effect of porosity on the thermal buckling analysis of power and sigmoid law functionally graded material sandwich plates based on sinusoidal shear deformation theory.” *Int. J. Struct. Stab. Dyn.*, 22(5), 2250063.

Saleh, B., Jiang, J., Fathi, R., Al-hababi, T., Xu, Q., Wang, L., Song, D. and Ma, A. (2020). “30 Years of functionally graded materials: An overview of manufacturing methods, Applications and Future Challenges.” *Compos. Part B Eng.*, 201, 108376.

Shariat, B. S. and Eslami, M. R. (2006). “Thermal buckling of imperfect functionally graded plates.” *Int. J. Solids Struct.*, 43(14–15), 4082–4096.

Sharma, K. and Kumar, D. (2017). “Elastoplastic analysis of FGM plate with a central cutout of various shapes under thermomechanical loading.” *J. Therm. Stress.*, 40(11), 1417–1441.

Sinha, L., Das, D., Nayak, A. N., and Sahu, S. K. (2021). “Experimental and numerical

study on free vibration characteristics of laminated composite plate with/without cut-out.” *Compos. Struct.*, 256, 113051.

Singh, D., Krishna, V., Vemulapalli, P. and Gupta, A. (2022). “Influence of circular cutouts and elastic foundation on vibration characteristics of porous sandwich FGM plates under hygro-thermal environments.” *Mech. Based Des. Struct. Mach.*, 1–27.

Singh, S. J. and Harsha, S. P. (2020a). “Thermal buckling of porous symmetric and non-symmetric sandwich plate with homogenous core and S-FGM face sheets resting on Pasternak foundation.” *Int. J. Mech. Mater. Des.*, 16(4), 707–731.

Singh, S. J. and Harsha, S. P. (2020b). “Analysis of porosity effect on free vibration and buckling responses for sandwich sigmoid function based functionally graded material plate resting on Pasternak foundation using Galerkin Vlasov’s method.” *J. Sandw. Struct. Mater.*, 23(5), 1717–1760.

Singh, S. J., and Harsha, S. P. (2020c). “Thermo-mechanical analysis of porous sandwich S-FGM plate for different boundary conditions using Galerkin Vlasov’s method: A semi-analytical approach.” *Thin-Walled Struct.*, 150, 106668.

Sundaresan, P., Singh, G. and Rao, G. V. (1998). “Buckling of moderately thick rectangular composite plates subjected to partial edge compression.” *Int. J. Mech. Sci.*, 40(11), 1105–117.

Swaminathan, K. and Naveenkumar, D. T. (2014). “Higher order refined computational models for the stability analysis of FGM plates – Analytical Solutions.” *Eur. J. Mech. / A Solids*, 47, 349–361.

Swaminathan, K., Naveenkumar, D. T., Zenkour, A. M. and Carrera, E. (2015). “Stress, vibration and buckling analyses of FGM plates-A state-of-the-art review.” *Compos. Struct.*, 120, 10–31.

Swaminathan, K. and Sangeetha, D. M. (2017). “Thermal analysis of FGM plates – A critical review of various modeling techniques and solution methods.” *Compos. Struct.*, 160, 43–60.

Talha, M. and Singh, B. N. (2010). “Static response and free vibration analysis of FGM plates using higher order shear deformation theory.” *Appl. Math. Model.*, 34(12), 3991–

4011.

Talha, M. and Singh, B. N. (2011). "Thermo-mechanical buckling analysis of finite element modeled functionally graded ceramic-metal plates." *Int. J. Appl. Mech.*, 3(4), 867–880.

Thai, H. T. and Choi, D. H. (2013). "A simple first-order shear deformation theory for the bending and free vibration analysis of functionally graded plates." *Compos. Struct.*, 101, 332–340.

Thai, H. T. and Kim, S. E. (2015). "A review of theories for the modeling and analysis of functionally graded plates and shells." *Compos. Struct.*, 128, 70–86.

Torki, M. E., Kazemi, M. T. and Talaeitaba, S. B. (2015). "Effect of axial deformation on flutter of cantilevered FGM cylindrical shells under axial follower forces." *Int. J. Civ. Eng.*, 13(2), 160–170.

Whitney, J. M. and Pagano, N. J. (1972). "Shear deformation in heterogeneous anisotropic Plates." *J. Compos. Mater.*, 6(2), 316–319.

Udupa, G., Rao, S. S. and Gangadharan, K. V. (2014). "Functionally Graded Composite Materials: An Overview." *Procedia Mater. Sci.*, 5, 1291–1299.

Uymaz, B. (2021). "Buckling characteristics of FGM plates subjected to linearly varying in-plane loads." *Mech. Compos. Mater.*, 57, 69–80.

Van Do, V. N. and Lee, C. H. (2019). "Free vibration analysis of FGM plates with complex cutouts by using quasi-3D isogeometric approach." *Int. J. Mech. Sci.*, 159, 213–233.

VanVinh, P. and Huy, L. Q. (2021). "Finite element analysis of functionally graded sandwich plates with porosity via a new hyperbolic shear deformation theory." *Def. Technol.*, 18(3), 490–508.

Vynnycky, M. (2020). "On the formation of centreline shrinkage porosity in the continuous casting of steel." *J. Math. Ind.*, 10(1), 14.

Yaghoobi, H. and Yaghoobi, P. (2013). "Buckling analysis of sandwich plates with FGM face sheets resting on elastic foundation with various boundary conditions: An analytical approach." *Meccanica*, 48, 2019–2035.

- Yu, T., Bui, T. Q., Yin, S., Doan, D. H., Wu, C. T., Do, T. Van, and Tanaka, S. (2016). “On the thermal buckling analysis of functionally graded plates with internal defects using extended isogeometric analysis.” *Compos. Struct.*, 136, 684–695.
- Zang, M., Hu, Y., Zhang, J., Yang, M., Ye, W., and Mao, G. (2021). “Experimental and numerical studies on free vibration of CFRP laminate with cutout.” *Compos. Struct.*, 269, 114014.
- Zenkour, A. M. (2005). “A comprehensive analysis of functionally graded sandwich plates: Part 2-Buckling and free vibration.” *Int. J. Solids Struct.*, 42(18–19), 5243–5258.
- Zenkour, A. M. and Sobhy, M. (2010). “Thermal buckling of various types of FGM sandwich plates.” *Compos. Struct.*, 93(1), 93–102.
- Zghal, S. and Dammak, F. (2021). “Buckling responses of porous structural components with gradient power-based and sigmoid material variations under different types of compression loads.” *Compos. Struct.*, 273, 114313.
- Zhang, N., Khan, T., Guo, H., Shi, S., Zhong, W. and Zhang, W. (2019). “Functionally graded materials: An overview of stability, buckling, and free vibration analysis.” *Adv. Mater. Sci. Eng.*, 2019.
- Zhao, J., Choe, K., Xie, F., Wang, A., Shuai, C. and Wang, Q. (2018). “Three-dimensional exact solution for vibration analysis of thick functionally graded porous (FGP) rectangular plates with arbitrary boundary conditions.” *Compos. Part B Eng.*, 155, 369–381.
- Zhao, X., Lee, Y. Y. and Liew, K. M. (2009a). “Free vibration analysis of functionally graded plates using the element-free kp-Ritz method.” *J. Sound Vib.*, 319(3–5), 918–939.
- Zhao, X., Lee, Y. Y. and Liew, K. M. (2009b). “Mechanical and thermal buckling analysis of functionally graded plates.” *Compos. Struct.*, 90(2), 161–171.

## LIST OF PUBLICATIONS BASED ON PRESENT RESEARCH WORK

### Publications in Journals:

1. Swaminathan, K., Sachin, H., and Rajanna, T. (2022). "Vibration and stability characteristics of functionally graded sandwich plates with/without porosity subjected to localised edge loadings." *Mechanics Based Design of Structures and Machines*, 51(11), 6254-6292. (Q1, IF: 3.9, SCIE)
2. Swaminathan, K., Sachin, H., and Rajanna, T. (2022). "Influence of porosity and non-uniform in-plane edge loads on vibration and buckling response of power law and sigmoid function-based FG sandwich plates with geometrical discontinuities." *Mechanics Based Design of Structures and Machines*, 51(10), 5636-5668. (Q1, IF:3.9, SCIE)
3. Sachin, H., Swaminathan, K., and Rajanna, T. (2023). "Thermo-Mechanical vibration and buckling analysis of porous FG sandwich plates with geometric discontinuity based on physical neutral surface." *Mechanics of Advanced Materials and Structures*, 1-25. (Q2, IF: 2.8, SCIE)
4. Swaminathan, K., Sachin, H., and Rajanna, T. "Vibration and stability characteristics of functionally graded plates subjected to localised edge loadings." *Journal of The Institution of Engineers (India): Series C*. (Revision Submitted after Review) (SCOPUS)
5. Sachin, H., Rajanna, T., Pavan, G.S., and Swaminathan, K. "Dynamic instability studies of porous functionally graded sandwich plates with and without cutout subjected to nonuniform loads." (To be communicated)

### Publications in Conference Proceedings:

1. Swaminathan, K., Sachin, H., and Rajanna, T. "Buckling analysis of functionally graded materials by dynamic approach." *Proc. of 4<sup>th</sup> International Conference on Advanced Research in Mechanical, Materials and Manufacturing Engineering*, July 9-13, 2020, Bangalore, India.
2. Swaminathan, K., Sachin, H., and Rajanna, T. (2020). "Effect of initial stresses on the vibration behaviour of functionally graded materials." *Proc. of 4<sup>th</sup> International Conference on Advanced Research in Mechanical, Materials and Manufacturing Engineering*, July 9-13, 2020, Bangalore, India.
3. Swaminathan K., Sachin H., Rajanna T. (2020) "Buckling response of functionally graded material plates with cutouts subjected to linearly varying loads." *Proc. of 1<sup>st</sup> Online International Conference on Recent Advances in Computational and Experimental Mechanics*, September 4-6, 2020, Kharagpur, India.
4. Swaminathan K., Sachin H., Rajanna T. (2021) "Effect of porosity distribution on vibration and stability characteristics of FGM plates subjected to nonlinearly varying edge loads." *Proc. of 4<sup>th</sup> International Conference on Advances in Structural Mechanics and Applications*, October 6-8, 2021, Silchar, India.

6. Swaminathan K., Sachin H., and Rajanna T. (2022) “Influence of porosity and temperature load on buckling characteristics of functionally graded material plates.” *Proc. of 13<sup>th</sup> International Symposium on Plasticity and Impact Mechanics*, August 21-26, 2022, Chennai, India.

**Bio- data**

Name : Sachin .H  
Date of birth : 10<sup>th</sup> April 1991  
Permanent Address : #308, Hombisilu, 19<sup>th</sup> main, Vijayanagar 2<sup>nd</sup> stage  
Mysore – 570017,  
(Karnataka) INDIA  
Contact Number : +91-8971660968  
Email : sachin43.h@gmail.com

**Academic Qualification:**

- 1) B. E (Civil) : Visveswaraya Technological, University, Belgaum,  
Sri Jayachamarajendra College of Engineering  
(Autonomous), Mysore, in year 2013
- 2) M. Tech. (Structures) : Manipal Academy of Higher Education, Manipal  
Manipal Institute of Technology, Manipal in year 2016
- 3) Date of Joining Ph.D. : 12<sup>th</sup> July 2017